BNL-NUREG-33940
INFORMAL REPORT
Limited Distribution

CONTAINER ASSESSMENT - CORROSION STUDY OF HLW CONTAINER MATERIALS

QUARTERLY PROGRESS REPORT
July-September 1983

T. M. Ahn, H. Jain and P. Soo

Manuscript Completed November 1983

Prepared by the Nuclear Waste Management Division
D. G. Schweitzer, Head
Department of Nuclear Energy, Brookhaven National Laboratory
Associated Universities, Inc.
Upton, New York 11973

Prepared for the U.S. Nuclear Regulatory Commission
Office of Nuclear Regulatory Research
Contract No. DE-AC02-76CH00016
FIN No. A-3237

ABSTRACT

In addition to presenting work performed in this quarter, a brief summary is given of accomplishments to date on the corrosion failure modes of Grade-12 titanium in simulated rock salt brine at 150°C. In this work, immersion tests and surface analyses have been used to identify the existence of crevice corrosion. Electrochemical studies have provided quantitative data on the classical four-stage crevice corrosion process. Based on this information, simple calculations are performed to give guidelines for long term prediction methods. Repassivation of crevice surfaces is characterized by the observed loss of corrosion current. Hydrogen embrittlement is identified by tensile testing and quantitative information is obtained from slow crack growth tests at various temperatures. Revised hydrogen diffusion models are developed and used to obtain the threshold stress intensity for crack propagation to provide long term prediction of container failure. Grade-12 titanium is found to be immune to stress corrosion cracking in brine. Small changes at the surfaces of stress-corrosion samples are more likely to be caused by internal hydrogen effects, rather than aqueous corrosion. Gamma radiolysis is probably beneficial with respect to crevice corrosion but may cause hydrogen embrittlement. Caustic environments can also cause enhanced hydrogen uptake and uniform corrosion rates although it reduces the crevice corrosion rate. Passive dissolution of metal during uniform corrosion is responsible for the continuous loss of Grade-12 titanium over extended periods. Pitting is observed in the presence of crevice corrosion. Welds generally have less corrosion resistance.

Work has been initiated on the evaluation of corrosion failure for low-carbon steel exposed to basaltic groundwater. Initial studies are directed at measuring the rate of hydrogen uptake in simulated Grande Ronde basaltic water at 150°C under gamma radiolysis conditions.

CONTENTS

CONTENTS (Continued)

FIGURES

FIGURES (Continued)

TABLES

ACKNOWLEDGMENTS

The authors gratefully acknowledge the assistance of R. Jones and C. Anderson in the technical parts of the program. Special thanks are extended to R. Sabatini for electron microscopy, G. Campbell for polarization study, A. L. Hanson for Rutherford Backscattering and INCO for Auger Analysis. Also, they would like to thank G. Searles and M. McGrath for their patience and skill in the typing and preparation of this report.

1. INTRODUCTION

In addition to presenting work performed in this quarter, we summarize in this report all data and analyses carried out to date (FY81-82 and FY82-83) since the work on Grade-12 titanium is scheduled for completion at the end of fiscal year 1983.

We have determined that crevice corrosion and hydrogen embrittlement are the major failure modes in the Grade-12 titanium/brine system. Extensive work on stress corrosion has also been pursued along with radiation effects, caustic corrosion and uniform corrosion. Relatively small efforts have been given to weld evaluation.

Efforts to study carbon steel corrosion in basaltic groundwater environment were initiated this quarter. A brief description of accomplishments to date is given.

2. CREVICE CORROSION OF GRADE-12 TITANIUM

2.1 Electrochemical and Morphological Characteristics

The experimental details of the electrochemical test cell and general observations on the crevice corrosion of Grade-12 titanium in Brine A at ~150°C are described in a paper to be published in an ASTM Special Technical Publication.[1] The abstract of the paper is given in Appendix A. In addition to the results described in previous quarterly reports, this paper describes the sequence of crevice corrosion in neutral 1:10 diluted Brine A. Since a significant amount of corrosion was observed after dilution, a test was also conducted in neutral Brine A which was diluted by a factor of one hundred. The electrochemical behavior of the crevice during this test is shown in Figure 2.1. It was noted that the incubation period starting from the end of the solution heating period to the first breakdown of passivity is approximately 55 hours. A more complete loss of passivity occurs after 70 hours. Figure 2.2 shows the two sides of the pH-specimen after the test. There is considerable corrosion on one side (Figure 2.2a), but the opposite side (Figure 2.2b) having the pH-wells shows only a corrosion film. Therefore, the observed pH (4.5) of the solution is probably higher than what is representative of the severe crevice corrosion conditions of this test. The time dependence of current and potential for the crevice corrosion test in neutral Brine A is shown in Figure 2.3. In this case the pH of the crevice solution was found to be 3.2.

The general features of the variation of current and potential with time are essentially the same for various test conditions, as described in Reference 1. However, in view of the later results shown in Figure 2.1 we note that although a negative current or the drop in potential starts with the heating of the autoclave, it is not limited to the initial solution heating period. Thus, this period of the test may not be characterized as simply a response to the changing temperature, but may be a distinct stage within the incubation period. During this stage the uncoupled potential of the cathode shows a much larger change than that of the anode. The negative current is then consistent with the fact that the cathode is at a lower potential than the anode. At the end of this period, the crevice potential rises, the cathode is once again at a higher potential than the anode, and the current becomes negligible.

The common observations after the initial breakdown of the passive film in all the tests are a decrease in current, and the presence of sharp peaks on this slowly varying current. In the case of neutral and acidic Brine A, the current reaches a negligible positive value. However, for the ten times diluted Brine A the final magnitude of the current is relatively large, and for the hundred times diluted Brine A there appears to be a second major increase in current. After the breakdown of the passive film the decoupled cathode potential varies little (probably due to temperature fluctuations), and the changes in crevice current or potential follow the changes in the anode potential (Figure 2.1). Therefore, a possible explanation for the decrease in current is that the active dissolution of the anode is retarded due to its repassivation, at least in part of the crevice. Glass[2] has recently shown that

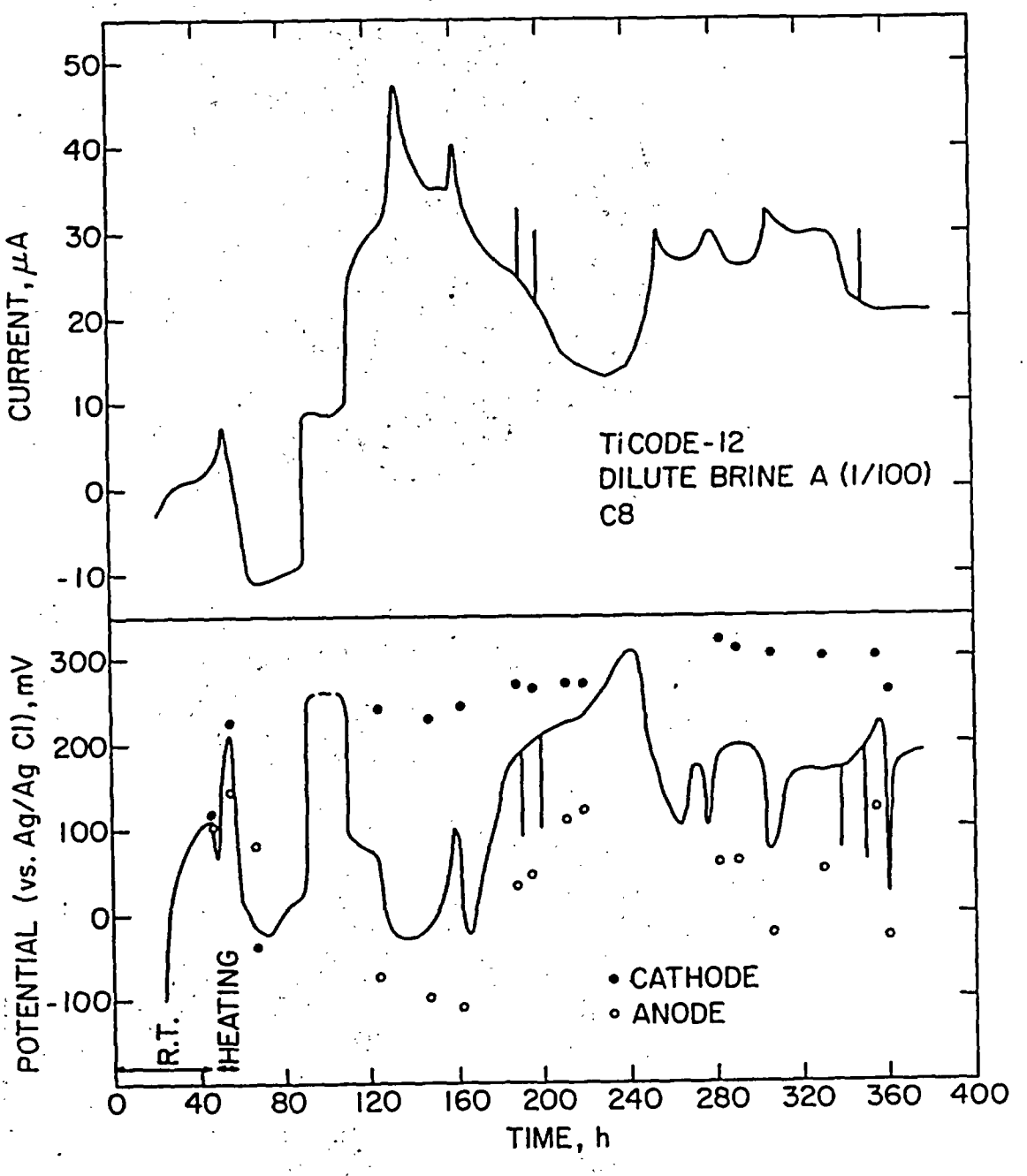

Figure 2.1. Time dependence of current and potential for Grade-12 titanium in one hundred times diluted Brine A. The closed and open circles represent uncoupled potentials of the freely exposed cathode disk and the anode assembly, respectively. The steady state temperature is ~150°C. The broken line between 90 and 110 hours on the potential curve represents the period during which the potential overshot the recorder scale.

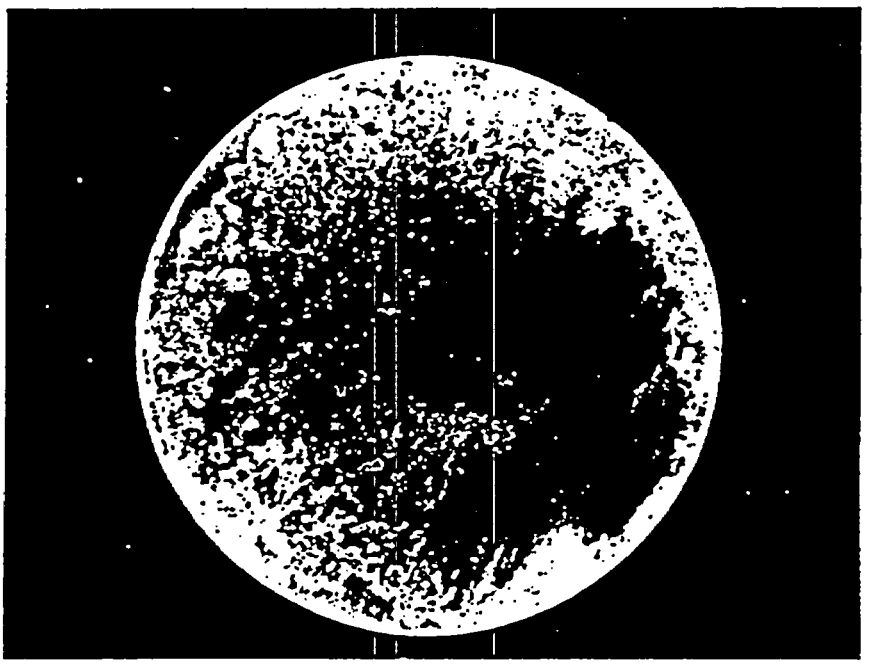

(a)

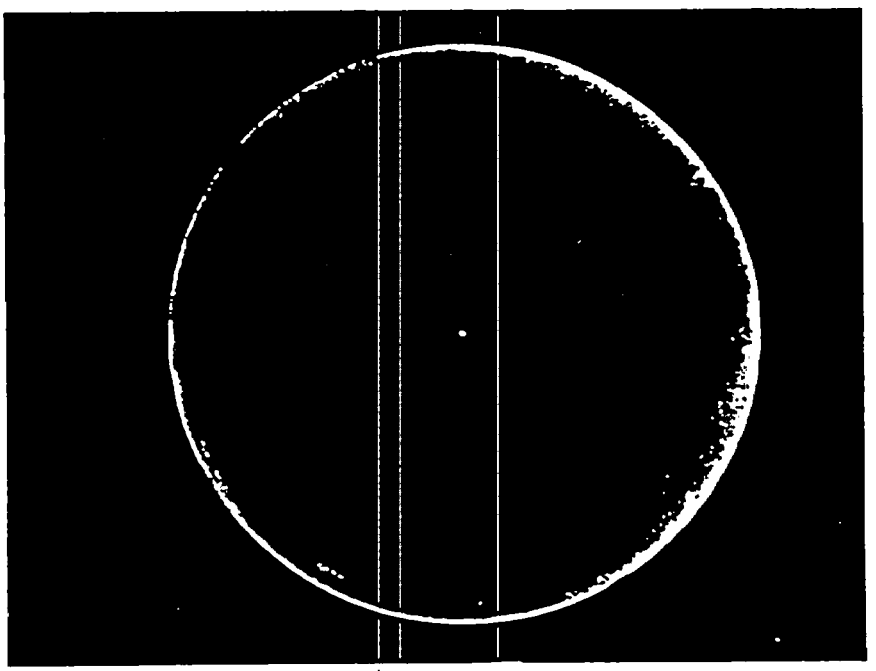

(b)

Figure 2.2. The Grade-12 titanium pH-anode after the test in one hundred times diluted Brine A. (a) Showing severe corrosion and the TiO_2 corrosion product. (b) Showing the oxide scale typical of early stages of corrosion. This side had two small wells to collect the crevice solution.

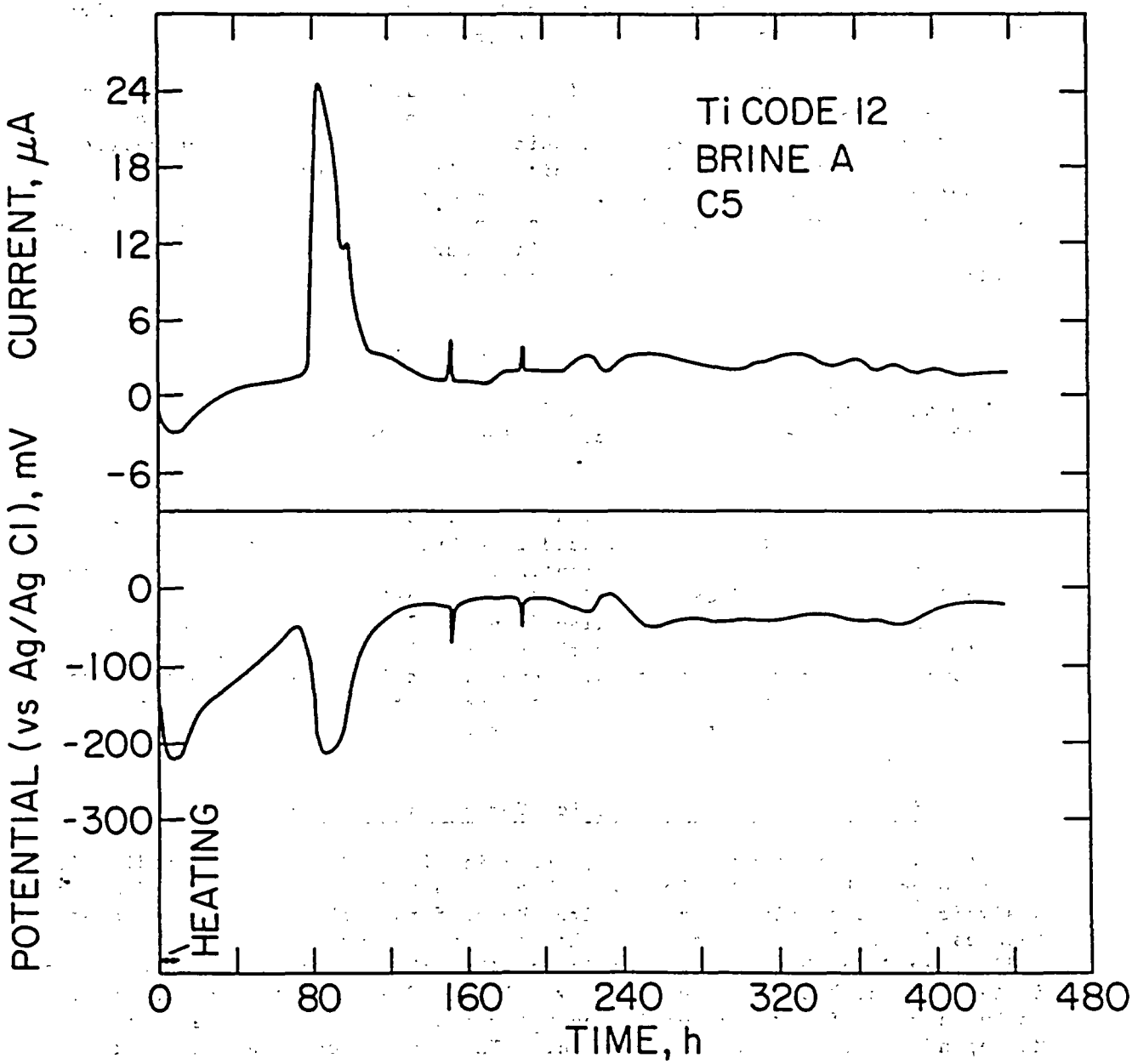

Figure 2.3. Time dependence of current and potential for Grade-12 titanium in neutral Brine A. The steady state temperature is ~150°C.

an active titanium surface in an acidic medium easily passivates if Na_2MoO_4 is added to the solution. This passivation occurs due to the strong bonding of polymolybdate species on the metal surface. Such a mechanism of repassivation is possible in the present tests if the molybdenum present in the solution from the active dissolution of Grade-12 titanium redeposits on the active surface. As mentioned in our earlier reports, an enrichment of molybdenum was sometimes detected by the microprobe analysis of the oxide scale obtained after a crevice corrosion test.

Kelly[3] has shown that a titanium surface actively dissolving in an acidic medium to Ti^{+3} can be repassivated if the local concentration of Ti^{+4} ions exceeds a critical value which is determined by the properties of the crevice solution. At present this critical concentration of Ti^{+4} for our test conditions is not known, but apparently this concentration is more easily achieved in neutral Brine A than in a highly diluted neutral Brine A. Also, the second increase in current in Figure 2.1 can be interpreted as a result of the fluctuation in the concentration of Ti^{+4} which is a mobile ion.

The present crevice corrosion tests were limited to a duration of two weeks. Based on the information from such limited tests, it is very difficult to accurately predict the life of a Grade-12 titanium crevice in Brine A. Nevertheless, several important conclusions are drawn, which will be included in Section 2.4.

Limited efforts have been given to polarization studies*. The intent was to find: (1) the active peak in acidified brine, (2) the overlapping of pitting potential and active peak potential. A small active peak is observed, generally at 90°C, in deoxygenated solutions while the pitting potential drop was not significant as was also found by Sandia National Laboratories.[5] From this study, it is clear that the potential drop inside the crevice is accompanied by active dissolution. However, it is not known whether the observed pitting results from the overlapping of the pitting and active potentials or from a transient phenomenon caused by uniform dissolution at the active peak.

2.2 Chemical Analysis of the Crevice Corrosion Products

Auger spectroscopy results**, shown in Figure 2.4, gave no indication of Ni or Mo enrichment. Previously we have reported the enrichment of Mo in EDAX analysis.[6] To confirm these results, Rutherford Backscattering has also been used***. The results again show that no Mo and Ni are present (Figure 2.5). Based on these results it is possible that the corrosion products originate from the hydrolysis of dissolved ions. The energetics of the hydrolysis is known to be favorable for Ti and unfavorable for Ni, but the hydrolysis of Mo depends on the pH of the solution.[7] Therefore, local variation of pH may

* This work was performed by G. Campbell, an MIT senior, during his summer work at BNL.

** Work carried out by INCO.

***Work performed by A. L. Hanson, Physics Department, BNL.

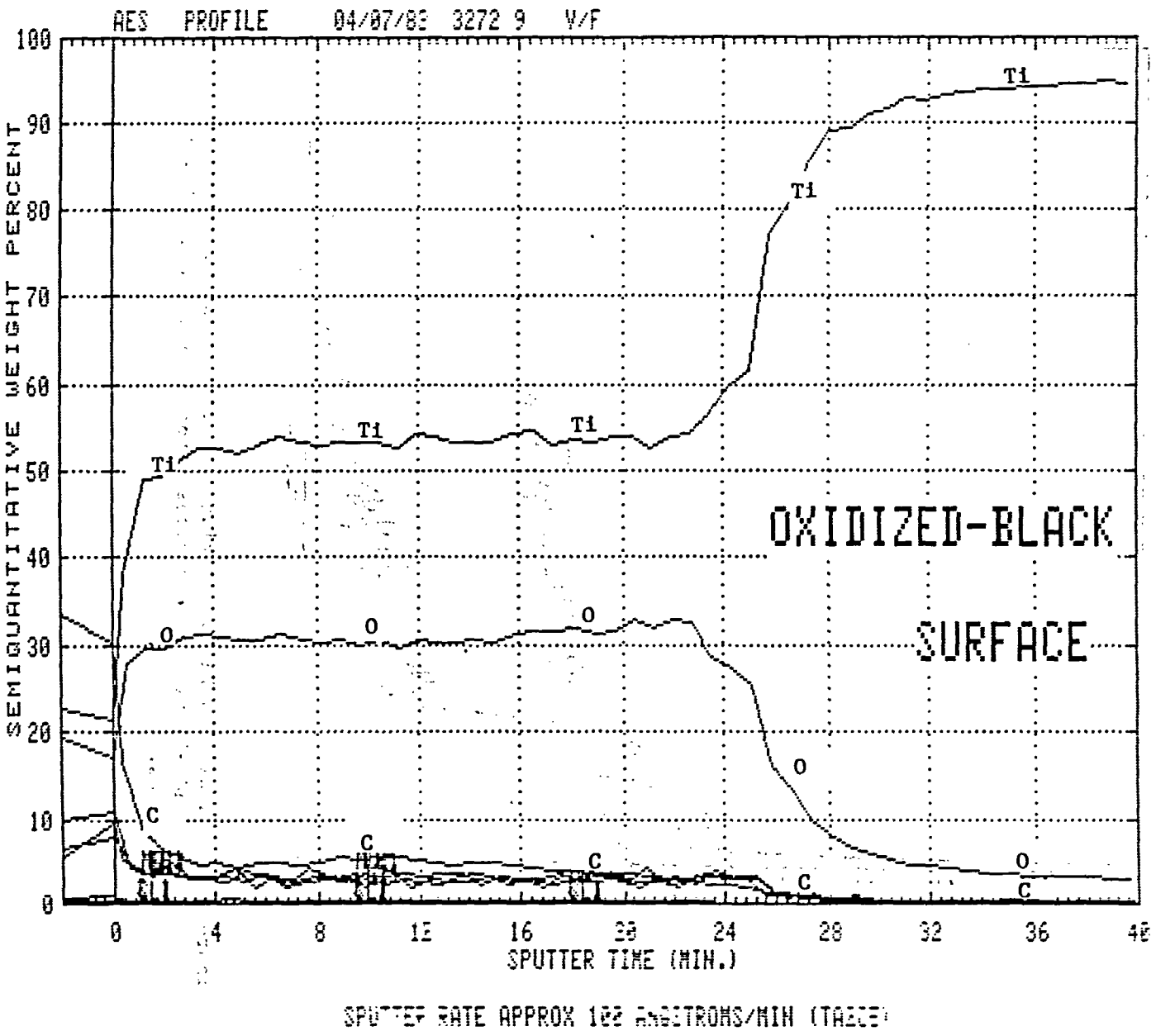

Figure 2.4. Auger profiles of the corrosion products in Grade-12 titanium crevices exposed to aerated Brine A for two weeks.

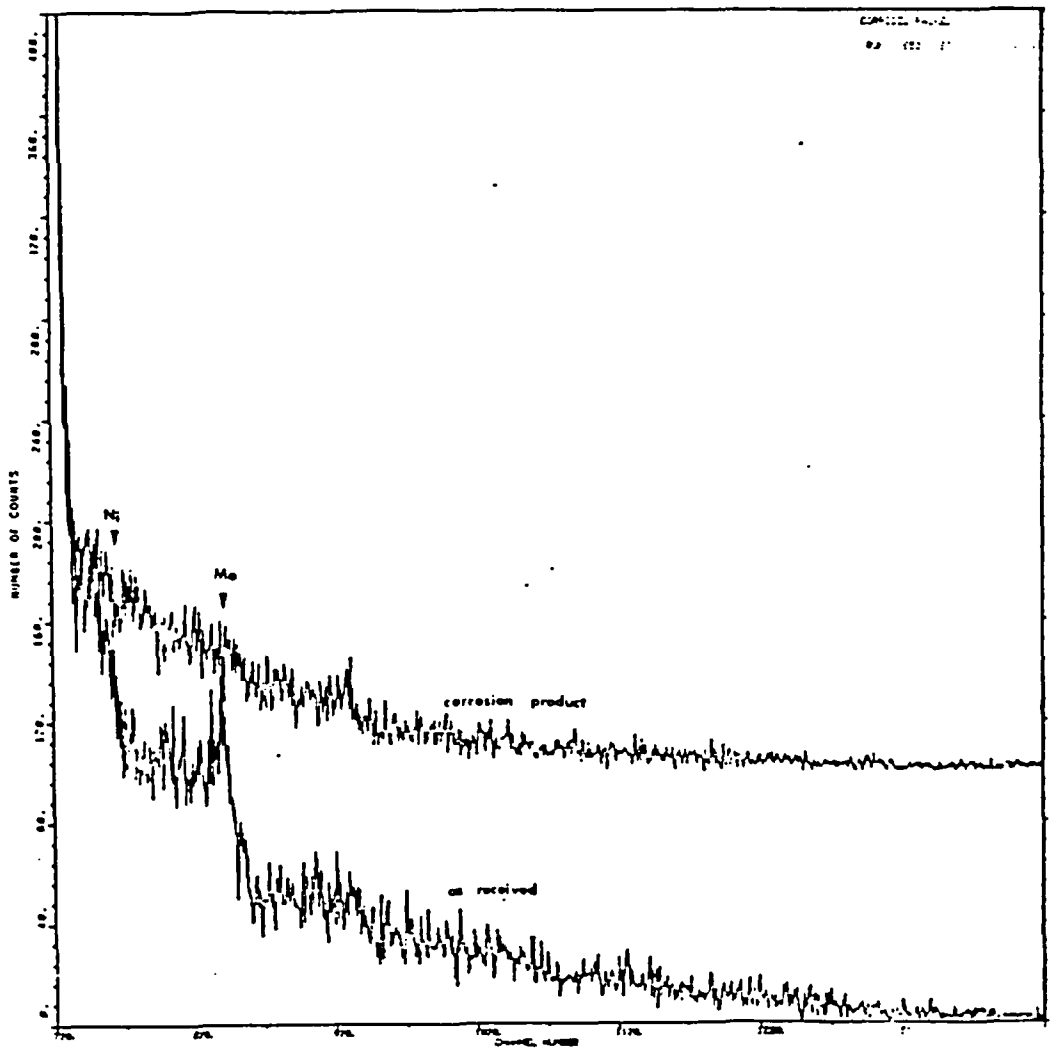

Figure 2.5. Rutherford backscattering profiles of the corrosion products in Grade-12 titanium crevices exposed to aerated Brine A for two weeks.

have resulted in Mo hydrolysis. Recently, the formation of other molybdenum complexes has been suggested,[2] as discussed in Section 2.1. However, it is not known whether molybdate ions are formed in the crevice in addition to Mo^{+2} ions.

2.3 Predictive Models for the Initiation of Crevice Corrosion

A paper describing a model for crevice corrosion initiation has been submitted for publication in Corrosion '84.[8] The abstract is given in Appendix B.

A summary will be given of the data fitting procedure using the basic formulation proposed in the last quarterly progress report.[9] A slight modification of the formulation is used in the calculation. We have used the initial values of current and potential as those measured at the time when appreciable current flow (~1 μA range) is observed. The anode potential increases continuously during the growth of a barrier oxide (anatase form of TiO_2)[10,11] until the maximum potential is reached. After the maximum potential, anatase starts to disappear or become unstable with the change in solution chemistry. Probably, porous rutile is forming and dissolving continuously in this stage. While the oxide is mainly responsible for the electrode potential, the potential change is also influenced by solution chemistry changes, namely, (1) a potential drop caused by oxygen concentration change,[12,13] (2) an ohmic potential drop,[14,15] (3) a potential rise due to pH change,[13] (4) a potential rise due to excess proton generation. Contribution (2) is approximately negated by contribution (3) based on calculations for estimating the ohmic potential.[15] Also, contribution (4) is, typically, negligible because of the conservation of charge neutrality. Therefore, below the maximum potential, the net effects of oxide growth and oxygen depletion are observed.

After the maximum potential is reached, the potential drop is determined by complicated corrosion processes. The complicated potential drop may be explained by two hypotheses. The first hypothesis is that the potential drop from the oxide thinning and subsequent transition to a monolayer[4] appears as a Flade potential[12] (the Flade potential is the potential before rapid decay of passivity to the active state). The second hypothesis is that complete oxygen removal is a prerequisite for the potential drop.[16] As a consequence of oxygen depletion, the oxide film starts to thin and dissolve due to the presence of chloride ions,[4] or chloride ions penetrate the oxide without thinning the film first.[17,18] Since the initial chloride ion concentration and pH did not affect the initiation time significantly, it is reasonable to conclude that complete oxygen depletion is an important factor for the initiation of the passivity breakdown. This is accompanied by a significant potential drop in the anodic region.[16] We adopt the second hypothesis for this reason. This also eliminates the consideration of the complicated kinetic process of monolayer formation at the Flade potential in pits (not on the whole surface), which is not formulated in the current study.

The best fit to our experimental data is shown in Figure 2.6 for $\delta = 0.3$ cm (effective distance of concentration gradient), $Ip = 7.6 \times 10^{-10}$ amp/cm^2

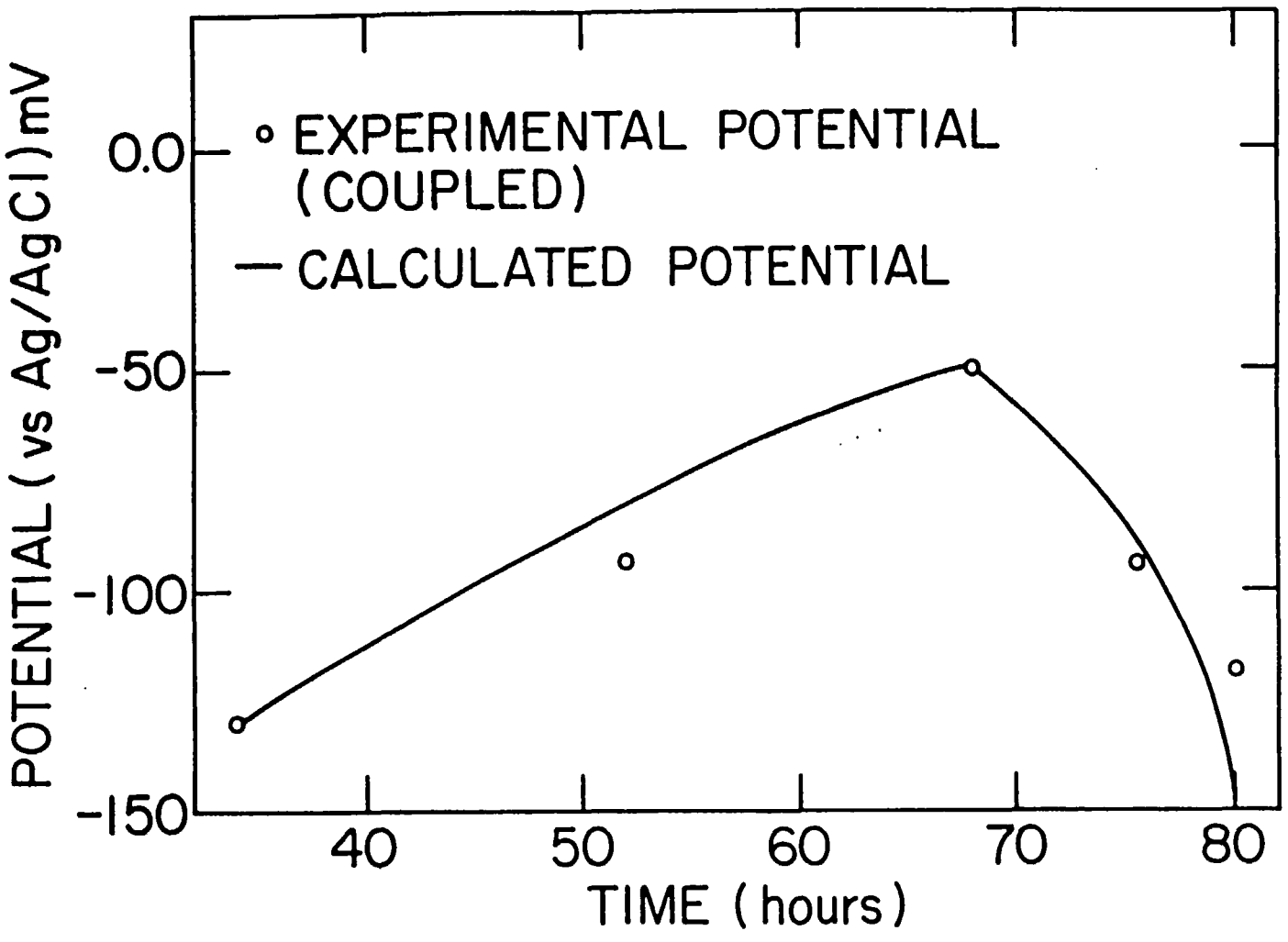

Figure 2.6. Experimental potential (open circles) and calculated potential (solid line) of coupled Grade-12 titanium crevices in aerated neutral Brine A at 150°C.

(passive current with oxygen reduction), c = 2.5×10^{-7} cm/volt[19,20] (a proportionality constant between oxide thickness and electrode potential), crevice depth = 2.54 cm, crevice gap = 2 μm, an oxygen diffusivity (cm^2/sec) of 0.0821 exp(-2440/T),[21] a proton diffusivity (cm^2/sec) of 0.02838 exp (-1700/T),[21] chloride diffusivity (cm^2/sec) of 0.0508 exp(-2327/T),[21] and an anatase density of 3.84 gm/cc. Very little change occurs in Figure 2.6 with a current variation of 0.24 to 10 μA/cm^2 because the main potential drop arises from oxygen effects. Figure 2.7 shows the concentration profiles in the crevice at various testing times for a current density of 10 μA/cm^2. Because the brine solution has a near saturated Cl^- ion concentration, the calculated large value indicates the types of precipitates which may form. Also, the low pH level indicates that the actual pH at higher temperatures is much lower than that measured at room temperature. Two curves are shown for oxygen concentrations. As expected, increased crevice gap size delays the oxygen depletion time significantly.

As described in previous BNL work[9] the solution within a crevice will tend to a limiting composition as corrosion time tends to infinity. From the predictive equations developed it has been shown that there is no limiting pH, and this parameter can theoretically fall to extremely low values within the crevice. Table 2.1 uses the approach described in Reference 9 to compute the limiting values of Cl^- concentration within the crevice for assumed values of pH. Note that these Cl^- levels are in excess of 10^6 ppm which is not physically possible. However, the analytical approach serves to show that extremely high levels of chloride will accumulate with time. Other anion species have not been considered in this work because of their much lower diffusivities compared to that for chloride ions.[22]

Table 2.1. Calculated limiting chloride concentrations in the crevice of Grade-12 titanium in aerated neutral Brine A at 150°C and infinite time.

Limiting pH	-1	0	1	2	3
Limiting Cl^- Concentration (ppm)	3,690,560	3,279,590	2,815,420	2,377,850	1,940,280

The initial Cl^- concentration is 190,000 ppm. A Cl^- concentration of more than 10^6 ppm implies that there is no theoretical limitation on chloride ion accumulation as time progresses.

The above outline of a crevice corrosion model may be used as a basis for long term corrosion prediction. Using pH = -1.19 in Figure 2.7 and the critical value of chloride ion concentration for passivity breakdown as 190,000 ppm (near-saturation of brine with chloride ions) a map (Figure 2.8) is drawn in the space of temperature and the initial chloride concentration Ci(Cl^-) necessary to attain the critical concentration at various times (detailed

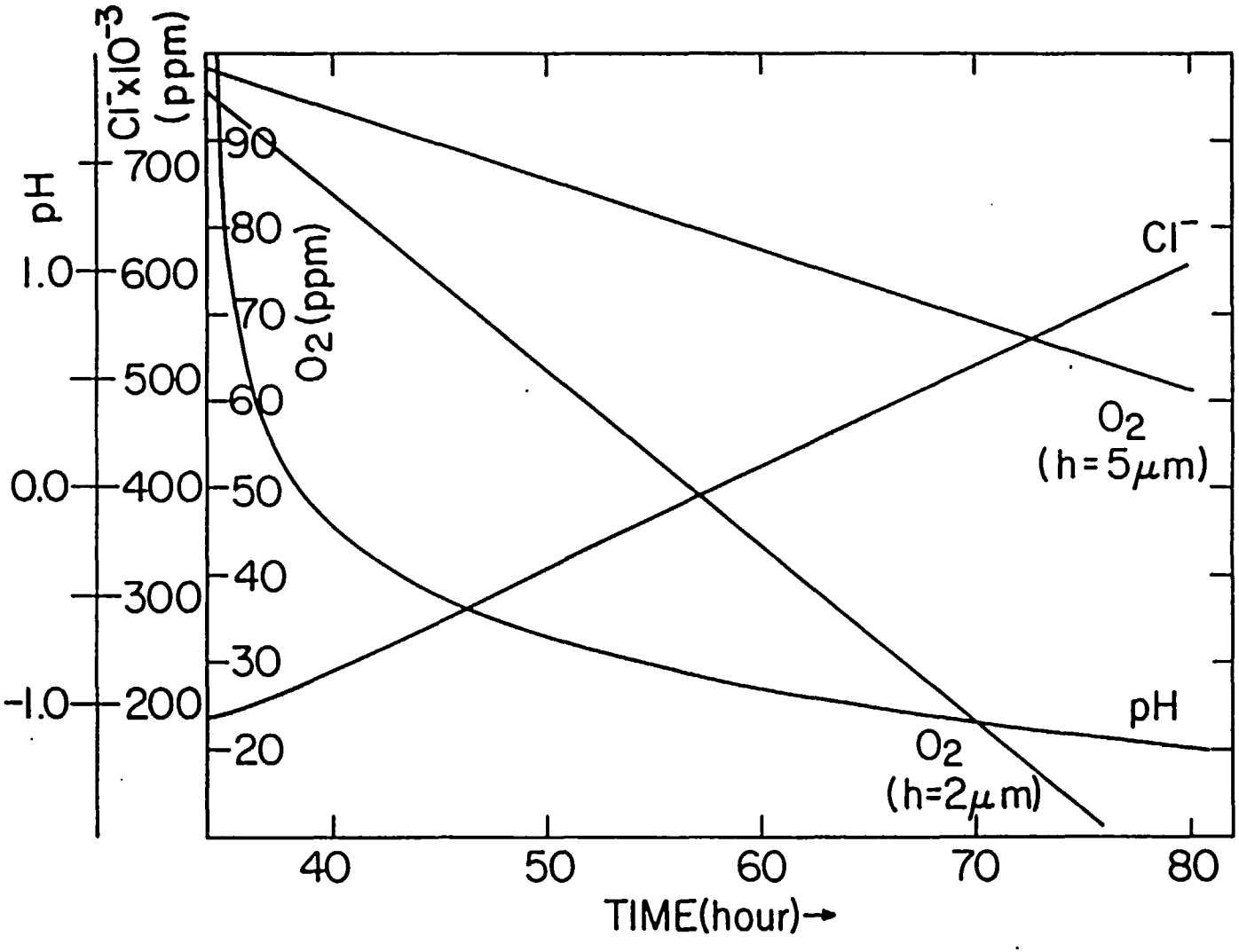

Figure 2.7. Calculated concentration profiles in the crevice of Grade-12 titanium in aerated neutral Brine A at 150°C.

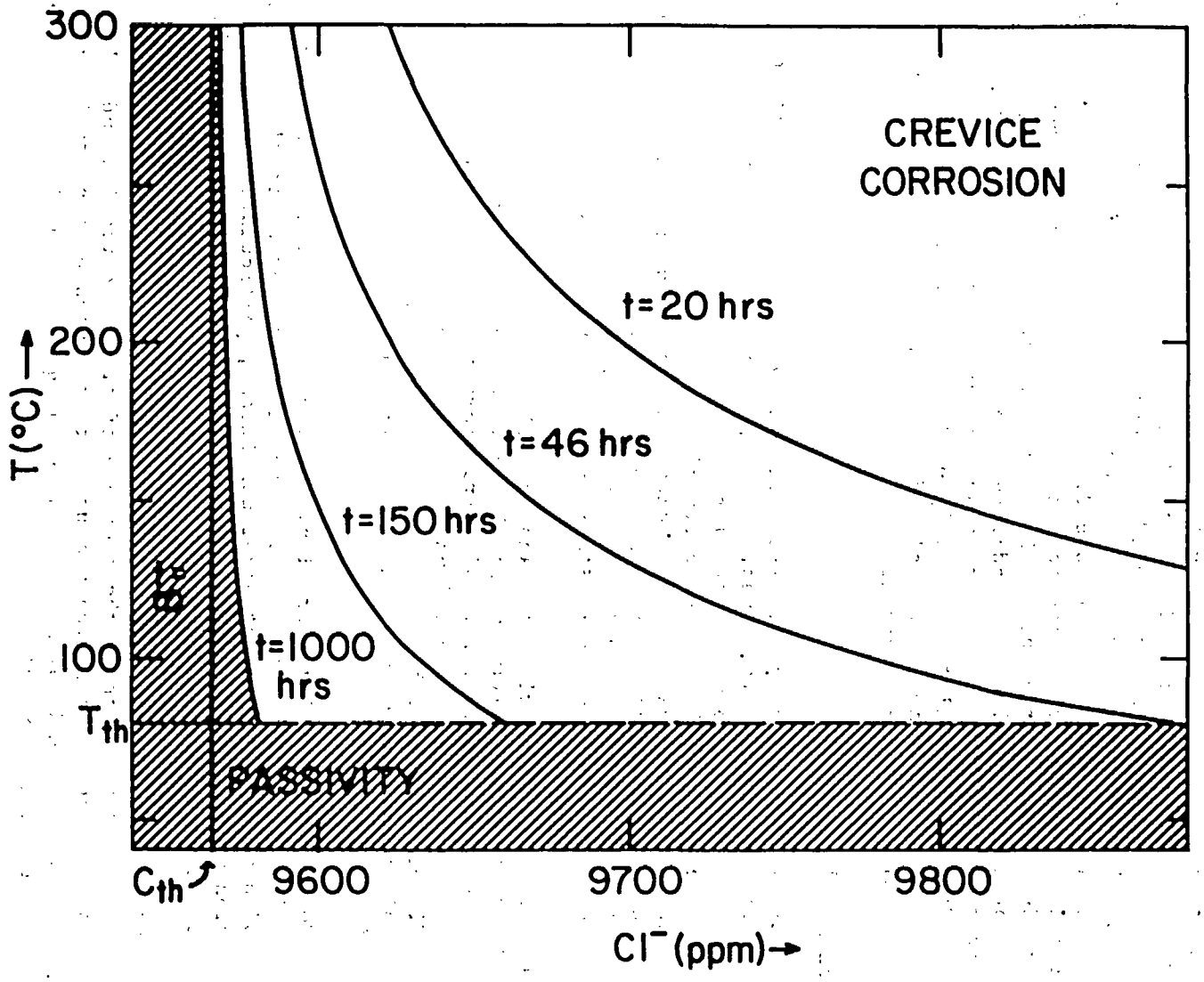

Figure 2.8. Calculated immunity domain of crevice corrosion of Grade-12 titanium in aerated neutral Brine A at 150°C.

equation is given in Reference 9). Such domains have been experimentally determined in CP-Ti and Ti-Pd alloy.[23] Therefore, our simple formulation is promising. Further, this calculation permits the extrapolation to long term behavior. Inside the unshaded area of Figure 2.8, crevice corrosion occurs while the hatched area shows immunity to crevice corrosion. The boundary of the two domains is also affected by the corrosion time. The domain for crevice corrosion (unshaded area) is enlarged as corrosion times are increased. At infinite corrosion time, the boundary becomes a straight line designated by C_{th}, below which crevice corrosion does not occur even at infinite corrosion time. Note that the curves in Figure 2.8 have been calculated on the basis of a corrosion current which is independent of test temperature. When the temperature dependence of the current is considered the curves in this Figure will be modified.[5,8] Also, the model developed shows that there will be a temperature limit, T_{th}, below which mass flow in the corrosion system ceases. Since the calculated T_{th} is lower than the freezing point of the test solution, it does not have a significant meaning at low temperatures where the solution becomes frozen.

2.4 Conclusions

- Crevice corrosion of Grade-12 titanium was identified at 150°C in simulated rock salt brines. Lower pH accelerated the reaction rates and deaerated solution gave less corrosion than aerated ones. Also, increasing specimen size, decreasing crevice gap, the preoxidation of the cathodic area gave more voluminous corrosion products. These results are consistent with those expected from macroscopic concentration cell formation which is accompanied by oxygen depletion, a potential drop, and acidification inside the crevice.

- The results of oxide film analysis show that compact anatase crystals are formed initially inside the crevice. As the macroscopic cell develops, the anatase form will transform into rutile which grows further by hydrolysis reactions. The corrosion products are depleted in Ni while Mo is either enriched or depleted by local pH variations. This is consistent with the energetics for the hydrolysis of dissolved ions.

- To quantify crevice corrosion, an electrochemical cell was developed, which provides a very useful method to characterize crevice corrosion of a metal under hydrothermal conditions, particularly in the situation when the crevice gap is minimized to accelerate the Grade-12 titanium corrosion process.

- By measuring the variation of current and potential with time, the above technique shows the sequence of crevice corrosion under hydrothermal conditions. The measurement of pH inside the crevice along with current and potential measurement quantify the initial simple immersion test results.

- The crevice corrosion of Grade-12 titanium in Brine A at 150°C is approximately three orders of magnitude smaller than that of Grade-2

titanium. However, even after 100 times dilution, Brine A shows crevice corrosion in Grade-12 titanium.

- The incubation time for the breakdown of passivity of a Grade-12 titanium crevice exposed to WIPP Brine A at 150°C is approximately two days which, within the accuracy of the measurements, is the same for various diluted test solutions. In the case of Grade-2 titanium, the incubation period is negligible as the metal starts corroding during solution heating.

- The classical four-stage model of crevice corrosion seems to be applicable for Grade-12 titanium. Even though the variation of current and potential soon after solution heating is somewhat complex, there is a consistent trend as observed in other systems.[24,25] Initially, barrier oxide growth is accompanied by a potential rise and the subsequent potential drop arises from the solution chemistry change and passivity breakdown.

- Based on this general observation, simple mass balance equations were used to obtain the boundary between crevice corrosion and immunity as a function of chloride concentration and temperature at infinite time. The equations were solved using measured potential, current and pH and by adjusting unknown physical parameters to obtain results consistent with experimental data. This is an approach to provide a methodology for long term prediction of crevice corrosion.

- The domain of crevice corrosion is enlarged as the corrosion time is increased, resulting in a threshold chloride concentration and a threshold temperature at infinite time. There is a limiting solution chemistry inside the crevice. Depending on the crevice geometry, the limiting current may not allow the onset of crevice corrosion. This is because diffusion leakage will prevent the critical chloride level from forming within the crevice.

- After initial breakdown of passivity within a Grade-12 titanium crevice, the current and, therefore, the rate of corrosion decreases slowly, primarily due to a Mo complex or Ti^{+4} formation (except in the case of 100 times diluted Brine A where a second increase in current is observed). The implications of this kind of repassivation of a crevice in predicting the life of a container are important. Considering the present two-week tests, the ability for repassivation cannot be determined until the underlying mechanisms are completely understood. Unknown gamma radiation effects on the stability of Mo complexes or Ti^{+4} ions are such examples. Furthermore, the production of TiO_2 corrosion products is shown to generate stresses which can introduce cracks in the metal. In such cases, crevice corrosion can start at the newly formed metal surface.

- Gamma radiation effects possibly prevent crevice corrosion by increasing the pH inside the crevice as shown in Section 5. However, complicated irradiation effects on passive film formation may make gamma

irradiation detrimental. The details of such processes are not known at the present time.

- We have not considered the temperature variations in the repository over extended periods. However, the estimation of the crevice corrosion behavior at 150°C is probably a conservative analysis of performance at lower temperatures for extended periods, since it is generally accepted that the crevice corrosion mechanism does not change as the temperature varies from room temperature to the solution boiling point.[26]

2.5 References

1. H. Jain, T. M. Ahn and P. Soo, "A Technique for Characterizing Crevice Corrosion Under Hydrothermal Conditions," submitted for publication in ASTM STP, Laboratory Corrosion Tests and Standards, 1983.

2. R. E. Glass, "Passivation of Titanium by Molybdate Ion," Abstract No. 153, Extended Abstracts Vol. 83-2, Electrochemical Society Meeting, Washington, D.C., 1983.

3. R. B. Diegle, Materials Performance, National Association of Corrosion Engineers, March 1982, p. 43.

4. E. J. Kelly, "Anodic Dissolution and Passivation of Titanium in Acidic Media," J. Electrochem. Soc. 126 (12), 2065 (1979).

5. M. A. Molecke, High-Level Waste Package Materials Quarterly Report, Sandia National Laboratory Report to ONWI, July, 1983.

6. T. M. Ahn and others, "Container Assessment - Corrosion Study of HLW Container Materials, Quarterly Progress Report, January-March 1983," BNL-NUREG-33012, Brookhaven National Laboratory, 1983.

7. M. Pourbaix, Atlas of Electrochemical Equilibria in Aqueous Solutions, National Association of Corrosion Engineers, 1974.

8. T. M. Ahn and H. Jain, "Prediction of Long Term Crevice Corrosion and Hydrogen Embrittlement Behavior of Grade-12 Titanium," submitted for publication in Corrosion/84, 1983.

9. T. M. Ahn and others, "Container Assessment - Corrosion Study of HLW Container Materials, Quarterly Progress Report, April-June 1983," BNL-NUREG-33603, Brookhaven National Laboratory, 1983.

10. N. D. Tomashov, G. P. Chernova, Y. S. Ruscol and G. A. Ayuyan, "The Passivation of Alloys on Titanium Bases," Electrochemica Acta 19, 159 (1974).

11. T. M. Ahn, B. S. Lee and P. Soo, "Identification of Crevice Corrosion in Titanium Alloy TiCode-12 in Rock Salt Brine at 150°C," submitted for

publication in ASTM STP Titanium and Zirconium Industrial Applications, 1982.

12. H. H. Uhlig, Corrosion and Corrosion Control, John Wiley and Sons, Inc., p. 11, p. 26, 1971.

13. J. O'M. Bockris and D. M. Drazic, Electrochemical Science, Barnes and Noble Books, New York, p. 244, 1972.

14. F. A. Posey and D. V. Subrahmanyam, "Kinetics of Initiation of Crevice Corrosion of Titanium," ORNL-TM-4099, Oak Ridge National Laboratory, 1973.

15. D. A. Vermilyea and C. S. Tedmon, Jr., "A Simple Crevice Corrosion Theory," J. Electrochem. Soc. 117, 437 (1970).

16. F. A. Posey and E. G. Bohlman, "Pitting of Titanium Alloys in Saline Waters," Desalination 3, 269 (1967).

17. F. A. Posey and others, "Kinetics of Pitting Attack of Titanium in Chloride Solutions," ORNL-TM-4099, Oak Ridge National Laboratory, 1973.

18. J. Kruger and V. K. Hardman, "Current Understanding of Pitting and Crevice Corrosion and Its Application to Test Methods for Determining the Susceptibility to Such Corrosion of Nuclear Waste Metallic Containers," NBSIR 82-2477, National Bureau of Standards, 1982.

19. T. R. Beck, "Initial Oxide Growth Rate on Newly Generated Surfaces," J. Electrochem. Soc. 129, 2501 (1983).

20. J. F. McAleer and L. M. Peter, "Instability of Anodic Oxide Films on Titanium," J. Electrochem. Soc. 129, 1252 (1982).

21. A. Lerman, Geochemical Processes Water and Sediment Environments, John Wiley and Sons, Inc., p. 103, 1979.

22. Y. H. Li and S. Gregory, "Diffusion of Ions in Sea Water and in Deep-Sea Sediments," Geochimica et Cosmochimica Acta 38, 703 (1974).

23. "Titanium Heat Exchangers for Service in Seawater, Brine, and Other Aqueous Environments," Titanium Information Bulletin from IMI, Birmingham, England, 1979.

24. J. W. Oldfield and W. H. Sutton, "Crevice Corrosion of Stainless Steels, II. Experimental Studies," Br. Corros. J. 13, 104 (1978).

25. D. Tromans and L. Frederick, "Electrochemical Studies of Crevice Corrosion Rates in Stainless Steels," Corrosion 39, 305 (1983).

26. M. G. Fontana and N. D. Greene, Corrosion Engineering, Second Edition, McGraw-Hill Inc., New York, 1978.

3. HYDROGEN EMBRITTLEMENT OF GRADE-12 TITANIUM

3.1 Slow-Crack-Growth Tests

We have continued to analyze slow crack growth rate data obtained for the Grade-12 titanium/hydrogen system. The difficulties lie in identifying the stage I and stage II crack propagation regimes since the internal hydrogen embrittlement behavior in titanium based alloys does not give a unique stage II plateau region in the crack velocity-stress intensity curve.[1] Typically for extended test times, two types of crack growth rate curves are observed as shown in Figures 3.1 and 3.2. The accelerating growth rate section of the curve in the latter Figure precedes sample fracture and is designated as stage III crack growth. For the slower growth rates shown in the two figures, however, it is difficult to determine whether crack growth is in stage I (elastic stress controlled) or stage II (plastic stress controlled). To clarify this situation calculations were performed to compare the sizes of the plastic zones and hydride particles at the propagating crack tips. It was determined that the plastic zone size was typically larger than the hydride size (which is equal to the crack striation distance separation shown in Figure 3.3) showing that in most cases the crack tip is subjected to plastic stress conditions, i.e. crack growth is usually in stage II in our studies.

As discussed in the last quarterly report,[2] we propose two types of crack propagation jump, namely, (1) that associated with hydride fracture resulting in striation formation (Figure 3.3) on fracture surfaces, (2) that associated with the passage of the crack front through the alpha-beta interface phase, as shown in Figure 3.4 schematically. In Figure 3.4, the zigzagged line A shows that the crack path is either transgranular (regions 1 and 3) in the alpha phase (white grain) or interfacial (region 2) in the alpha phase adjacent to the beta phase (black area). For transgranular growth, crack growth rates (regions 1 and 3) are steady and slower than those for interfacial growth which is associated with a crack jump (region 2) because of a high hydrogen concentration in this region. In this work we have measured crack growth rates on the specimen surface. However, the crack growth process averaged over the sample thickness may not be the same because of the statistical averaging of the crack growth behavior over many grains. A test is being performed on crack growth rates as determined by potential difference measurements made across the plane of the crack to clarify this point.

Figure 3.5 gives the temperature dependence of crack velocity obtained from the solid circles in Figure 3.6 (open circles represent the fast stage II transient crack growth stage in Figure 3.4) at stress intensity values from 60 to 80 MPa$\sqrt{m}$. This curve is for the same microstructure and hydrogen concentration in the specimen (35-40 ppm). As expected, a maximum is observed. The details will be discussed in the next section.

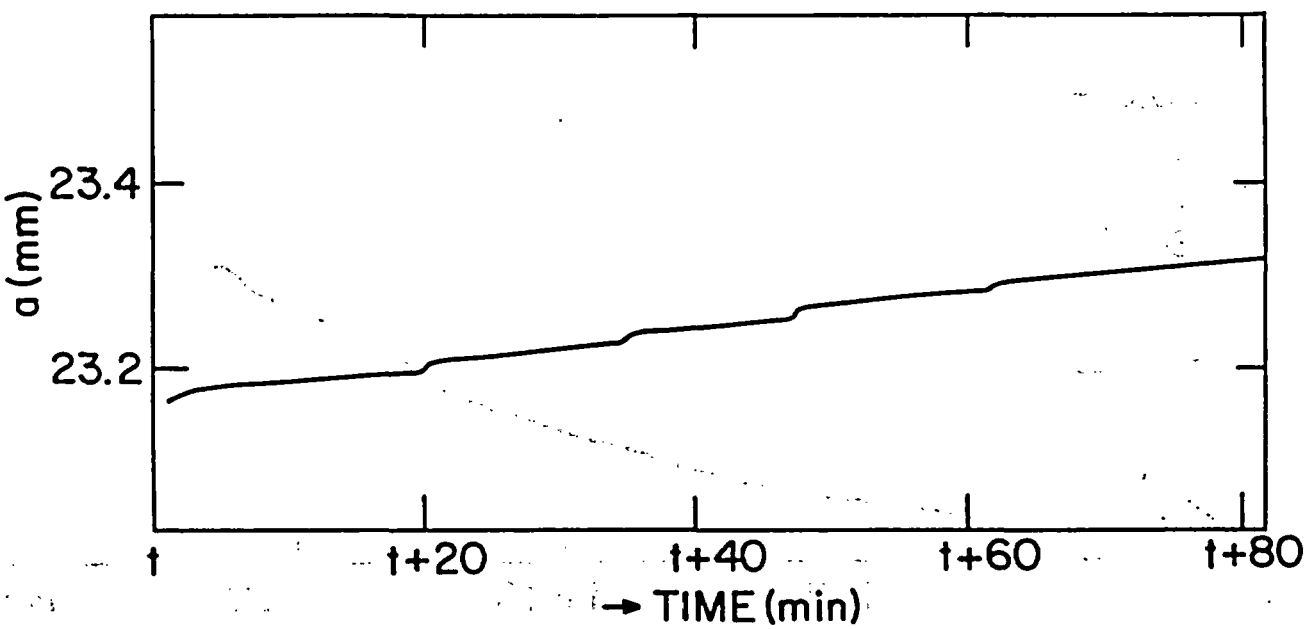

Figure 3.1. Crack length - time curve observed in the beginning of crack growth for extended times. This curve is from a test on an as-received Grade-12 sample at 20°C.

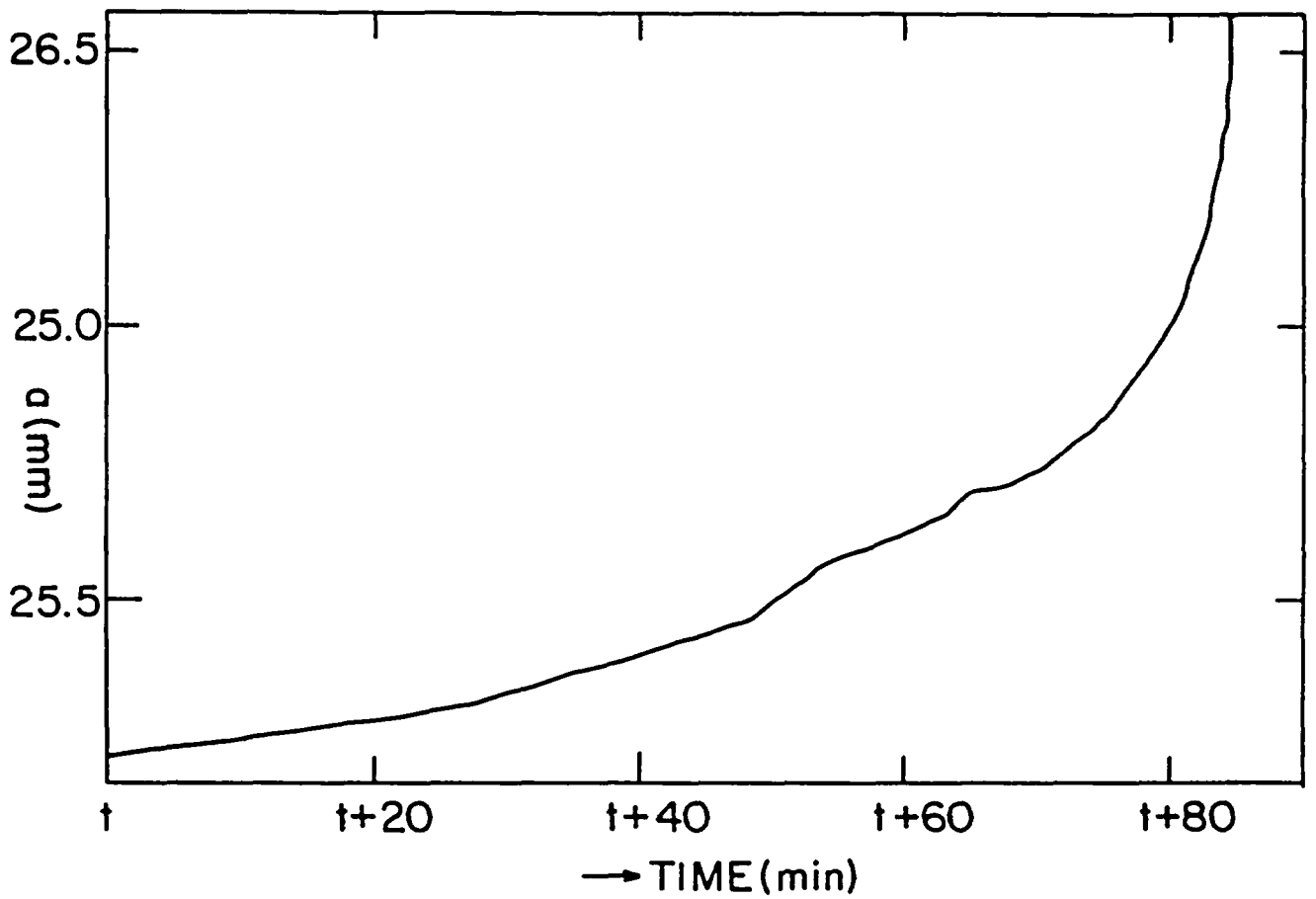

Figure 3.2. Crack length - time curve observed in the final stage of crack growth. This curve is from a test on an as-received Grade-12 sample at 50°C.

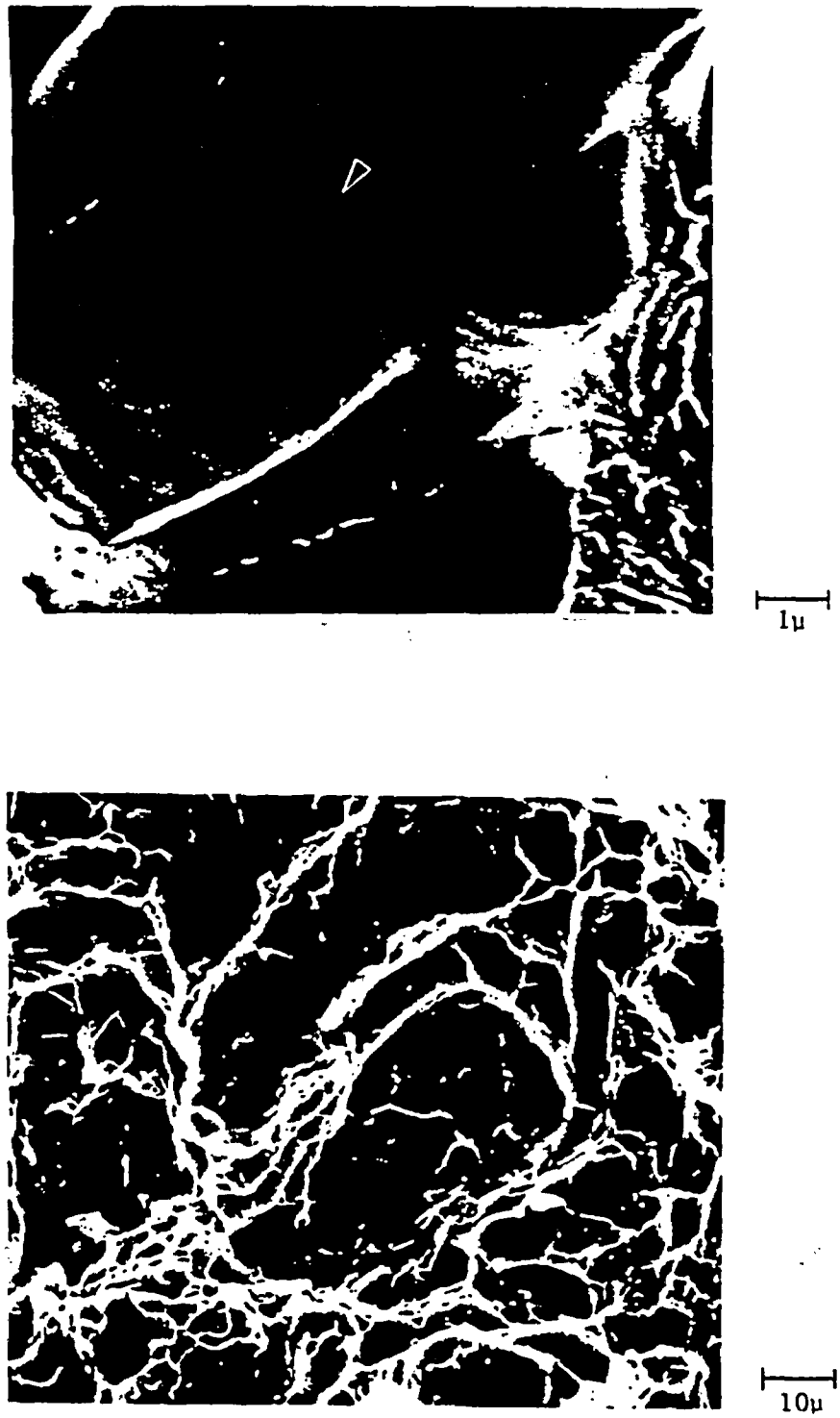

Figure 3.3. Striations observed in the fracture surface of as-received Grade-12 titanium tested at temperatures varying from 20 to 148°C. The upper view is an enlargement of a flat region in the lower picture.

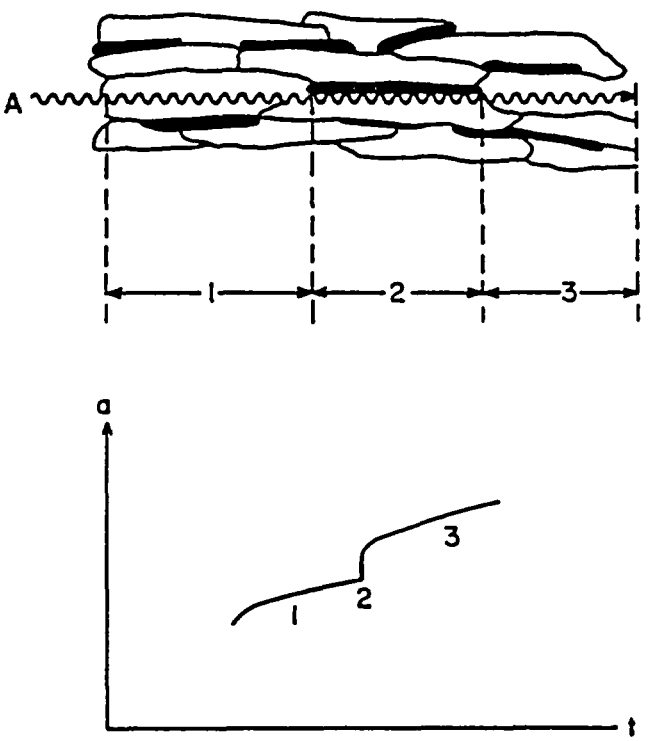

Figure 3.4. A schematic of crack growth as the crack front passes through the alpha and beta regions.

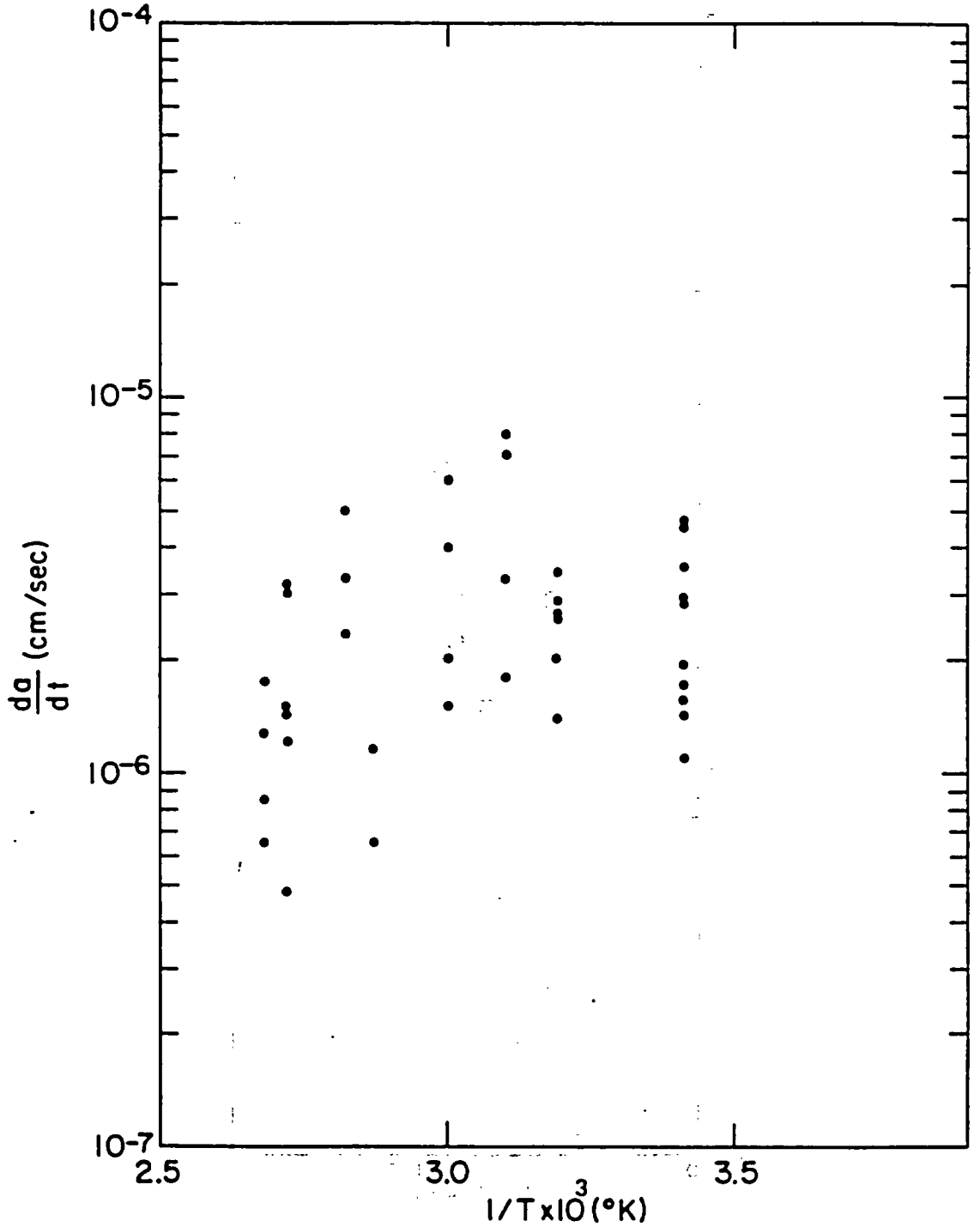

Figure 3.5. The measured slow crack growth rates of as-received Grade-12 titanium for K = 60 to 80 MPa$\sqrt{m}$ at various temperatures.

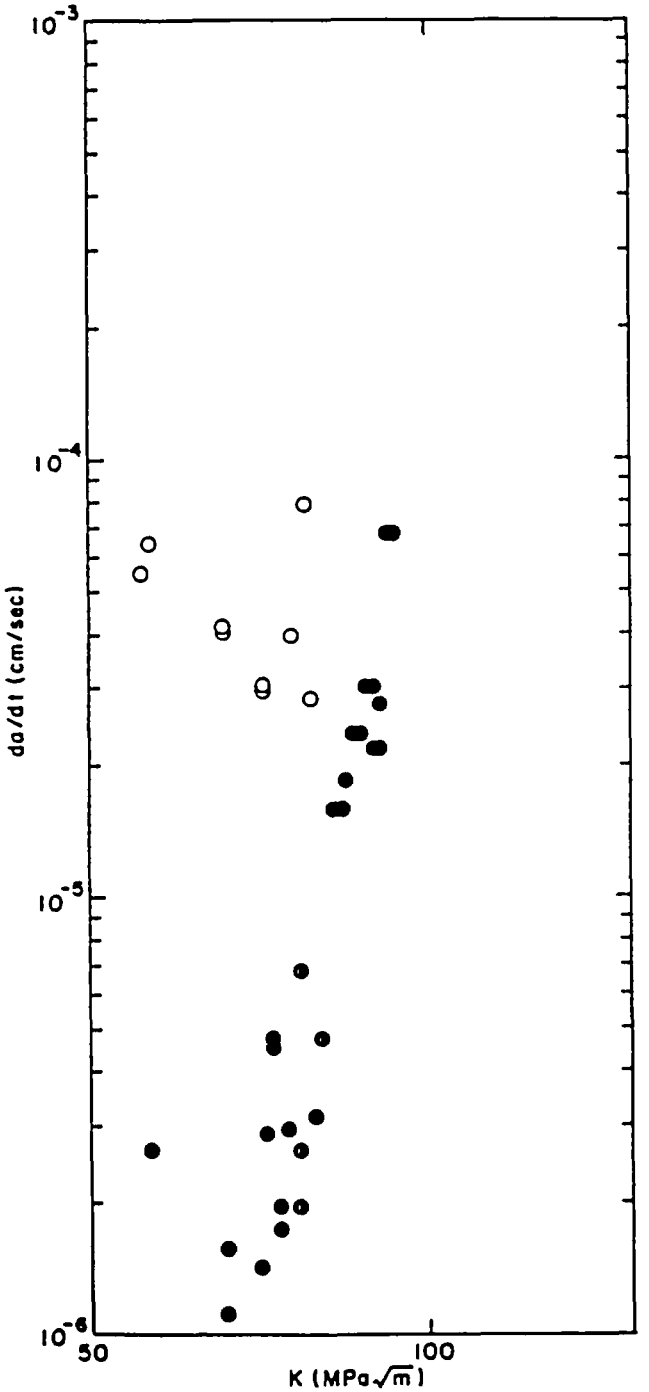

Figure 3.6. Slow crack growth rates of as-received Grade-12 titanium at room temperature. Solid circles represent the steady state (1 and 3 in Figure 3.4) and open circles represent the transient state (2 in Figure 3.4).

3.2 Calculated Crack Growth Kinetics and Long Term Prediction

We have modified a crack growth kinetics model by incorporating dislocation pipe hydrogen diffusion and hydride nucleation kinetics in the last quarterly report.[2] The modification is based on a rationale that (1) the measured activation energy for crack growth is lower than the activation energy for hydrogen diffusion in the alpha matrix, (2) there is a maximum temperature above which crack growth rates are lowered. Figure 3.7 is a revised schematic of strain-induced hydride formation at a crack tip, with which the above modification has been performed. In stage I crack growth (Figure 3.7a), the hydride size (x) is greater than plastic zone size and, therefore, subject to an elastic stress with hydrogen transfer through the alpha-beta interface. On the other hand in the stage II crack growth period (Figure 3.7b), hydride is formed in the semi-cohesive zone through dislocation transport of hydrogen inside the well-developed plastic zone. Figure 3.7c shows the hydrogen concentration change in front of a growing hydride. Other parameters in this Figure are defined in Appendix 3-1.

Additionally, we adopted the threshold stress intensity model by Moody and Gerberich.[3] Using the same parameters used in fitting the crack velocity vs temperature curve, these threshold values are evaluated for long term prediction purposes. In the regime of the threshold stress intensity value (K_{th}), the crack growth mode is in stage I. Also, when K approaches K_{th}, hydride nucleation is the rate-controlling step because hydride nucleation rates become much slower than hydrogen diffusion rates, and therefore, the diffusion profile will disappear. To obtain K_{th}, a hydrogen solubility limit consideration has been adopted for stage I.[3] In this the hydrogen solubility in the presence of hydride and an applied stress is given by:

$$C_E = \exp[(-\Delta G^o + P_E \bar{V}_H - W_p - E_{KK} \bar{V}_h P_E)/RT] \qquad (1)$$

where

$$P_E = \frac{4\ (1+\nu)\ K}{3\ (2\pi)^{1/2}\ d^{1/2}} \qquad (2)$$

ΔG^o is the free energy of hydride formation, ν is Poisson's ratio, W_p is the plastic work done during hydride formation by dislocation movement, E_{KK} is the stress free transformation strain, $\bar{V}_h$ is the partial molar volume of hydrogen in hydride. The concentration of hydrogen due to external stress effects is given by:[3]

$$C_{EX} = C_o \exp(P_E \bar{V}_H/RT) \qquad (3)$$

Equating Equation (1) and Equation (3) gives the stress intensity at which the crack tip hydrogen concentration reaches the solubility limit. At this K value, the incubation time[2] for hydride nucleation is infinite because of the zero driving force for nucleation (C_E is equal to C_{EX}). The K_{th} value obtained this way is, therefore, the true threshold value at infinite time.

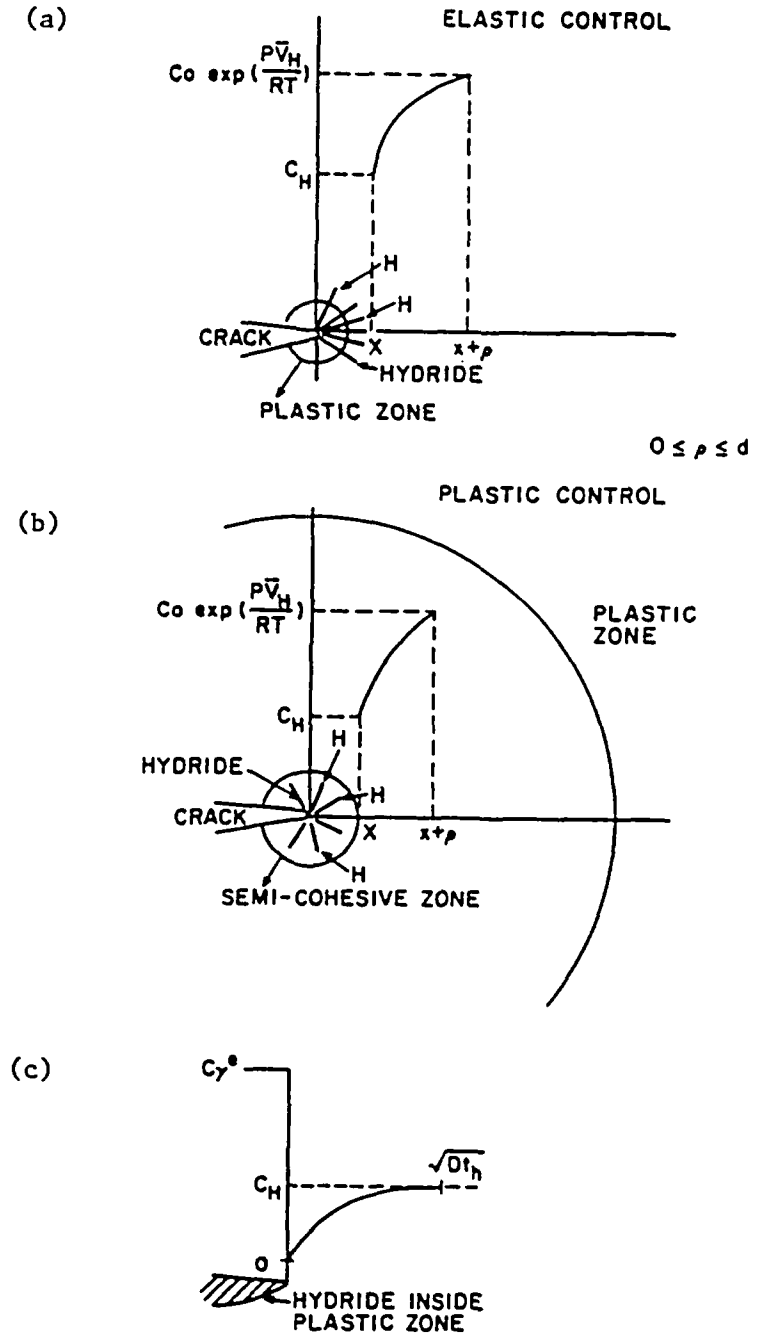

Figure 3.7. A schematic of hydride growth at crack tip (a) stage I, (b) stage II, (c) hydrogen concentration in front of a growing hydride. C_H is the hydrogen concentration at the interface due to the formation of a concentration profile. D is the hydrogen pipe diffusivity. The rest of the parameters are given in Appendix 3-1.

However, there is a possibility that a K value slightly higher than K_{th} may still result in a very long incubation time for hydride nucleation. Therefore, depending on the time considered, the practical threshold value can be greater than the ideal K_{th} value obtained from Equations (1) and (3). To clarify this possibility, the K values have been varied above the K_{th} values until the incubation time for nucleation kinetics becomes negligible. This enables us to determine K_{th} at a given canister service time.

First, we address the data in Figure 3.5 (temperature dependence of crack growth rates) using a previous formulation[2] and evaluate K_{th}. The parameters used in the calculation are given in Appendix 3-1. Figure 3.8 gives the calculated crack growth rates which are controlled by hydrogen pipe diffusion at various temperatures (for all K values) to be compared with Figure 3.5 ($L = 10^9/cm^2$, $E_B = 0.35$ eV, $t_H = 1$ sec, $Q = 0.65$, 0.70, 0.75 and 0.80). Q is the ratio of the activation energy for pipe diffusion to that for lattice diffusion. Figure 3.9 shows calculated crack growth rates which are controlled by diffusion kinetics (the solid line is for $L = 10^{11}/cm^2$, $E_B = 0.25$ eV, $t_H = 1$ sec, $Q = 0.70$ and 0.80). Nucleation kinetics are evaluated (triangles) at 90°C and 120°C since significant decreases in crack growth rates are present in these temperature regimes. In Figure 3.9, the kinetics over the entire temperature regime are obtained by connecting a solid line to a triangle indicated by an arrow mark. At 90°C, values of $\alpha = 0.6$ and $\sigma = 67$ erg/cm^2 are used while $\alpha = 0.5$ and $\sigma = 85$ erg/cm^2 are used at 150°C (see Appendix 3-1 for the definition of these parameters). The four triangles are for K = 42, 56, 80, 127 MPa$\sqrt{m}$ at 120°C and the three triangles are for K = 42, 56, 80 MPa$\sqrt{m}$ at 90°C. Open triangles are for Q = 0.70 and solid triangles are for Q = 0.80. A smooth curve (as in Figure 3.8) using one set of α and σ values in this temperature regime is not shown because the kinetics are too sensitive to temperature variation. Figure 3.8 shows a smooth decrease in the crack growth rates at higher temperatures while Figure 3.9 shows a sharp drop from solid line to triangles either at 90°C or at 120°C which are chosen arbitrarily for comparison. In reality, a combination of the behavior shown in Figure 3.8 and the triangles in Figure 3.9 may explain the behavior in Figure 3.5.

The threshold stress intensity, K_{th} is obtained using Equation (1) and Equation (3), and the parameters used in obtaining Figures 3.8 and 3.9. At 150°C and $C_o = 35$ ppm with a hydrogen accumulation factor of 2 in the alpha phase adjacent to the beta phase,[4,5] the K_{th} value is found to be 4.86 MPa$\sqrt{m}$. At and below $K = K_{th}$, the incubation time[2,6] for hydride nucleation is infinity. As mentioned before, to check whether there are K values greater than K_{th} which give also very long incubation time, the incubation time is calculated for various K values above the K_{th} value. If K is increased to K_{th} plus a maximum of 2×10^{-6}% of K_{th}, the incubation time is reduced to be 85-250 seconds within the parameter variations used in Figure 3.8. Therefore, there are no such K values in practice and we may conclude that the container will not fail when it is subjected to a stress intensity below 4.86 MPa$\sqrt{m}$ at 150°C and an initial hydrogen concentration of 35 ppm for very extended time periods. Table 3.1 shows an estimated minimum crack size allowed from the K_{th} values at various applied stress levels. It is

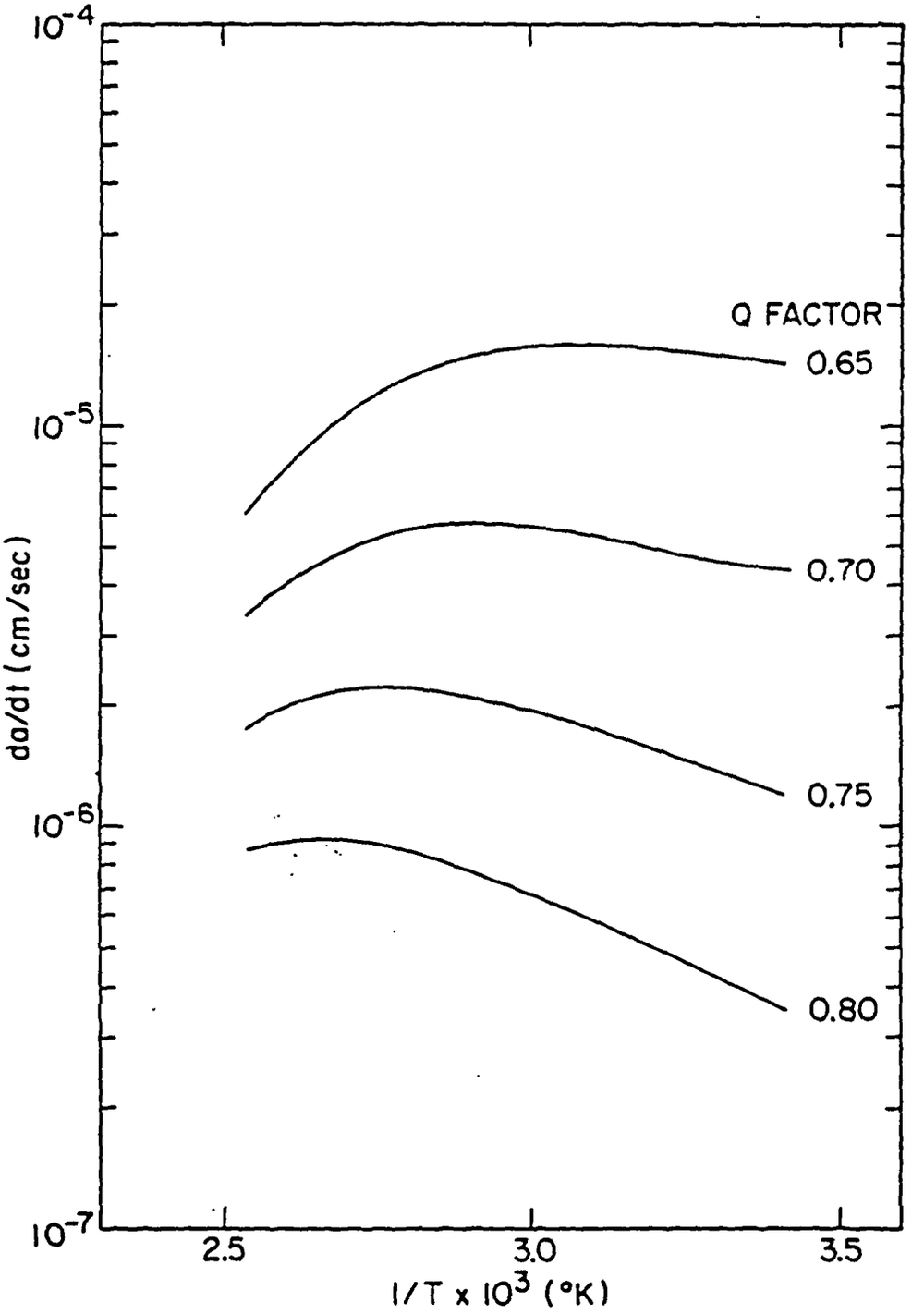

Figure 3.8. Calculated slow crack growth rates of as-received Grade-12 titanium controlled by hydrogen pipe diffusion for all K values at various temperatures. The Q factor is a ratio of activation energy of pipe diffusion to that of lattice diffusion.

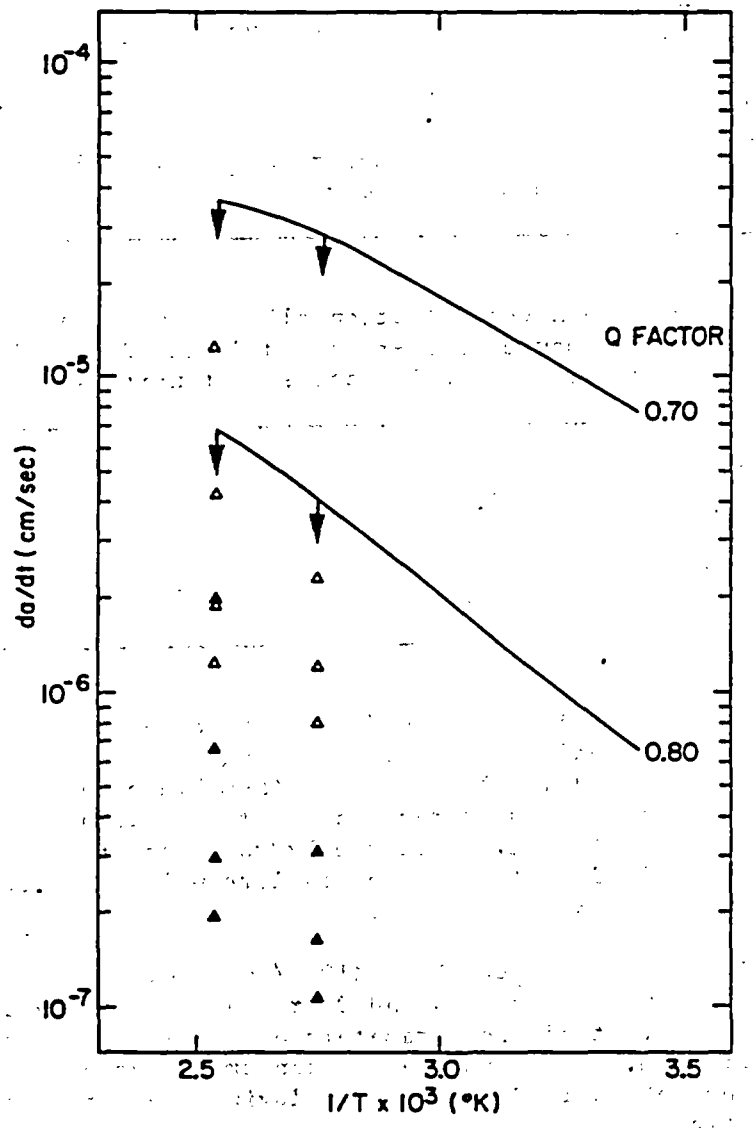

Figure 3.9. Calculated crack growth rates of as-received Grade-12 titanium assuming hydrogen pipe diffusion kinetics plus nucleation kinetics (triangles). For nucleation control, four triangles are for K = 42, 56, 80, 127 MPa$\sqrt{m}$, respectively, at 120°C and three triangles are for 42, 56, 80 MPa m, respectively, at 90°C. Open triangles are for Q = 0.70 and solid triangles are for Q = 0.80.

Table 3.1. Estimated minimum safe flaw size of as-received Grade-12 titanium at various applied stresses (at 150°C).

Stress, σ	YS	0.5 YS	0.1 YS	0.05 YS	0.01 YS
Crack size, a (mm)	0.073	0.292	7.309	28.738	730.874

Yield strength (at 150°C = 320.6 MPa$\sqrt{m}$, K_{th} = 4.86 MPa$\sqrt{m}$
The calculation is based on $K_{th} = \sigma\sqrt{\pi a}$

Table 3.2. Hydrogen concentration allowed in the alpha phase for safe performance of as-received Grade-12 titanium at 150°C for various applied stress intensities.

Stress intensity (MPa$\sqrt{m}$)	0.39	1.23	3.87	12.25	38.74	122.51
Hydrogen conc. (ppm)	42.2	40.7	36.37	25.42	8.20	0.23

seen that crack sizes less that 0.29 mm can cause failure at and above a stress level of one-half of the yield strength. Also, an estimate has been made from Equation (1) to obtain the maximum hydrogen concentration at 150°C to avoid failure at various stress intensity levels using the same parameters. At a given stress intensity, when the hydrogen concentration levels are below the values in Table 3.2, the delayed failure will be avoided for an infinite time according to this calculation.

There is ample evidence that $L \leq 10^{11}/cm^2$,[7] $0.1 \leq E_B \leq 0.5$ eV,[8] and $10 \leq \sigma \leq 1000$ erg/cm^2.[9] α and Q are known to be less than unity.[10,11] The rest of the parameters quoted in Appendix 3-1 are for either CP titanium, near alpha-beta titanium alloys or Grade-12 titanium. Since the alpha phase is depleted of alloying elements, these parameters are not unrealistic.

Conclusions for this work are also given in Appendix B.

3.3 Feasibility Study of In Situ Deformation of Hydrogenated Thin Foils of Grade-12 Titanium

In the early stage of this project, we intended to deform hydrogenated thin foils in a TEM to determine whether hydride formation at a crack tip is responsible for crack initiation. Since there is ample evidence from extensive fractographic studies that this is true,[26] we have not pursued this subject. Further, preliminary tests have shown that it might be difficult to

identify the hydride formation in the presence of beta phase and alpha-beta interface phase where hydrogen solubiilty is very high and the interface structure is complex.

3.4 Hydrogen Uptake Efficiency

Limited efforts have been given on this subject since the as-received Grade-12 titanium has 35-40 ppm hydrogen which is sufficient to cause delayed failure as discussed in the previous sections. Since it is known that gamma radiolysis of groundwater produces abundant hydrogen (see Section 5), we should not eliminate the possibility of further hydrogen uptake in unshielded waste packages. Also, colloidal sodium produced by gamma irradiation of rock salt generates hydrogen when the salt is exposed to brine.[21] Once passivity is lost, the hydrogen penetration into the matrix will be significant. We have presented data on the enhanced hydrogen uptake in alkaline brines[22] and in creviced samples at 150°C.[23] Even though, the precise mechanism for hydrogen uptake is not known, our conclusion is that there are many possibilities of hydrogen uptake in repositories once the passivity is destroyed such as in crevice or other corrosion processes. This will enhance the probability of delayed failure at smaller applied stress levels.

3.5 Conclusions

- Internal hydrogen embrittlement of Grade-12 titanium was identified at room temperature by tension testing unnotched and notched samples which are cathodically or thermally charged with hydrogen. Cathodically charged smooth tensile specimens showed slow-strain rate embrittlement (reduced elongation) with microcleavage features. Cathodically charged coupons showed impact embrittlement in buckling tests. In the buckling tests, hydride fracture, interfacial separation and microcleavage were observed. In fracture testing of SEN (single-edged-notched) samples charged thermally, the embrittlement becomes significant as the hydrogen level is increased to 197 ppm. At 7187 ppm H_2, impact embrittlement was also observed. Hydrogen-induced alteration of the initial microstructure did not change the general features of embrittlement.

- An extensive comparison of fractographs with those for other alpha/beta alloys results in the conclusion that hydride formation is responsible for the embrittlement of Grade-12 titanium at room temperature, and hydride is probably formed in the alpha phase adjacent to the interface phase.

- We have quantified the above results by measuring the slow crack growth rates at various hydrogen concentration levels and temperatures. The general mechanism obtained at room temperature is applicable at temperatures up to 150°C. However, from the analysis of activation energy the detailed rate determining step at room temperature is found to be different from that at high temperatures.

- Based on the above observations and the results from other types of alpha-beta titanium alloys, a rationale for a new crack growth formula has been presented, and necessary new formulations have been developed. At lower temperatures, dislocation pipe diffusion of hydrogen is responsible for the crack growth while hydride nucleation or dislocation pipe diffusion with a large binding energy of hydrogen to the dislocations is controlling the crack growth rates at higher temperatures. In stage I crack growth, hydride growth is controlled by the elastic stress field while the plastic stress field is responsible for the hydride growth in the semi-cohesive zone inside the plastic zone in stage II.

- Two types of crack jump were defined. One is associated with hydride fracture and typically forms striations in the fractographs. The other is from the movement of the crack front in the alpha phase adjacent to alpha-beta interface phase. These latter kinetics, observed in surface crack measurements, were mathematically modeled.

- The data fitting to the stage II crack growth rates vs temperature plots determines the parameters used in the equations developed. These parameters are used to estimate the threshold stress intensity and hydrogen solubility limit at infinite container service time by the calculation of incubation time for hydride nucleation. This value gives a crack size below which container failure will not occur for a given applied stress and hydrogen concentration, and a hydrogen concentration limit below which the container will not fail at a given stress intensity. The threshold evaluation at infinite time is what we propose for the long term prediction of hydrogen embrittlement for extended periods such as 100-300 years. Once the crack starts to propagate, the container probably will fail in a short period.

- Radiation produces large amounts of hydrogen (see Section 5). Whenever there is passivity breakdown, it tends to cause hydrogen uptake in the metal, leading to effective degradation of the threshold stress intensity. Such cases of passivity breakdown include those associated with crevice corrosion and alkaline environments formed during the interaction of gamma-irradiated rock salt with brine.

3.6 References

1. N. R. Moody and W. W. Gerberich, "Hydrogen Induced Slow Crack Growth in Ti-6Al-6V-2Sn," Met. Trans. A 11A, 973 (1980).

2. T. M. Ahn, H. Jain and P. Soo, "Container Assessment-Corrosion Study of HLW Container Materials, Quarterly Progress Report, April-June 1983," BNL-33603, Brookhaven National Laboratory, 1983.

3. N. R. Moody and W. W. Gerberich, "Solubility Considerations for Threshold Stress Intensities Controlled by Hydride Fracture," Scripta Metallurgica 15, 709 (1981).

4. S. V. Nair, R. R. Jensen and J. K. Tien, "Kinetic Enrichment of Hydrogen at Interfaces and Voids by Dislocation Sweep-in of Hydrogen," Met. Trans. A 14A, (1983).

5. D. A. Meyn, "Effect of Hydrogen Content on Inert Environment Sustained Load Crack Propagation Mechanisms of Ti-6Al-4V," in Environmental Degradation of Engineering Materials, M. R. Louthan, Jr., R. P. McNitt and R. D. Sisson, Jr., Editors, Virginia Polytechnic Institute, 1981.

6. T. M. Ahn and P. Soo, "The Kinetics of Internal Hydrogen Embrittlement in ASTM Grade-12 Titanium Alloy," Abstract for the TMS-AIME Fall Meeting, Philadelphia, Pennsylvania, October 2-6, 1983.

7. R. Casea-Neri and D. W. Nix, "A Model for the Mobile Dislocation Density," Acta Metallurgica 22, 257 (1974).

8. A. S. Nowick and J. J. Burton, Diffusion in Solids - Recent Developments, Academic Press, p. 272, 1975.

9. J. P. Hirth and J. Lothe, Theory of Dislocations, McGraw Hill, 1963, Appendix 2.

10. J. W. Cahn, "Nucleations on Dislocations," Acta Met. 5, 169 (1957).

11. N. A. Cjostein, "Short Circuit Diffusion," Diffusion, ASM, Edited by H. I. Aaronson, 1972.

12. Handbook of Chemistry and Physics, CRC Press, 62nd Ed., 1981-1982.

13. R. Gasca-Neri and W. D. Nix, "A Model for the Mobile Dislocation Density," Acta Metallurgica 22, 257 (1974).

14. J. P. Hirth and J. Lothe, Theory of Dislocations, McGraw-Hill, 1963, Chapter 17.

15. A. S. Nowick and J. J. Burton, "Diffusion in Solids - Recent Developments," Academic Press, 1975, p. 272.

16. Metals Handbook, Ninth Edition, Vol. 3, Properties and Selection: Stainless Steels, Tool Materials and Special-Purpose Metals, ASM, 1980.

17. N. E. Paton, B. S. Hickman and D. H. Leslie, "Behavior of Hydrogen in Alpha-Phase Ti-Al Alloys," Met. Trans. 2, 2791 (1971).

18. T. P. Papazoglou and M. T. Hepworth, "The Diffusion of Hydrogen in Titanium," Met. Trans. 242, 682 (1968).

19. L. Darken and R. Gurray, Physical Chemistry of Metals, McGraw-Hill, 1953, p. 240.

20. T. M. Ahn and P. Soo, "Internal Hydrogen Embrittlement in ASTM Grade-12 Titanium Alloy," BNL-NUREG-51671, Brookhaven National Laboratory, 1983.

21. S. V. Panno, "Chemical Changes in Radiation Damaged Natural Rock Salt: Preliminary Results," BNL-NUREG-32523, Brookhaven National Laboratory, 1982.

22. T. M. Ahn and others, "Container Assessment-Corrosion Study of HLW Container Materials, Quarterly Progress Report, January-March 1983," BNL-NUREG-33012, Brookhaven National Laboratory, 1983.

23. T. M. Ahn and P. Soo, "Container Assessment-Corrosion Study of HLW Container Materials, Quarterly Progress Report, April-June 1982," BNL-NUREG-31611, Brookhaven National Laboratory, 1982.

APPENDIX 3-1

PARAMETERS USED IN THE CALCULATION OF HYDROGEN EMBRITTLEMENT

Hydride Concentration in Hydride Phase[12]
C_γ^e = 0.6580

The Average Initial Hydrogen Concentration
C_o = 35 ppm. There will be an enrichment factor near the beta phase or grain boundary[4,5] (a factor of 2 is used).

Dislocation Density in Plastic Zone[13]
L = $10^9/cm^2$ (Figure 3.8), $10^{11}/cm^2$ (Figure 3.9)

Burgers Vector[14]
B = 0.59 nm

Binding Energy of Hydrogen to Dislocation Core[15]
E_B = 0.35 eV (Figure 3.8), 0.25 eV (Figure 3.9)

Partial Molar Volume of Hydrogen in Titanium[3]
$\overline{V}_H$ = 1.68 cm^3/mol

Partial Molar Volume of Hydrogen in Hydride[3]
$\overline{V}_h$ = 12.50 cm^3/mol

Grain Size
d = 2μ (experimental)

Hydride Size
ℓ = 0.67μ (experimental)

Hydride Fracture Time
t_h = 1 sec (adjustable)

Young's Modulus[16]
E_y = 110.3 MPa

Free Energy of Hydride Formation[17]
ΔG^o = 18.6 KJ/mol

Plastic Work Done During Hydride Formation by Dislocation Movement[3]
W_p = 0.67 KJ/mol

The Stress Free Transformation Strain[3]
E_{KK} = 0.24

Yield Strength[16]

σ_y (20°C) = 538 MPa
σ_y (40°C) = 400 MPa
σ_y (60°C) = 386 MPa
σ_y (80°C) = 372 MPa
σ_y (100°C) = 359 MPa
σ_y (130°C) = 334 MPa

Poisson's Ratio[16]

$\nu = 0.33$

Hydrogen Diffusivity in Dislocation[18]

$D_H = 0.06 \exp(-Q \cdot 7200/T)\ cm^2/sec$

Activation Energy for Hydride Nucleation on Dislocations

$$\Delta G^* = \alpha\, 16\, \pi\, \sigma^3/(3\, G_v^2)$$

where $G_v = -[C_H \bar{V}_H + (1-C_H) \bar{V}_{Ti}]^{-1}$
$(TANT + GM + GMIN + \Delta G^\circ)$

where TANT = $R\ T\ (C_\gamma^e - C_H)\ [\ln C_H - \ln (1-C_H) + \ln (GAM)]$
GAM = $1/C_E \exp[(1-C_E)*(\Delta G^\circ)/((C_\gamma^e - C_E)\ R\ T)]$
GMIN = $1/(1 + GAM)$
GM = $R\ T\ [(1-C_H) \ln (1-C_H) + C_H \ln (GAM\ C_H)]$

C_H is the hydrogen concentration at the end of semicohesive zone or hydride, and has a similar expression for crack growth rates.[2]
α is the ratio of nucleation barrier in dislocation to that in bulk matrix.[10]
σ is the interfacial energy and $\bar{V}_{Ti}$ is obtained from $\bar{V}_H$.[19]

4. STRESS CORROSION CRACKING OF GRADE-2 AND GRADE-12 TITANIUM

The slow-strain-rate tests on Grade-2 and Grade-12 titanium in WIPP Brine A and Brine B at 83°C have been completed. These tests were conducted in solutions with pH ranging from 1 to 11.6, and at a strain rate of 3.0×10^{-7}/sec or 1.5×10^{-6}/sec. The stress corrosion susceptibility of each alloy is evaluated by comparing the results obtained in brine with those in helium.

In general, Grade-12 titanium shows superior mechanical properties compared to Grade-2 titanium; it has appreciably higher values of maximum stress, total elongation and reduction in area. Most of the differences in the formation of necks, the stress-strain curves, the strain hardening behavior, and the fractographs of the two materials can be explained in terms of grain size differences, additional alloying elements and the beta phase present in Grade-12 titanium. Neither Grade-2 nor Grade-12 titanium shows any evidence of stress corrosion cracking. However, for both alloys there is a small loss in ductility (reduction in area and/or total elongation) when tested in brine solutions.

An examination of the fracture surfaces of Grade-12 titanium under an SEM shows that the fracture plane near the edge is at approximately 45° with respect to the macroscopic fracture plane. The edge area also shows some flat features which are indicative of a cleavage type fracture mode. Similar observations were made earlier by Abrego et al.[1] who believed them to be caused by the presence of the corrosive brine. However, in the present tests the width of this quasi-cleavage zone does not correlate with the presence of brine, and it is, therefore, probably related to some internal effects. A detailed discussion on this observation and other results has been presented elsewhere.[2]

4.1 References

1. L. Abrego and H. J. Rack, Paper No. 97 in Corrosion '81, NACE, April 6-10, 1981, Toronto, Canada.

2. H. Jain, T. M. Ahn and P. Soo, TMS Paper Selection No. F83-1. Presented at the TMS-AIME Fall Meeting, October 2-6, 1983, Philadelphia, Pennsylvania.

5. GAMMA RADIOLYSIS OF BRINE

The effects of gamma radiolysis have been studied in both neutral and acidic brines. After a total gamma radiation dose of 10^9 rads (2.4×10^6 rads/h), the solution pH approaches the neutral value, suggesting possible beneficial effects of radiation on the localized corrosion of metallic containers for use in nuclear waste disposal. In agreement with earlier investigations, G (H_2) is found to be 0.3-0.4. Large amounts of this hydrogen, however, will accelerate delayed failure kinetics. THe presence of oxygen and solutes may have reduced the total molecular yield. There is also an indication of Cl_2 and H_2O_2 in the solution. The effects of such species on the localized corrosion are not known at the present time. More detailed information will appear in a future topical report.

6. CAUSTIC CORROSION OF GRADE-12 TITANIUM

Caustic formation in a rock salt repository has been discussed previously[1] and some data on the corrosion of Grade-12 titanium have been reported in the past quarterly progress report.[2] The results of our last test were obtained for crevice corrosion in alkaline brine. The pH of Brine B was adjusted to 11.13 and 2x4 cm metal/metal crevice coupons were immersed for 21 days at 150°C. The black scale typically observed in neutral brine was not detected. However, a blue and yellow colored film was observed, which is an indication of an early stage of crevice corrosion. Since passivity breakdown in the crevice requires a critical pH (see Section 2) it takes more time to reach such conditions in a higher pH solution.

The caustic corrosion data may be summarized as follows.

- Uniform corrosion rates and hydrogen uptake efficiency are increased significantly.
- Stress corrosion cracking is not observed.
- The kinetics of crevice corrosion are significantly retarded.

The detailed data will be given in a future topical report.

6.1 References

1. S. V. Panno, "Chemical Changes in Radiation Damaged Natural Rock Salt: Preliminary Results," BNL-NUREG-32523, Brookhaven National Laboratory, 1982.
2. T. M. Ahn and others, "Container Assessment-Corrosion Study of HLW Container Materials, Quarterly Progress Report, January-March 1983," BNL-NUREG-33012, Brookhaven National Laboratory, 1983.

7. UNIFORM CORROSION OF GRADE-12 TITANIUM

Previous immersion tests showed that a significant amount of metal loss will be produced during the long term immersion of passivated Grade-12 titanium. This is attributed to slow oxide dissolution by the passive current. To confirm this hypothesis, the samples were sandblasted to remove the oxide formed. After sandblasting, the weight loss in each sample is the sum of (1) oxide weight, (2) dissolved metal weight, and (3) underlying metal loss during the sandblasting. Contribution (3) is of the order of contribution (1), even though exact amounts are not known. Since the true corrosion kinetics are the sum of (1) and (2), it is necessary to determine contribution (3). Assuming that the sandblasting time for oxide removal is very short compared to that for underlying metal loss, due to the easy spallation of oxide, an equal amount of underlying metal is removed in each sample for the same sandblasting time. Therefore, the measured weight loss is due to the uniform corrosion plus a constant increment caused by sandblasting. Figure 7.1 shows that the weight loss kinetics have a non-linear time dependence. Higher weight loss was observed in welded samples.

The following conclusions may be made regarding uniform corrosion.

- The formation of a precipitate on the samples was observed upon solution heating. This precipitate was identified by X-ray analysis as an amorphous compound of Mg and Si.

- During the long-term immersion test, a significant amount of metal loss was observed. This has been attributed to slow oxide dissolution. The metal loss kinetics appear to be non-linear.

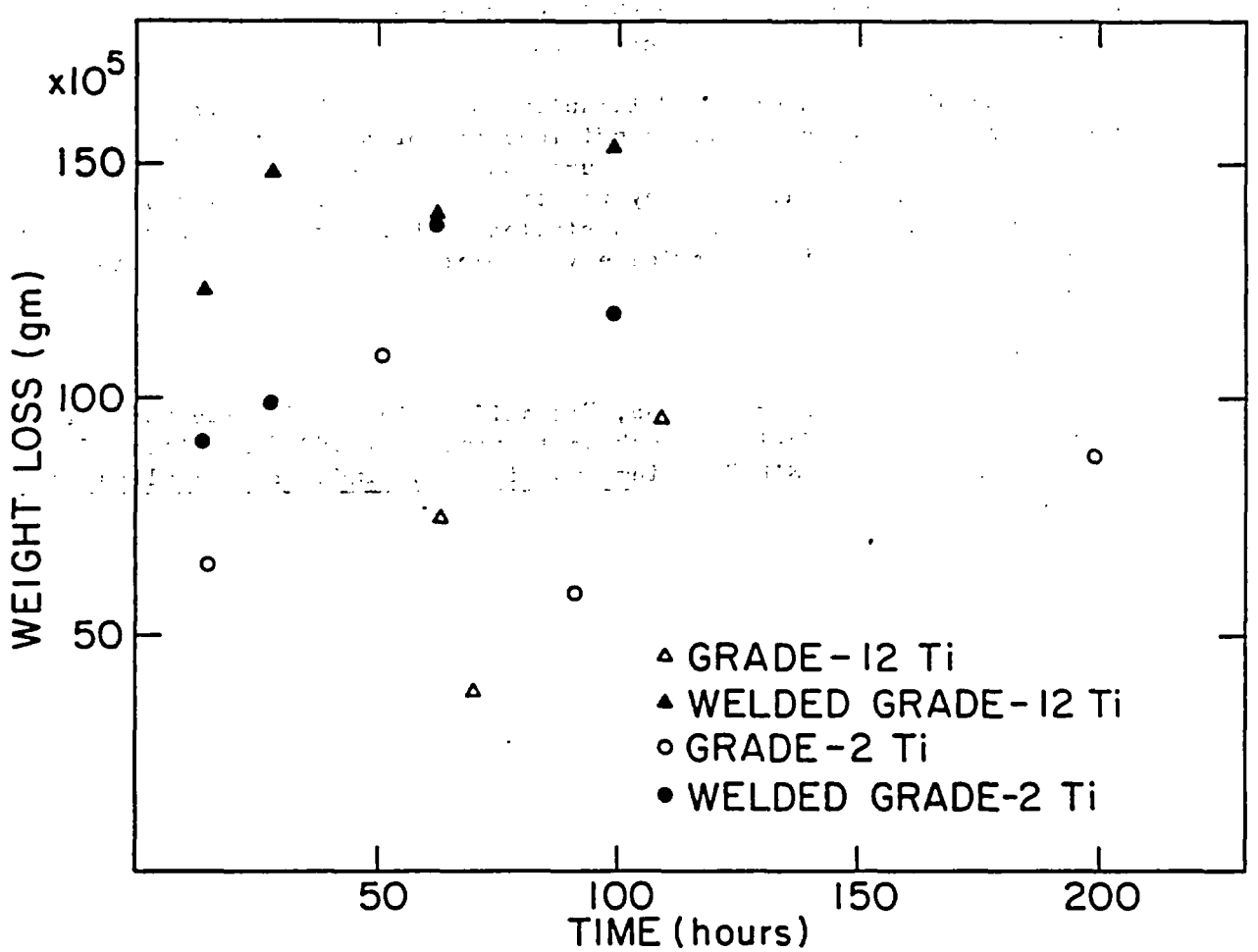

Figure 7.1. Long term weight loss data of single and welded coupons of Grade-12 and Grade-2 Ti in Brine A at 150°C.

8. PITTING CORROSION OF GRADE-12 TITANIUM

Earlier work in this program has shown that passivity breakdown in Grade-12 titanium crevices starts with pitting.[1] However, there is uncertainty whether the observed pitting is a true transpassive behavior or simply a transient phenomenon followed by active dissolution. To study these alternatives, single coupons (2x2 cm) are currently being immersed in acidified Brine A (pH = 1.1) for two weeks. The low pH is used in order to simulate crevice conditions for which pitting is encouraged.

Since the pitting on Grade-12 titanium in neutral brines has not been observed unless crevice corrosion conditions are present, it appears that pitting alone is not an important failure mode for the container. Within a crevice it is possible that pits may penetrate the container even if the average crevice surface has been repassivated. Therefore, determination of the kinetics of pitting in a crevice environment represents an important area for future study.

8.1 Reference

1. T. M. Ahn, B. S. Lee and P. Soo, "Identification of Crevice Corrosion in Titanium Alloy TiCode-12 in Rock Salt Brine at 150°C," submitted for publication in ASTM STP Titanium and Zirconium Industrial Applications, 1982.

9. WELD CORROSION EFFECTS

Limited work was carried out on weld corrosion. In the immersion tests for crevice corrosion at 150°C in Brine A, 1x2 cm^2 sandwiched coupons usually did not show crevice attack. However, when the coupons were electron beam welded, they tended to show a black film both in the fused as well as in the heat-affected zones. The severity of the attack, however, is less than that for larger non-welded samples.

In uniform corrosion tests, weight loss kinetics are typically faster than for simple coupons (see Section 7). Both crevice and uniform corrosion phenomena may be attributed to the presence of Ti_2Ni in the welded zone. Ti_2Ni is known to enhance hydrogen reduction rates due to the presence of Ni.[1] This may also lead to enhanced hydrogen uptake. Even from these limited data, it appears that welds will have significant deleterious effects on container corrosion resistance.

9.1 Reference

1. R. S. Glass, J. A. Ruppen and R. B. Diegle, "Sensitization to Corrosion of Ticode-12 Alloys," Extended Abstract, Electrochemical Society, Fall Meeting, Detroit, 1982.

10. HYDROGEN UPTAKE BY LOW CARBON STEEL IN CONCENTRATED BASALTIC GROUNDWATER UNDER GAMMA IRRADIATION

Presently, low carbon steel is specified as the principal reference material for the container to be used in a basalt repository. There is very little information on the stress corrosion behavior of this material under anticipated repository conditions. Absorption of hydrogen produced by radiolysis or corrosion, and the presence of some of the anions in groundwater are likely to enhance the SCC susceptibility. Therefore, to evaluate this mode of failure under simulated repository conditions an approximately two-year long program was initiated during the last quarter.

The concentration of ionic species in basaltic groundwater possibly can reach near saturation values when water vaporizes near the hot surface of the container. Therefore, in the present experiment a concentrated form of Grande Ronde basaltic water was prepared according to the composition given in Reference 1. Two solutions called A and B are prepared separately and then mixed in equal amounts. Solution A contains the sodium salts of carbonate, silicate, sulfate, fluoride and hydroxide, whereas Solution B is acidic and contains HCl and the chloride salts of potassium, calcium and magnesium. In our preparation, one-half of the saturation limit of Solution A was first determined, and then Solution B was adjusted to the same dilution. However, when the two solutions were mixed in equal volumes (to maintain the prescribed relative ratio of various ions), some precipitation occurred. Therefore, each solution was then diluted eight times and mixed in equal volumes. The concentrated form of groundwater prepared in this manner and referred to as 1/8 saturation is being used in the first exploratory experiment.

The low carbon cast steel (Type 1017) used in the present test was provided by Battelle Columbus Laboratory. To evaluate stress corrosion susceptibility as well as uniform corrosion, three U-bend specimens prepared from a strip of this steel were immersed in the concentrated groundwater and then subjected to gamma irradiation at a dose rate of 1.3×10^6 rads/h. The stainless steel capsule described earlier[2] in reference to the radiolysis of brine is being used in this experiment with the addition of a furnace to maintain the test temperature at 150°C. To avoid any galvanic effects the specimens are insulated from other metallic parts with the help of quartz spacers. At the end of one-month test period, there appears to be about 10 psi pressure increase in the capsule. After two more weeks, this test will be terminated and the gases in the capsule analyzed. The steel specimens also will be analyzed for their hydrogen content. A parallel test is being conducted in an autoclave but with no radiation present. A comparison of the two tests will indicate the effects of irradiation on the hydrogen uptake properties of steel samples.

10.1 References

1. RHO-RE-SR-5, "Reference Material Chemistry - Synthetic Groundwater Formation," T. E. Jones, Rockwell Hanford, April 1982.

2. NUREG/CR-2317, Vol. 1, No. 3, "Container Assessment - Corrosion Study of HLW Container Materials," T. M. Ahn and P. Soo, January 1982.

11. REPORTS ON GRADE-12 AND GRADE-2 CORROSION IN BRINE ENVIRONMENTS

Below are listed quarterly progress reports, topical reports and technical papers presented during the course of the current program:

- Container Assessment - Corrosion Study of HLW Container Materials
  Quarterly Progress Report, T. M. Ahn and P. Soo
  April-June 1981, BNL-NUREG-51449, Vol. 1, Nos. 1-2,
  July-September 1981, BNL-NUREG-51449, Vol. 1 No. 3
  October-December 1981, BNL-NUREG-51449, Vol. 1 No. 4
  January-March 1982, BNL-NUREG-51449, Vol. 2, No. 1
  April-June 1982, BNL-NUREG-31611
  July-September 1982, BNL-NUREG-32047
  September-December 1982, BNL-NUREG-32512
  January-March 1983, BNL-NUREG-33012
  April-June 1983, BNL-NUREG-33603
  July-September 1983, present report.

- Identification of Crevice Corrosion in Titanium Alloy TiCode-12 in Rock Salt Brine at 150°C
  T. M. Ahn, B. S. Lee and P. Soo
  Submitted for publication in ASTM STP Titanium and Zirconium in Industrial Applications, 1982.

- Crevice Corrosion of Titanium in a Brine Solution
  B. S. Lee, T. A. Ahn and P. Soo
  Extended Abstract in The Symposium of Crevice Corrosion, The Electrochemical Society, Fall Meeting, Detroit, 1982.

- Corrosion of TiCode-12 in a Simulated Waste Isolation Pilot Project (WIPP) Brine
  T. M. Ahn, B. S. Lee, J. Woodward, R. L. Sabatini and P. Soo
  In the Proceedings of the Materials Research Society Symposium on Scientific Basis for Nuclear Waste Management, 1982, Boston, 1982.

- Internal Hydrogen Embrittlement of Titanium Alloy TiCode-12 at Room Temperature
  T. M. Ahn and P. Soo
  BNL-NUREG-51671, 1983.

- The Kinetics of Internal Hydrogen Embrittlement in ASTM Grade-12 Titanium Alloy
  T. M. Ahn and P. Soo
  Abstract for the TMS-AIME Fall Meeting, Philadelphia, Pennsylvania, October 2-6, 1983.

- Immersion and Surface Studies for Crevice Corrosion of Grade-12 Titanium in a Brine Solution
  T. M. Ahn and P. Soo
  Extended Abstract for the Electrochemical Society Fall Meeting, Washington, D. C., October 9-14, 1983.

- Current, Potential and pH Measurements for the Crevice Corrosion of Grade-12 Titanium in a Brine Solution
  H. Jain and T. M. Ahn
  Extended abstract for the Electrochemical Society Fall Meeting, Washington, D. C., October 9-14, 1983.

- Models for the Initiation of Crevice Corrosion of Grade-12 Titanium in a Brine Solution
  T. M. Ahn
  Extended abstract for the Electrochemical Society Fall Meeting, Washington, D. C., October 9-14, 1983.

- Stress Corrosion of Grade-2 and Grade-12 Titanium in Simulated Rock Salt Brines at 83°C
  H. Jain, T. M. Ahn and P. Soo
  Abstract for the TMS-AIME Fall Meeting, Philadelphia, Pennsylvania, October 2-6, 1983. TMS Paper Selection No. F83-1.

- A Technique for Characterizing Crevice Corrosion Under Hydrothermal Conditions
  H. Jain, T. M. Ahn and P. Soo
  To appear in ASTM STP, Laboratory Corrosion Tests and Standards.

- Long Term Prediction of Crevice Corrosion and Hydrogen Embrittlement of TiCode-12
  T. M. Ahn and H. Jain
  To appear in CORROSION '84.

- Gamma Irradiation Effects on Simulated Rock Salt Brines
  (draft report completed).

- Models for Internal Hydrogen Embrittlement in Hydride Forming Materials
  (in preparation).

- Alkali Formation and Its Effects on TiCode-12 Corrosion in Simulated Rock Salt Brine at 150°C
  (in preparation).

APPENDIX A

A TECHNIQUE FOR CHARACTERIZING CREVICE CORROSION UNDER HYDROTHERMAL CONDITIONS*

H. Jain, T. M. Ahn and P. Soo

Department of Nuclear Energy

Brookhaven National Laboratory

Upton, New York 11973

*This work was performed under the auspices of the United States Nuclear Regulatory Commission.

ABSTRACT

A technique was developed to monitor crevice corrosion of Grade-12 titanium in a high magnesium synthetic brine under hydrothermal conditions. The current between the cathode and anode, and the potential of the whole crevice assembly, provide information on the various stages of corrosion. Occasionally, the decoupled potential of the cathode and anode are measured to give supporting information about the crevice conditions. A parallel test is run on a specimen which has small wells to collect crevice solution whose pH is determined at room temperature.

The current/potential results show that the crevice corrosion incubation period for a Grade-12 titanium crevice formed between two Teflon plates is approximately two days at 150°C. Optical and SEM observations show that the corrosion starts as isolated pitting which spreads along the surface as shallow pits. The corrosion conditions change significantly as the TiO_2 corrosion product fills the crevice, and the rate of corrosion may be greatly reduced after several days. The rate of crevice corrosion of commercial purity (Grade-2) titanium under similar conditions is approximately three orders of magnitude higher. In this case, active dissolution of metal starts during the initial heating of the autoclave and the incubation period is negligible.

KEY WORDS

Crevice Corrosion, Hydrothermal, Titanium and alloys, Brine, Pitting, Electrochemical Techniques, Incubation Period.

PAPER NUMBER 202 BNL-NUREG-33731R

To be presented at CORROSION 84, April 2-4, 1984, New Orleans, Louisiana

PREDICTION OF LONG TERM CREVICE CORROSION AND HYDROGEN EMBRITTLEMENT BEHAVIOR OF ASTM GRADE-12 TITANIUM*

T. M. Ahn and H. Jain
Brookhaven National Laboratory
Upton, NY 11973

ABSTRACT

Crevice corrosion and hydrogen embrittlement are potential failure modes of Grade-12 titanium high level nuclear waste containers emplaced in rock salt repositories. A method is presented to estimate the environment domains for which immunity to these failure modes will exist for periods of hundreds of years. The estimation is based on the identification and quantification of mechanisms involved. Macroscopic concentration cell formation is responsible for crevice corrosion. The cell formation is accompanied by oxygen depletion, potential drop, anion accumulation and acidification inside the crevice. This process is quantified by simple mass balance equations which show that the immunity domain is a function of the time the container is exposed to the corrosion environment. Strain induced hydride formation is responsible for hydrogen assisted crack initiation. A simple model for slow crack growth is developed using data on growth rates measured at various temperatures. The parameters obtained in the model are used to estimate the threshold stress intensity and hydrogen solubility limit in the alloy at infinite container service time. This value gives a crack size below which container failure will not occur for a given applied stress and hydrogen concentration, and a hydrogen concentration limit at a given stress intensity.

*This work was performed under the auspices of the United States Nuclear Regulatory Commission.

BNL-NUREG -34220
INFORMAL REPORT
LIMITED DISTRIBUTION

CONTAINER ASSESSMENT - CORROSION STUDY OF HLW CONTAINER MATERIALS

QUARTERLY PROGRESS REPORT
OCTOBER-DECEMBER 1983

T. M. AHN AND P. SOO

JANUARY 1984

NUCLEAR WASTE MANAGEMENT DIVISION
DEPARTMENT OF NUCLEAR ENERGY BROOKHAVEN NATIONAL LABORATORY
UPTON, NEW YORK 11973

Prepared for the U.S. Nuclear Regulatory Commission
Office of Nuclear Regulatory Research
Contract No. DE-AC02-76CH00016

NOTICE

BNL-NUREG-34220
INFORMAL REPORT
Limited Distribution

CONTAINER ASSESSMENT - CORROSION STUDY OF HLW CONTAINER MATERIALS

QUARTERLY PROGRESS REPORT
October-December 1983

T. M. Ahn and P. Soo

Manuscript Completed January 1984

Prepared by the Nuclear Waste Management Division
D. G. Schweitzer, Head
Department of Nuclear Energy, Brookhaven National Laboratory
Associated Universities, Inc.
Upton, New York 11973

Prepared for the U.S. Nuclear Regulatory Commission
Office of Nuclear Regulatory Research
Contract No. DE-AC02-76CH00016
FIN No. A-3237

ABSTRACT

Low carbon cast steel is a candidate container material for high level waste to be emplaced in a basalt repository. The current study is an evaluation of potential hydrogen embrittlement and stress corrosion effects in this steel which could be present in basaltic groundwater. In this quarter, Type 1017 low carbon cast steel was evaluated using constant extension rate tests (CERT) in concentrated Grande Ronde basaltic water at 85°C for strain rates usually in the range 1.33×10^{-7} to 3.28×10^{-7}/sec. A cathodic hydrogen charged sample showed a distinctive cleavage fracture and a sample tested in moisture above the solution gave an indication of reduced elongation. Tests at the open circuit corrosion potential also gave an indication of degradation although less distinctive than the above two test conditions. Strain rate effects were not significant in tests performed in air at strain rates of 1.72×10^{-7}/sec and 1.69×10^{-4}/sec.

Hydrogen uptake tests on Type 1017 low carbon cast steel were completed after two months in concentrated Grande Ronde basaltic water at 150°C under a gamma irradiation flux of 1.3×10^{6} rad/h. No sign of stress corrosion cracking or significant uniform corrosion was observed. After the tests the welded specimen contained 10 ppm hydrogen and the unwelded specimen contained 19 ppm hydrogen. In contrast, tests without gamma irradiation showed severe corrosion with an indication of pitting. Hydrogen produced by uniform corrosion was significant since welded and unwelded specimens absorbed significant quantities of the gas. For welded material, U-bend and flat samples contained 10 and 23 ppm hydrogen, respectively. For unwelded material the U-bend and flat samples contained 53 and 31 ppm of hydrogen. Gas in the plenum above the test solution was mainly H_2 with smaller amounts of O_2 and CO_2.

Tests on Grade-12 titanium were finalized by analyzing the remaining samples. There was no indication of spontaneous pitting from immersion test on coupons exposed to acidified brine at 150°C which simulates the crevice solution condition. For slow crack growth measurements, a direct potential change method was used to confirm the crack jump process observed in surface crack measurements. Tensile test results for Grade-12 titanium were obtained from tests performed at various temperatures and hydrogen concentrations. Lower strength values were obtained in as-received material compared with values from the literature, which could be caused by differences in strain rate or grain size.

CONTENTS

FIGURES

FIGURES (Continued)

TABLES

ACKNOWLEDGMENTS

The authors gratefully acknowledge Dr. H. Jain who was involved in the early studies on hydrogen uptake in carbon steel. Special thanks are extended to C. Anderson for general assistance, R. Wilson for hydrogen analysis and R. Sabatini for SEM work. Also, they would like to thank G. Searles for her patience and skill in the typing and preparation of this report.

1. INTRODUCTION

The objective of this program is to identify and evaluate some of the potential corrosion failure modes in low carbon steel which is the reference container material for high level waste packages to be emplaced in basalt repositories. Experimental work on ASTM Grade-12 titanium pertinent to behavior in a salt repository was essentially terminated in Fiscal Year 1983. However, analysis of the data will continue for a short time, after which the work will focus exclusively on carbon steel corrosion.

In the carbon steel program two main areas will be emphasized. One involves an evaluation of hydrogen assisted embrittlement effects, and the other is concerned with the measurement of hydrogen uptake in the presence of basaltic water and a gamma irradiation field. Preliminary results are described below.

2. SLOW STRAIN RATE TESTING OF CAST LOW CARBON STEEL

Low carbon cast steel rod (ASTM A216-Grade WCA) was obtained from Axiom Machine and Foundry, Inc. with the maximum composition given in Table. 1. The composition is currently being determined by BNL. This steel was recommended by Westinghouse Advanced System Division for their proposed waste package design for a basalt repository.[1] Specimens with the geometry shown in Figure 1 were machined from the steel for constant extension rate tests (CERT) or slow strain rate tests. The gauge lengths were polished to 0.5 μm alumina powder and tensile tested at 85°C in air, moist air over concentrated basaltic water and approximately 7.7 times concentrated Grande Ronde groundwater.[2] This concentrated water composition is given in Table 2.

Table 1. Maximum composition of ASTM A216-WCA steel (weight percent, balance is iron).

C	Mn	Si	S	P	Cu	Ni	Cr	Mo	V
0.25	0.7	0.3	0.65	0.045	0.50	0.50	0.04	0.25	0.03

Preliminary CERT data are presented in Table 3. For the tests in the aqueous solution, both open circuit potential and cathodic charging (-1.4 V SCE) conditions have been used in order to evaluate the effects of hydrogen uptake on strength and ductility. Figures 3 through 7 show fractographs obtained from failed specimens. Figure 8 is a reference cathodic polarization curve obtained for the cast steel in the concentrated groundwater. Point (a) represents the potential for which oxygen is reduced and point (b) gives the potential for which hydrogen is produced. Based on values for total elongation the moist air environment gives the most embrittling condition. However, the large reduction-in-area value indicates that there is high ductility compared ?

to the other environments. The test will be repeated to confirm the preliminary ductility data in Table 3. The fractured surface for the moist air test given in Figure 7 shows that significant amounts of oxide are present. This may be connected with a well-known effect in which water vapor condenses in the capillary region of a crack tip to give the aqueous phase.[3]

Table 2. Concentrated Grande Ronde basaltic water composition*.

Ion	Nominal Composition, mg/L
Na^+	2774.5
K^+	26.6
Ca^{+2}	21.5
Mg^{+2}	0.25
F^-	258.9
Cl^-	2418.0
SO_4^{-2}	1340.8
SiO_2	614.6
pH	10.3

*2.95 g/L Na_2CO_3 were dissolved initially to obtain the CO_3^{-2} concentration. However, CO_3^{-2} concentration varies during test due to the loss of CO_2.

The next most severe environment was for the test in which the specimen was at a cathodic potential. Under such conditions the effective hydrogen fugacity f_H is approximately given by:[4]

$$f_H = \exp(\eta F/ZRT)$$

where F is Faraday's constant, Z is a constant equal to 2 and η is the hydrogen overpotential. At the present overpotential of -1.4 V SCE, the fugacity approaches 660 atms which is much larger than expected under repository conditions. The fractographs for the test specimen show the presence of cleavage areas as shown in Figure 6(b).

The test performed in the aqueous solution at open circuit potential also shows a small degradation in reduction-in-area even though the elongation does not clearly indicate this. Currently, this test is being repeated. In the fractograph for this specimen [Figure 5(c)] there is an indication of non-ductile behavior. In order to evaluate whether crack propagation occurs by the active path mechanism,[5] a test is being carried out under an anodic potential.

Table 3. Results of cast low carbon steel CERT tests conducted at 85°C in various environments.

Sample No.	Average Strain Rate (/sec)	Environment	Total Elongation (%)	Reduction In Area (%)	(0.2% offset) Yield Strength (MPa)	Tensile Strength (MPa)	Fracture Strength (MPa)	Fracture Surface
SS1	2.72×10^{-7}	Air	17.0	58.0	330	561	439	Figure 3
SS5	1.69×10^{-4}	Air	17.0	57.0	333	414	276	Figure 4
SS2	1.33×10^{-7}	Solution (Open Circuit Potential)	18.5	48.2	383	578	462	Figure 5
SS3	2.89×10^{-7}	Solution (Cathodic Charging)	15.0	25.5	272	443	325	Figure 6
SS4	3.28×10^{-7}	Moist air above solution	13.0	63.9 ?	412	556	484	Figure 7

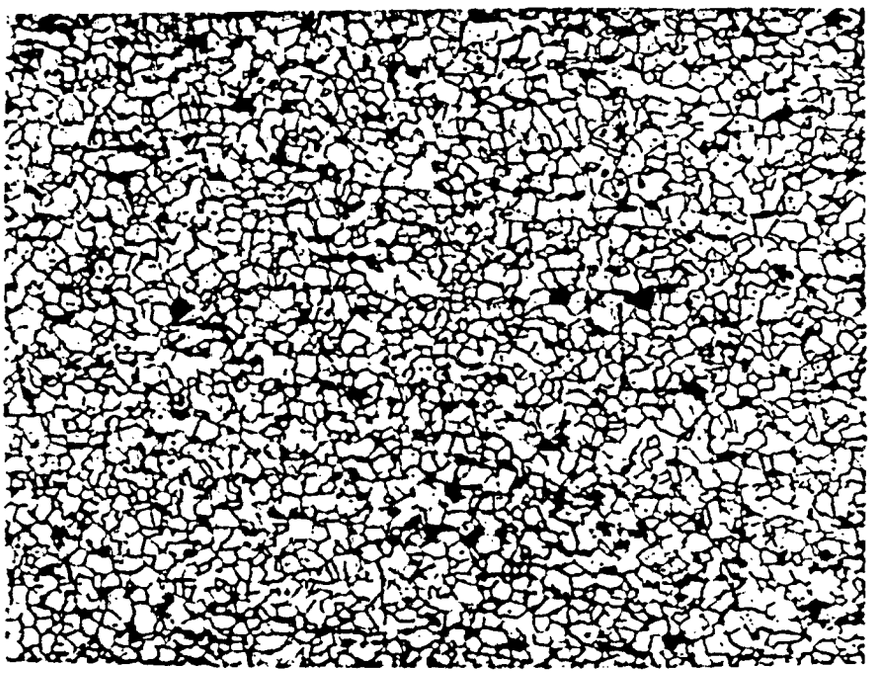

Longitudinal section

100 μm

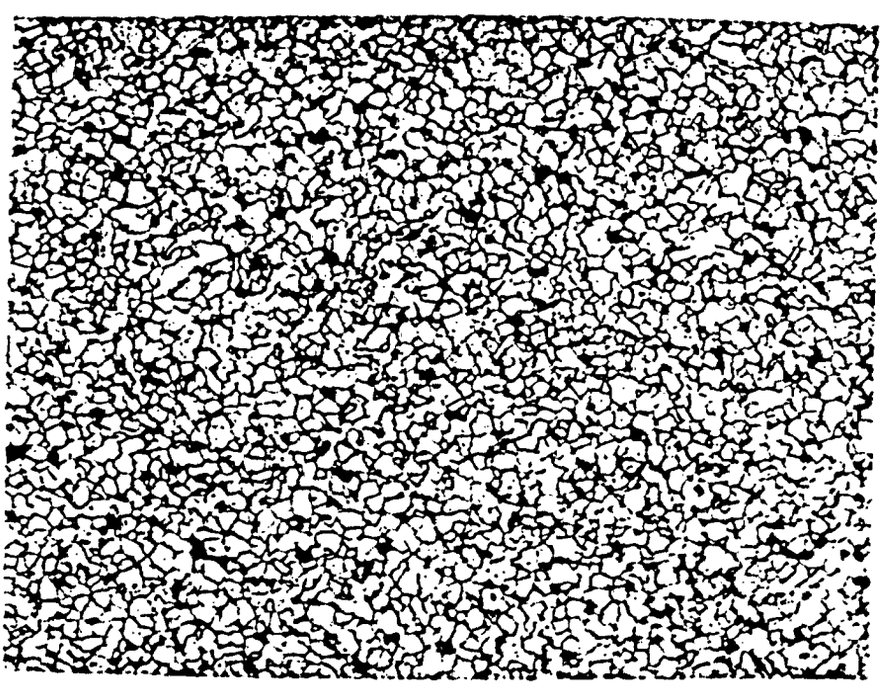

Transverse section

100 μm

Figure 1. Initial microstructure of ASTM A216-Grade WCA cast steel rod.

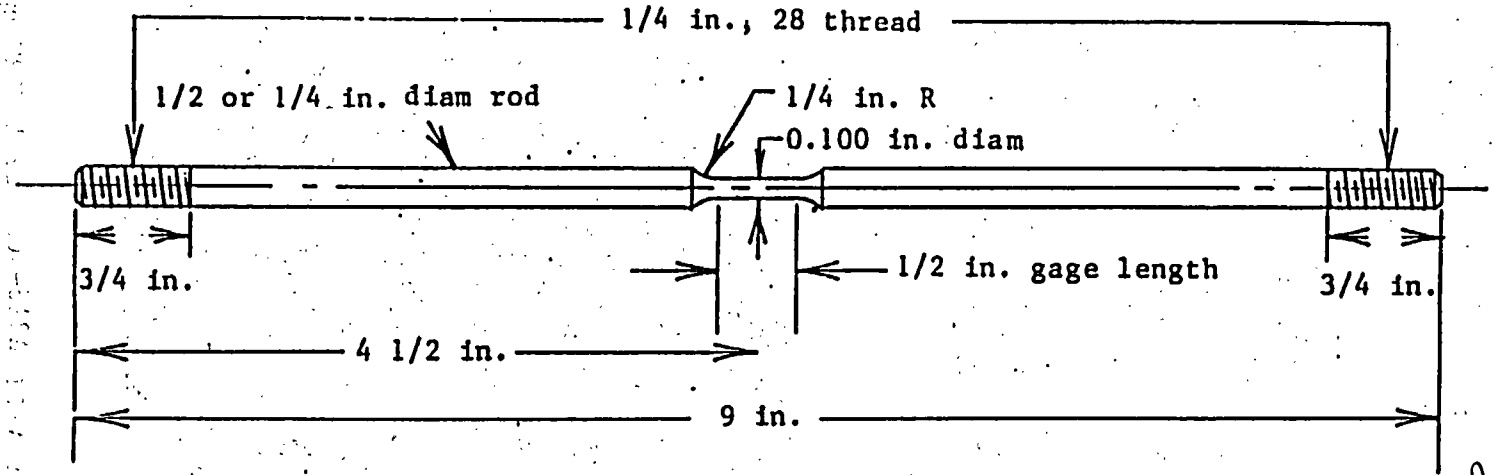

Figure 2. CERT test specimen configuration for stress corrosion cracking and hydrogen embrittlement tests.

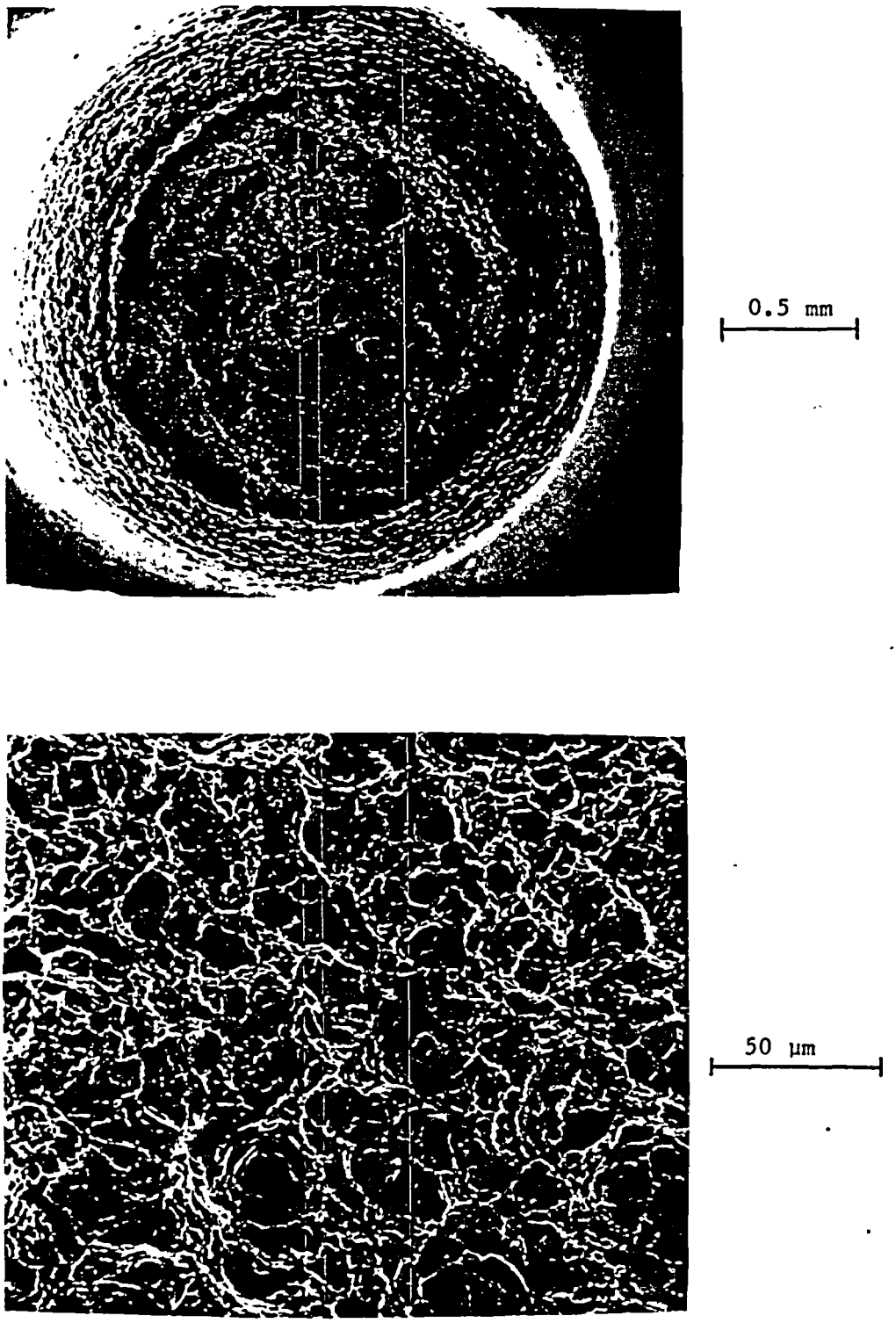

Figure 3. Fractograph of ASTM A216-WCA steel CERT specimen tested in air at a strain rate of 2.72×10^{-7}/sec, showing ductile fracture.

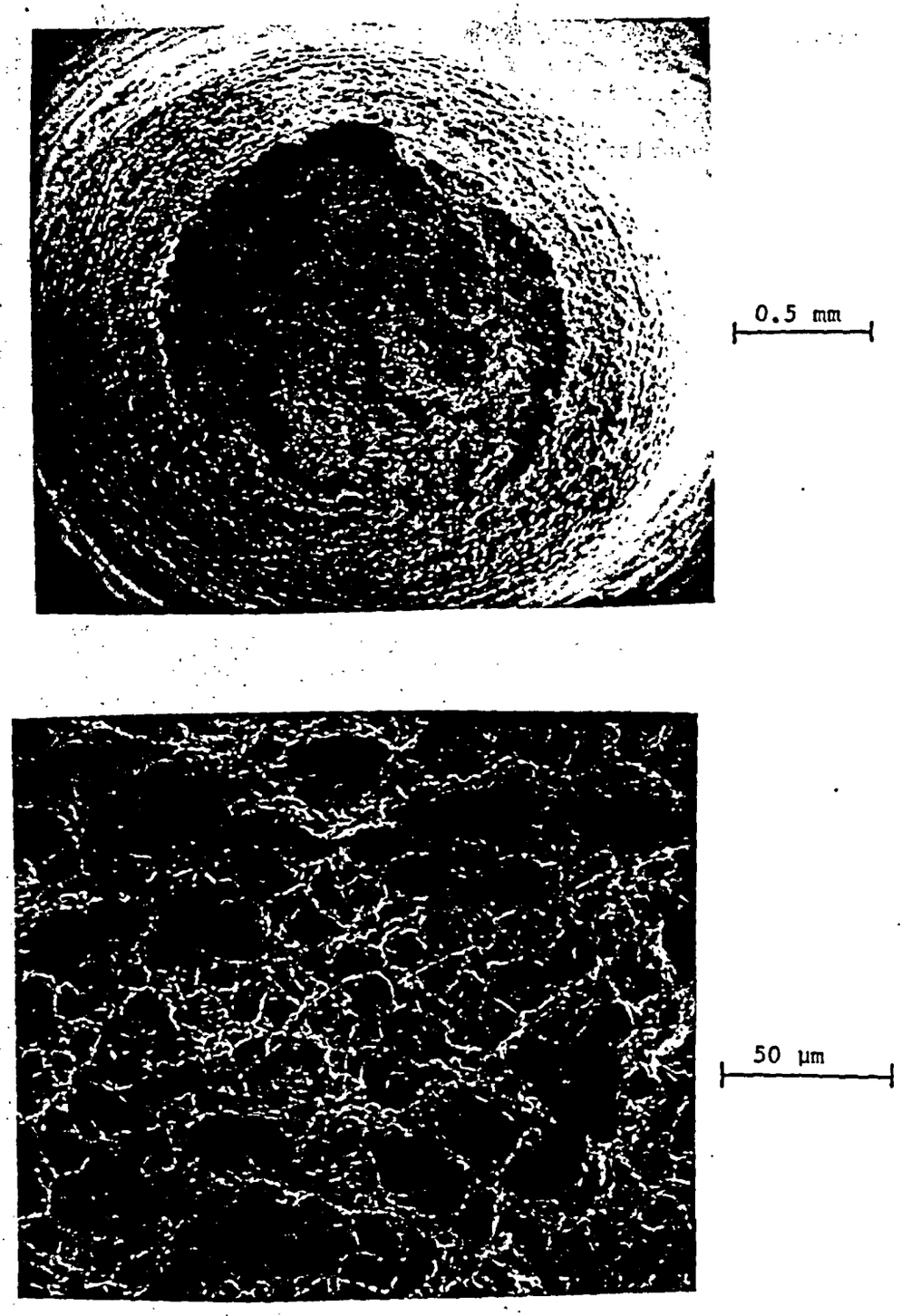

Figure 4. Fractograph of ASTM A216-WCA steel CERT specimen tested in air at a strain rate of 1.69×10^{-4}/sec, showing ductile fracture.

Figure 5. Fractographs of ASTM A216-WCA steel CERT specimen tested at a strain rate of 1.33×10^{-7}/sec in concentrated Grande Ronde basaltic water; (a) whole fracture surface, (b) magnified view of 5(a) showing mostly ductile fracture and (c) some localized embrittled regions.

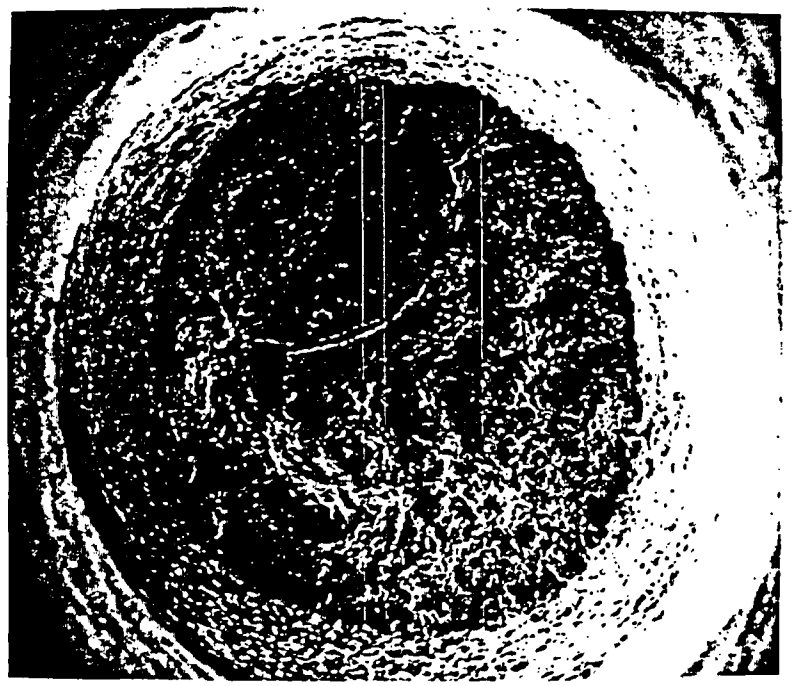

5(a)

0.5 mm

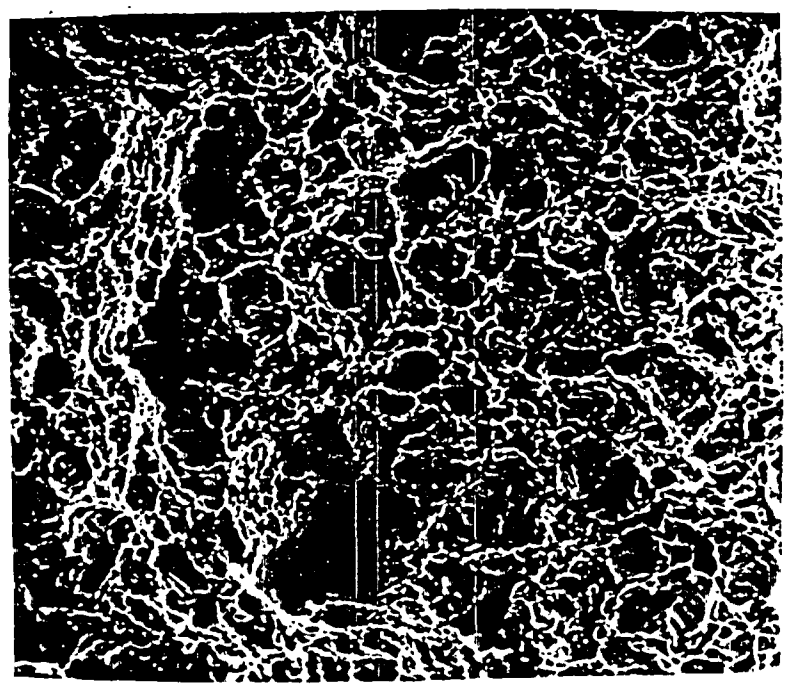

5(b)

50 µm

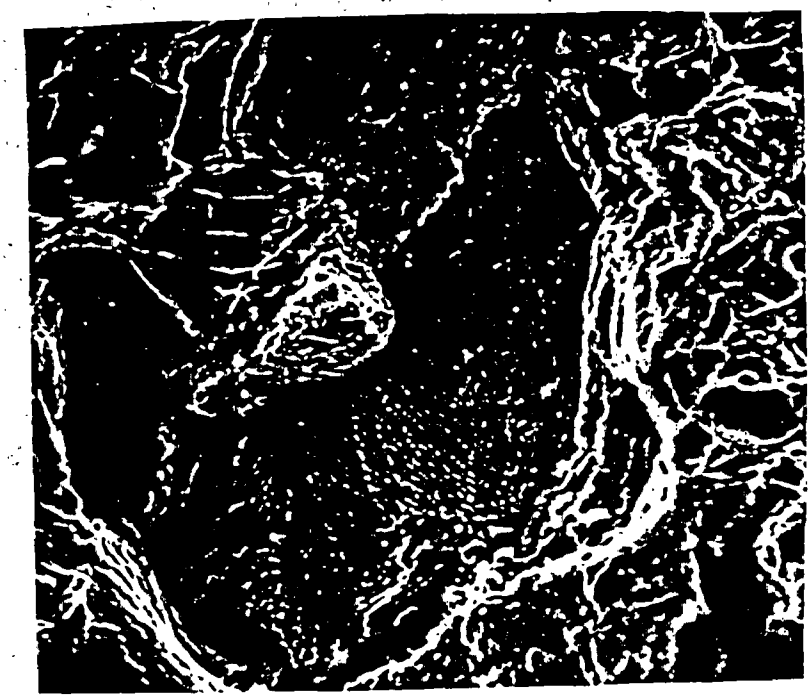

5(c)

10 µm

Figure 6. Fractographs of ASTM A216-WCA steel CERT specimen tested at a strain rate of 2.89 x 10^{-7}/sec in concentrated Grande Ronde basaltic water with cathodic charging at -1.4 volt SCE; (a) whole fracture surface, (b) magnified view of 6(a) showing cleavage fracture regions and (c) surface cracking on side of sample.

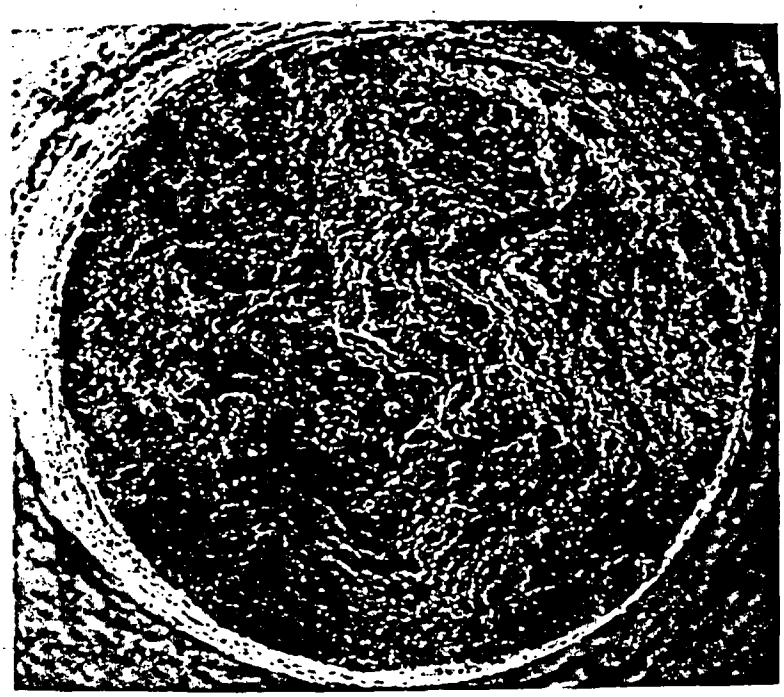

6(a)

0.5 mm

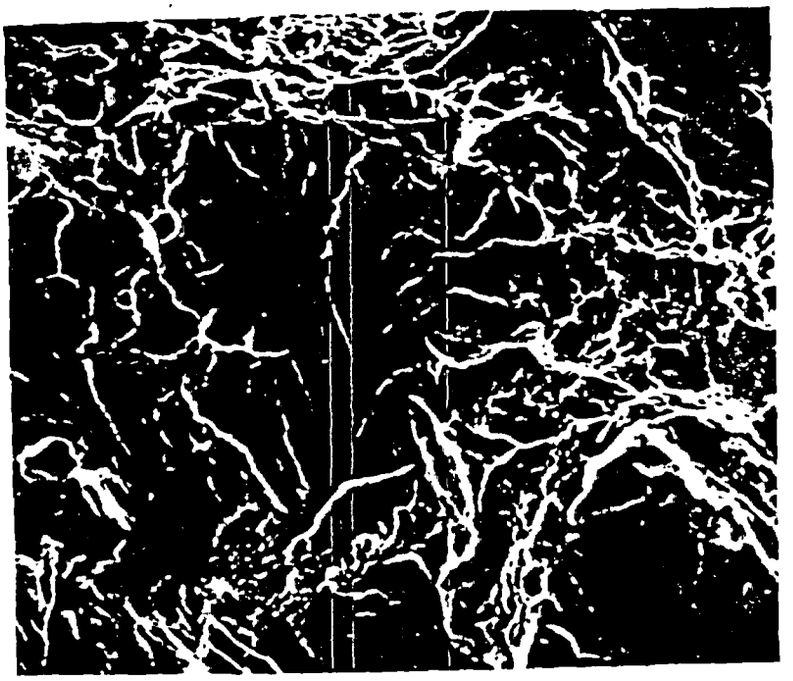

6(b)

10 μm

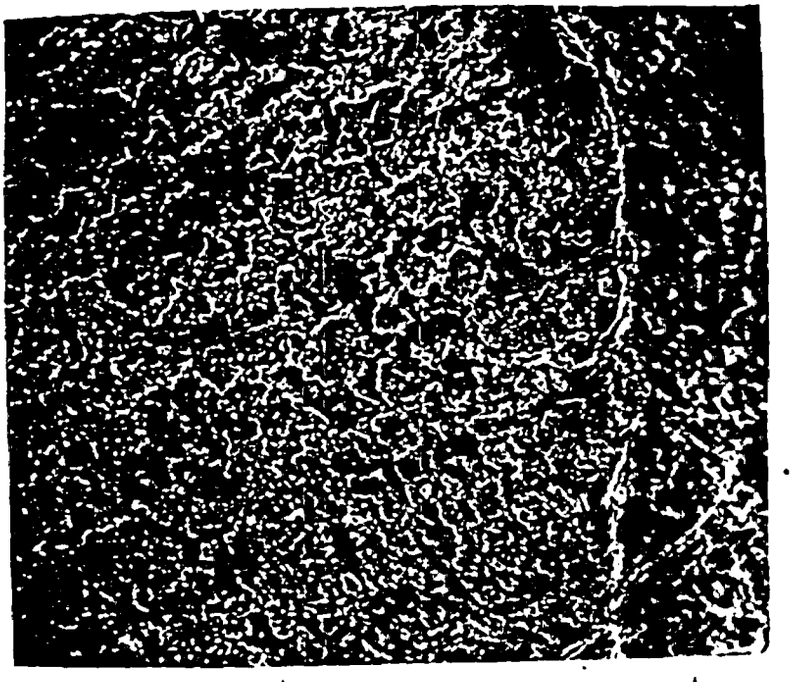

6(c)

100 μm

Side Surface

Fracture Surface

Figure 7. Fractographs of ASTM A216-WCA steel CERT specimen tested at a strain rate of 3.28×10^{-7}/sec in moist air; (a) whole surface covered with oxides, (b) magnified view of 7(a) showing secondary cracking and (c) enlarged view of secondary cracking.

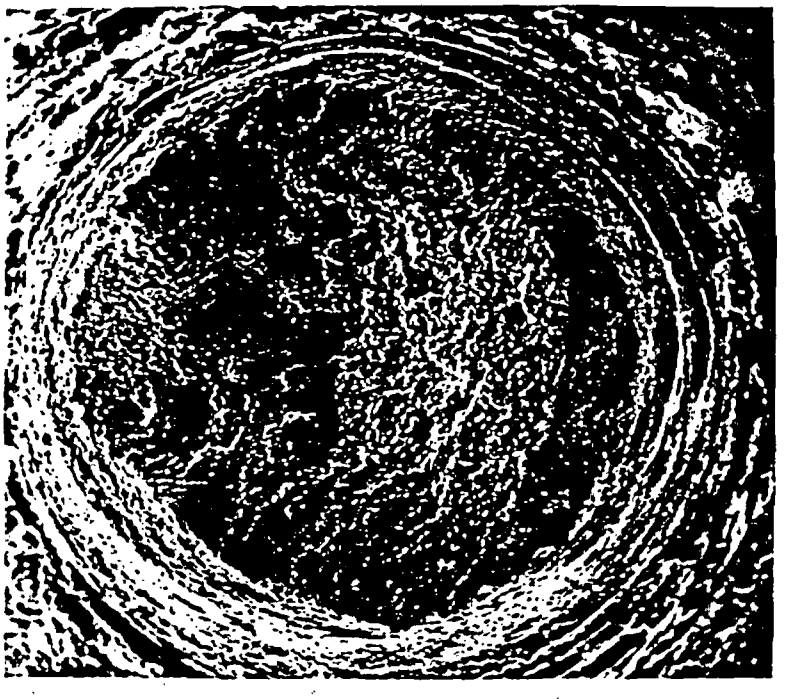

7(a)

0.5 mm

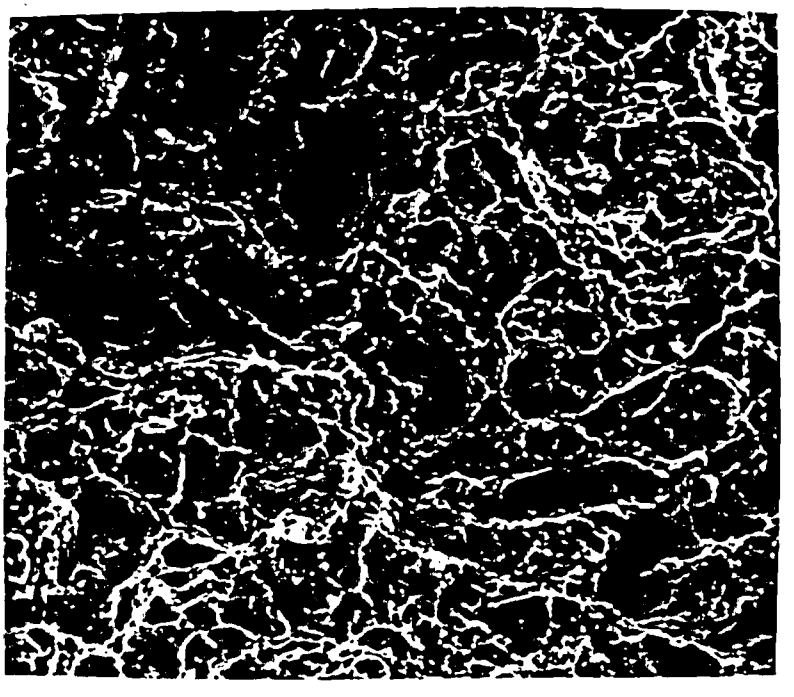

7(b)

50 µm

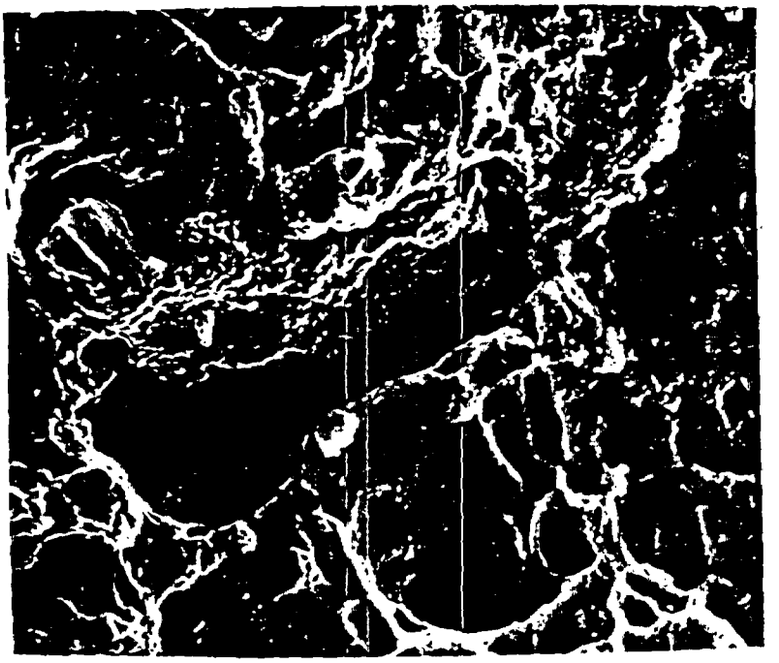

7(c)

10 µm

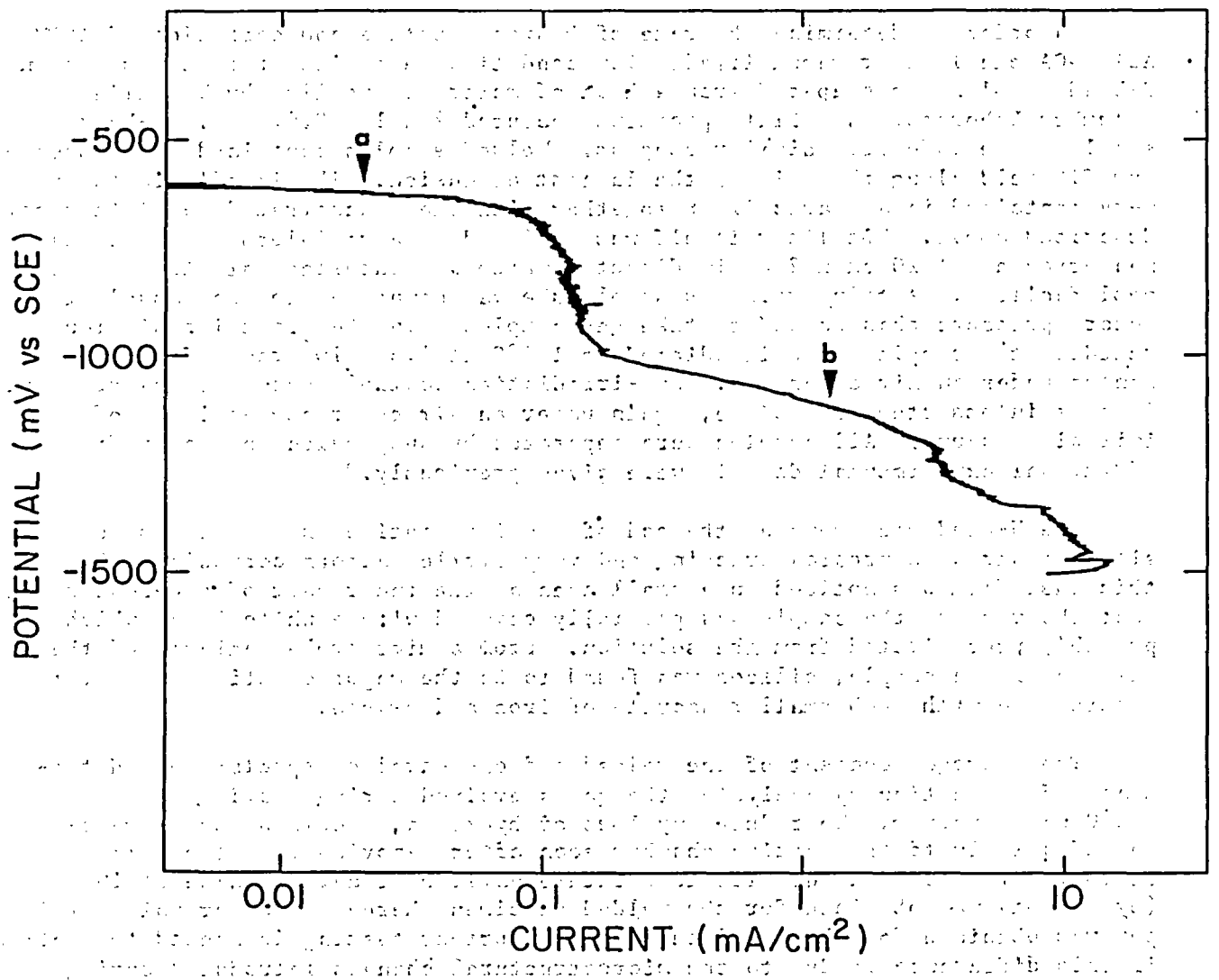

Figure 8. Cathodic polarization curve of ASTM A216-WCA steel at 85°C. Point (a) represents the oxygen reduction potential while point (b) represents the hydrogen reduction potential.

A potentially important observation for the air test data is that the strain rate does not influence the ductility although the tensile and fracture strengths are higher for the slow strain rate.

3. HYDROGEN UPTAKE AND RADIATION CORROSION OF CAST STEEL

In order to determine the rate of hydrogen uptake and corrosion of ASTM A216-WCA steel under gamma irradiation conditions a series of flat coupons and U-bend samples was prepared from a heat of material supplied by Battelle Columbus Laboratories. Flat specimens measured 2 x 1 x 0.075 cm. U-bend samples were made from similar coupons. Welded samples contained an autogeneous TIG weld along the axis of the largest dimension. The irradiation samples were contained in a quartz liner together with the concentrated basaltic water described above. The liner itself was enclosed in a stainless steel capsule measuring about 20 cm x 2 cm in diameter which was inserted into the BNL gamma pool facility. A thin stainless steel tube was connected to the capsule to record pressure changes and to take gas samples. In the first irradiation schedule the samples were irradiated at 150°C at 1.3×10^6 rad/h for two months under an air cover gas. Non-irradiation control tests were carried out in a stainless steel autoclave, again under an air cover gas at 1 atm of initial pressure. All samples were separated by suspension on quartz frames. Additional experimental details were given previously.[6]

The U-bend specimens at the end of the irradiation experiment showed no signs of stress corrosion cracking and very little uniform corrosion. Only a thin rust film was noticed on a small area at the inner part of a U-bend specimen; the rest of the sample was partially covered with a white layer which had probably precipitated from the solution. From a microprobe analysis of the surface of the sample, silicon was found to be the major constituent of this precipitate with much smaller amounts of iron and oxygen.

The hydrogen content of one welded and one unwelded specimen was determined after testing by analyzing the gases evolved during heating to ~900-950°C under vacuum. To reduce any loss of hydrogen, specimens were transferred quickly to the heating chamber soon after removing from the gamma pool or they were stored at dry ice temperature until heating. A value of 10 ppm (by weight) was obtained for the welded specimen whereas a larger value of 19 ppm was obtained for the unwelded sample. Further testing is needed to confirm if this difference is due to the microstructural changes introduced during welding or to differences in the surface conditions. Clearly, large amounts of hydrogen are absorbed during the test because as-received steel samples have typically less than one ppm hydrogen.[7]

In contrast to the steel specimens subjected to gamma irradiation, the unirradiated specimens showed a thick dark brown layer of rust on the surface. An SEM micrograph of the specimen cross-section shows that the thickness of the oxide (rust) layer was in the range of one to several microns (Figure 9). The spalling of rust from the metal surface is connected with the formation of blisters (Figure 9) which were observed at several locations. The oxide layer

was usually thicker under these regions. There is also some sign of pitting under the present test conditions. Figure 10 shows the cross section across a pit formed on the metal surface which is covered with a layer of rust.

The hydrogen contents of various specimens in this non-irradiation test are given in Table 4. As in the case of the radiation experiment, the hydrogen concentration in welded specimens is smaller than in the as-received condition. Also, the quantities of hydrogen are generally lower for the specimens which were subjected to irradiation although a significant amount of hydrogen was generated during radiolysis. This suggests that the hydrogen generated at the metal surface during uniform corrosion is more readily absorbed than that produced during the radiolysis of the solution.

Table 4. Hydrogen content of ASTM A216-WCA steel specimens exposed to concentrated basaltic groundwater at ~150°C for two months.

Specimen Type	Concentration (ppm by weight)
As-recieved flat	31
As-received U-bend	53
Welded flat	23
Welded U-bend	10

A chemical analysis of a gas sample taken from the irradiation corrosion capsule is given in Table 5. Apart from the N_2 originally present in the air cover gas, the main radiolytic product is hydrogen. The oxygen level is much less than the anticipated value for radiolysis, possibly indicating that it has reacted with constituents in the groundwater to produce the silicon rich phase described above. A significant quantity of CO_2 is also present and probably originates from the decomposition of Na_2CO_3. The gas pressure as a function of time is given in Figure 11. The pressure shows an initial very fast increase as the temperature of the capsule is raised to 150°C after which it tended to stabilize except for two small abrupt increases.

The very low corrosion rate under gamma irradiation may be caused by passivation processes although preliminary anodic polarization studies using non-irradiated solution indicate that a passive region is absent. A possible explanation of the low irradiation corrosion rate is that a radiolytic specie, such as hydrogen, gives rise to a reducing environment.

Some work by Westerman and others[8] on the corrosion of ductile iron and 2 1/2Cr-1Mo steel in basaltic groundwater at 250°C in the presence of a gamma flux of about 2×10^5 rad/h also shows that irradiation reduces the uniform corrosion rate for tests lasting one month. After three months' immersion, however, the corrosion rate is greater than for non-irradiation conditions; at

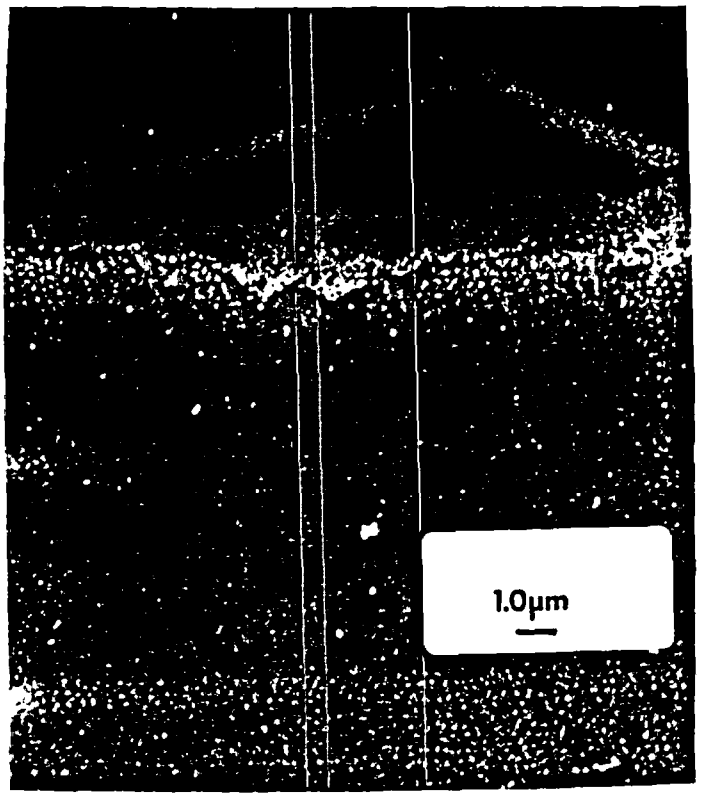

Figure 9. SEM micrograph of ASTM A216-WCA steel specimen exposed to concentrated Grande Ronde basaltic water for two months at 150°C, showing an oxide blister on the surface.

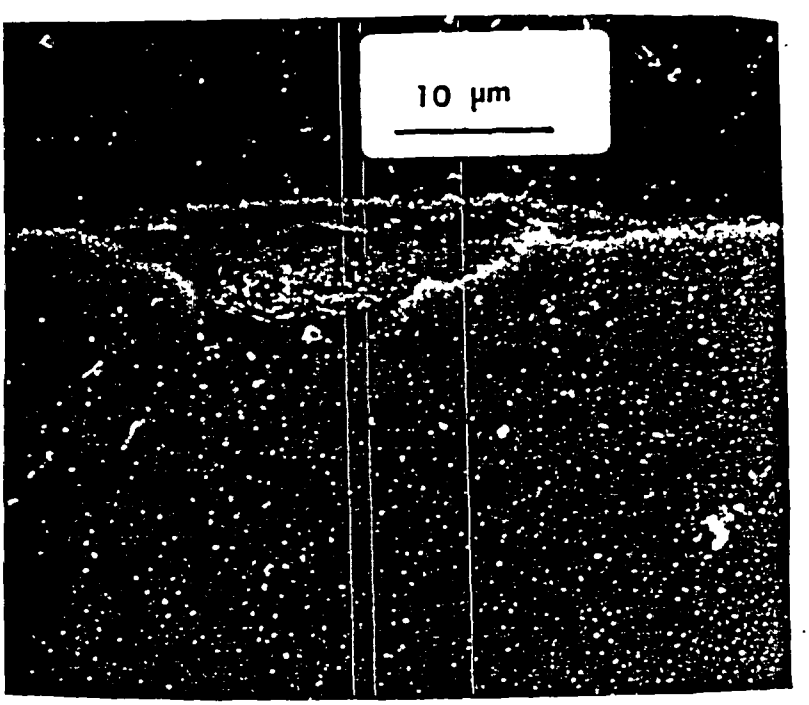

Figure 10. SEM micrograph of ASTM A216-WCA steel specimen exposed to concentrated Grande Ronde basaltic water for two months at 150°C, showing a cross section through a pit.

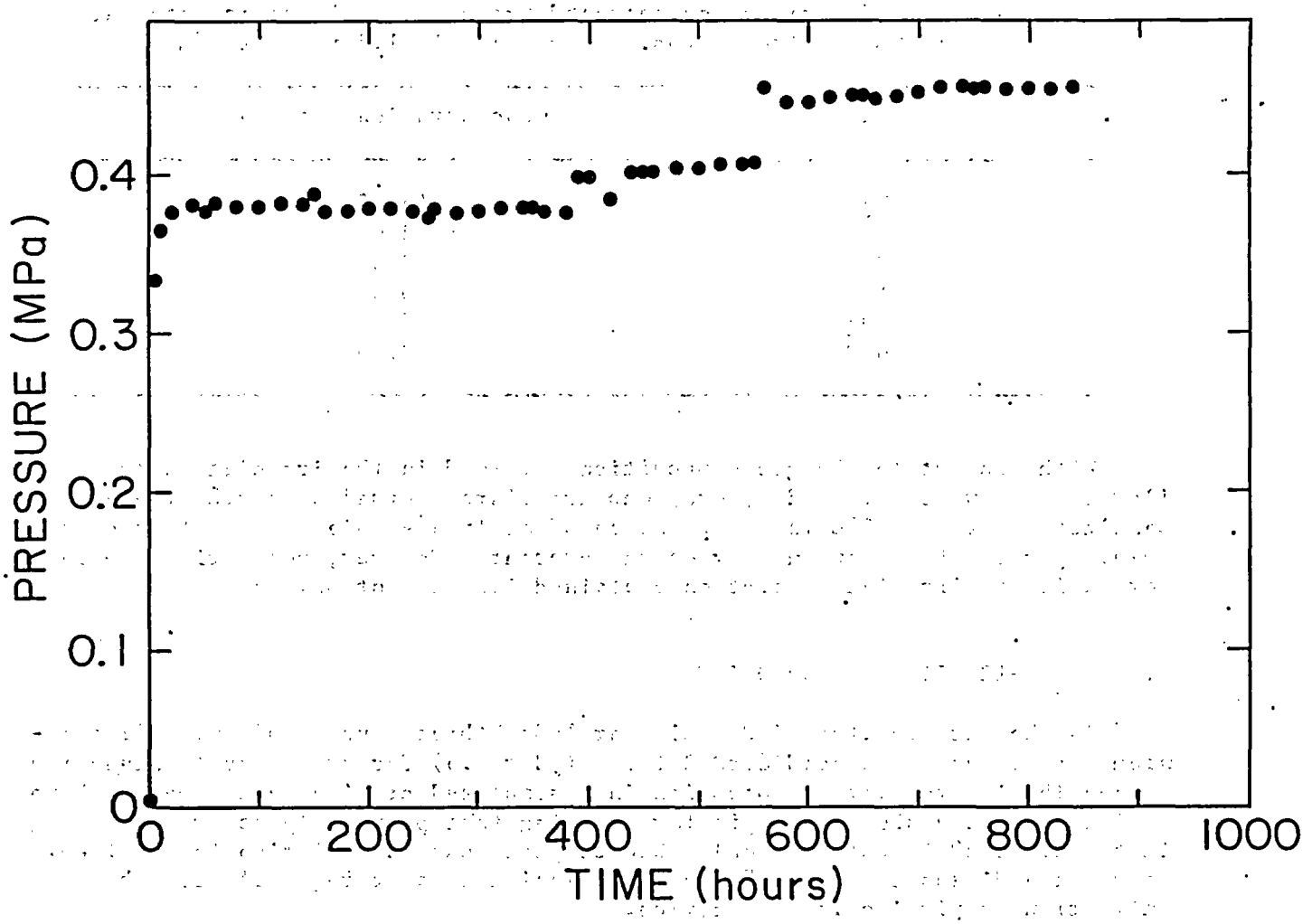

Figure 11. Gas pressure changes during gamma irradiation of concentrated Grande Ronde basaltic water/cast steel system at 150°C. The dose rate was 1.36×10^6 rad/h.

longer times, the rates for irradiation and non-irradiation conditions tend to converge. Additional work will be carried out at BNL to determine the reason for the low irradiation-corrosion rate.

Table 5. Chemical analysis of the gas sample collected after radiolysis of a 7.7 times concentrated Grande Ronde basaltic water at 150°C for two months. Gamma flux is 1.3×10^6 rad/h.

Gas	Concentration (mol %)
H_2	44.23
N_2	43.08
O_2	3.86
Ar	0.57
CO_2	7.50
H_2O	0.76

With respect to the gas composition obtained in the irradiation tests similar results were obtained by Gray who irradiated normal strength Grande Ronde basaltic water at 150°C in the presence of an iron sample.[9] He detected 22 volume percent hydrogen; no oxygen was present. However, polymeric material formed in the irradiated solution contained 1.2 percent oxygen.

4. GRADE-12 TITANIUM CORROSION

In the last quarter of Fiscal Year 1983, three coupons of Grade-12 titanium were immersed in acidified Brine A (pH = 1.6) for two weeks to study the susceptibility to pitting corrosion in a simulated crevice environment. None of the specimens showed any pitting implying that previously observed pitting in the crevice[6] is obtained only when complete oxygen depletion is obtained. As we have discussed before,[6] oxygen depletion is a prerequisite for the initiation of pitting in the crevice.

Studies were completed in the evaluation of oxide formation on Grade-12 titanium crevice samples exposed to caustic environments at 150°C. Caustic environments could be formed in a salt repository if gamma irradiated salt containing colloidal sodium interacts with brine inclusions. In this work 4 x 2 cm creviced specimens were immersed in WIPP Brine B, adjusted to pH 11.13, for a period of 21 days at 150°C. The black crevice scale normally observed for neutral brine was not observed. However, a blue-yellow film was present which indicates that crevice corrosion, if it is present, is at a very early stage because of the greater time it would take to reach the required low crevice solution pH for passivity breakdown. Using the SEM the main surface oxides in the crevice were observed to be blocky shaped crystals which we have previously identified as being of the anatase barrier type (Figure 12). A small amount of

rutile in the form of needle shape crystals was also detected (Figure 13). Under neutral brine conditions rutile is the dominant oxide for the immersion time studied here.[6] No evidence of pitting was found for the crevice corrosion tests in alkaline brine.

In prior work on crack propagation paths in hydrided Grade-12 titanium we have proposed that the crack follows a transgranular path through alpha grains, forming striations during each incremental jump.[6] The crack growth rate through the alpha phase is relatively slow compared to the rate when the crack reaches a beta grain when the crack propagates very quickly along the hydrogen-rich alpha-beta interphase region. Crack propagation measurements carried out on the surfaces of fracture mechanics specimens show a large step in the growth rate at this time. Between the two crack propagation regions is a transient with an intermediate crack growth rate. To compare surface crack growth rates with bulk (internal) growth rates, an experiment was carried out in which the potential across the plane of the crack was measured during the crack growth process for an input current of 10 A. Figures 14 and 15 show crack growth data obtained by the potential change method for a single specimen tested at room temperature and stress intensity level of 15-20 $MPa\sqrt{m}$. In the early stage of crack growth a "parabolic" rate is observed with small superimposed incremental steps. Apparently, these are caused by the advance of small segments of the crack front. As the crack accelerates (Figure 15) these incremental crack propagation segments are not resolvable and a smooth curve is obtained. Nevertheless, the potential change technique confirms that crack propagation indeed occurs as incremental crack jumps along the crack front as predicted in the BNL surface analysis work.

In order to validate the tensile mechanical property data obtained from the literature,[10] which were used in our earlier crack propagation analysis,[6] a series of tensile tests was carried out on Grade-12 titanium over a range of temperature and dissolved hydrogen levels. Table 6 shows that for as-received material the yield and tensile strength at room temperature are about 70 percent of the values from the literture.[10] The discrepancy may be attributable to differences in strain rate or grain size. In general, the data in Table 6 show that at 21 and 70°C the yield and tensile strengths are little affected by hydrogen up to the concentrations studied. However, there is a marked loss in elongation with increasing hydrogen content, as expected. At 120°C vacuum-annealed and as-received material have similar tensile properties but the yield strength for the 90 ppm hydrogen sample was greatly reduced. The reason for this is not apparent at this time.

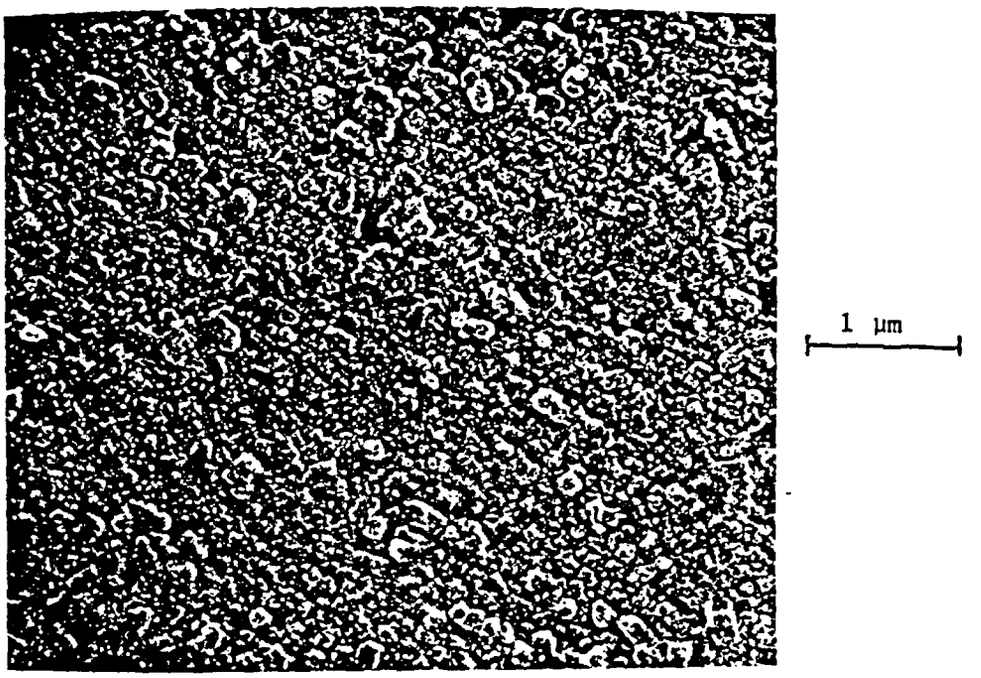

Figure 12. Blocky shape anatase barrier oxide formed in a Grade-12 titanium crevice sample exposed to caustic brine for two weeks at 150°C.

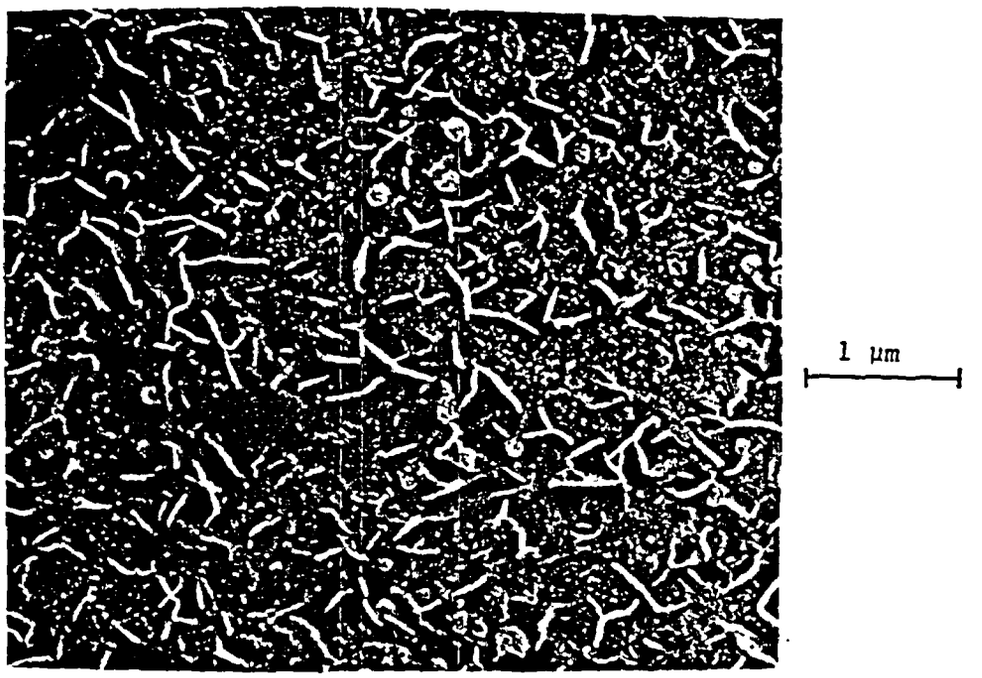

Figure 13. Needle shape rutile non-barrier oxide forming in a Grade-12 titanium crevice sample exposed to caustic brine for two weeks at 150°C.

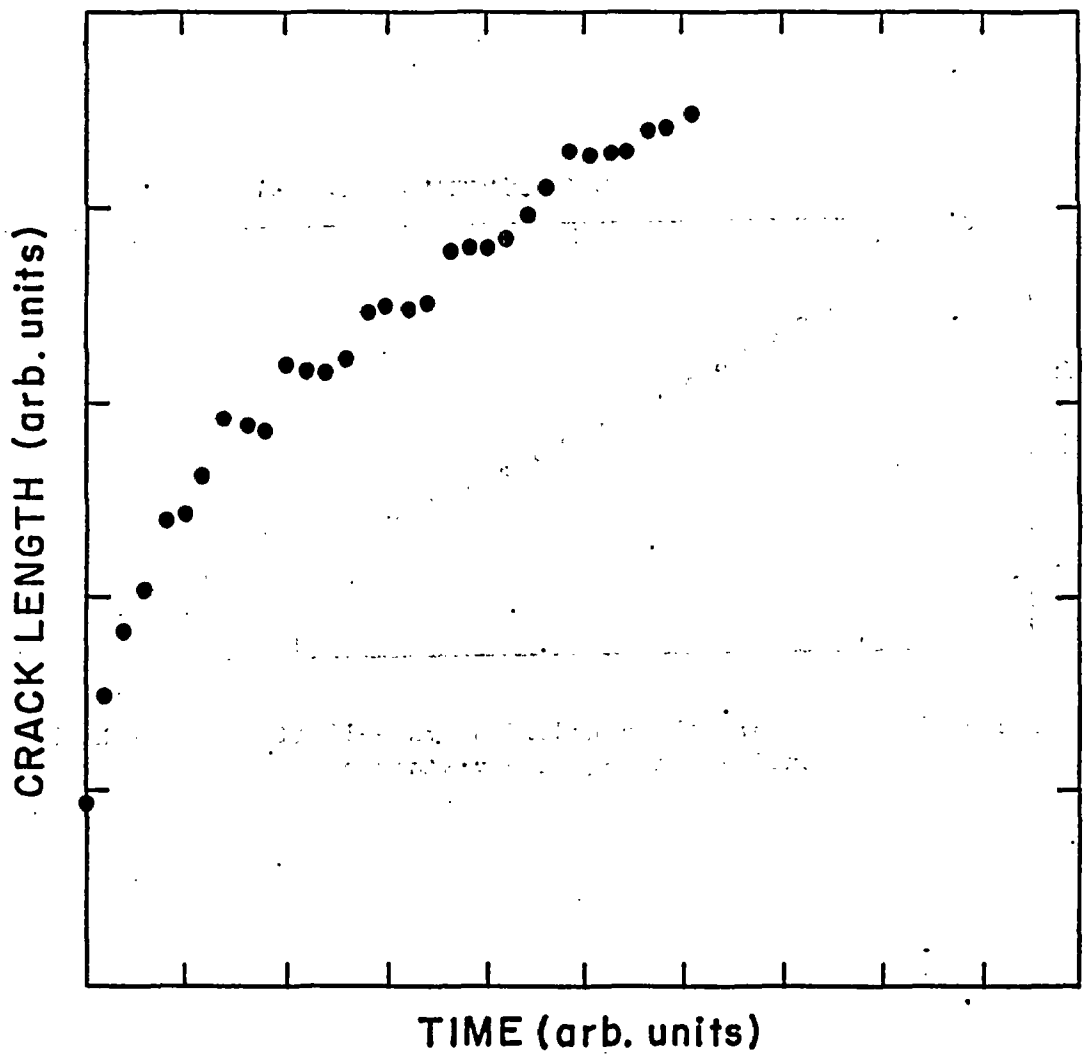

Figure 14. Early stage of crack growth in hydrided Grade-12 titanium showing transient growth (parabolic) behavior and some superimposed incremental crack jumps.

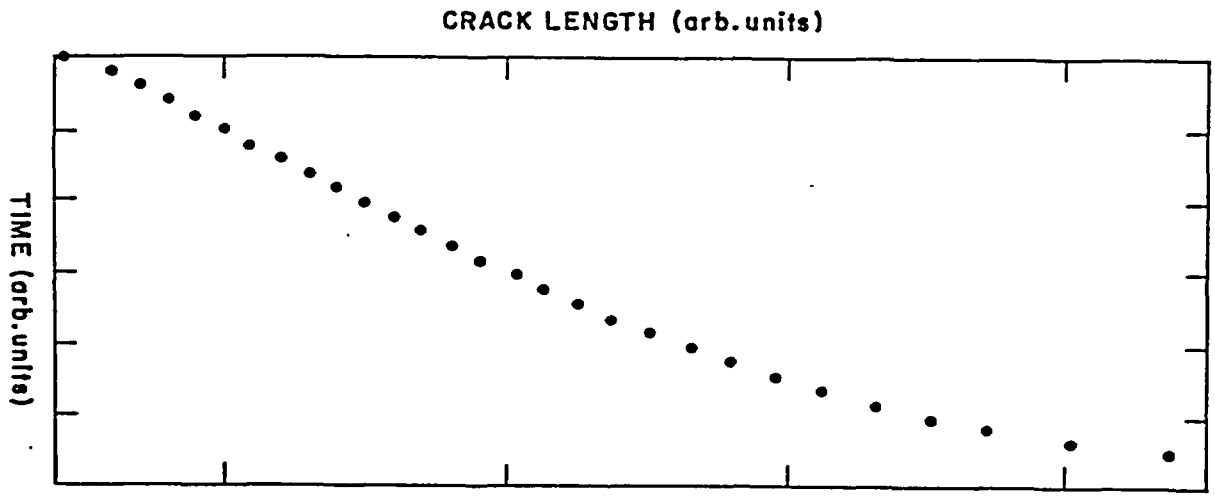

Figure 15. Crack growth in hydrided Grade-12 titanium at high stress intensity showing steady state growth.

Table 6. Tension testing results for Grade-12 titanium (strain rate ~3.3 x 10^{-5}/sec).

Test Temperature (°C)	Yield Strength* (MPa)	Tensile Strength (MPa)	Fracture Strength (MPa)	Elongation (%)	Specimen Condition
21	600	700	550	25	Vacuum Annealed**
21	610	710	560	16	As-received**
21	570	700	560	14	130 ppm
70	465	545	410	25	Vacuum Annealed
70	490	580	445	22	As-received
70	470	590	450	14	540 ppm
120	420	460	330	22	Vacuum Annealed
120	430	500	380	25	As-received
120	220	420	360	30	90 ppm

* Yield strength was obtained from upper yield point.
**As-received sample has about 35 ppm hydrogen concentration and vacuum annealed sample has about 5 ppm hydrogen concentration.

5. REFERENCES

1. AESD-TME-3142, "Waste Package Conceptual Designs for a Nuclear Repository in Basalt," Westinghouse Electric Corporation, 1982.

2. T. E. Jones, "Reference Material Chemistry - Synthetic Groundwater Formation," Rockwell Hanford Operations, RHO-RE-SR-5, 1982.

3. G. P. Cherepanov and others, Mechanics of Brittle Fracture, McGraw Hill International, 1974, p. 400.

4. J. A. Kargol, N. F. Fiore and R. J. Coyle, Jr., "A Model for H-absorption by Metals," Met. Trans. Vol. 12A, 183, 1981.

5. F. P. Ford, "Stress Corrosion Cracking" in Corrosion Processes, edited by R. N. Paskins, Applied Science Publishers, 1982.

6. R. Dayal and others, "Nuclear Waste Management Technical Support in the Development of Nuclear Waste Form Criteria for the NRC. Task 1: Waste Package Overview," NUREG/CR-2333, Vol. 1, BNL-NUREG-51458, 1982.

7. T. M. Ahn, H. Jain and P. Soo, "Container Assessment - Corrosion Study of HLW Container Materials," BNL-NUREG-33940, 1983.

8. J. P. Hirth, "Effects of Hydrogen on the Properties of Iron and Steel," Met. Trans. 11A, 861, 1980.

9. R. E. Westerman and others, "General Corrosion, Irradiation-Corrosion, and Environmental-Mechanical Evaluation of Nuclear Waste Package Structural Barrier Materials," PNL-4364, 1982.

10. W. J. Gray, "Gamma Radiolysis Effects on Grande Ronde Basalt Groundwater," Rockwell Hanford Operations, RHO-BW-SA-315P, 1983.

11. Metals Handbook, Ninth Edition, Vol. 3, Properties and Selection: Stainless Steels, Tool Materials and Special-Purpose Metals, ASM, 1980.

INFORMAL REPORT

CONTAINER ASSESSMENT--CORROSION STUDY OF HLW CONTAINERS MATERIALS

QUARTERLY PROGRESS REPORT APRIL--JUNE 1984

T. M. AHN AND P. SOO

NUCLEAR WASTE MANAGEMENT DIVISION

DEPARTMENT OF NUCLEAR ENERGY BROOKHAVEN NATIONAL LABORATORY
UPTON, NEW YORK 11973

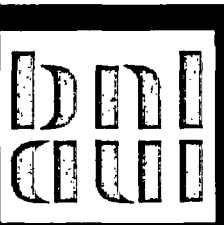

Prepared for the U.S. Nuclear Regulatory Commission
Office of Nuclear Regulatory Research
Contract No. DE-AC02-76CH00016

NOTICE

INFORMAL REPORT

CONTAINER ASSESSMENT--CORROSION STUDY OF HLW CONTAINER MATERIALS

QUARTERLY PROGRESS REPORT APRIL--JUNE 1984

T. M. Ahn and P. Soo

Manuscript Completed--August 1984
Date Published--August 1984

Donald G. Schweitzer, Head
Nuclear Waste Management Division
Department of Nuclear Energy
Brookhaven National Laboratory
Upton, New York 11973

Prepared for the U. S. Nuclear Regulatory Commission
Office of Nuclear Regulatory Research
Contract No. DE-AC02-76CH00016
FIN A-3237

ABSTRACT

Low carbon cast steel is a candidate container material for high level waste to be emplaced in a basalt repository. The current study is an evaluation of potential hydrogen embrittlement and radiation corrosion effects in this steel which could be present in basaltic groundwater.

Slow strain rates testing of Type ASTM A216-Grade WCA cast steel was performed for hydrogen embrittlement evaluation under cathodic charging conditions in a concentrated (x 7.7) basaltic groundwater at 80°C. As the strain rate is decreased, the ductility loss becomes more pronounced as the cathodic potential is increased. To interpret the cathodic potential in terms of expected repository conditions, a thermodynamic calculation was performed and the calculated hydrogen overpressure was found to be realistic.

Hydrogen uptake by the cast steel was studied by immersion testing for one week to obtain absorption kinetics. By incorporating previous two-month test results into the analysis, it is found that hydrogen is continuously absorbed during the two-month period without saturation occurring. The reason for the observed large hydrogen uptake was analyzed and we conclude that the hydrogen is trapped internally.

Kinetics of uniform corrosion and pitting corrosion were obtained under irradiation and nonirradiation conditions. Generally, the corrosion rates are higher than those obtained elsewhere for less concentrated solutions and deaerated solutions. The increased corrosion rates are attributed to the high solution concentration (x 7.7) and air-saturated oxygen levels. The corrosion products were amorphous under irradiation testing and crystalline under nonirradiation conditions. To understand these results, D.C. polarization tests were conducted. When a simulated radiolytic product (H_2O_2) was added to the solution, it was found that, (1) the corrosion potential is increased, (2) the corrosion current is decreased, and (3) new cathodic reactions are operative.

Studies on hydrogen permeation, corrosion fatigue and uncertainty analysis are also under way. A paper submitted during this quarter for publication is included as an appendix.

PREVIOUS REPORTS IN SERIES

Container Assessment--Corrosion Study of HLW Container Materials, Quarterly Progress Reports, T. M. Ahn and P. Soo.

January-March, 1984, Informal Report.
October-December, 1983, BNL-NUREG-34220
July-September, 1983, BNL-NUREG-33940

CONTENTS

FIGURES

TABLES

ACKNOWLEDGMENTS

The authors are grateful to C. I. Anderson for general technical assistance, R. Sabatini carried out the scanning electron microscopy, G. A. Foelsche performed the D. C. polarizations tests, and Ms. S. Bennett prepared the manuscript.

1. INTRODUCTION

The objective of this program is to identify and evaluate some of the potential corrosion failure modes in low carbon steel, which is the reference container material for high level waste packages to be emplaced in basalt repositories. The two main concerns of this study are: (1) to evaluate hydrogen assisted embrittlement effects and (2) to measure hydrogen uptake in the presence of basaltic waters and a gamma irradiation field. This study also addresses the problems of radiation corrosion and stress corrosion cracking. The present report describes the results obtained in the third quarter of fiscal year 1984.

2. MICROSTRUCTURAL CHARACTERIZATION OF CAST LOW CARBON STEEL

In this quarter, a second heat of cast low carbon steel rod was used for slow strain rate testing. The initial microstructure of the heat, shown in Figure 1, is very close to that of the first heat as described previously.[1,2] The chemical and mechanical characterization of the new material are under way.

3. CONSTANT EXTENSION RATE TESTING (CERT) OF LOW CARBON CAST STEEL

Until the last quarter, we concentrated on identifying the environmental conditions for which stress corrosion cracking and hydrogen embrittlement take place. In this quarter, we have concentrated on studying hydrogen embrittlement under applied cathodic potentials.

Table 1 shows the results of the constant extension rate tests (CERT) for ASTM A216-Grade WCA cast steel under applied cathodic potentials in concentrated (x 7.7) basaltic groundwater at various strain rates. Three different potentials were applied for each strain rate, namely, -1.4 V SCE, -1.0 V SCE, and the open circuit potential for air-saturated solutions which is typically -0.57 to -0.58 V SCE. The majority of the tests were conducted at strain rates of 3.0×10^{-7}/s, 6.0×10^{-6}/s and 1.5×10^{-4}/s for each potential. Test results in an air environment are also included for the purpose of comparison.

The first group of tests in Table 1 (SS1, SS6, SS2, SS16, SS19, SS3) shows that the ductility is significantly reduced for the -1.0 V SCE and -1.4 V SCE potential. On the other hand, at the higher strain rate of 6.0×10^{-6}/s (SS22, SS21, SS20, SS18), the reduction rates of the ductility are more gradual for the potential changes applied. At the fastest strain rate of 1.5×10^{-4}/s (SS26, SS25, SS24, SS23), hydrogen effects are much less pronounced. Figure 2 shows this behavior quite well from the plot of the reduction in area versus the applied potential. Compared to the reduction in ductility, there was no systematic trend for other parameters such as strength and solution pH versus the applied potential. The last group of specimens in Table 1 (SS11, SS12, SS17) shows the ductility loss for the weld samples. In this group, the weld effects are shown to be insignificant for both open-circuit potential and for -1.4 V SCE compared to results obtained on non-welded samples. As was done previously,[1] the fractographs are being analyzed. At the present time, we have not found any new fractographic features.

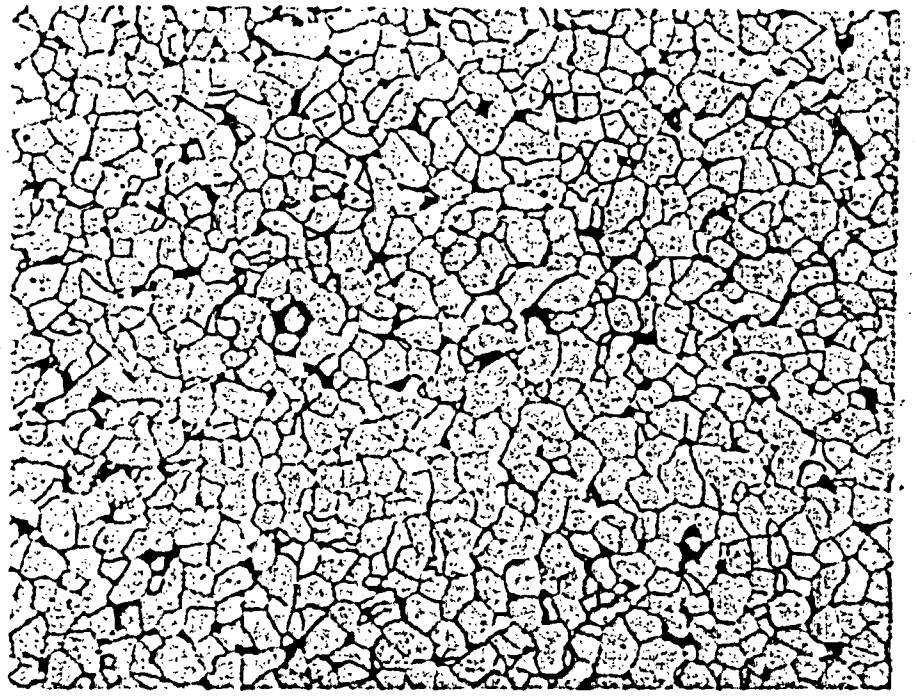

cross section x250

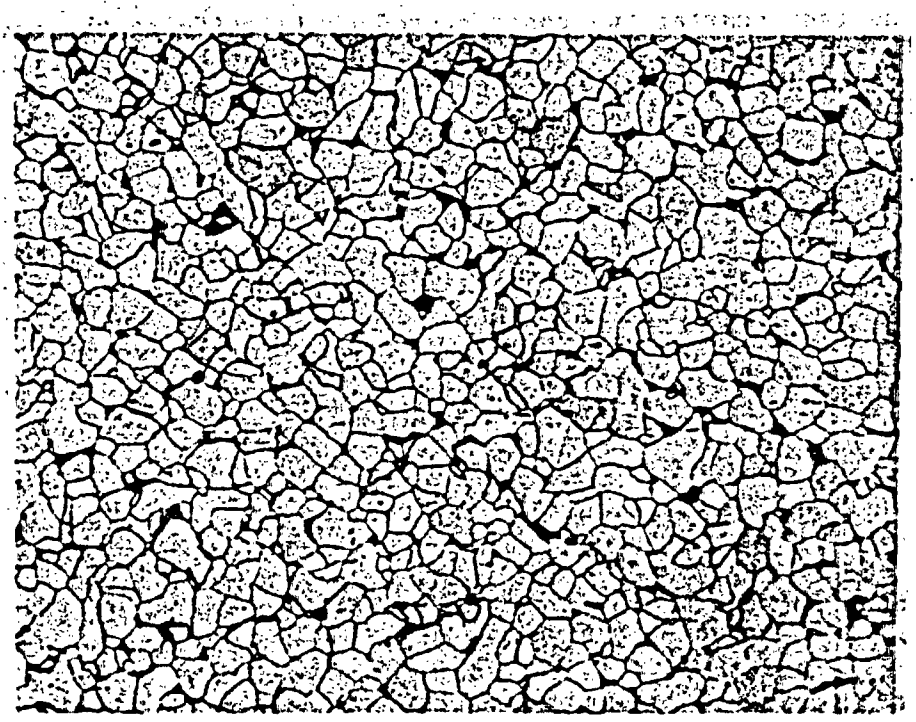

longitudinal section x250

Figure 1. Initial microstructure of a second heat, of ASTM A216-Grade WCA cast steel rod.

Table 1. Results of ASTM A216-Grade WCA cast steel CERT tests under cathodic conditions at various strain rates.

Sample No.	Test Environment	Temp. (°C)	Average Strain Rate[c] (sec^{-1})	Total Elongation (%)	Reduction in Area (%)	0.2% Offset Yield Strength (MPa)	Tensile Strength (MPa)	Fracture Strength (MPa)	Final Solution (pH)
SS1	Air	85	3.1×10^{-7}	19.0	58.0	330	561	439	--
SS6	Air	80	3.0×10^{-7}	21.0	53.8	324	537	413	--
SS2	Solution (o/c)[a]	85	3.1×10^{-7}	21.7	48.2-50.4	383	578	467	10.0
SS16	Solution (o/c)	80	3.1×10^{-7}	17.6	41.3	346	504	397	4.6
SS19	Solution (-1.0V)[b]	80	3.1×10^{-7}	15.9	26.6	348	519	472	5.0
SS3	Solution (-1.4V)	85	3.1×10^{-7}	15.0-15.9	24.6	272	443	325	10.5
SS22	Air	80	6.0×10^{-6}	21.4	68.0	333	444	286	
SS21[d]	Solution (o/c)	80	5.9×10^{-6}	20.8	55.2	310	508	388	9.1
SS20	Solution (-1.0V)	80	6.1×10^{-6}	18.4	36.9	299	471	423	4.6
SS18	Solution (-1.4V)	80	6.0×10^{-6}	14.6	22.7	331	537	495	9.6
SS26	Air	80	3.3×10^{-4}	28.2	77.9	385	466	263	--
SS25	Solution (o/c)	80	1.5×10^{-4}	21.4	67.9	346	442	286	8.1
SS24	Solution (-1.0V)	80	1.5×10^{-4}	19.6	58.5	311	421	297	9.2
SS23	Solution (-1.4V)	80	1.5×10^{-4}	20.1	55.7	352	443	313	4.1
SS11 (Weld)	Air	80	2.7×10^{-7}	21.1	52.9	373	580	457	--
SS12 (Weld)	Solution (o/c)	80	3.2×10^{-7}	22.9	47.2	327	553	430	not measured
SS17 (Weld)	Solution (-1.4V)	80	3.0×10^{-7}	15.6	20.1	307	524	500	9.7

[a] o/c (open circuit potential) in air saturated solution at testing temperatures (typically -0.57 to -0.58 volt SCE).
[b] Potential with respect to SCE.
[c] Gauge length of 1.27 cm.
[d] From specimen SS21 onward, the second heat of materials was used.

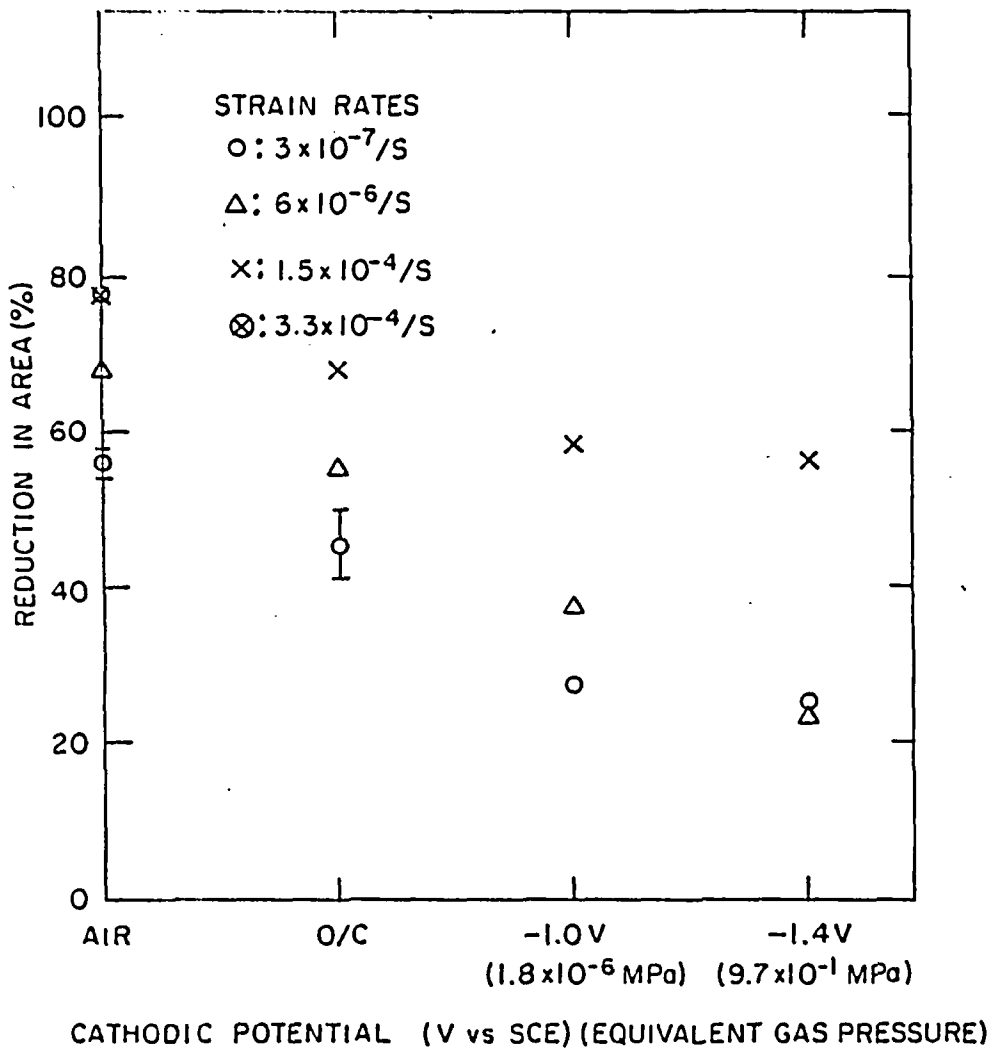

Figure 2. Reduction in area versus applied potential in CERT tests for hydrogen embrittlement of ASTM A216-Grade WCA steel in concentrated (x7.7) basaltic groundwater at 80-85°C.

The cathodic potential has little useful application with respect to defining repository conditions. Therefore, it is necessary to correlate the hydrogen overpotential to the effective hydrogen gas pressure present near a container. Based on a previous literature search,[2] we have drawn the following conclusions in the correlation.

The effective hydrogen fugacity, f_H, is the activity of hydrogen atoms adsorbed on the metal surface and may be expressed in terms of hydrogen overpotential, η, by[3]:

$$f_H = \exp(\eta F/ZRT) \qquad (1)$$

where F is Faraday's constant, Z is a constant equal to 2 and η is the hydrogen overpotential. Hydrogen atoms are in equilibrium with hydrogen gas molecules according to the reaction

$$H_2(gas) \underset{k_d}{\overset{k_a}{\rightleftharpoons}} H_2(ad) \underset{k_2}{\overset{k_1}{\rightleftharpoons}} 2(H\text{-}Fe) \qquad (2)$$

where H_2(gas) is a hydrogen molecule in the gas, H_2(ad) is a hydrogen molecule adsorbed on the metal surface; H-Fe is a hydrogen atom on the sample surface, and k_a, k_d, k_1, and k_2 are rare constants for each reaction in equation (2). Therefore, the overall equilibrium constant K for the reaction (2) is:

$$K = \left(\frac{k_a}{k_d}\right)\left(\frac{k_1}{k_2}\right) = f_H^{\,2}/p_{H_2} \qquad (3)$$

where p_{H_2} is the partial pressure of hydrogen gas. By substituting equation (1) into equation (3), we obtain:

$$p_{H_2} = \frac{1}{K} \cdot \exp(2\eta F/ZRT) \qquad (4)$$

There are data available[4] to evaluate K value for pure iron at various temperatures as shown in Table 2. The overpotential η is estimated by the applied potential minus the hydrogen evolution potential which is -0.96 V SCE for the solution of pH = 10.3 at 80°C. From this evaluation, we determined that potentials of -1.4 V SCE and -1.0 V SCE are equivalent to hydrogen partial pressures of 9.7×10^{-1} MPa (9.8 atm) and 1.8×10^{-6} MPa (1.8×10^{-5} atm), respectively, at 80°C. These values may be compared with hydrogen pressures developed under laboratory conditions. For instance, the hydrogen pressure build-up by gamma radiolysis in this program was as high as 0.65 MPa after two months' exposure of the groundwater to a gamma flux of 1.2×10^{-6} rad/h. This value is comparable to those calculated above. However, since the estimation is based on data for pure iron, there may be a difference in the calculated values for the present steel. Unfortunately, the K value for the present steel is not available. Also, we have not considered the solution chemistry in the calculation of the equivalent pressure. Since it is possible that the solution chemistry only affects the metal surface condition, which determines the hydrogen uptake efficiency, the correlation of η and p_{H_2} could be independent of solution chemistry itself.

Table 2. Rate constants for H_2 adsorption on iron for reaction[4]

$$H_2(gas) \underset{k_d}{\overset{k_a}{\rightleftharpoons}} H_2(ad) \underset{k_2}{\overset{k_1}{\rightleftharpoons}} 2(H\text{-}Fe)$$

k_a ($Nm^2\ sec^{-1}$)	k_d (sec^{-1})	k_1(sec^{-1})	k_2(sec^{-1})
3×10^2	$11 \cdot T \cdot \exp(-28.9/RT)$	$604 \cdot T \cdot \exp(34.7/RT)$	$3.45 \times 10^{13} \cdot T \cdot \exp(-87.9/RT)$

R is in units of kJ/mole, and T is the absolute temperature.

4. HYDROGEN UPTAKE IN CAST LOW CARBON STEEL

In order to determine the rate of hydrogen uptake, specimens of the cast steel and Ferrovac-E were previously immersed in the concentrated basaltic water at 150°C for two months under a gamma dose rate 1.3×10^6 rad/h. Control tests without irradiation were also performed. Previous quarterly progress reports show the details of the two tests.[1,2] In this quarter, more test results were obtained for immersion test lasting for one week. Tests for extended periods, such as six months', are also under way at the present time. Tables 3 and 4 are a summary of the hydrogen uptake data under irradiation and non-irradiation conditions. Generally, the hydrogen uptake under irradiation is higher. Also, cast steel absorbs more hydrogen than Ferrovac-E. However, there was no systematic variation for weld structures and U-bend samples. From the results obtained for different test times, given in Tables 3 and 4, it is seen that the hydrogen concentration does not reach a steady state (saturation) value.

There is a question whether the cast steel can absorb such a high level of hydrogen. We have, therefore, attempted to determine the reason for such high hydrogen concentrations. In order to check the variation of as-received hydrogen concentration in different samples, two more samples of as-received cast steel were analyzed and the results show hydrogen concentrations of 7, 2 and 22 ppm as shown in Table 5. The large scatter is attributed to the nonuniform distribution of the pearlite structure, which is known to provide trap sites for hydrogen.[5] Therefore, the significant variation in the original hydrogen concentration for as-received samples will depend on microstrucural variations.

A possible reason for the high hydrogen levels centers on hydrogen trapping in the oxide scale or in the silica which was found to deposit on immersed samples. Using data obtained by Shelby[6] and Lee,[7] it was calculated that hydrogen solubilities in these two phases was less than 1 ppm at 150°C and 1 atm of hydrogen pressure. Therefore, such a trapping mechanism is not feasible.

Table 3. Hydrogen concentration of ASTM A216-Grade WCA steel and Ferrovac-E specimens exposed to concentrated basaltic groundwater at 150°C under a gamma dose rate of 1.3×10^6 rad/h.

Material	Concentration (ppm)		
	One Week Tests	Two-Month Tests	
		Run 1[a]	Run 2
Ferrovac-E	5 (2-2-0)	not determined	20 (13-4-3)
As-Received Steel	7 (0-3-1-1-2-0-1-0)	19 (10-7-2)	549 (427-90-23-9)
Welded Steel	54 (17-4-3-5-6-3-2-3-1-1-3-2-1-1-1)	10 (4-1-3-1)	215 (156-51-8)
U-bend Steel (as-received)	16 (4-9-2-1-1)		
U-bend Steel (welded)	8 (5-2-1)		

[a]The specimens were exposed to air during analysis.
The values in parentheses indicate the increments of gas evolution during sequential heating periods at 950°C.

Other studies to determine the reasons for the high levels of dissolved hydrogen involved measurements of the hydrogen evolved during vacuum extraction tests. The data in parentheses in Tables 3 and 4, show the amounts of hydrogen evolved during sequential heating periods (one sample was heated several times until complete removal of hydrogen was achieved). It was found that hydrogen evolution is quite gradual for high hydrogen concentrations (549 ppm, 215 ppm). If the majority of the hydrogen is in the oxide, or the silica deposits as gas molecules trapped in the pores, then the hydrogen evolution should have been complete in the first heating stage since the oxides and silica deposits are very porous. Therefore, from the hydrogen solubility calculation mentioned above and the slow release of hydrogen during heating, we conclude that hydrogen is trapped in the bulk metal.

To determine the mechanism by which hydrogen is trapped in the matrix, samples were mounted, polished, etched for metallographic examinations. Generally, Ferrovac-E and welded sample with martensitic (or bainitic) structures did not show microcracks. On the other hand, the steel specimens showed grain-boundary cracking (blistering or fissuring) or surface cracking under both irradiation and non-irradiation conditions. However, the cracking is more severe under an irradiation environment. Typical examples of grain-

boundary cracking and surface cracking are shown in Figure 3. Ferrovac-E is so ductile that we could not detect cracking since the mechanical polishing smears the metallographic surface as shown in Figure 4.

The results for welded samples may be understood in terms of hydrogen solubility limits. It is known that martensite (or bainite) in the weld can absorb several orders of magnitude more hydrogen than ferrite.[5] Therefore, cracking may not be observed in welded samples. Cracking probably occurs in the ferrite phase of non-welded samples, especially in surface areas where hydrogen is enriched. Also, we have found that the high hydrogen concentration does not seem to increase the density of cracking. For instance, above 200 ppm hydrogen, only a few cracks were observed. One probable reason for high hydrogen uptake without forming extensive cracking is hydrogen trapping in pearlite structures. In fact, for similar materials,[4] the effective increase in hydrogen concentrations can be several times the as-received concentration because of the presence of trap sites.

Finally, it may be mentioned that the majority of hydrogen solubility data in literature is from permeation test results. In such tests, only mobile hydrogen is measured. Since no trapped hydrogen can be detected, hydrogen levels are underestimated.

Table 4. Hydrogen concentration of ASTM A216-Grade WCA steel and Ferrovac-E specimens exposed to concentrated basaltic groundwater at 150°C.

Material	Concentration (ppm)		
	One Week Tests	Two-Month Tests	
		Run 1	Run 2[a]
Ferrovac-E	3 (3-1-0)	not determined	4 (4-0)
As-Received Steel	7 (7-1)	31 (26-5-1)	6 (6-1-0)
Welded Steel	2 (1-1-0)	23 (19-2-2-1)	17 (10-3-4-0)
U-bend Steel (As-Received)	3 (2-1-0)	53 (49-2-2-1)	5 (5-1-0)
U-bend Steel (Welded)	2 (2-0)	10 (8-2-1)	not determined

[a]The specimens were exposed to air during analysis.
The values in parentheses indicate the increments of gas evolution during sequential heating at 950°C.

At the request of the NRC prgoram manager, we have included, in Appendix A, details of our hydrogen analysis procedures.

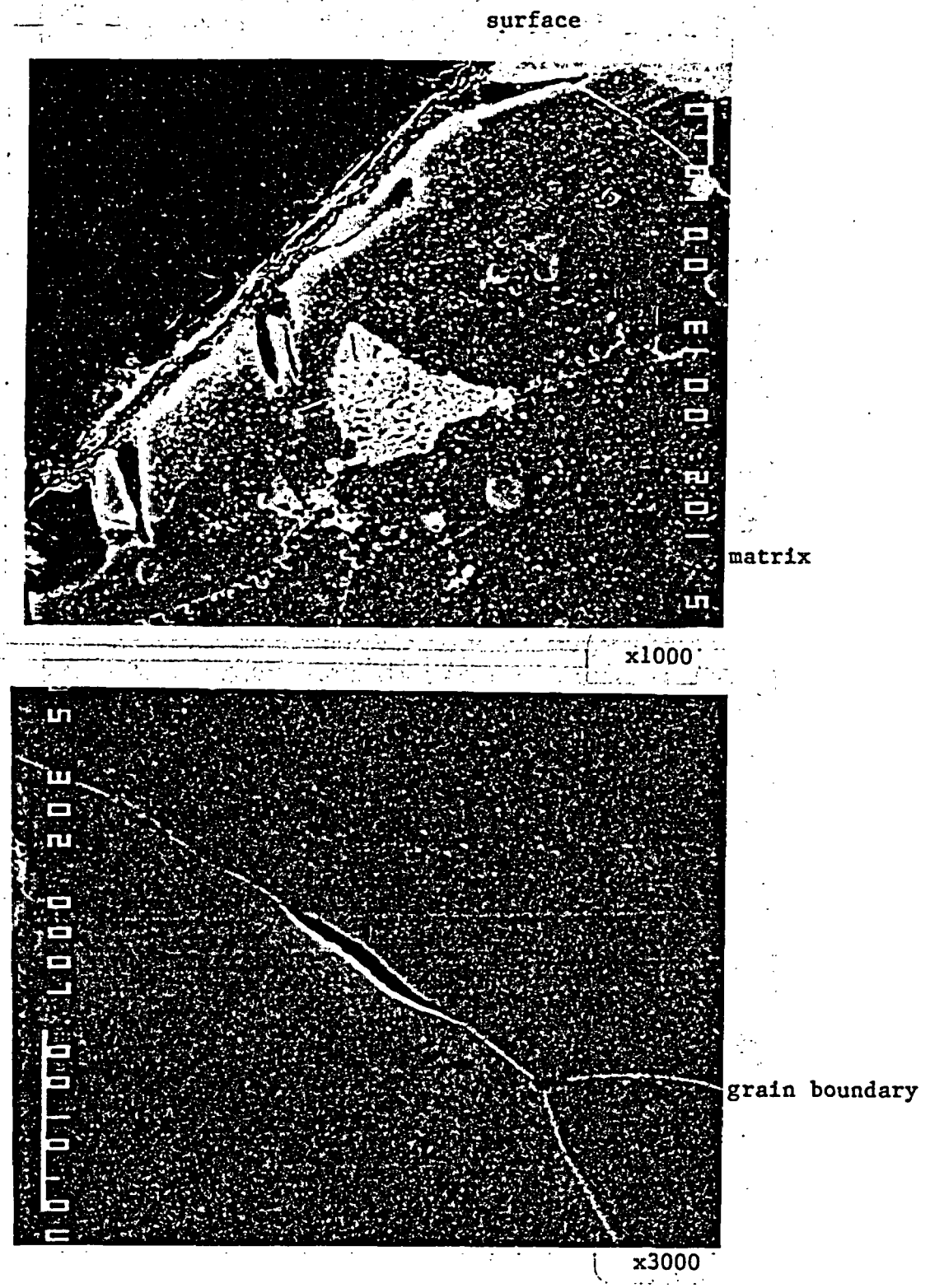

Figure 3. Surface cracking and internal cracking observed in ASTM A216-Grade WCA steel exposed to concentrated (x7.7) basaltic groundwater under a gamma dose rate of 1.3×10^6 rad/h at 150°C for two months.

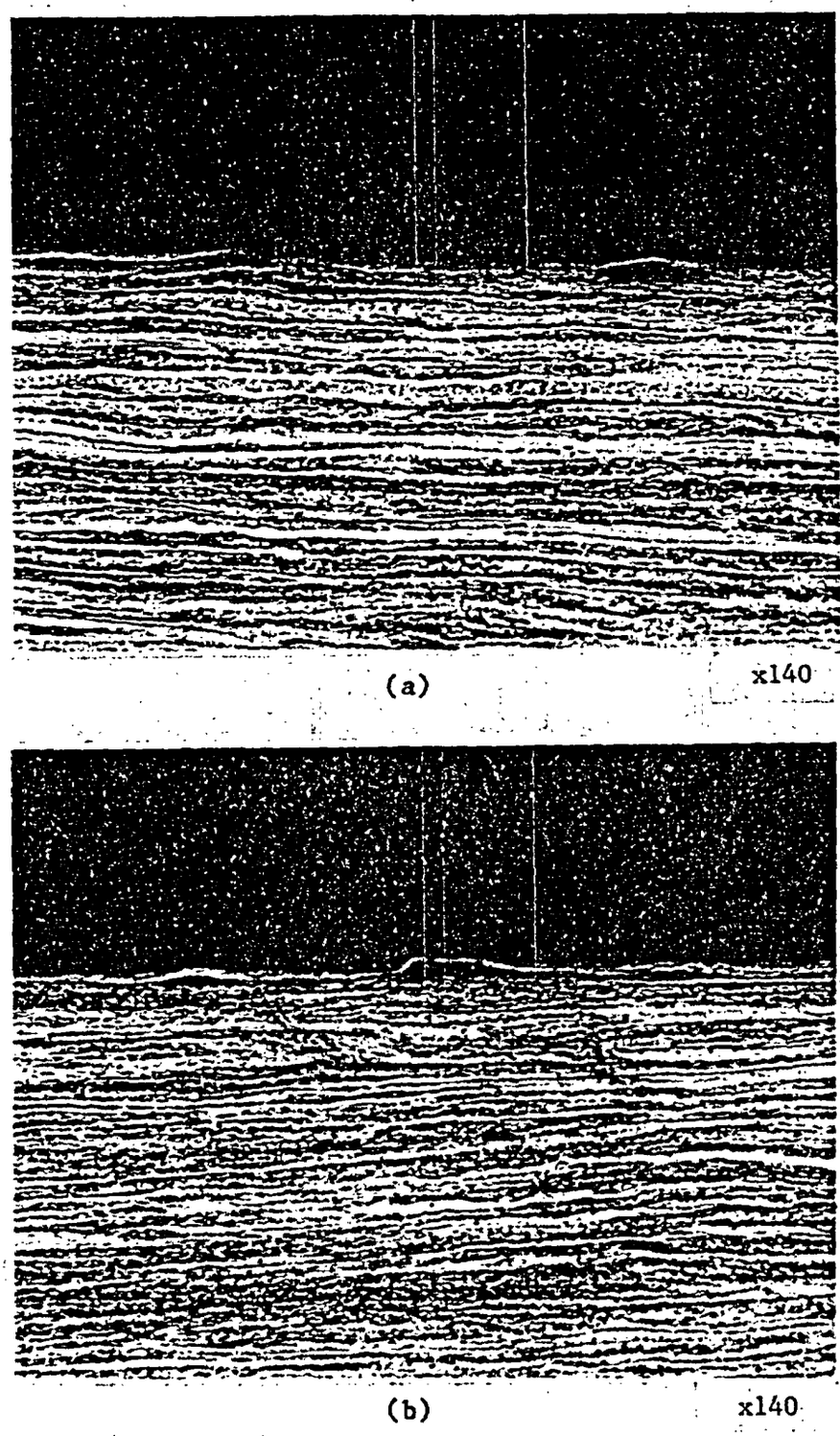

Figure 4. Cross section of Ferrovac-E showing that high ductility effects mask the subsurface structure. The sample was exposed to concentrated (x7.7) basaltic groundwater (a) under a gamma dose rate of 1.3×10^6 rad/h at 150°C for two months (b) at 150°C for two months.

Table 5. Hydrogen concentration of as-received ASTM A216-Grade WCA steel and Ferrovac-E

Material	Concentration (ppm)
Ferrovac-E	0.4
As-Received Steel	7, 2, 22
Welded Steel	<0.5

To quantify hydrogen uptake kinetics under irradiation conditions, a hydrogen permeation cell was constructed.[1] Currently, the pressure change caused by hydrogen permeation through steel sheet is being measured for extended periods in the BNL gamma pool.

5. RADIATION CORROSION OF CAST LOW CARBON STEEL

Preliminary corrosion results were reported in the previous quarterly progress report[1] for samples immersed in concentrated basaltic water for two months at 150°C. In this quarter, the oxides or the precipitates deposited on the sample surfaces were removed by cathodic charging in ENDOX solution and subsequent cleaning in an ultrasonic bath. Typical charging conditions in ENDOX solutions were 250 mA/cm^2 for 30 seconds and the sample was cleaned ultrasonically for over an hour. This procedure was repeated until complete oxide removal was achieved. After removal of the oxide, the samples were weighed and the weight loss was normalized to a standard surface area.

Table 6 shows the corrosion rates for irradiation and non-irradiation conditions. Generally, the irradiation corrosion rates are much lower than the non-irradiation corrosion. This is especially true for the Ferrovac-E which shows good corrosion resistance under gamma irradiation. This is consistent with the visual observation of the coupon after testing, which showed that the majority of Ferrovac-E surface was shiny except in a small area adjacent to the silica spacer. For non-irradiation conditions, the cast steel is more resistant to corrosion than Ferrovac-E. However, for welded or U-bend specimens, there were no systematic difference.

Pitting corrosion rates were also measured from the metallographic examinations. Each coupon was sectioned, mounted and polished for the measurement of pit density (number/cm, using two dimensional measurements), average pit depth and maximum pit depth. The results of the measurements are listed in Table 7 and the typical pit morphology is shown in Figure 5. For irradiation conditions, the pitting is less severe compared to non-irradiation conditions. For non-irradiation conditions, deeper pits and a higher pit density were observed for the cast steel compared to Ferrovac-E. Also, it was found that the effects of U-bend configurations and welding are not significant.

Table 6

Corrosion products for irradiation and non-irradiations were analyzed by x-ray diffractometer, and found to be amorphous for irradiation corrosion and crystalline for non-irradiation corrosion. Relevant data are shown in Figure 6. The crystal structure of the corrosion products for non-irradiation corrosion was not of any normal type of iron oxide. At this time it seems that the corrosion products may be a compound of iron and silicon. However, this has not been confirmed.

Table 6. Corrosion rates of ASTM A216-Grade WCA steel and Ferrovac-E in air saturated concentrated basaltic groundwater at 150°C (μm/yr) (parenthesis in g/cm^2)

Materials	Non-Irradiation		Irradiation
	One Week Test	Two-Month Test	Two-Month Test
Ferrovac-E	1813 (2.74×10^{-2})	333 (4.36×10^{-2})	64 (8.44×10^{-3})
As-Received Steel	1369 (2.07×10^{-2})	141 (1.85×10^{-2})	84 (1.10×10^{-2})
Welded Steel	1231 (1.89×10^{-2})	376 (4.93×10^{-2})	82 (1.08×10^{-2})
U-Bend Steel (As-Received)	1680 (2.54×10^{-2})	622 (8.15×10^{-2})	78 (1.02×10^{-2})
U-Bend Steel (Welded)	1647 (2.49×10^{-2})	not determined	46 (6.07×10^{-3})

Limited efforts were given to D.C. polarization tests for the characterization of the electrochemical behavior of the cast steel for irradiation and non-irradiation conditions. In the last quarterly progress report,[1] we presented the polarization curves in the anodic regime of cast steel at 80°C with and without hydrogen peroxide additions, and correlated them with observed immersion test results. In this quarter, we confirmed the previous results which showed an increased corrosion potential, and decreased corrosion current, with the addition of 36 cc H_2O_2 to 800 cc concentrated basaltic solution. Also, we obtained the cathodic curved for the two solutions as shown in Figures 7 and 8. Oxygen reduction and hydrogen evolution are clearly seen in the solution without hydrogen peroxide, while an entirely different cathodic curve is shown in the solutions with hydrogen peroxide.

Table 7. Pitting corrosion of ASTM A216-Grade WCA steel and Ferrovac-E in air saturated concentrated (x7.7) basaltic groundwater at 150°C.

Material	Non-Irradiation One Week Tests			Non-Irradiation Two-Month Tests			Irradiation Two-Month Tests		
	average pit depth (μm)	maximum pit depth (μm)	pit density (number/cm)	average pit depth (μm)	maximum pit depth (μm)	pit density (number/cm)	average pit depth (μm)	maximum pit depth (μm)	pit density (number/cm)
Ferrovac-E	7	7	4	9	11	3	11	18	6
As-Received Steel	5	14	13	17	32	20	11	21	10
Welded Steel	15	46	23	26	71	47	7	7	5
U-Bend Steel (As-Received)	16	50	23	40	129	66	10 8	11 14	15 21
U-Bend Steel (Welded)	40 25	43 83	11 54	a 40	a 186	a 44	a 11	a 34	a 11

[a]Not determined

x140

x140

Figure 5. Pit morphology of welded ASTM A216-Grade WCA steel exposed to concentrated (x7.7) basaltic groundwater at 150°C for two months.

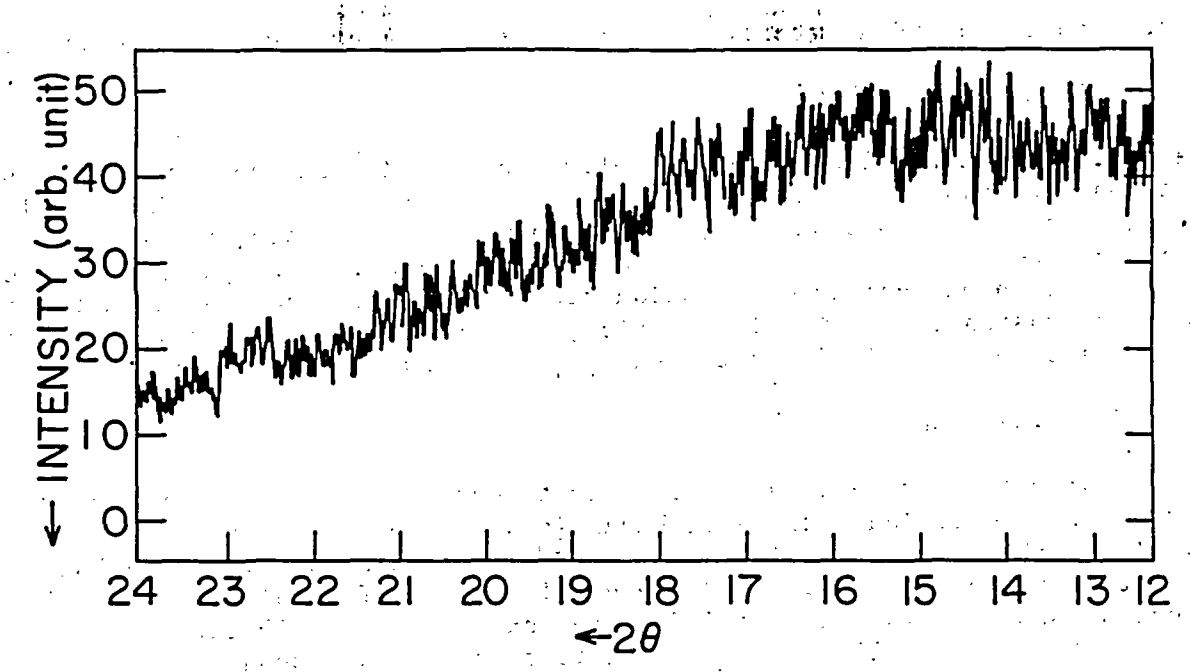

(a)

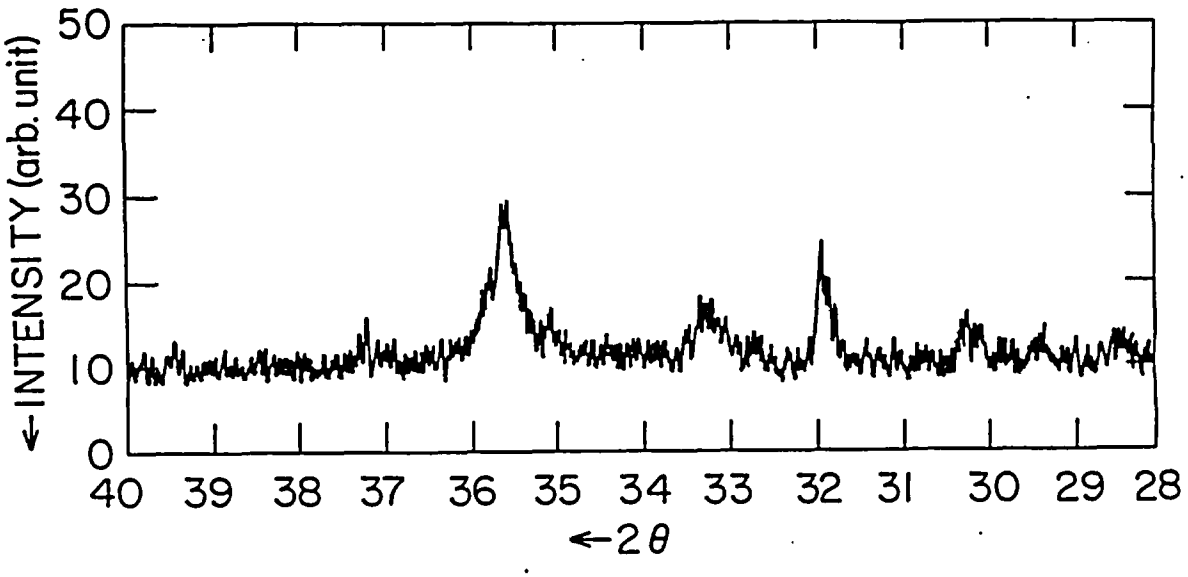

(b)

Figure 6. X-ray diffraction results for corrosion products of ASTM A216-Grade WCA steel exposed together with Ferrovac-E to concentrated (x7.7) basaltic groundwater at 150°C for two months, (a) under a gamma irradiation of dose rate 1.3 x 10^6 rad/hr; (b) without irradiation.

From potential-pH diagrams,[8] it appears that the cathodic reactions are

$$H_2O_2 + 2H^+ + 2e \rightarrow 2H_2O$$

Since most steel corrosion is cathodically controlled,[9] the corrosion rates seem to be determined by this reaction. Also, Figure 8 does not show any indication of oxygen reduction or hydrogen evolution; therefore, the above reaction might be faster than the rates of oxygen reduction or hydrogen production, leading to an increased corrosion rate. However, since we did not see enhanced corrosion rates with irradiation, it appears that anodic inhibition effects might be more significant when H_2O_2 is added to the solution.

6. OTHER ACTIVITIES

Corrosion fatigue tests are under way to obtain the cyclic stress-strain conditions for corrosion fatigue in basaltic water environments at 80°C. A Bayesian method for uncertainty analysis[10] was initiated using a Weibull distribution to obtain the 5 and 95 percentile values for failure. In this quarter, an abstract was submitted for presentation in the Electrochemical Society meeting this fall. The abstract is attached as Appendix B.

figure 7

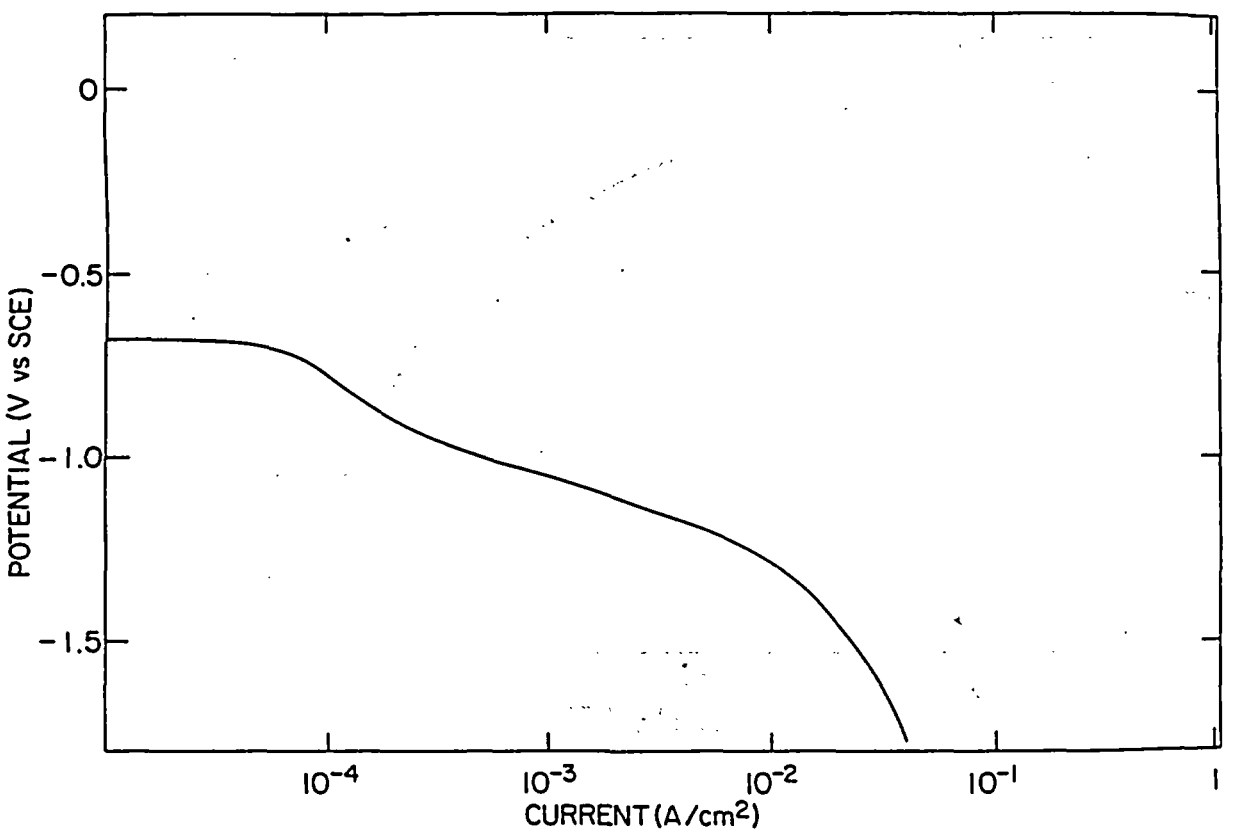

Figure 7. Cathodic polarization curve of ASTM A216-Grade WCA steel in concentrated (x7.7) basaltic water at 80°C. The scan rate was 0.2 mV/sec.

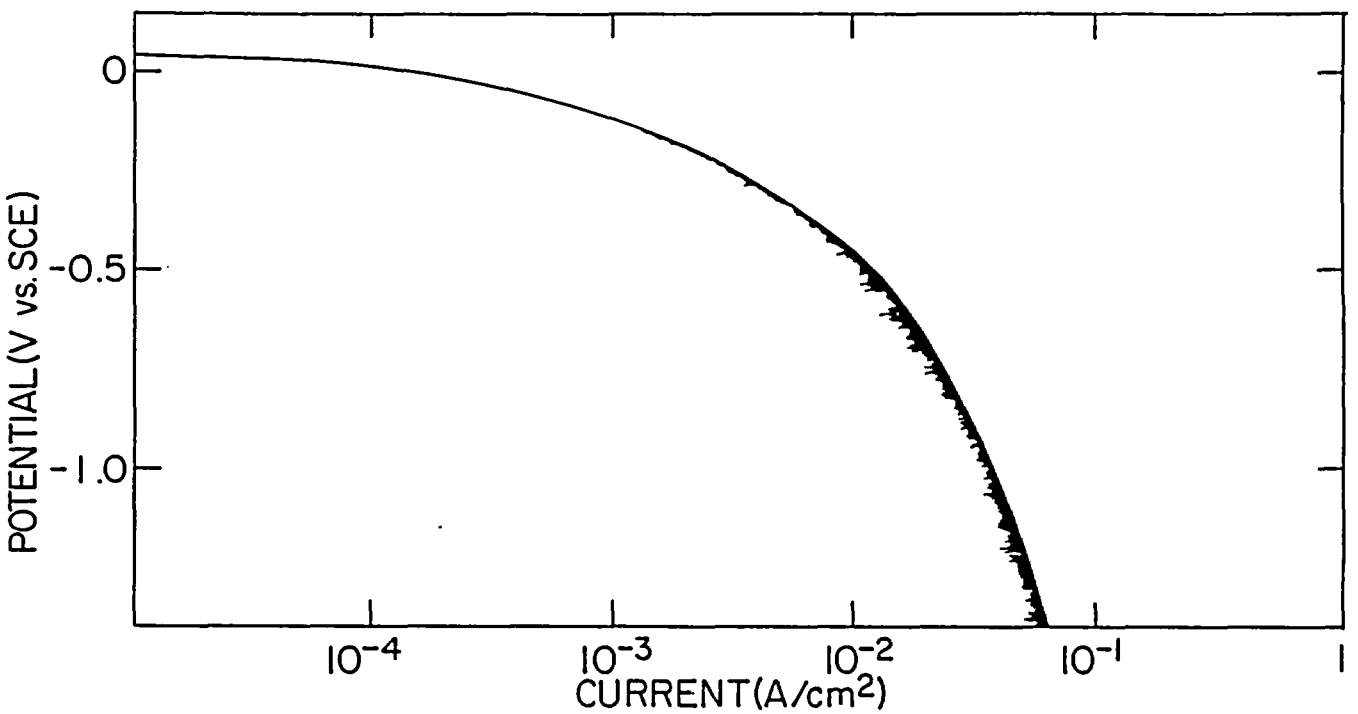

Figure 8. Cathodic polarization curve of ASTM A216-Grade WCA steel in 800 cc of concentrated (x7.7) basaltic water and 36 cc H_2O_2 at 80°C. The scan rate was 0.2 mV/sec.

7. REFERENCES

(1) T. M. Ahn and P. Soo, "Container Assessment--Corrosion Study of HLW Container Materials, Quarterly Progress Report, January-March 1984," Brookhaven National Laboratory, 1984.

(2) T. M. Ahn and P. Soo, "Container Assessment--Corrosion Study of HLW Container Materials, Quarterly Progress Report, October-December 1983," Brookhaven National Laboratory, 1984.

(3) J. A. Kargol, N. F. Fiore, and R. J. Coyle, Jr., " A Model for H-absorption by Metals," Met. Trans, 12A, 183 (1981).

(4) M. R. Shanabarger, "A Comparison of Adsorption Kinetics on Iron of H_2 and H_2S," in Hydrogen Effects in Metals, edited by I. M. Bernstein and A. W. Thompson, AIME (1981).

(5) G. W. Hong and J. Y. Lee, "The Interaction of Hydrogen and the Cementite-Ferrite Interface in Carbon Steel," J. of Materials Science, 18, 271 (1983).

(6) J. E. Shelby, "Helium, Deuterium and Neon Migration in a Common Borosilicate Glass," J. Appl. Phys. 45, 2146 (1974).

(7) R. W. Lee, "Diffusion and Hydrogen in Natural and Synthetic Fused Quartz," J. Chem. Phys. 38, 448 (1963).

(8) M. Pourbaix, Atlas of Electrochemical Equilibria in Aqueous Solutions, p. 106, NACE 1974.

(9) H. H. Uhlig, Corrosion and Corrosion Control, p. 92, John Wiley & Sons, Inc. (1971).

Appendix A

EXPERIMENTAL PROCEDURES FOR THE HYDROGEN ANALYSIS OF CARBON STEEL

1. Coupon Preparation

(0.7-1.0) x (2.0-3.0) x (0.05-1.0) cm coupons were mechanically polished up to 600 SiC and immersed in 25 mL of basaltic water (for irradiation tests) and 200 mL of basaltic water (for nonirradiation tests). The water is contained in a silica lined autoclave. After immersion tests for one week, one month, two months and six months, with and without radiation (1.3×10^6 rad/h), the coupons were quenched in liquid nitrogen immediately after the autoclave is opened. In later experiments, the coupons were mechanically polished up to 600 SiC to remove oxide formed. Typically it took 5 minutes to remove the oxide before quenching the coupons in liquid nitrogen.

2. Vacuum Extraction Method.

2.1 The samples submitted for H_2 analysis arrived frozen in liquid nitrogen. They are kept that way until ready for analysis. However, if this is not possible, they are packed in dry ice and stored in a dry ice chest.

2.2 A schematic of the vacuum extraction facilities is given in the figure.

2.3 A sample to be analyzed is placed in the combustion tube on the vacuum rack. Excess air is immediately pumped off; then a dewar containing liquid nitrogen is placed around the tube to keep the sample cold.

2.4 After the system has been evacuated to $\approx 5 \times 10^{-5}$ torr, the stopcocks to the vacuum pumps are closed to isolate that portion of the system used to collect the H_2. A liquid nitrogen dewar is placed over the trap to freeze out H_2O and other contaminants that may be released.

2.5 The sample in the combustion tube is then heated to 950°C by a furnace that is controlled by a Honeywell temperature controller, using a Pt/PtRh thermocouple. The Toeppler pump is switched on, and automatically pumps the H_2 from the combustion tube to the sample bulb. If large amounts of H_2 are collected, a pressure reading can be obtained on the Hg manometer. However, in most cases, the small amount of H_2 collected must be measured on the mass spectrometer. A C.E.C. model 21-130 mass spectrometer is used for quantitative analysis of the gas.

2.6 The sample bulb used to collect the gas is removed from the system for analysis after one or two hours. The process is repeated until the H_2 yield is about 1μg. Blanks have yielded about 0.5 μg H_2.

3. Representative Results (ppm Hydrogen)

Sample	Without Oxide Removal (two month test)	With Oxide Removal (one month test)
As-cast	31	48
Welded	23	49

Note there is about 20 ppm variation in the original samples.

4. Source of High Hydrogen Concentration

4.1 Blistering and fissuring, which was observed experimentally

4.2 Hydrogen trapping at cementite-ferrite interfaces at 150°C

volume percentage (%) of interface	trap parameter
0.1	2
1.0	21

The trap parameter is the interface density times the exponential of the binding energy of hydrogen to interface divided by the gas constant and temperature. 26.8 kJ for binding energy was used [W. M. Robertson and A. W. Thompson, Met. Trans. 11A, 553 (1980)].

4.3 Hydrogen absorption in cementite

Carbide may have high hydrogen concentration as observed in Niobium Carbide (up to 16 atomic % hydrogen, I. E. Pavlov, S. I. Alamovskii and G. P. Shveikim, Inorganic Material, USSR, 14, 2202 (1978).

4.4 Literature on high hydrogen concentration

(1) 50-220 ppm for 308 and 310 stainless steels.
N. F. Fiore and J. A. Kargol in Environmental Degradation of Engineering Materials in Hydrogen, edited by M. R. Louthan, Jr., R. P. McNitt, and R. D. Sissor, Jr., Virginia Polytechnic Institute, Blacksburg, 1981, p. 101.

(2) 44-63 ppm for 304 stainless steels.
H. Hanninen, S. P. Hanninen and S. Tahtinen, ibid ref. (1) p.347.

(3) 10-20 ppm for 4340 steel (up to 35 ppm for surface area) after charging less than an hour.
J. A. Kargol and L. D. Paul in Current Solutions to Hydrogen Problems in Steels, p. 91, edited by C. G. Interrante and G. M. Pressouyre, ASM, 1982.

(4) 15 ppm for low alloy Cr-Mo-V steel
J. Koutsky, K. Splichal, J. Otruba, P. Novosad, and M. Brumovsky, ibid ref. (3), p. 291.

No apparent data on long-term test results comparable to the BNL 2-month data.

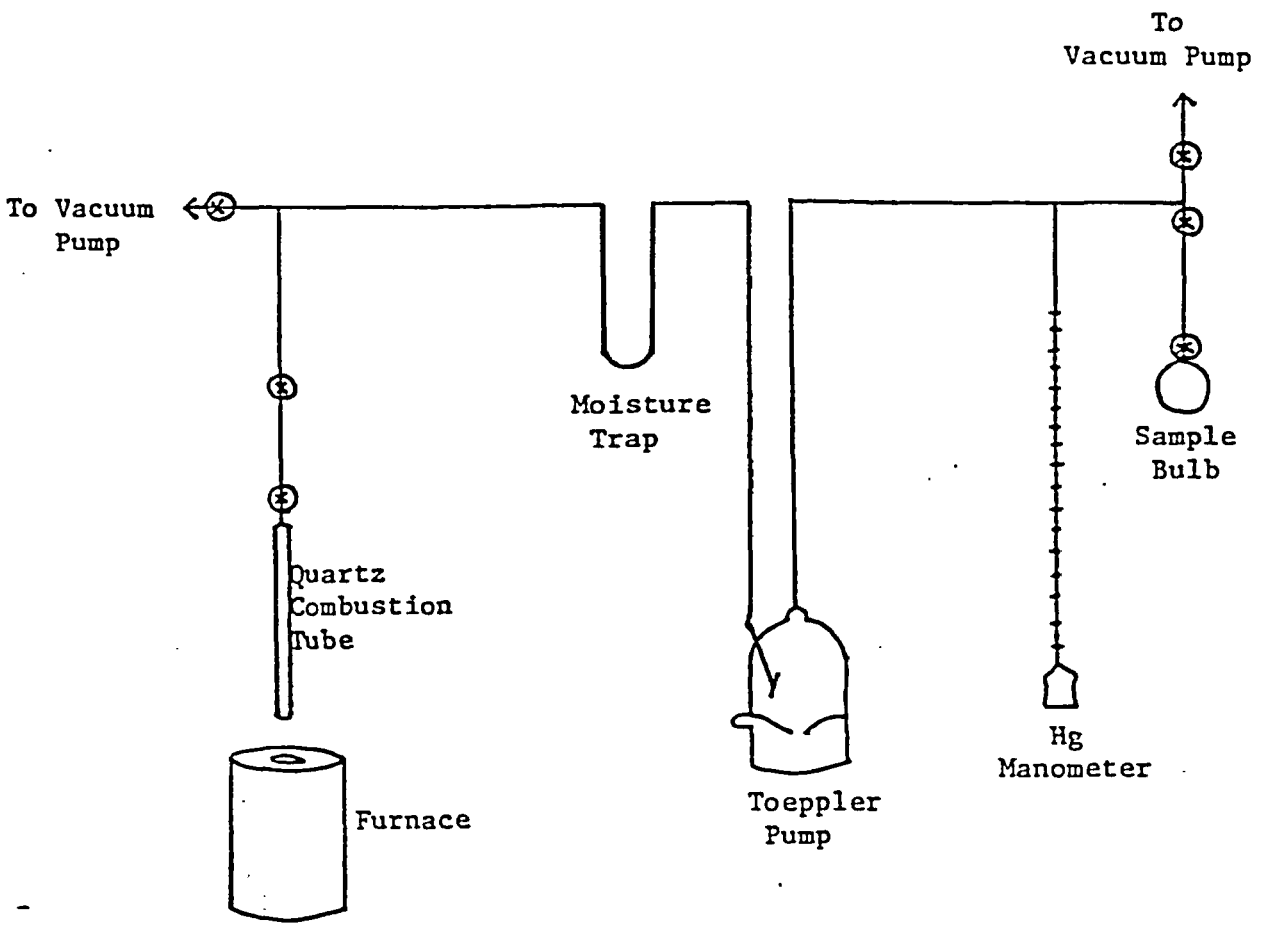

Vacuum extraction apparatus for hydrogen analysis.

Appendix B

75-Word Abstract Form

(New Deadline—Extended Abstract must be submitted with the 75-Word Abstract by May 1, 1984)

NEW ORLEANS, LOUISIANA—OCTOBER 7-12, 1984

Submit to: The Electrochemical Society, Inc.
10 South Main Street, Pennington, NJ 08534-2896

Abstract No. ..... (to be assigned by the Society)

Schedule for Corrosion of Nuclear Waste Containers
(Title of Symposium)

Sponsored by CORROSION/NEW TECHNOLOGY
(Division/Group)

Title of paper Corrosion of Low Carbon Cast Steel (ASTM A216-Grade WCA) in Concentrated Basaltic Groundwater at 80-150°C.

Authors (Underline name of author presenting paper.) T. M. Ahn and P. Soo

Business affiliation and address Brookhaven National Laboratory, Upton, New York, 11973

(State or Country) (ZIP Code) (516) 282 5369 (Telephone No.)

(Type abstract in this area—double-spaced.)

The corrosion properties of ASTM A216-Grade WCA low carbon cast steel were evaluated in concentrated basaltic groundwater at 80-150°C. Stress corrosion cracking and hydrogen embrittlement were observed in constant extension rate tests under various corrosion potentials at 80-85°C. Uniform corrosion rates were greatly reduced at 150°C under gamma irradiation at a dose rate of 1.36×10^6 rad/h while hydrogen uptake was enhanced by the radiolytic hydrogen generated under the same conditions.

Do you require any audiovisual equipment?

- ☐ 35 mm (2 x 2 in.) slide projector
- ☐ Vu-Graph
- ☐ other (specify)

Has the information in this abstract been presented verbally, submitted for publication, or published?
☐ Yes ☐ No
If the answer is yes, please provide the reference (except in the case of invited review presentations). _____

Is a full length paper on this work to be submitted for Society Journal publication? ☒ Yes ☐ No

..... Insert name of Society member author or sponsor

Corrosion of Low Carbon Cast Steel (ASTM A216-Grade WCA) in Concentrated Basaltic Groundwater at 80-150°C

T. M. Ahn and P. Soo
Brookhaven National Laboratory
Upton, NY 11973

Currently in the United States, ASTM A216-Grade WCA type low carbon cast steel is being considered for use as a high level nuclear waste container to be emplaced in a basaltic repository.[1] In this paper, corrosion results are presented from tests carried out at 80-150°C in concentrated basaltic groundwater. The steel has alloying elements with maximum permissible concentrations of 0.25% C, 0.7% Mn, 0.04% P, 0.045% S and 0.6% Si. It also includes residual elements such as Cu, Ni, Cr, Mo and V (total maximum 1%). Concentrated basaltic water is expected to be present in sealed repositories if dissolved solids which are deposited during early groundwater boiling are redissolved by incoming cooler water. The test solution chemistry consists of 2774.5 Na^+, 26.6 K^+, 21.5 Ca^{+2}, 0.25 Mg^{+2}, 258.9 F^-, 2418.0 Cl^-, 1340.8 SO_4^{-2}, 614.6 SiO_2 (all in mg/L). It also initially contains 2.95 g/L Na_2CO_3 which during testing will form an equilibrium state with CO_3^{-2} and CO_2.

CERT (constant extension rate test) tests were performed at 80-85°C at an average strain rate of ~3 x 10^{-7}/s in various environments with rod shaped tensile specimens. Tests in the solution at the open circuit corrosion potential and at an anodic potential (-0.2 V SCE) show an indication of environmentally-induced mechanical degradation, including specimen surface cracking. When a cathodic potential was applied (-1.4 V SCE), there was a severe decrease in ductility and the fracture surface showed transgranular cleavage. Samples were also tested in moisture environments over the solution. With the addition of HCO_3^- ions to the solution, degradation again became significant. The cathodic polarization tests indicate that hydrogen embrittlement is present. The other cracking phenomenon are considered to be associated with stress corrosion cracking because of different fracture morphologies. In this study, weld effects were not significant, and base and welded steel behaved similarly.

Coupon immersion tests were performed in the concentrated solution to measure corrosion rates and hydrogen uptake efficiency at 150°C under a gamma irradiation flux of 1.36 x 10^6 rad/h. Similar tests were conducted without irradiation. After two months' exposure under irradiation conditions, the coupons were found to be covered with salt deposits (mainly silicon oxide) and little attack occurred. On the other hand, significant attack was seen under non-irradiation conditions. Parallel tests on pure iron (Ferrovac-E) showed that it was inert and no surface deposits were detected. Among the possible reasons for the corrosion retardation under radiation conditions, anodic inhibition of oxidizers formed during irradiation seems to be most important. For non-irradiation conditions, uniform corrosion seems to be an important failure mode in addition to localized corrosion processes, as described above.

From parallel coupon experiments, hydrogen concentrations in the coupons were analyzed by a vacuum extraction method. Under gamma irradiation, the hydrogen uptake was several hundred ppm for the cast steel while 20 ppm was observed for Ferrovac-E. The hydrogen uptake is considered to be from the 4% mole % hydrogen in the gases generated during solution radiolysis. Under non-irradiation conditions, hydrogen uptake was significantly reduced in the range of 10-50 ppm. This hydrogen is apparently from cathodic reactions since hydrogen was detected in the gas phase above the test solution. Welded and U-bend samples did not show a significant difference in the hydrogen uptake efficiency when compared to non-deformed base metal specimens.

In summary, low carbon cast steel is susceptible to stress corrosion cracking and hydrogen embrittlement in concentrated basaltic water at high temperatures. Uniform corrosion rates are greatly reduced under gamma irradiation. Local corrosion may be an important failure mode under gamma irradiation while uniform corrosion is a major failure mode under non-irradiation conditions. Hydrogen uptake by the steel is significant under gamma irradiation while non-irradiation conditions only give a slight increase in hydrogen levels.

Acknowledgement

This work was performed under the auspices of the United States Nuclear Regulatory Commission (NRC). The authors acknowledge the program coordination by Dr. M. McNeil of the NRC.

Reference

1. T. M. Ahn and P. Soo, "Container Assessment - Corrosion Study of HLW Container Materials, Quarterly Progress Report, October-December 1983," BNL-NUREG-34220, Brookhaven National Laboratory, 1984.

INFORMAL REPORT

CONTAINER ASSESSMENT - CORROSION STUDY OF HLW CONTAINERS MATERIALS

QUARTERLY PROGRESS REPORT
July-September 1984

T. M. Ahn and P. Soo

Manuscript Completed November 1984

Prepared by the Nuclear Waste Management Division
D. G. Schweitzer, Head
Department of Nuclear Energy, Brookhaven National Laboratory
Upton, New York 11973

Prepared for the U. S. Nuclear Regulatory Commission
Office of Nuclear Regulatory Research
Contract No. DE-AC02-76CH00016
FIN A-3237

ABSTRACT

Low carbon cast steel is a candidate container material for high level waste to be emplaced in a basalt repository. The current study is an evaluation of potential hydrogen embrittlement and radiation corrosion effects in this steel which could be present in basaltic groundwater. Other potential failure modes are also addressed to a more limited extent.

Slow-strain-rate testing of ASTM A216-Grade WCA cast steel was continued to confirm previous results on hydrogen embrittlement, stress corrosion cracking, and moisture-induced cracking. The moisture-induced cracking and hydrogen embrittlement are more pronounced than stress corrosion cracking. Data for hydrogen embrittlement under various conditions are generally in a good agreement with previous results.

Corrosion rates were obtained for ASTM A216-Grade WCA steel in concentrated basaltic water of 150°C under gamma irradiation and non-irradiation conditions. It was confirmed that radiation corrosion rates were lower than the non-irradiation rates for oxic solutions. The reduced corrosion rates are attributed to the oxidizers formed, which act as inhibitors or lead to a new cathodic reaction. Electrochemical results and the analysis of corrosion products support this hypothesis.

The kinetics of hydrogen uptake by the cast steel were obtained at 150°C for various test durations. Hydrogen solubility tends to reach a saturation value in a short period, such as one week.

A fatigue test was also completed to help define environmental effects on crack initiation and propagation. It was found that the steel is susceptible to corrosion fatigue in concentrated basaltic water at a cycling rate of 30 Hz for various stress levels.

Finally, a computer program was written to assess the uncertainties associated with the fracture of low carbon steel.

PREVIOUS REPORTS IN THIS SERIES

Container Assessment - Corrosion Study of HLW Container Materials, Quarterly Progress Reports, T. M. Ahn and P. Soo:

July-September, 1983, BNL-NUREG-33940
October-December, 1983, BNL-NUREG-34220
January-March, 1984, Informal Report.
April-June, 1984, Informal Report

CONTENTS

FIGURES

TABLES

ACKNOWLEDGMENT

The authors acknowledge C. Brewster and C. Anderson for general technical assistance, R. Sabatini and J. Taftor for electron microscopy, L. Gerlach for fatigue machine operation, R. Wilson for hydrogen analysis, and A. Foelsche for polarization testing. N. Z. Cho developed a computer code for the analysis of uncertainties associated with the probability of fracture.

1. INTRODUCTION

The objective of this program is to identify and evaluate some of the potential corrosion failure modes in low carbon steel, which is the reference container material for high level waste packages to be emplaced in basalt repositories. The two main parts of this study are: (1) to evaluate hydrogen assisted embrittlement effects and (2) to measure hydrogen uptake in the presence of basaltic waters and a gamma irradiation field. This study also addresses the problems of radiation corrosion, stress corrosion cracking, corrosion fatigue, and uncertainties associated with the experimental procedures. The present report describes the results obtained in the final quarter of Fiscal Year 1984.

2. CHEMICAL ANALYSIS OF CAST LOW CARBON STEEL

The chemistry of the second heat of cast low carbon steel was analyzed in this quarter. The results are very close to those of the first heat, as shown in Table 1.

Table 1. Composition of the second heat of ASTM A216-Grade WCA cast steel for CERT tests (weight percent, balance is iron).

Element	First Heat	Second Heat
C	0.07	0.09
Mn	0.43	0.44
P	0.001	0.002
S	0.01	0.010
Si	0.10	0.09
Cu	N.D.	N.D.
Ni	0.06	0.08
Cr	0.06	0.09
Mo	0.01	0.02
V	N.D.	N.D.

N.D.: Not detectable
Analysis performed by New York Testing Laboratories

3. CONSTANT EXTENSION RATE TENSILE (CERT) TESTING OF CAST LOW CARBON STEEL

Until the last quarter, we concentrated on identifying the environmental conditions for which stress corrosion cracking, moisture-induced cracking, and hydrogen embrittlement take place. In this quarter, we repeated some of the experiments to check reproducibility.

Table 2 and Figure 1 show the results obtained in this quarter for various environmental conditions. The first group of tests (SS33 and SS37) in Table 2 is for a reference air environment. In the second group (SS27, SS34, SS29, SS30) there is no strong indication of environmental degradation at open circuit (o/c) potential in air saturated solution for strain rates of 6.0×10^{-6}/s and 1.5×10^{-4}/s (SS27 and SS34). However, for moist air over solutions containing HCO_3^-, the ductility loss was significant (SS29), and there was severe dissolution at anodic potentials (SS30). The final group (SS28, SS38, SS32, SS36, SS26, SS31, SS35) represents duplicate tests conducted under cathodic potentials, and the results are in reasonably good agreement with previous data.[1] Figure 1 also shows reduction in area values versus the applied potential in CERT tests.

4. RADIATION CORROSION OF CAST LOW CARBON STEEL

In this quarter, one-week tests were repeated to check reproducibility. Other data for four-month tests were also obtained, as shown in Table 3. The one-week test results show large differences compared to previous results (1813 μm/yr for Ferrovac-E and 1369 μm/yr for as-received steel).[1] From this type of immersion test it seems that significant scatter is to be expected.

As reported previously[1], the corrosion rates obtained from short term tests are much higher than those from long term tests indicating that the uniform corrosion rate decreases with time. Also, the corrosion rates under irradiation are much lower than those under non-irradiation conditions. There were no discernible indications of microstructural effects on the corrosion rate, as shown in the results for U-bend and welded samples.

Usually, gamma irradiation is shown to enhance the rate of corrosion because of the generation of oxidants in solution.[2] The current study, however, demonstrates that for oxic solutions the opposite behavior is present. This anomalous behavior requires detailed additional work to develop an understanding of the irradiation corrosion processes present.

To interpret the test results, anodic polarization curves were obtained for specimens immersed in solution purged with commercial purity argon to remove dissolved oxygen, with and without addition of H_2O_2 (36 cc to 800 cc concentrated solution) at 80°C. Open circuit potentials were also measured in air-saturated solutions with and without similar additions of H_2O_2. Figure 2 (2-a, 2-b, 2-c, 2-d) shows the anodic polarization curves for BCL cast steel and Ferrovac-E. For basaltic water only (2a, 2-c) both materials show a passive regime. On the other hand for basaltic water containing H_2O_2, there is no indication of passivity (2-b, 2-d). For all these cases, there is a tendency for spontaneous pitting as shown by the measured protection potentials. Even though water alone shows passive regimes, there was no indication of the growth of protective oxide during the measurement of open circuit potentials (Figure 3). We discussed the probable reason for the reduced corrosion rates in the last quarterly progress report.[1] The lowered corrosion rates were attributed to an anodic-inhibitor effect, caused by the H_2O_2 addition and to a new cathodic reaction with H_2O_2. The present results on polarization curves

Table 2. Results of ASTM A216-Grade WCA cast steel CERT tests conducted for various environmental conditions at 80°C.

Sample No.	Test Environment	Average Strain Rate (sec^{-1})	Total Elongation[c] (%)	Reduction in Area (%)	0.2% Offset Yield Strength (MPa)	Tensile Strength (MPa)	Fracture Strength (MPa)	Final Solution pH
SS33	Air	6.0×10^{-6}	18.1	68.6	365	457	321	---
SS37	Air	1.5×10^{-4}	23.6	70.8	366	430	261	---
SS27	Solution (o/c)[a]	6.0×10^{-6}	18.9	60.8	395	567	413	8.2
SS34	Solution (o/c)	1.5×10^{-4}	17.4	74.5	386	505	325	9.3
SS30	Solution (-0.2 V)[b]	3.0×10^{-7}	18.5	95.5	180[d]	193[d]	N.D.	12.5
SS29	Moist air over solution containing 1.0 g/ℓ $NaHCO_3$	3.1×10^{-7}	4.9	41.1	391	562	474	10.2
SS28	Solution (-1.0V)	3.0×10^{-7}	21.0	41.9	343	527	466	9.2
SS38	Solution (-1.0V)	3.0×10^{-7}	13.9	15.0	334	544	512	4.9
SS32	Solution (-1.0V)	N.D.	N.D.	44.2	N.D.	527	439	7.9
SS36	Solution (-1.0V)	1.5×10^{-4}	18.4	61.5	312	417	277	9.4
SS26	Solution (-1.4V)	2.7×10^{-7}	14.1	28.4	367	529	502	10.0
SS31	Solution (-1.4V)	6.0×10^{-6}	16.0	27.2	351	536	492	9.5
SS35	Solution (-1.4V)	1.5×10^{-4}	18.6	46.8	314	430	291	9.0

N.D.: Not determined

[a]o/c (open circuit potential) in air-saturated solution at 80°C is typically -0.57 to -0.58 Volt SCE.

[b]Potential with respect to SCE.

[c]Gauge length is 1.27 cm.

[d]Calculated from the original sample cross sectional area.

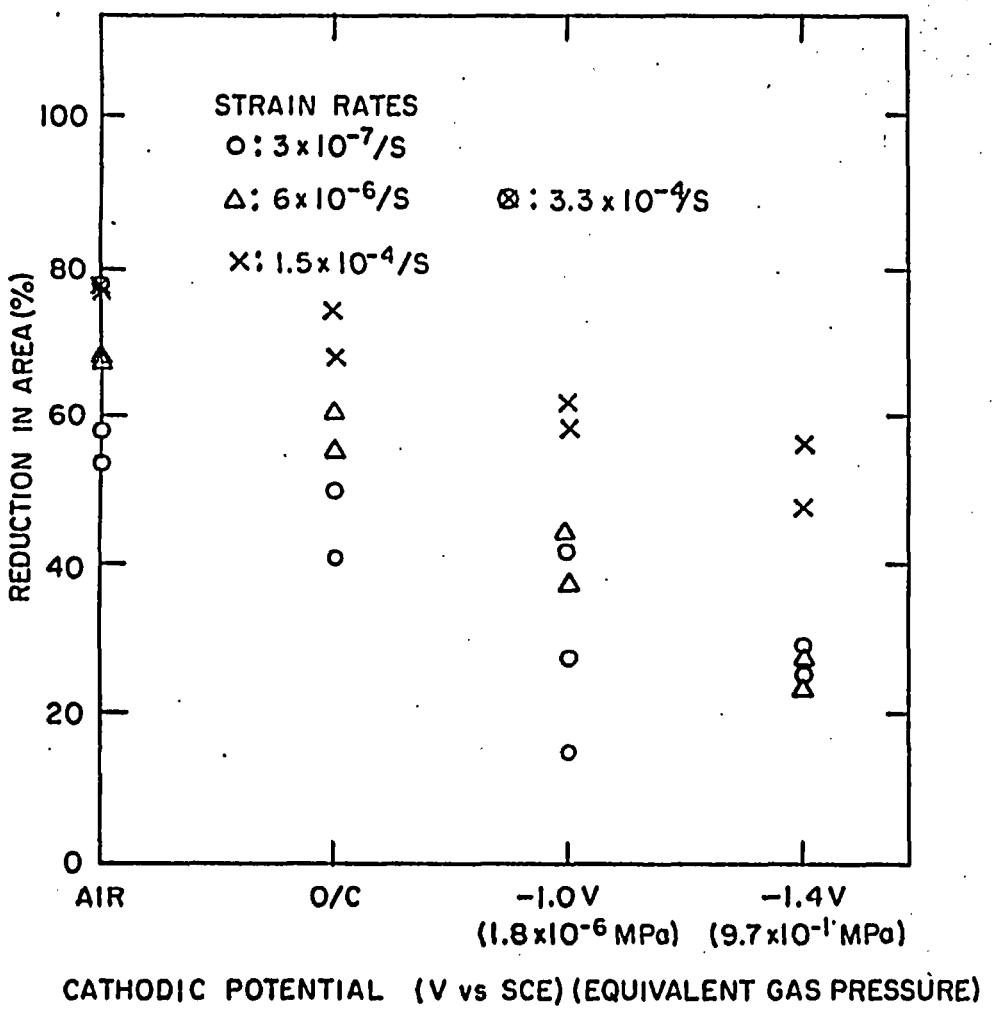

Figure 1. Reduction in area versus applied potential in CERT tests for ASTM A216-Grade WCA steel in concentrated (x7.7) basaltic groundwater at 80°C.

and open circuit potentials support part of this hypothesis by ruling out the possibility of protective oxide growth.

Table 3. Corrosion rates of ASTM A216-Grade WCA steel and Ferrovac-E in air saturated concentrated basaltic groundwater at 150°C (μm/yr).

	Non irradiation		Irradiation
Material	One-Week Test	Four-Month Test	Four-Month Test
Ferrovac-E	2870	22	20
As-Received Steel	3083	41	10
Welded Steel	N.D.	107	11
U-Bend, Steel (As-Received)	N.D.	29	44
U-Bend, Steel (Welded)	N.D.	25	26

N.D.: Not determined

In order to fully characterize the uniform corrosion mechanism the corrosion products were analyzed more extensively. Figure 4 shows typical EDAX results for both the non-irradiation and irradiation conditions. For non-irradiation conditions, the majority of the area shows the presence of Si, O, and Fe (Figure 4). A sulfur (S) peak is also seen occasionally. An X-ray diffraction analysis (Table 4) shows the crystal structure is of the type, $FeSiO_4$, Fe_2O_3, or $FeSO_4$. On the other hand, for irradiation conditions, the majority of the area studied on a macroscopic scale is amorphous as reported previously, with Si, O and Fe present.[1] Microscopically, however, the corrosion products were occasionally found, using scanning transmission electron microscopy, to be composed of very small crystals, approximately 100 Å in diameter. These corrosion products were usually deposited on the bottom of the autoclave and, therefore, they do not seem to be the type that would give a protective scale on the steel specimens.

A few of the immersion specimens from earlier tests were reexamined to obtain additional pit growth kinetics. The results are summarized in Table 5. Similar data are currently being obtained for the specimens listed in Table 3.

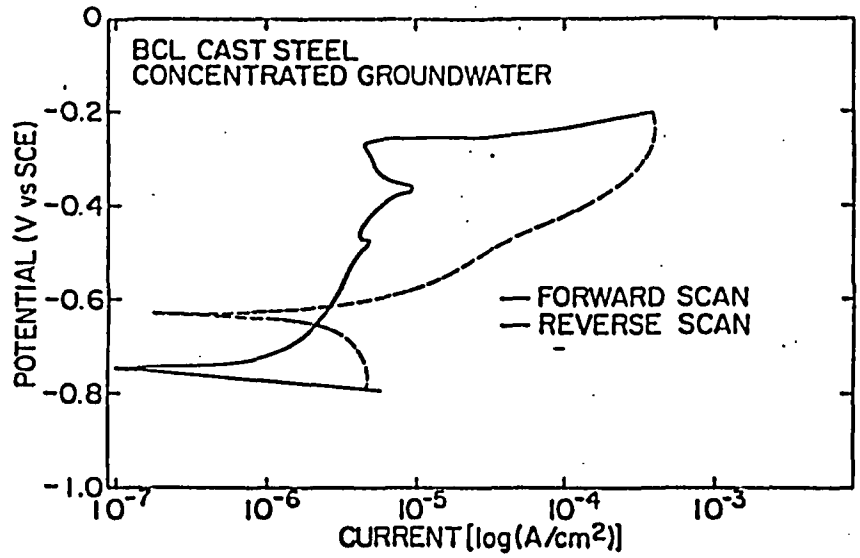

(a)

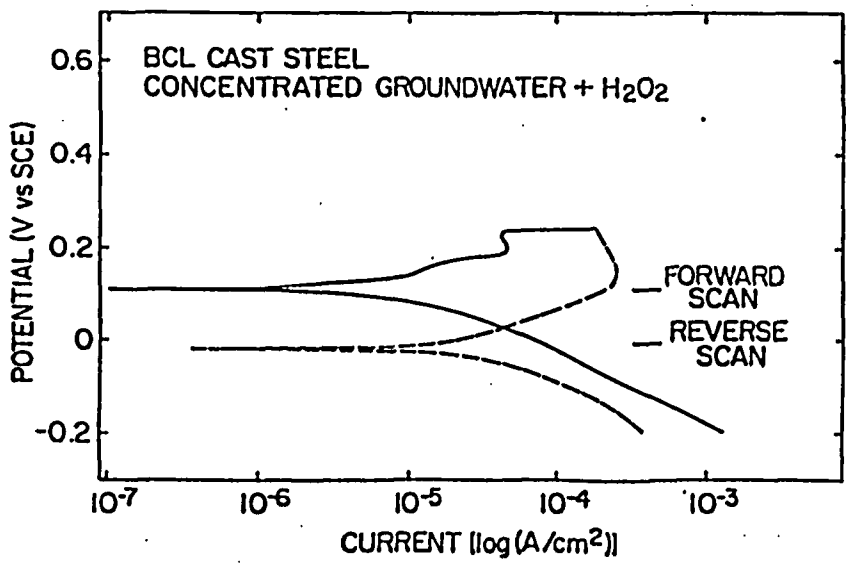

(b)

Figure 2. Anodic polarization curves for Ferrovac-E and ASTM A216-Grade WCA steel in argon-purged concentrated (x7.7) basaltic water at 80°C. The scan rate was 0.2 mV/second.
(a) BCL cast steel in concentrated groundwater
(b) BCL cast steel in concentrated groundwater + H_2O_2
(c) Ferrovac-E in concentrated groundwater
(d) Ferrovac-E in concentrated groundwater + H_2O_2.

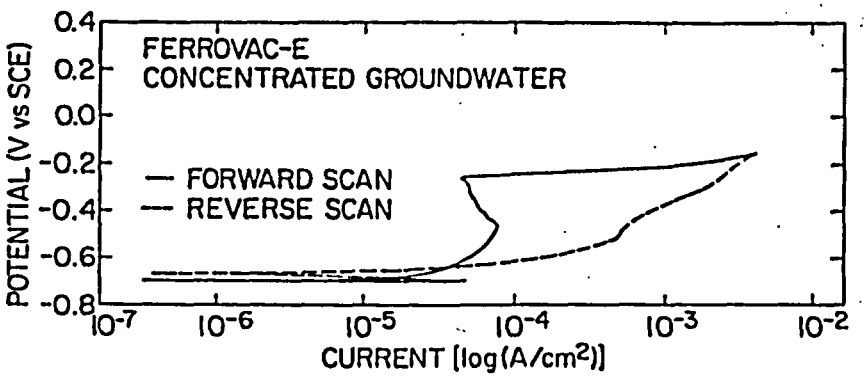
FERROVAC-E
CONCENTRATED GROUNDWATER
FORWARD SCAN
REVERSE SCAN
POTENTIAL (V vs SCE)
0.4
0.2
0.0
-0.2
-0.4
-0.6
-0.8
10-7
10-6
10-5
10-4
10-3
10-2
CURRENT [log(A/cm2)]

(c)

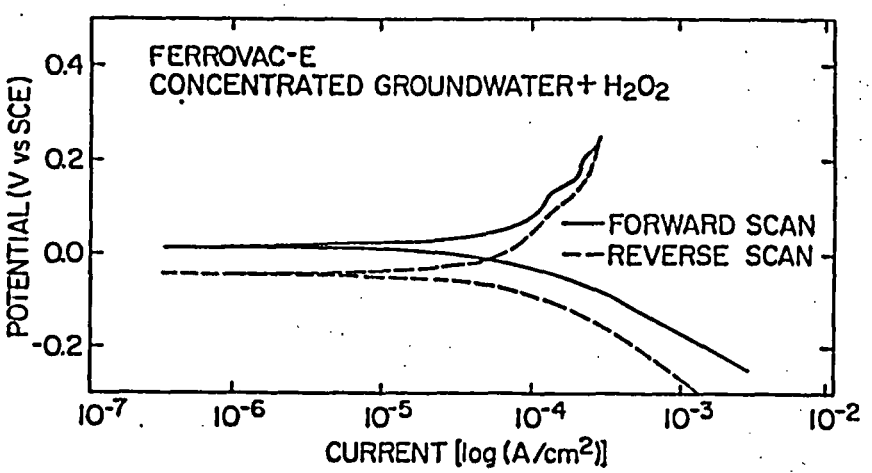
FERROVAC-E
CONCENTRATED GROUNDWATER + H2O2
FORWARD SCAN
REVERSE SCAN
POTENTIAL (V vs SCE)
0.4
0.2
0.0
-0.2
10-7
10-6
10-5
10-4
10-3
10-2
CURRENT [log (A/cm2)]

(d)

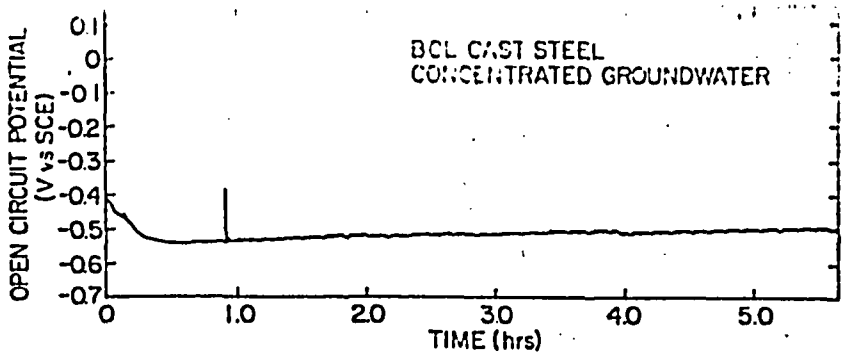

(a)

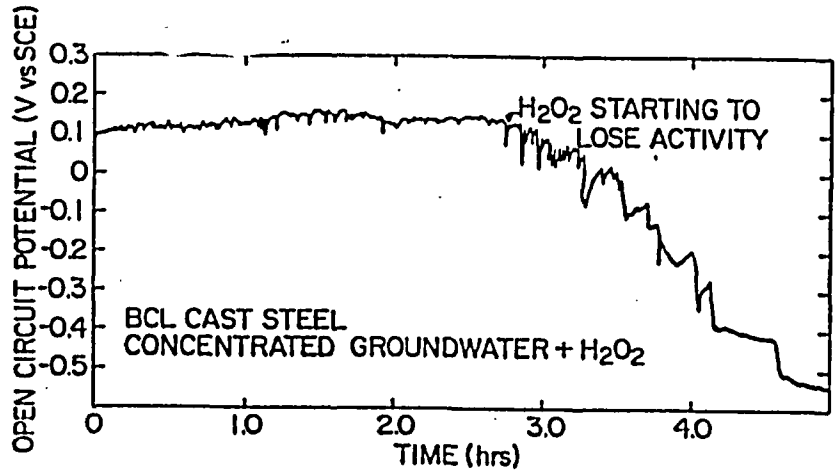

(b)

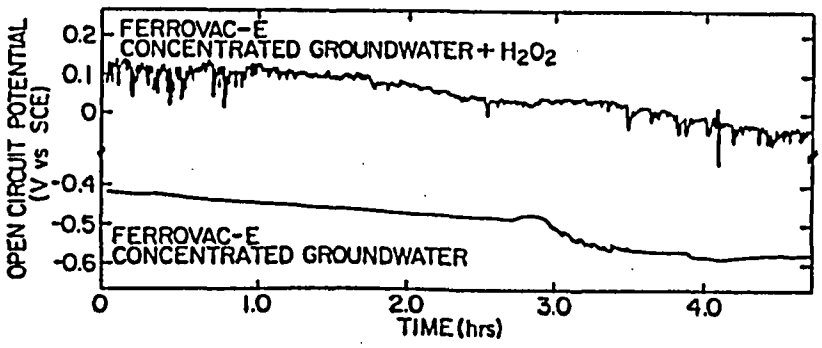

(c)

Figure 3. Open circuit potentials of Ferrovac-E and ASTM A216-Grade WCA cast steel in air-saturated concentrated (x7.7) basaltic water at 80°C.
(a) BCL cast steel in concentrated groundwater
(b) BCL cast steel in concentrated groundwater + H_2O_2
(c) Ferrovac-E for both solutions.

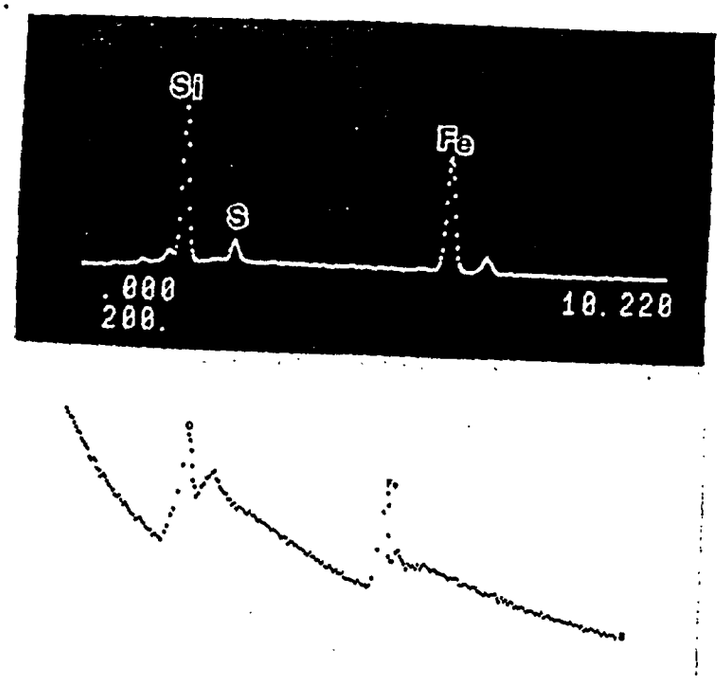

(a)

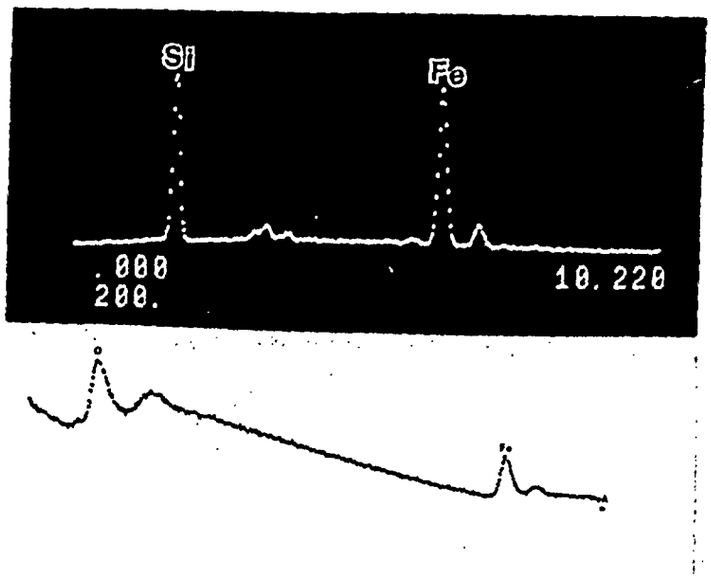

(b)

Figure 4. EDAX results on the corrosion products of ASTM A216-Grade WCA cast steel exposed for two months to concentrated basaltic groundwater at 150°C in (a) non-irradiated solution (b) solution irradiated at a gamma dose rate of 1.36×10^6 rad/h.

Table 4. The major peaks in X-ray diffraction patterns for corrosion products of ASTM A216-Grade WCA steel exposed with Ferrovac-E to concentrated (x7.7) basaltic groundwater at 150°C for two months.

		d (Å)	Probable Corrosion Product
(a)	Conventional X-ray Diffraction	2.52	$FeSiO_4$
		1.48	Not known
		2.80	$FeSiO_4$
(b)	STEM Results		
	Area 1	3.62	Fe_2O_3, $FeSO_4$
		3.04	Not known
		2.49	$FeSiO_4$
	Area 2	3.60	Fe_2O_3,$FeSO_4$
		3.00	Not known
		2.11	Not known

Table 5. Pitting corrosion of ASTM A216-Grade WCA steel U-bend specimens in air-saturated concentrated (x7.7) basaltic groundwater at 150°C.

Material	Average Pit Depth (μm)	Maximum Pit Depth (μm)	Pit Density* (number/cm)
U-Bend, As-Received Steel			
2-month irradiation tests	8	14	21
U-Bend Welded Steel			
1-week non-irradiation tests	25	83	54
2-month non-irradiation tests	40	186	44
2-month irradiation tests	11	34	11

*Average number of pits along 1 cm of sectioned surface.

5. HYDROGEN UPTAKE IN CAST LOW CARBON STEEL

5.1 Gas Generation and Solution Analysis

Tables 6 and 7, and Figures 5 and 6 summarize the gas generation results for basaltic water/metal systems at 150°C with and without gamma irradiation present. The cover gas was air at 1 atmosphere pressure and room temperature. In one-week tests, the hydrogen generation in the irradiated tests becomes significant as shown by both the gas analyses (Table 7) and pressure measurements (Figure 5). For a one-month test, the pressure after two days dropped below the steam pressure even though the temperature remained at 150°C and there was no significant amount of water loss. Results of gas analyses from this test are, therefore, questionable but are still given in Tables 6 and 7. In Figure 6, for the four-month test, the pressure remained constant after approximately one day. Two probable pressure scales are drawn because of the uncertainties in the input voltage to pressure transducer. There was also a significant amount of water loss in this test, but the loss did not seem to be due to leakage because the gas analysis (Table 7) shows abundant hydrogen present. Certainly more tests are desirable to confirm the above results. Nevertheless, it is important to note that a significant amount of oxidizers must have been formed to balance the hydrogen produced under gamma irradiation.

Solution pH was also measured in the corrosion testing. Table 8 shows that the final pH values are lower than the initial value (10.5) for both the irradiation and non-irradiation conditions.

5.2 Hydrogen Uptake

Work continued to measure the hydrogen uptake by iron and steel exposed ~~for one month~~ to the concentrated groundwater at 150°C to determine how much hydrogen was present in oxides or precipitates. In the hydrogen analysis, the corrosion products or precipitates were also analyzed separately after removal from the metal coupons, to determine their hydrogen uptake. The results showed 5.5 μg of hydrogen in samples weighing ≥1 g, which is relatively small compared to the hydrogen concentrations in metal coupons themselves. Therefore, the corrosion products and precipitates deposited in the solution trap negligible amounts of hydrogen.

Even though hydrogen uptake in the corrosion products or precipitates was found to be negligible, we removed the corrosion products or precipitates on the test specimens before hydrogen analysis this quarter. The amounts for the one-week and four-month tests were relatively low as shown in Tables 9 and 10, compared to our previous results. However, the concentrations are still higher than those for mobile hydrogen concentrations reported in the majority of the literature, such as Reference 3. This is attributed to trapped hydrogen at grain boundaries or second phases, which is not determined by conventional permeation tests for the measurement of mobile hydrogen concentrations. There were no significant effects of microstructural variations brought about by welding, on the rate of hydrogen uptake.

Table 6. Chemical analysis of the gas samples collected from autoclaves containing concentrated basaltic water/metal systems at 150°C.

Gas	Concentration (mol %)				
	One week[1]		One month	Four months[1]	
H_2	1.76	1.71	1.18	8.12	8.03
N_2	79.99	79.68	80.31	88.12	89.07
O_2	16.62	16.94	15.24	1.12	1.26
CO_2	0.62	0.64	2.27	0.18	0.17
CO	N.D.[2]	N.D.	N.D.	0.97	N.D.
Ar	1.00	1.02	0.79	1.19	1.20
H_2O	trace	trace	N.D.	0.29	0.27

Notes:
1. Duplicate results are for two separate samples taken from the autoclave.
2. Not determined.

Table 7. Chemical analysis of the gas samples collected after gamma irradiation of concentrated basaltic water/metal systems at 150°C. The gamma dose rate was 1.36×10^6 rad/h.

Gas	Concentration (mol %)				
	One week[1]		One month	Four months[1]	
H_2	34.55	29.13	0.77	73.69	73.69
N_2	33.29	38.05	74.01	19.08	20.45
O_2	20.12	18.48	21.42	0.06	0.03
CO_2	2.24	3.90	2.94	5.30	4.32
CO	1.04	1.36	N.D.	1.18	0.67
CH_4	N.D.[2]	N.D.	N.D.	0.16	0.15
Ar	8.31	8.54	0.86	0.28	0.28
H_2O	0.44	0.53	N.D.	0.25	0.40
Pressure Record	See Figure 5			See Figure 6	

Notes:
1. Duplicate results are for two separate samples taken from the test capsule.
2. Not determined.

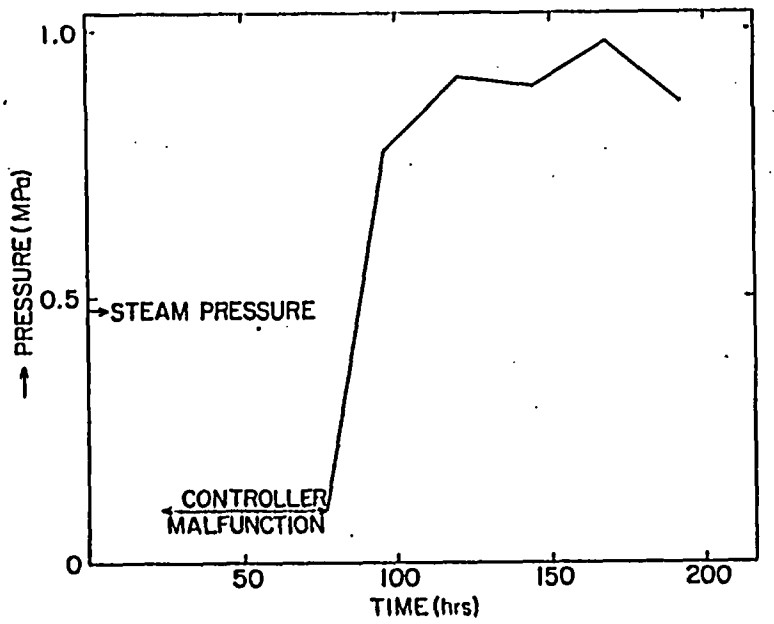

Figure 5. Gas pressure changes during the gamma irradiation of concentrated basaltic water/metal systems at 150°C for one week. The dose rate was 1.36×10^6 rad/h.

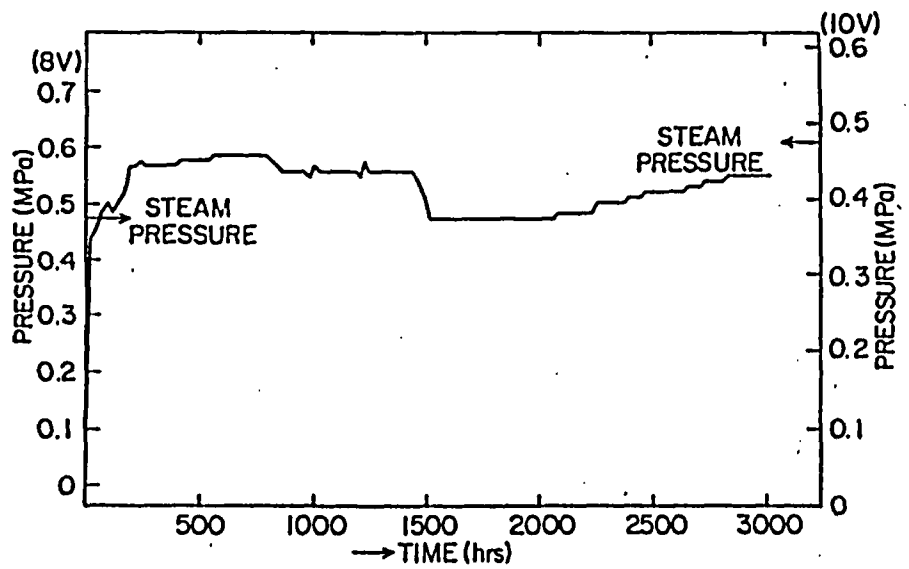

Figure 6. Gas pressure changes during the gamma irradiation of concentrated basaltic water/metal systems at 150°C for four months. The dose rate was 1.36×10^6 rad/h. Absolute values of pressure scales are not known.

Table 8. Solution pH after corrosion testing in concentrated basaltic water/metal systems at 150°C. The gamma dose rate was 1.36×10^6 rad/h.

	One Week[1]		One Month	Two Months[1]		Four Months
Non-irradiation	8.54	8.21	6.90	9.51	10.30	9.94
Irradiation	9.43	8.31	10.02	9.18	8.95	N.D.

N.D.: Not determined.
Note:
1. Results from duplicate tests.

Now, we consider why lower hydrogen concentrations were obtained in the samples with the corrosion products or precipitates removed. One probable reason is due to the hydrogen loss during the removal process of corrosion products or precipitates. A high hydrogen fugacity in the metal seems to be sufficient to give a rapid loss of hydrogen once the hydrogen overpressure in the test vessel is lost during specimen removal.

When the kinetics of hydrogen uptake are considered (hydrogen concentrations for different durations), it may be seen that the samples tend to be saturated with hydrogen in about one week, as shown in Tables 9 and 10.

6. CORROSION FATIGUE OF CAST LOW CARBON STEEL

A fatigue test was performed to investigate crack initition and crack growth of ASTM A216-Grade WCA cast steel in the concentrated basaltic groundwater at 30 Hz and 80°C. The sample configuration for the test is shown in Figure 7. It is an hourglass sample used to measure the fatigue cycles to failure. Table 11 shows the results obtained to date. In air, a sample did not fail after 3.4×10^7 cycles at a mean stress of 138 MPa (the ratio of maximum stress to minimum stress, R = 7.0), and 241 MPa (R = 2.5). However, samples failed at 1.7×10^6 and 1.4×10^6 cycles in the solution for a mean stress of 241 MPa (R = 2.5). When the mean stress was reduced to 174 MPa (R = 2.5), the cycles to failure increased significantly to 1.50×10^7 and 1.02×10^7. This is consistent with the phenomenon of corrosion fatigue.[4] However, when the R value is decreased to 1.7 at the same mean stress level of 174 MPa, the samples failed at shorter intervals of 1.6×10^6 and 1.2×10^6 cycles. This implies that the R value is an important parameter for this system in addition to the mean stress. Since the present steel is susceptible to corrosion fatigue in basaltic water, it may be related to the observed stress corrosion cracking, if both are caused by crack tip dissolution or hydrogen embrittlement.[5]

Table 9. Hydrogen concentration of ASTM A216-Grade WCA steel and Ferrovac-E specimens exposed to concentrated basaltic water at 150°C under a gamma dose rate of 1.36×10^6 rad/h.

Materials	Concentration (ppm)		
	One Week	One Month	Four Months
Ferrovac-E	2(2-0)	5(0-1-4-0)	89(8-36-40-4)
As-received Steel	15(8-2-2-2)	14(10-3-1)	10(4-2-1-1-1)
Welded Steel	N.D.	14(4-1-3-1)	9(4-0-3-1-1)
As-received U-bend Steel	N.D.	N.D.	2(2)
Welded U-bend Steel	N.D.	N.D.	9(8-1)

N.D.: Not determined.
The values in parentheses indicate the increments of gas evolution during sequential heating periods at 950°C.

Table 10. Hydrogen concentration of ASTM A216-Grade WCA steel and Ferrovac-E specimens exposed to concentrated basaltic water at 150°C.

Materials	Concentration (ppm)		
	One Week	One Month	Four Months
Ferrovac-E	8(8-0)	9(8-1)	3(3-0)
As-received Steel	43(8-9-26-1)	39(31-6-1)	11(7-1-2)
Welded Steel	N.D.	49(6-0-3-5-5-6-7-9-0-1)	2(2)
As-received U-bend Steel	N.D.	N.D.	19(18-1)
Welded U-bend Steel	N.D.	N.D.	9(9-0)

N.D.: Not determined.
The values in parentheses indicate the increments of gas evolution during sequential heating periods at 950°C.

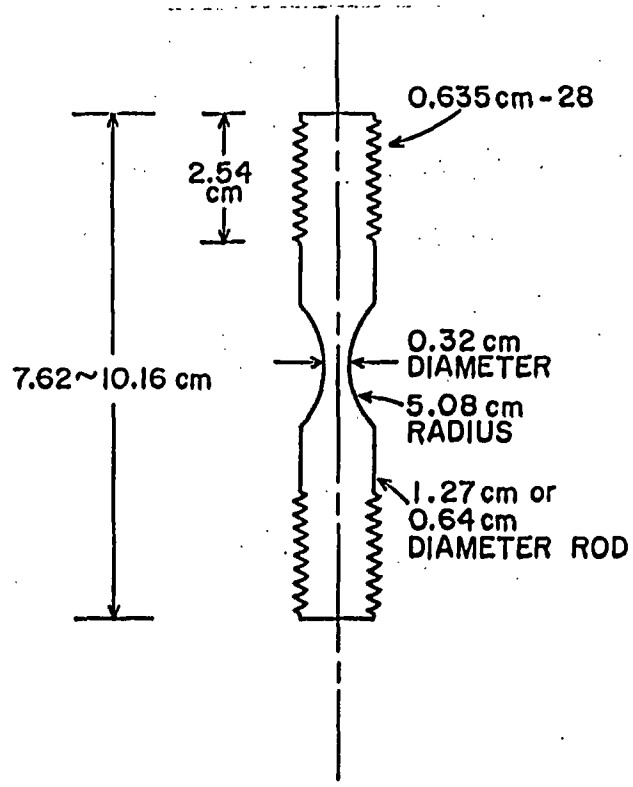

Figure 7. Corrosion fatigue specimen configuration of ASTM A216-Grade WCA cast steel rod.

Table 11. Corrosion fatigue results for ASTM A216-Grade WCA steel tested in concentrated basaltic water at 80°C and a cycling rate of 30 Hz.

Environment	Mean Stress (MPa)	R*	Failure Cycle ($\times 10^{-6}$)
Air	138	7.0	>30.8
Air	241	2.5	>34.0
Solution	241	2.5	1.7
Solution	241	2.5	1.4
Solution	174	2.5	15.0
Solution	174	2.5	10.4
Solution	174	1.7	1.6
Solution	174	1.7	1.2

*R is the ratio of maximum stress to minimum stress.

7. UNCERTAINTY ANALYSIS ON THE PROBABILITY OF FRACTURE

N. Z. Cho* has written a computer program for the analysis of uncertainties associated with the fracture probabilites. The Appendix of this report gives a detailed description of the work. This program can be used to analyze our data on hydrogen embrittlement to obtain uncertainties associated with them. An example is included in the Appendix.

8. REFERENCES

1. T. M. Ahn and P. Soo, "Container Assessment--Corrosion Study of HLW Container Materials, Quarterly Progress Report, April-June 1984," Brookhaven National Laboratory, 1984.

2. R. E. Westerman, J. L. Nelson, S. G. Pitman, and W. L. Kuhn, "Evaluation of Iron-Base Materials for Waste Package Containers in a Salt Repository, Pacific Northwest laboratory Report, PNL-SA-11713 (1983).

3. K. Kikuch and R. B. McLellan, "The Solubility and Diffusivity of Hydrogen in Well-Annealed and Deformed Iron," Acta Metallurgica, 31, 961 (1983).

4. J. Congleton and I. H. Craig, "Corrosion Fatigue" in Corrosion Processes edited by R. N. Parkins, Applied Science Publishers (1982), p. 209.

5. T. M. Ahn and P. Soo, "Container Assessment--Corrosion Study of HLW Container Materials, Quarterly Progress Report, January-March 1984," Brookhaven National Laboratory, 1984.

*Department of Nuclear Energy, BNL.

APPENDIX

BROOKHAVEN NATIONAL LABORATORY

MEMORANDUM

DATE: August 31, 1984

TO: T. M. Ahn

FROM: N. Z. Cho

SUBJECT: Bayesian Uncertainty Analysis of Fracture Probabilities

Attached is a summary of uncertainty analysis on fracture probabilities based on the Bayesian probabilistic method and the Monte Carlo sampling technique.

The computer programs developed or used in the course of this work are available from the CDC 6600 permanent file system:

(1) ATTACH,WEIB,ID=AHN.
(2) ATTACH,SAMPLE,ID=AHN,CY=2.

NZC:ep
cc: R. Youngblood
R. Bari

Bayesian Uncertainty Analysis of Fracture Probabilities

I. INTRODUCTION

Bayesian uncertainty analysis is based on the Bayes' formula (which can be found in most books on probability and statistics, e.g., Reference 1) and is being used increasingly in decision theory, in the design of experiments and in reliability analysis, especially in the case of insufficient data base. A specific field which uses the Bayesian analysis heavily is the probabilistic risk assessment of nuclear power plants (References 2 and 3).

Briefly, the Bayesian analysis is to update a prior probability distribution of an uncertain variable by incorporating new evidence or specific data in the analysis through the Bayes' formula:

$$P_r(\sigma_o|E,I) = \frac{P_r(\sigma_o|I)\, P_r(E|\sigma_o,I)}{\int P_r(\sigma_o|I)\, P_r(E|\sigma_o,I)\, d\sigma_o} \qquad (1)$$

where

$P_r(\sigma_o|E,I)$ = posterior probability of uncertain variable σ_o given new evidence E and prior information I,

$P_r(\sigma_o|I)$ = prior probability of σ_o given I,

$P_r(E|\sigma_o,I)$ = probability (likelihood function) of E given σ_o and I.

The prior probability $P_r(\sigma_o|I)$ is usually assessed from the generic information about the variable σ_o before specific evidence or data is available. For example, the general satistical data from other similar experiments or information resulting from any "analysis" on the variables could be used in assessing the prior probability.

The likelihood function $P_r(E|\sigma_o,I)$ is usually provided by the probabilistic model (parametric in σ_o) describing the process and mechanism of interest, e.g., an exponential distribution in the case of a Poisson process and a Weibull distribution in the case of a fracture process.

The integration in the denominator in Equation (1) is simply a normalization constant.

II. FRACTURE PROBABILITIES AND THEIR UNCERTAINTIES

The method of Bayesian analysis briefly described in Section I was applied to a set of fracture tests (Sample Nos. SS1 and SS6) reported in Reference 4 to estimate the fracture probabilities and associated uncertainties.

A well-established probabilistic model for fracture mechanism is the Weibull distribution (Reference 5):

$$1 - P_F = \exp\left[- \left(\frac{\sigma_F}{\sigma_o}\right)^m \right] \qquad (2)$$

where P_F is the fracture probability, m the shape parameter, σ_o the scale parameter, and σ_F the fracture stress.

It is noted that at a specific value of σ_F, P_F will be an uncertain variable since m and σ_o are uncertain variables.

The experimental results of Reference 5 were used as generic information to assess the prior probabilities for σ_o and m. A linearization approximation to the nonlinear regression problem resulting from the method of least-squares leads to the estimation of means and variances of $\ell n \sigma_o$ and m which both follow normal distributions.

Since it is known (References 6 and 7) that the shape parameter m is relatively constant across stress levels, m was not updated and only σ_o was updated.

The prior distribution of σ_o was updated using the evidence of the test SS1 (first-stage Bayesian procedure). The posterior distribution resulting from the first-stage Bayesian procedure was used, in turn, as the prior in the second-stage Bayesian procedure to include the evidence of the test SS6. This procedure can be repeated sequentially as long as the new evidence was not used in the assessment of the previous priors.

Once the second-stage posterior distribution of σ_o was found, the distribution of P_F was calculated by the Monte Carlo sampling technique operating on Equation (2) with the posterior distribution of σ_o and the regression-generated prior distribution of m.

The results are shown in Table I and Figure 1. The fracture probabilities and uncertainties (expressed as confidence levels) are those at σ_F = 420 MPa.

Table I. Fracture probabilities at σ_F = 420 MPa from Bayesian analysis and Monte Carlo sampling*.

Confidence Level (percent)	P_F
1.0	3.89(-3)
5.0	9.67(-3)
10.0	1.63(-2)
20.0	3.05(-2)
30.0	4.67(-2)
40.0	6.95(-2)
50.0	9.77(-2)
60.0	1.37(-1)
70.0	1.90(-1)
80.0	2.87(-1)
90.0	4.81(-1)
95.0	6.58(-1)
99.0	9.08(-1)
Mean	1.78(-1)

*Sample size of 4800 which assures 0.5 percent accuracy interval on the 95% confidence level.

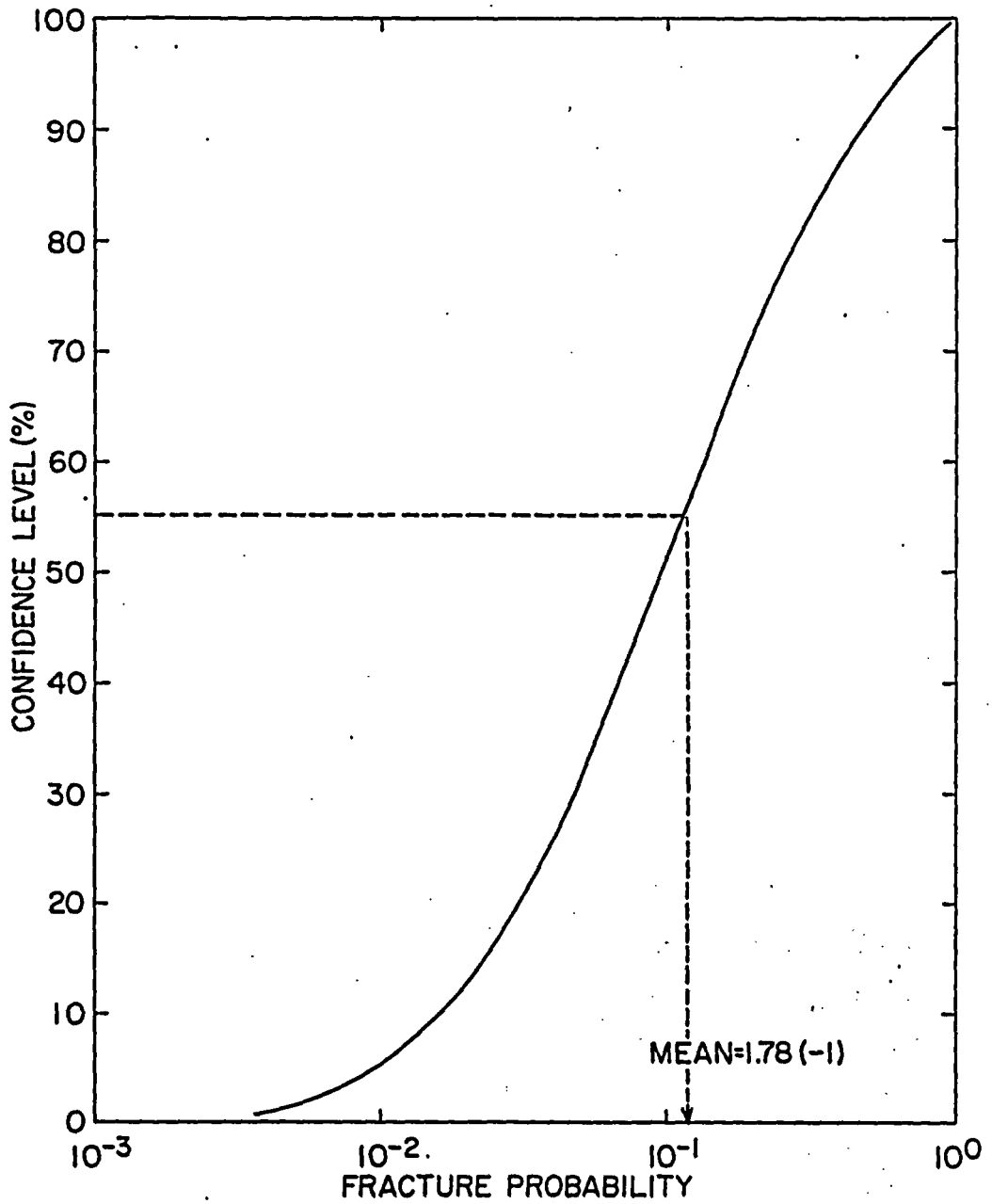
100
90
80
70
60
50
40
30
20
10
0
CONFIDENCE LEVEL (%)
MEAN=1.78 (-1)
10^{-3}
10^{-2}
10^{-1}
10^{0}
FRACTURE PROBABILITY

Figure 1

REFERENCES

1. L. J. Savage, The Foundations of Statistics, 2nd Revised Ed., Dover, New York, 1972.

2. S. Kaplan, "On a "Two-Stage" Bayesian Procedure for Determining Failure Rates from Experimental Data," IEEE Trans. Power Appar. Syst. (preprint).

3. I. A. Papazoglou, E. Anavim, and L. Lederman, "Bayesian Analysis under Population Variability with an Application to the Frequency of Loss of Offsite Power and Anticipated Transients in Nuclear Power Plants," Brookhaven National Laboratory, BNL-NUREG-31794, February 1983.

4. T. M. Ahn and P. Soo, "Containment Assessment - Corrosion Study of HLW Containers Materials," Quarterly Progress Report, April-June 1984, Brookhaven National Laboratory, August 1984.

5. T. H. Grundy, T. J. Davies, and D. A. Ryder, "A New Statistical Model of the Hydrogen Embrittlement of Steel" J. of Materials Science, 18, 3128 (1983).

6. H. T. Hahn and R. Y. Kim, "Fatigue Behavior of Composite Laminate," J. of Composite Materials, 10, 156 (1976).

7. J. N. Yang and M. D. Liu, "Residual Strength Degradation Model and Theory of Periodic Proof Testings for Graphite/Epoxy Laminates," J. of Composite Materials, 11, 176 (1977).

BNL-NUREG
INFORMAL REPORT
LIMITED DISTRIBUTION

CONTAINER ASSESSMENT - CORROSION STUDY OF HLW CONTAINER MATERIALS

QUARTERLY PROGRESS REPORT
JANUARY-MARCH 1984

T. M. AHN AND P. SOO

MAY 1984

NUCLEAR WASTE MANAGEMENT DIVISION

DEPARTMENT OF NUCLEAR ENERGY BROOKHAVEN NATIONAL LABORATORY
UPTON, NEW YORK 11973

Prepared for the U.S. Nuclear Regulatory Commission
Office of Nuclear Regulatory Research
Contract No. DE-AC02-76CH00016

NOTICE

INFORMAL REPORT

CONTAINER ASSESSMENT - CORROSION STUDY OF HLW CONTAINER MATERIALS

QUARTERLY PROGRESS REPORT
JANUARY-MARCH 1984

T. M. Ahn and P. Soo
Principal Investigators

Contributors:
C. I. Anderson

Manuscript Completed - May 1984
Date Published - May 1984

Donald G. Schweitzer, Head
Nuclear Waste Management Division
Department of Nuclear Energy
Brookhaven National Laboratory
Upton, New York 11973

Prepared for the U.S. Nuclear Regulatory Commission
Office of Nuclear Regulatory Research
Contract No. DE-AC02-76CH00016
FIN A-3237

ABSTRACT

Low carbon cast steel is a candidate container material for high level waste to be emplaced in a basalt repository. The current study is an evaluation of potential hydrogen embrittlement and stress corrosion effects in this steel which could be present in basaltic groundwater. Type ASTM A216-Grade WCA cast steel was procurred for this purpose. Chemical analyses and microstructural characterization were performed for as-received as well as TIG welded material. The compositions were within ASTM specifications. Welding caused recrystalization and martensite formation in the ferrite and pearlite structure of the as-received material. Work continued on constant extension rate testing (CERT) of steel in concentrated (7x) Grande Ronde basaltic water at 80-85°C for strain rates of about 3×10^{-7}/sec. An indication of environmental degradation was observed for samples immersed in the solution and exposed to the moisture over the solution. A cathodic hydrogen charged sample showed a distinctive cleavage fracture. Testing at an anodic potential gave less degradation than the cathodic charging condition. A solution with increased bicarbonate ion concentration caused a severe loss in mechanical integrity in a speciment tested in the vapor/air phase above the solution.

Hydrogen uptake tests on ASTM A216-Grade WCA steel were repeated for a two-month immmersion time in concentrated Grande-Ronde basaltic water at 150°C under a gamma irradiation flux of 1.3×10^{6} rad/h. As-received and welded samples absorbed 549 ppm and 215 ppm hydrogen respectively. On the other hand, pure iron (Ferrovac-E) absorbed only 20 ppm. Under non-irradiation conditions, the hydrogen contents varied over a wide range. The variations appear to be associated with large differences in the starting hydrogen levels and with hydrogen loss prior to analysis.

The corrosion rates under gamma irradiation were significantly inhibited. Cast steel coupons immersed in irradiated solutions were covered with deposits of a silicon oxide while pure iron maintained a shiny surface. On the other hand, the test performed under non-irradiation conditions caused severe corrosion. Currently the role of oxygen concentration and oxidizers formed under irradiation are being investigated to explain this phenomenon.

For the quantitative evaluation of hydrogen uptake, two types of permeation test cell were designed. A manometric method is being utilized in the gamma irradiation environment while an electrochemical method is being used for non-irradiation conditions. Preliminary data show an indication of radiolytic hydrogen permeation through a 1-mm thickness of steel after a few days' immersion.

PREVIOUS REPORTS IN SERIES

Container Assessment--Corrosion Study of HLW Container Materials, Quarterly Progress Reports, T. M. Ahn and P. Soo

October--December 1983, BNL-NUREG-34220
July--September 1983, BNL-NUREG-33940

CONTENTS

FIGURES

FIGURES (Continued)

TABLES

ACKNOWLEDGMENTS

The authors are grateful to Dr. K. S. Lee who designed the hydrogen permeation test cell during his visit to BNL as a visiting scientist. Mr. R. Sabatini carried out the scanning electron microscopy and Ms. S. Bennett and Mrs. M. McGrath prepared the manuscript.

1. INTRODUCTION

The objective of this program is to identify and evaluate some of the potential corrosion failure modes in low carbon steel which is the reference container material for high level waste packages to be emplaced in basalt repositories. Two main areas will be emphasized: one involves an evaluation of hydrogen assisted embrittlement effects, and the other is concerned with the measurement of hydrogen uptake in the presence of basaltic water and a gamma irradiation field. Radiation corrosion and stress corrosion cracking are also addressed. This report describes the results obtained in the second quarter of the fiscal year and is a continuation of the work reported in BNL-NUREG-34220.[1]

2. CHEMICAL ANALYSIS AND MICROSTRUCTURAL CHARACTERIZATION OF CAST LOW CARBON STEEL

Two types of low carbon cast steel (ASTM A216-Grade WCA) are being used in this study. For the tests on uniform corrosion and hydrogen uptake, the cast steel provided by Battelle Columbus Laboratory (BCL) was used. Pure iron (Ferrovac-E), from a BNL stockpile, was also used in these tests in order to help elucidate the mechanisms controlling corrosion and hydrogen uptake. Mechanical testing work was conducted on cast steel rods purchased from Axiom Machine and Foundry, Inc., NY. Chemical compositions of these materials are given in Table 1.

In addition to the microstructural analyses reported in the last progress report,[1] the microstructures of welded samples were characterized. Figure 1 shows the microstructure of welded cast steel provided by BCL. In the heat affected zone (HAZ), grains tend to recrystallize, and acicular martensite grains are formed in the fused zone. The cast steel rods were welded in a longitudinal direction. Figure 2 shows a cross section through the rod showing the microstructural variations in the welded zone. Again, acicular martensite is formed.

3. SLOW STRAIN RATE TESTING OF CAST LOW CARBON STEEL

CERT (constant extension rate test) testing was continued in this quarter using various environmental and sample microstructural conditions. Some of the previous tests were repeated for confirmation, and there was some reanalyses of previous results. Table 2 shows a summary of the CERT tests conducted. Besides the tests in aqueous and moisture environments, control data were obtained for air. These data were compared to the ASTM tensile requirements[2] for ASTM A216-Grade WCA steel at room temperature and high strain rates, which are given in Table 3. The test material properties fall within the limits of the requirements except for the total elongation. This may be attributed to the different testing conditions such as a higher temperature, a slower strain rate and a smaller gage length. Currently, tests at room temperature and fast strain rates are being conducted so that a more direct comparison may be made of test material mechanical properties and required ASTM values.

$Cu+Ni+Cr+Mo+V = 0.06+0.06+0.01 < 1$

$C+Mn/6+(Cr+Mo+V)/5+(Ni+Cu)/15$

$= 0.07+0.07+(0.06+0.01+)/5+(0.06+)/15$ Total Cr

$= 0.07+0.07+0.01+ \quad < 0.5$

Table 1. Composition of ASTM A216-Grade WCA cast steel for CERT tests (weight percent, balance is iron).

Element	ASTM A216-Grade WCA Specification (Maximum)(2)	BCL-Supplied A216-Grade WCA (coupon) beam	BNL A216-Grade WCA (rod) rod arm	New York Testing Laboratory Analysis of BNL cast steel	Ferrovac-E[c]
C	0.25[a]	0.18	0.09	0.07	0.003
Mn	0.70[a]	0.49	0.46-0.47	0.43	trace
P	0.04	0.004	0.0067-0.0070	0.001	
S	0.045	0.002	not determined	0.01	
Si	0.60	0.30	<0.2	0.10	faint trace
Residual Elements[b]					
Cu	0.30	0.006	0.29	--	trace
Ni	0.50	0.002	0.065	0.06	nil
Cr	0.50	0.007	0.059	0.06	nil
Mo	0.20	--	0.017	0.01	faint trace
V	0.03	0.000	<0.024	--	nil
Total residual elements[d]	1.00				
Al		0.10			
O					0.012
N					0.00018

[a]For each reduction of 0.01% below the specified maximum carbon content, an increase of 0.04% manganese above the specified maximum will be permitted up to a maximum of 1.10%.
[b]It is recognized that residual elements are unavoidable in steel, and, in the interest of uniform welding, the restrictions shown shall be complied with.
[c]Vacuum Metals Corporation Report.
[d]Not applicable if increased concentrations are required for weldability as specified in (a) and (b).

Figure 1. Microstructure of welded ASTM A216-Grade WCA cast steel supplied by Battelle Columbus Laboratory. The microstructure of base metal consists of ferrite (light area) and pearlite (dark areas). In the heat affected zone, recrystallization and martensite formation (acicular grains) are seen. In the fused zone, martensite is predominant.

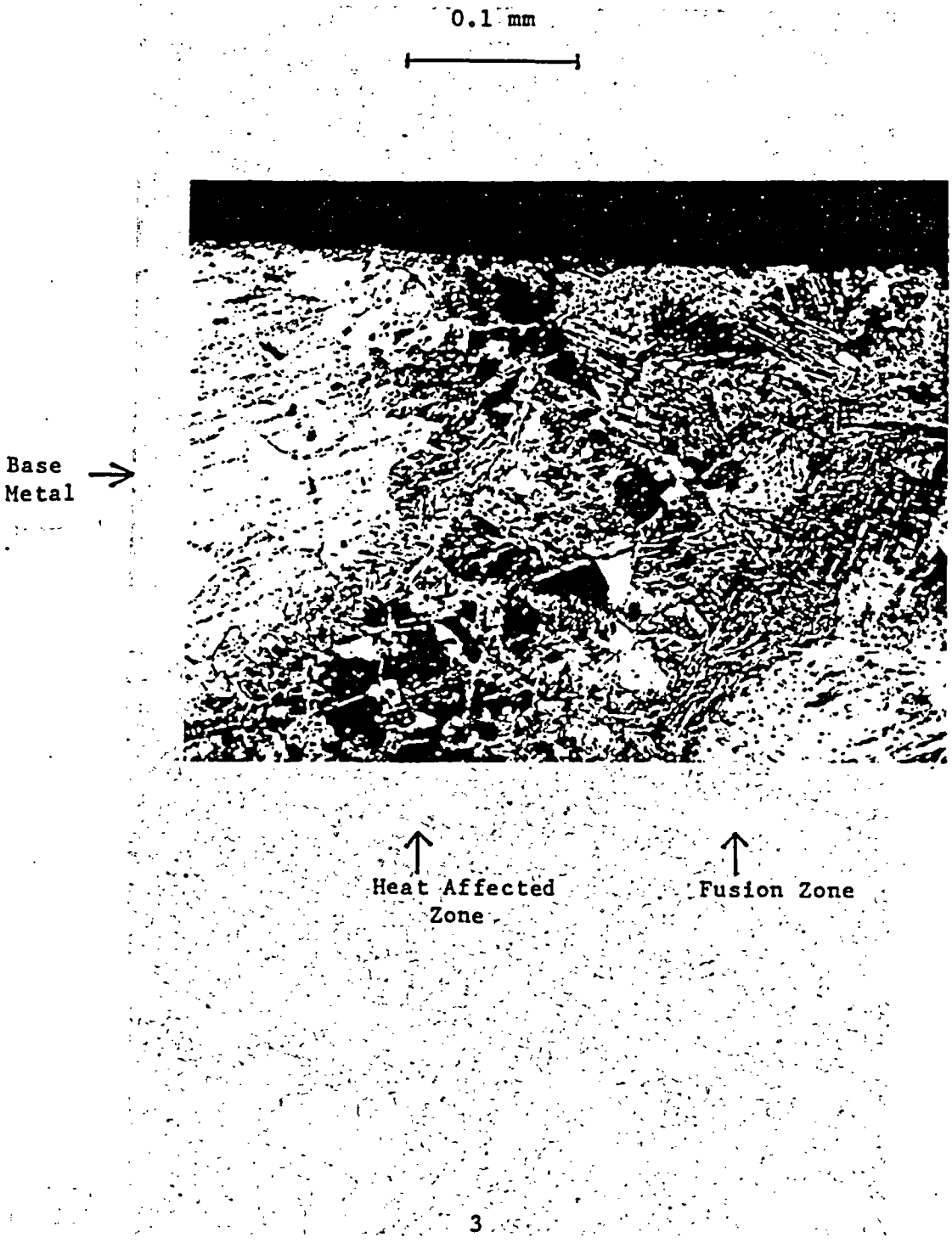

Figure 2. Microstructure of welded ASTM A216-Grade WCA cast steel for constant extention rate test (CERT) tests, (a) shows a cross section through the rod which was given a longitudinal weld pass, (b) shows the microstructure of base metal which consists of ferrite (light areas) and pearlite (dark area), (c) shows the microstructure of the heat affected zone. Acicular martensite and grain growth are observed, (d) shows the microstructure of the fused zone. Fusion was limited, and martensite formation, grain growth and recrystallization are observed.

(a)

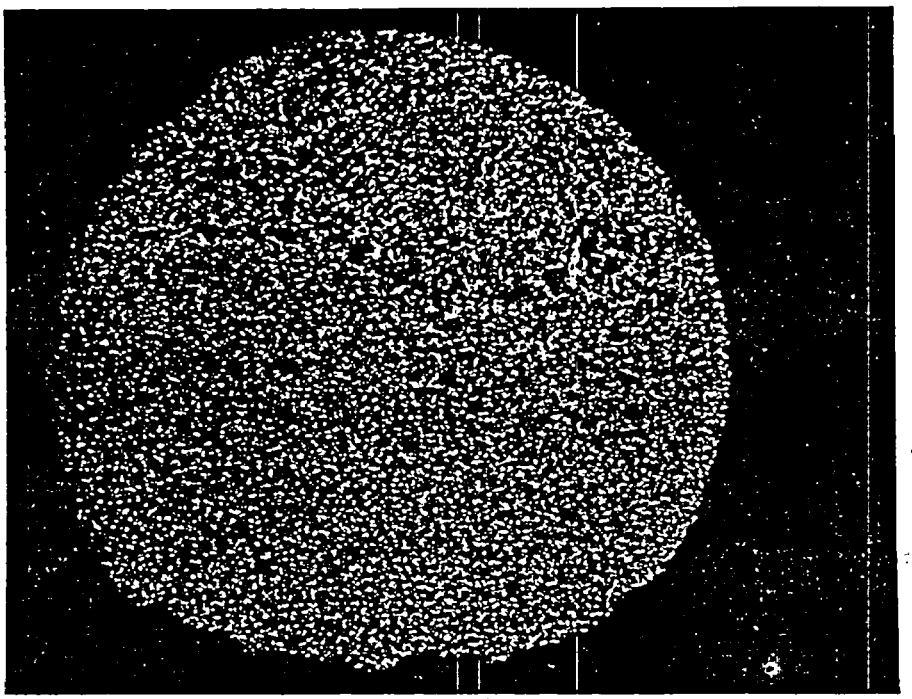

(b)

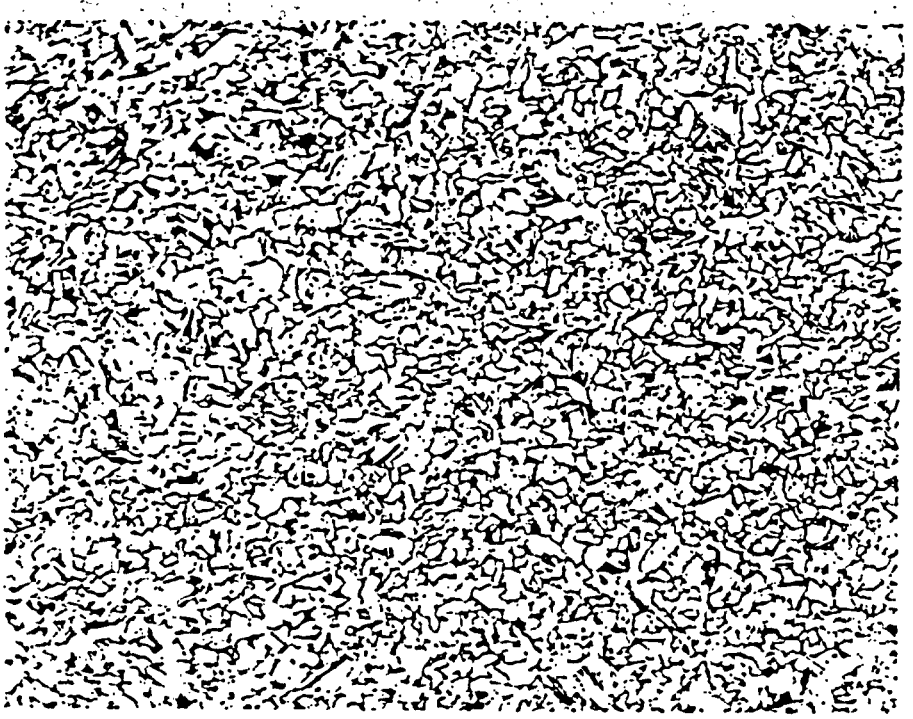

(c)

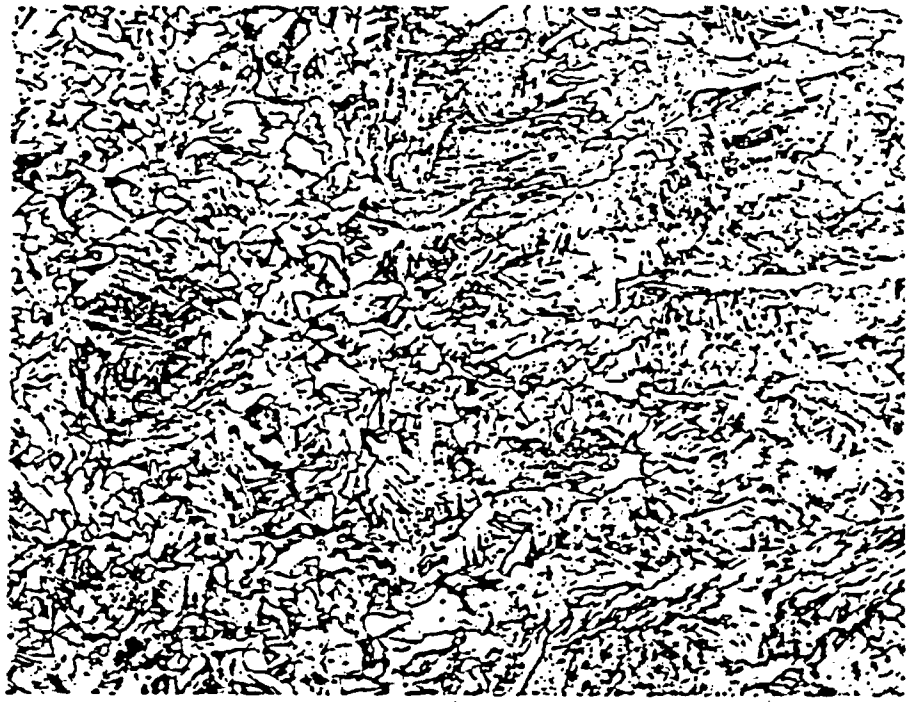

0.1 mm

(d)

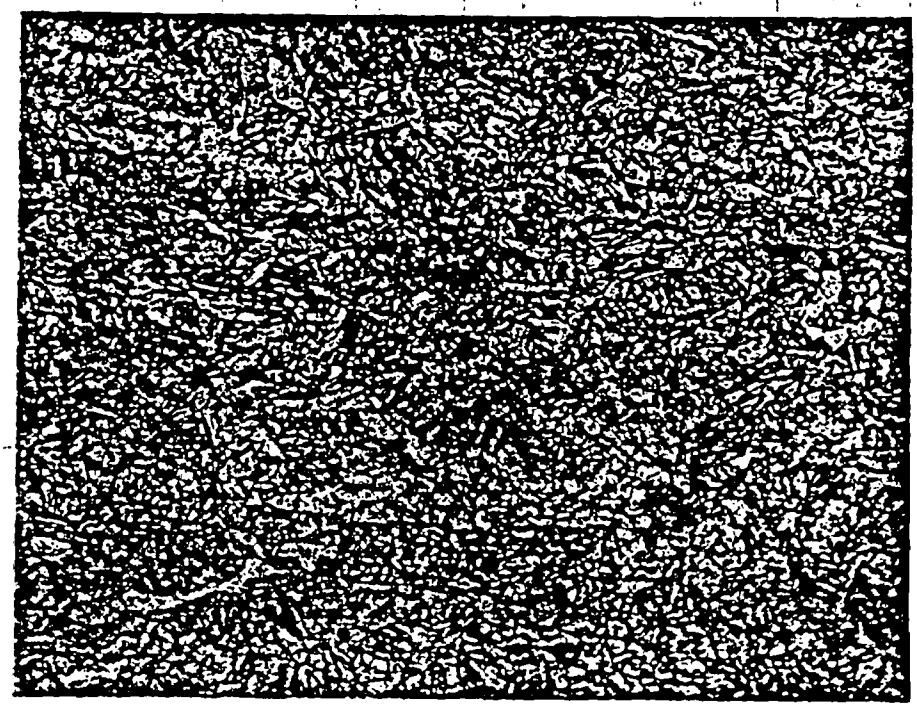

0.1 mm

Table 2

Results of ASTM A216-Grade WCA cast steel CERT tests conducted at 80-85°C in various environments.

Sample No	Test Environment	Temp. (°C)	Average[b] Strain Rate (sec^{-1})	Total[b] Elongation (%)	Reduction in Area (%)	0.2% Offset Yield Strength (MPa)	Tensile Strength (MPa)	Fracture Strength (MPa)	Final[d] Solution (pH)
SS1	Air	85	3.1×10^{-7}	19.0	58.0	330	561	439	
SS6	Air	80	3.0×10^{-7}	21.1	53.8	324	537	413	
SS2	Solution (open circuit potential)[a]	85	3.1×10^{-7}	21.7	48.2-50.4	383	578	462	10.0
SS16	Solution (open circuit potential)[a]	80	3.1×10^{-7}	17.6	41.3	346	504	397	4.6
SS8	Solution (anodic potential)[d]	80	3.9×10^{-7}	17.2	54.3	316	422	316	8.8
SS3	Solution (cathodic charging)[e]	85	3.1×10^{-7}	15.0-15.9	25.5 24.6	272	443	325	10.5
SS9	Solution and moisture	80	3.1×10^{-7}	20.5	48.4	308	504	373	
SS10	Moisture	80	3.4×10^{-7}	21.7	53.3	324	558	438	
SS7	Moisture with HCO_3^-	80	2.8×10^{-7} 3.1×10^{-7}	16.4 18.5	29.1	323 391	538 562	448 474	
SS11 (weld)	Air	80	2.7×10^{-7}	21.1	52.9	373	580	457	
SS12 (weld)	Solution (open circuit potential)[a]	80	3.2×10^{-7}	22.9	47.2	327	553	430	

[a]Open circuit potential in air saturated solution at testing temperatures (typically -0.57 to -0.58 volt SCE).
[b]Gage length of 1.27 cm.
[c]Initial solution pH is 9.51 at room temperature.
[d]-0.2 volt SCE.
[e]-1.4 volt SCE.

1 MPa = 145 psi

Table 3. Tensile requirements for ASTM A216-Grade WCA cast steel at room temperature and a standard strain rate.

Minimum Yield Strength[a] (MPa)	Tensile Strength (MPa)	Minimum Elongation[b] in 5 cm (%)	Minimum Reduction in Area (%)
205	415-585 = 60-85 ksi	24	35

[a]Determined by either the 0.2% offset method or the 0.5% extension-under-load method.

[b]When ICI test bars are used in tensile testing as provided for in specification A703 (ASTM), the gage length to reduced section diameter ratio shall be 4 to 1.

In the test carried out in 7-times concentrated Grande Ronde basaltic water for various applied potentials (specimens SS2, SS3, SS8 and SS16), several interesting observations were made. At open circuit potential (-0.57 to -0.58 volts SCE at 80°C at the beginning of the tests) a small decrease in ductility seems to occur, compared to air-tested samples. Figure 3 shows fractographs for samples SS2 and SS16. Small voids (or pits) are seen surrounded by areas showing ductile deformation. Specimen SS16 showed some side surface cracking which could be indicative of stress-corrosion; specimen SS2, however, did not show this effect. The final pH of the sample SS16 test solution was found to have decreased to 4.6. The reason for this is not known at the present time.

Specimen SS8, deformed under an applied anodic potential of -0.2 volts SCE, also showed a loss in mechanical integrity compared to air-tested samples. There was a small loss in ductility, tensile strength and fracture strength, which could be connected with severe pitting and/or void formation on the specimen and fracture surfaces (Figures 4a, 4b, and 4c). Under the anodic potential used, the specimen surface was found to be heavily etched (Figure 4d).

Specimen SS3, tested under a cathodic potential of -1.4 volts SCE, displayed the largest losses in ductility and strength, as reported previously.(1) There was severe side surface cracking and the fracture surface showed planar facets surrounded by regions which had undergone ductile deformation (Figures 5a and 5b).

Figure 3. Fractographs for ASTM A216-Grade WCA steel CERT specimen tested in 80°C concentrated basaltic groundwater at a strain rate of 3.1 x 10^{-7}/s, (a) specimen side surface cracking, (b) voids and/or pits on fracture surface and (c) some flat facets on fracture surface.

(a)

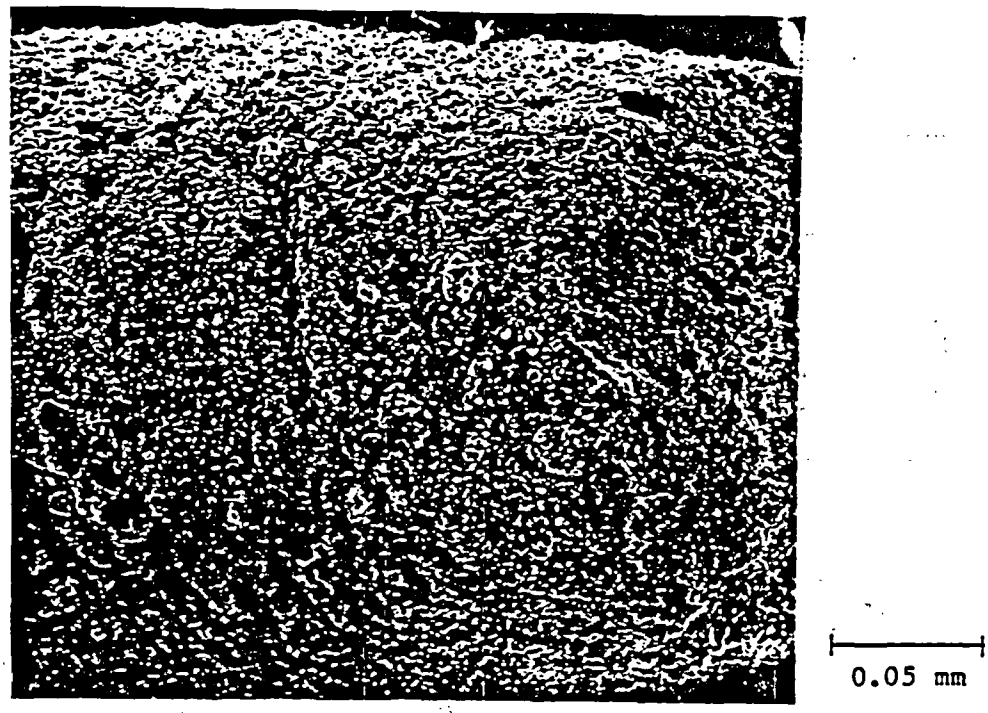

(b)

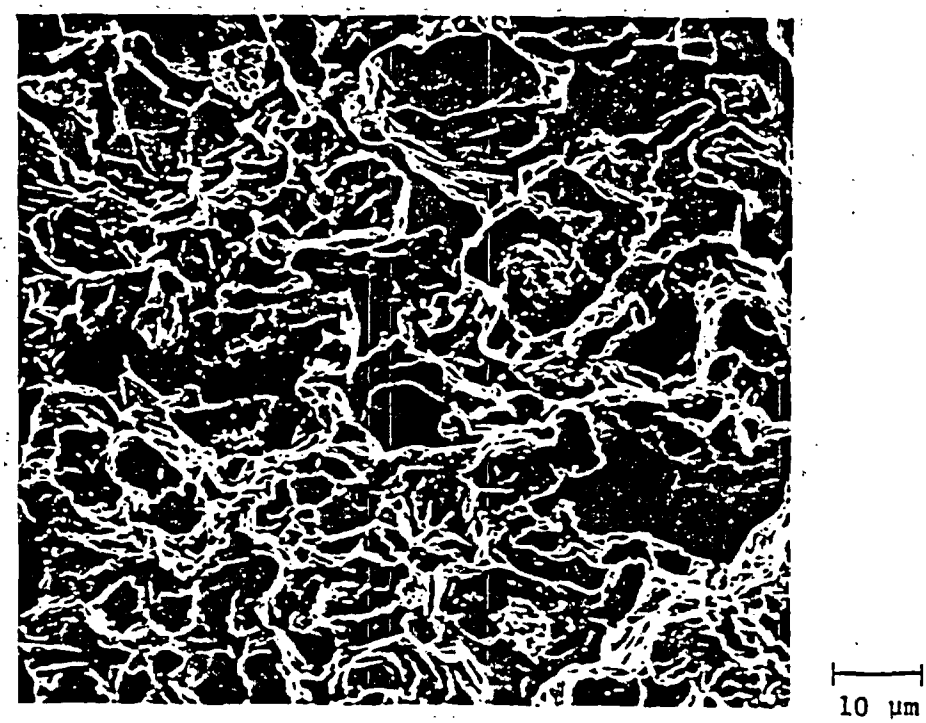

(c)

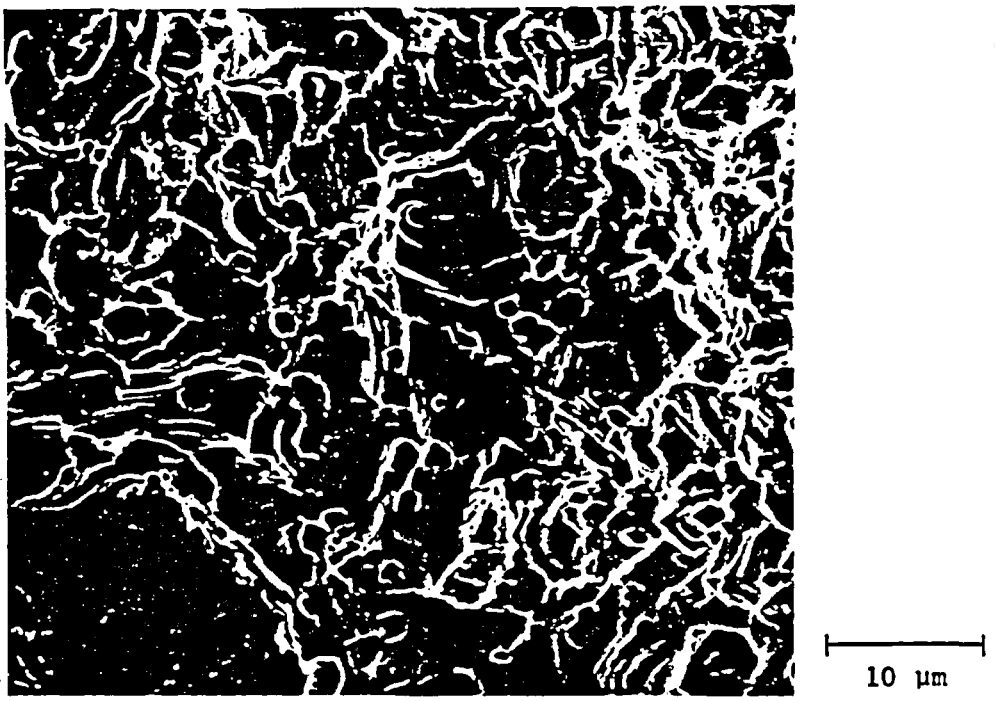

Figure 4. Fractographs for ASTM A216-Grade WCA steel CERT specimen tested at 80°C in concentrated basaltic groundwater at a strain rate of 3.9 x 10^{-7}/s. The sample was anodically polarized at -0.2 V SCE, (a) large voids and/or pits on fracture surface (low magnification), (b) large voids and/or pits on fracture surface (high magnification), (c) pits on specimen side surface, and (d) etching on specimen side surface.

(a)

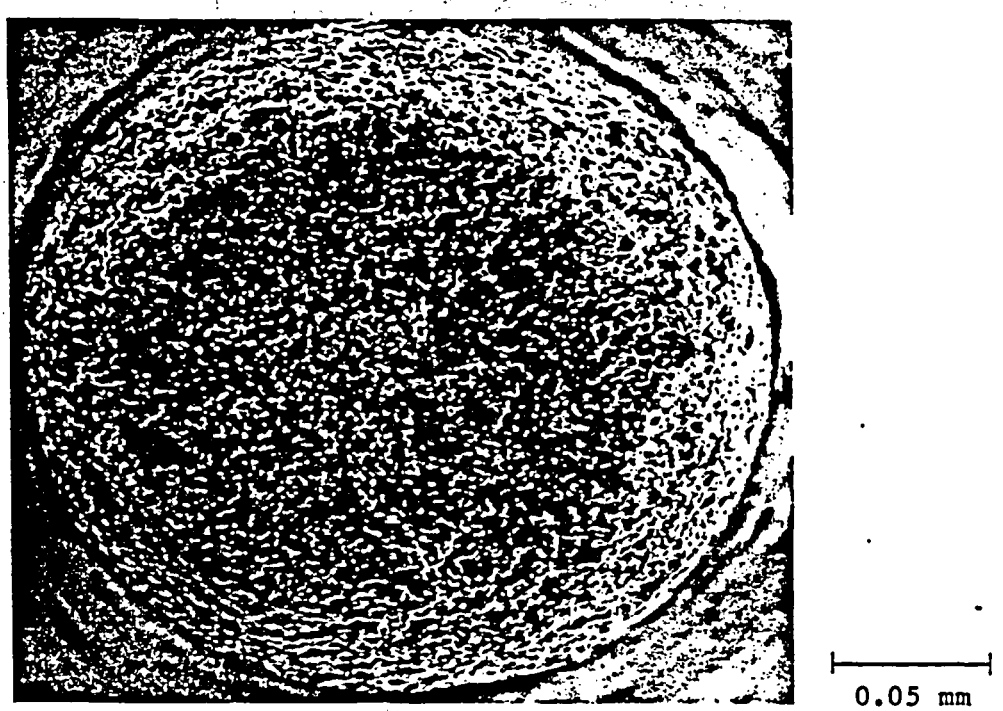

(b)

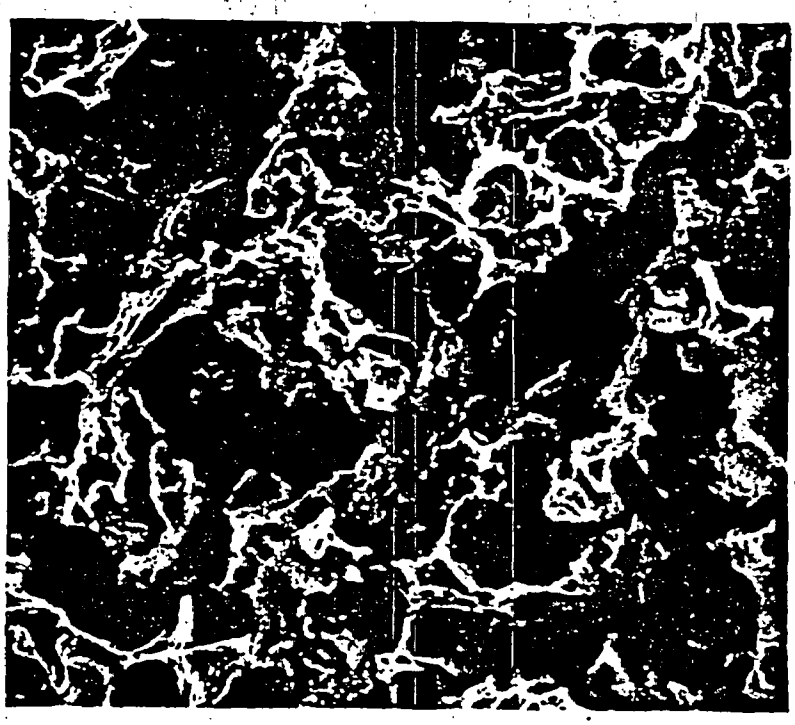

0.05 mm

(c)

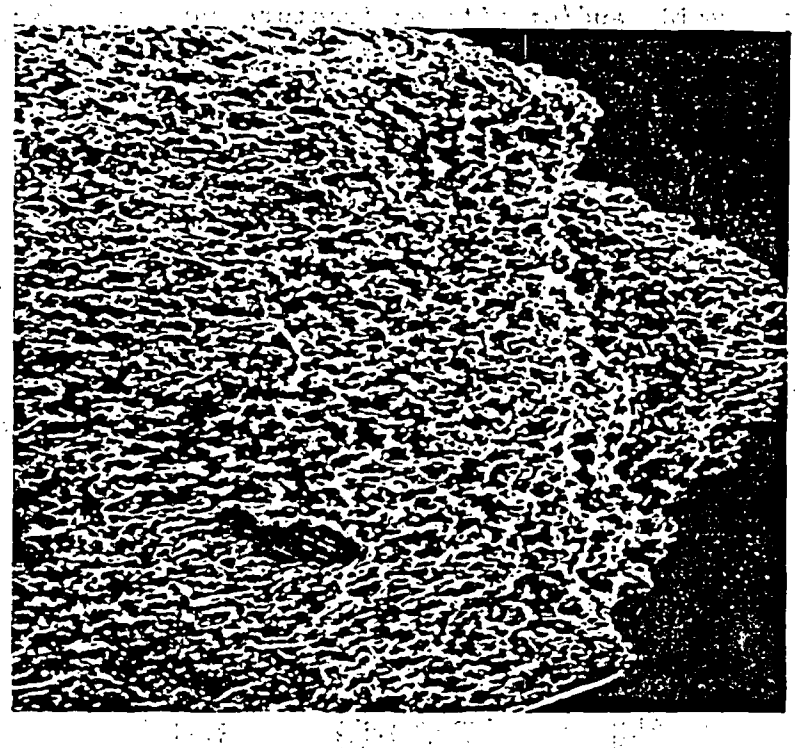

0.05 mm

(d)

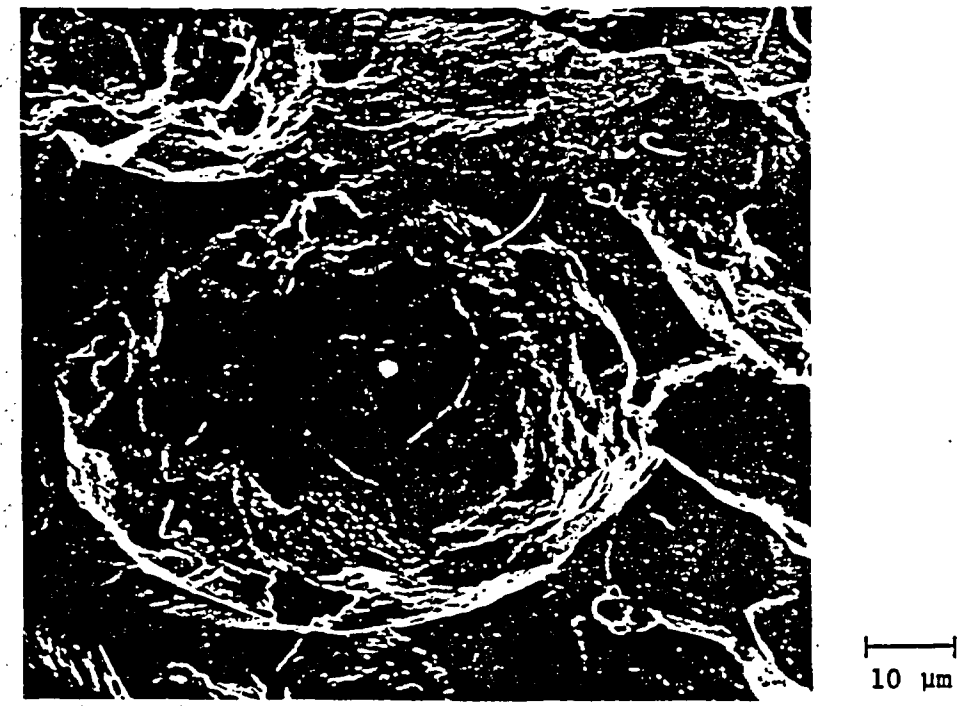

Figure 5. Fractographs for ASTM A216-Grade WCA steel CERT specimen tested in 85°C concentrated basaltic groundwater at a strain rate of 3.1 x 10^{-7}/s. The sample was cathodically polarized at -1.4 Volt SCE, (a) low magnification view, (b) severe specimen side surface cracking, (c) flat fracture regions.

(a)

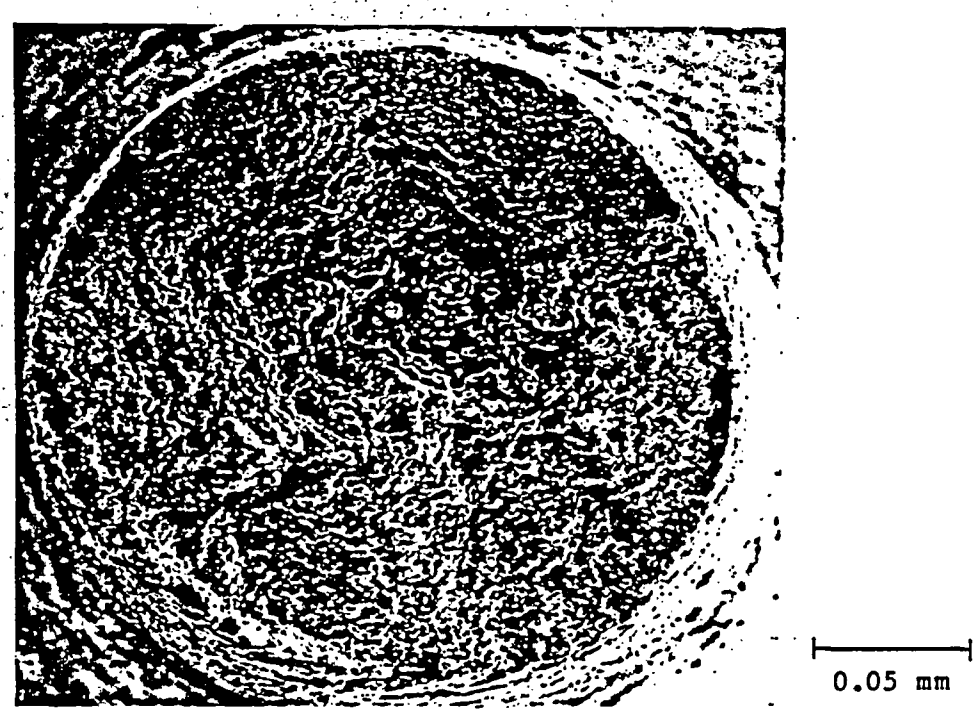

(b)

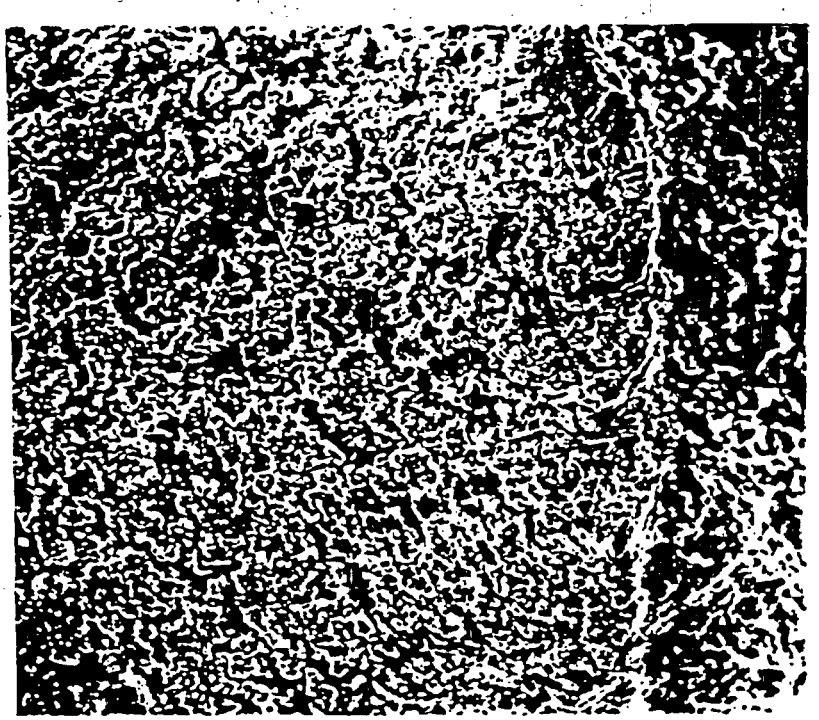

(c)

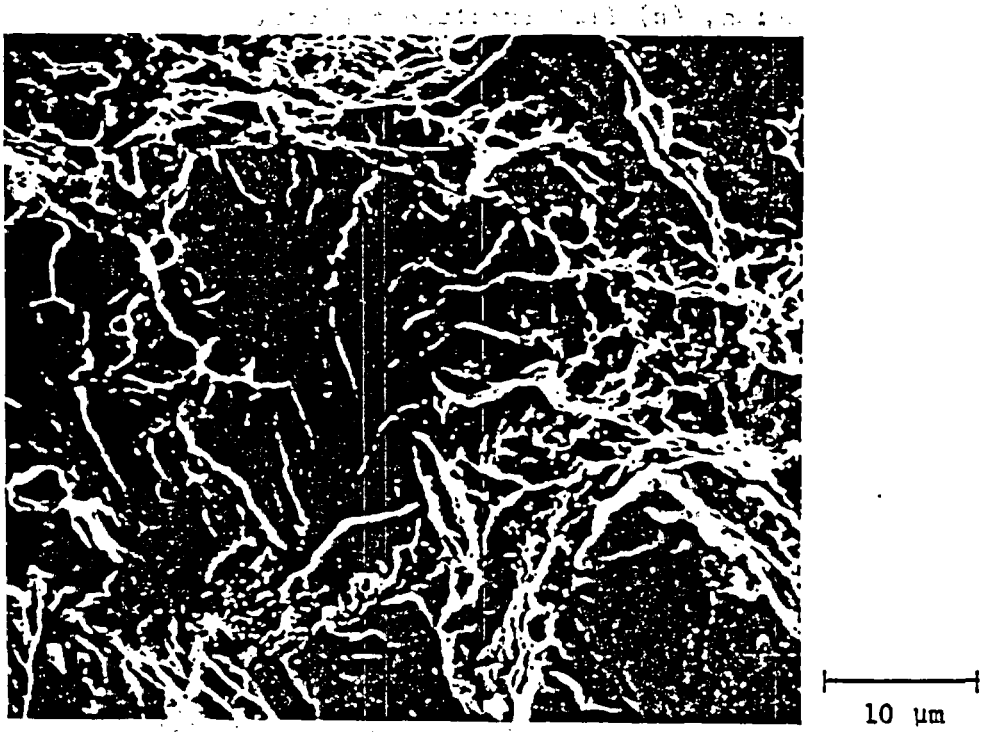

Another category of tests was performed in the moisture/air environment above the concentrated basaltic water (specimens SS7, SS9, and SS10). The test on sample SS9 was started under aqueous conditions but because of an inadvertant loss of solution, it was completed in a water vapor/air environment. The observed losses in ductility and strength (Table 2) prompted a more detailed analysis of tests in the vapor phase alone (specimens SS7 and SS10). Figure 6 shows a fractograph for specimen SS10 tested in the moist air above the regular concentrated basaltic water. Large flat fracture regions are seen surrounded by areas of ductile deformation. No indication of surface cracking was observed in this sample. In specimen SS9, which was exposed to water and water vapor, the fractograph shows numerous coalescing crystallographic facets. These may be indicative of stress corrosion effects.[3]

Figure 6. Fractograph of ASTM A216-Grade WCA steel CERT specimen tested at 80°C in moist air above concentrated basaltic groundwater at a strain rate of 3.4×10^{-7}/s, showing flat surface facets.

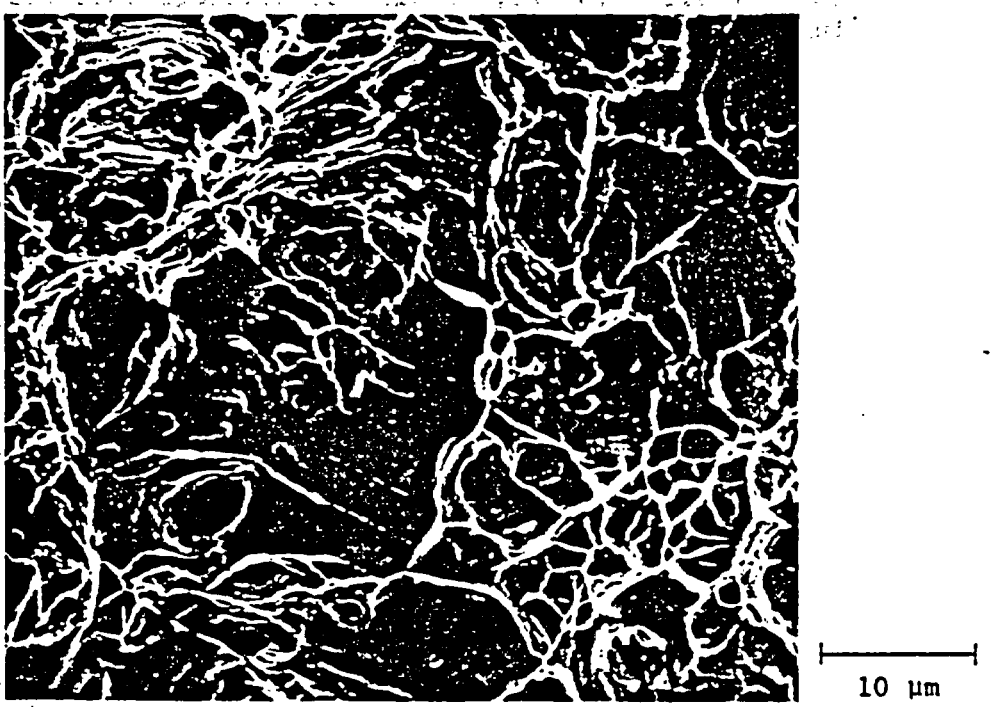

In a basalt repository it is expected that HCO_3^- and CO_3^{-2} ions will exist in equilibrium.[4] To evaluate high concentrations of these ions on corrosion, a test solution was made in which 1.0 g/L of $NaHCO_3$ was added to the standard concentrated basaltic water. Specimen SS7 was tested in the vapor above the solution. The specimen showed a large loss in ductility

although the strength did not show much change (Table 2). Very severe side surface cracking was observed, indicative of stress-corrosion. Most of the fracture surface showed ductile deformation with some discrete pit or void type features (Figures 8a, 8b, and 8c).

A comparison of the ductilities obtained for specimens SS7 and SS10, which were both tested in the moist air environment above the heat solutions, shows that specimen SS7 was more severely affected. The only difference in the two tests was the addition of $NaHCO_3$ to the solution for specimen SS7. It is not known if volatile constituents from the groundwater affect the mechanical behavior in the moist air test environment. At this time we have no explanation for the loss of ductility in specimen SS7 which results from the $NaHCO_3$ addition to the heated solution beneath the test specimen, but it could be caused by a CO_3^{-2}/HCO_3^- rich water film on the sample.

Figure 7. Fractograph of ASTM A216-Grade WCA steel CERT specimen tested in 80°C concentrated basaltic groundwater and moist air at a strain rate of 3.1×10^{-7}/s, showing crystallographic features indicative of stress corrosion.

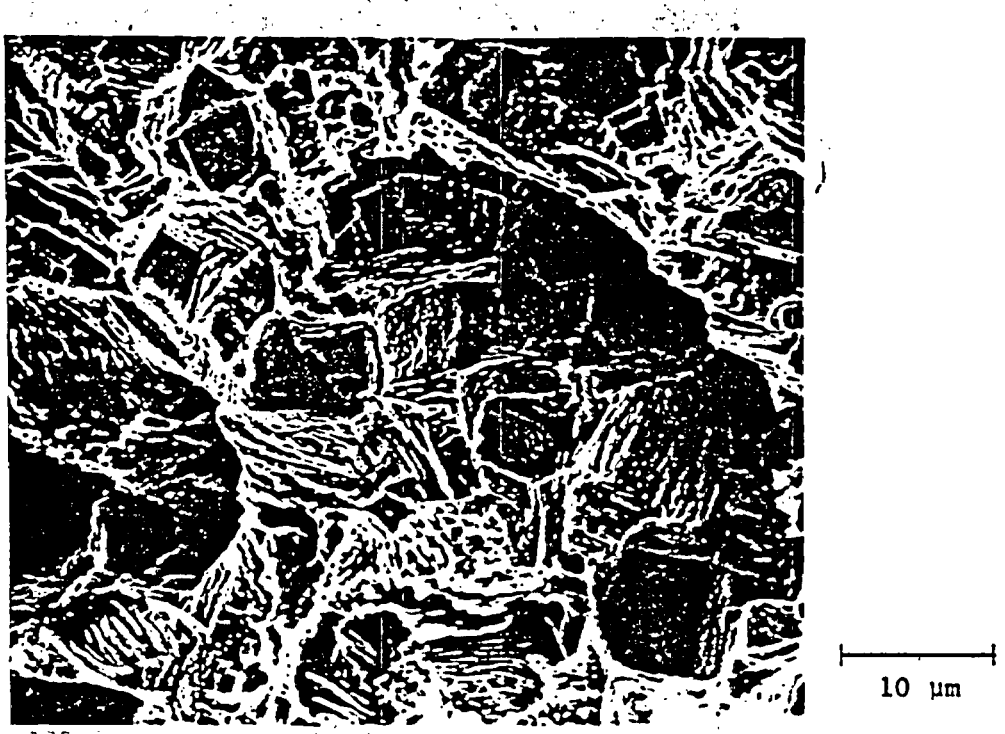

Figure 8. Fractographs for ASTM A216-Grade WCA steel CERT specimen tested at 80°C in moist air above concentrated basaltic groundwater containing HCO_3^- at a strain rate of 2.8×10^{-7}/s, (a) severe specimen side surface cracking, (b) voids/pits on fracture surface, (c) crystallographic features indicative of stress corrosion.

(a)

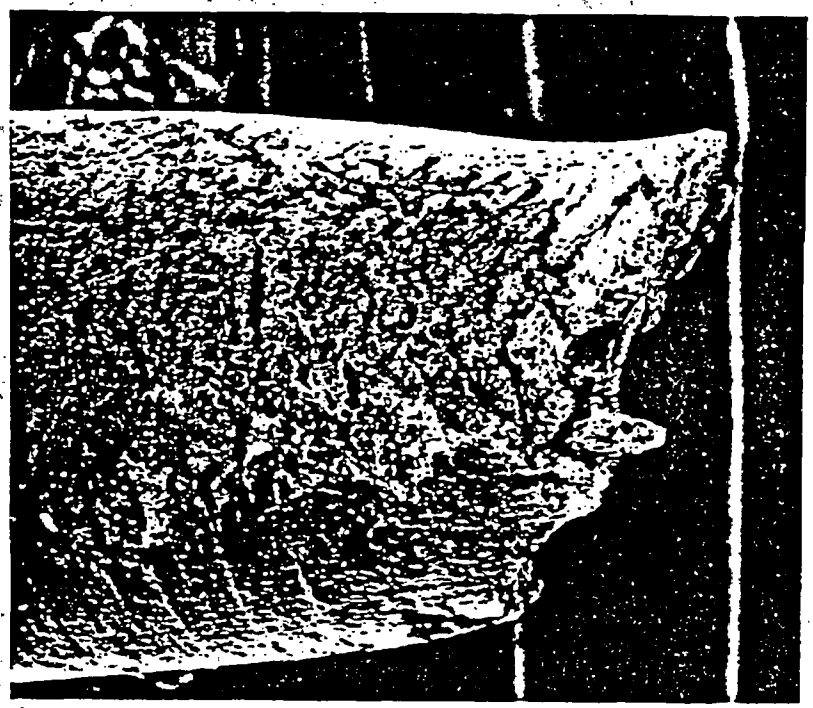

(b)

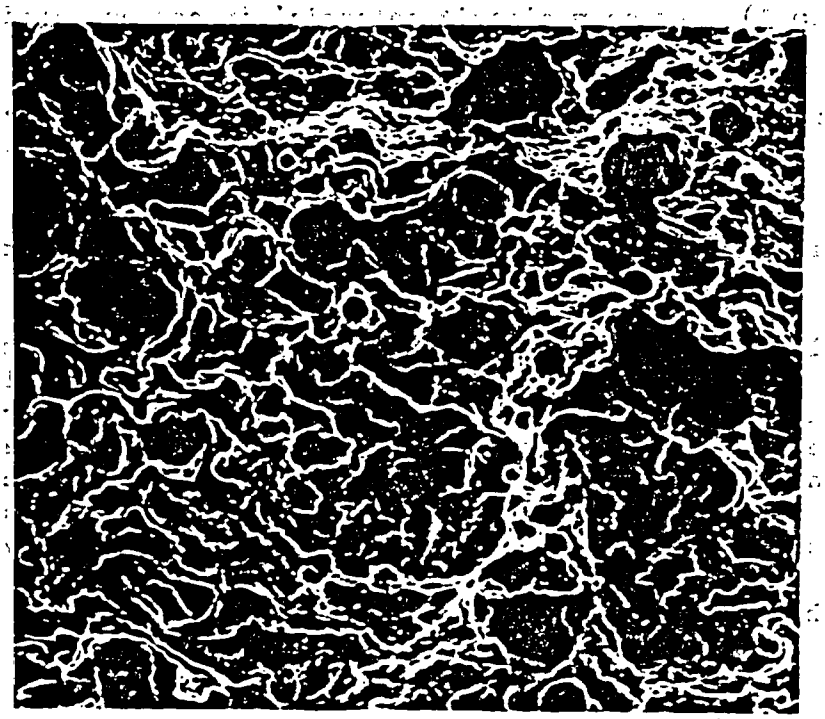

(c)

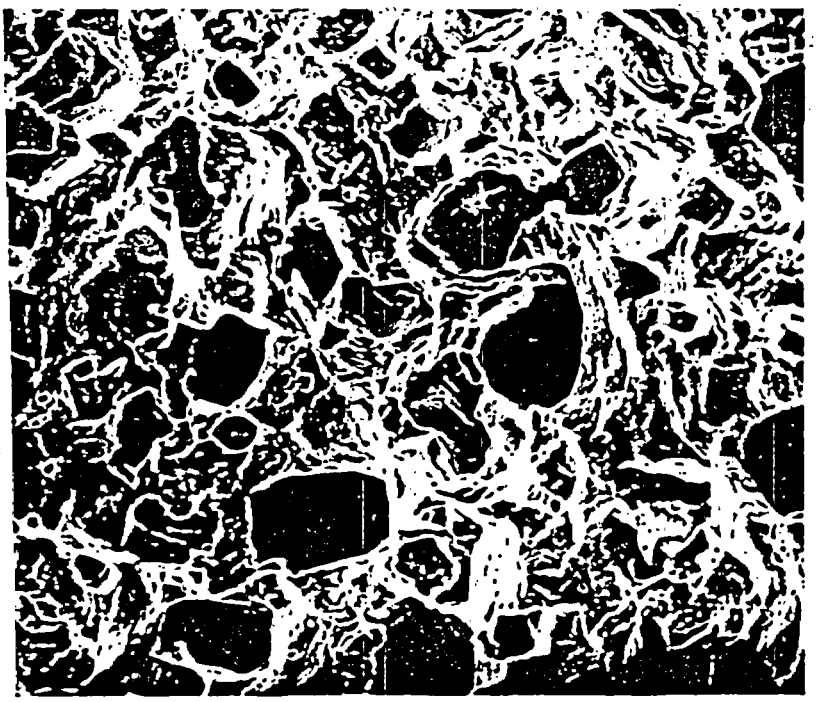

The final category of tests (sample numbers SS11 and SS12) was performed using samples containing a partial-penetration longitudinal weld bead. The microstructure of a specimen cross section is shown in Figure 2. The air test results (SS11) are similar to the results for nonwelded samples (SS1 and SS6) except for a slightly increased strength, probably due to the martensite formed (Figure 2). At open circuit potential in concentrated basaltic water, there was no environmental degradation. However, the fracture surface of the sample shows pit-type features (Figure 9). This type of feature was only observed in nonwelded samples when they were anodically polarized. The slight decrease in strength compared to air-test results seems to be due to the presence of electrochemical effects.

A summary of the fractographic studies for all CERT tests is given in Table 4.

In the last quarterly progress report,[1] a simple estimation was made of the effective hydrogen gas pressure due to the cathodically polarized condition at a known overpotential. The calculated fugacity was far too high compared to expected repository conditions. We examined more relevant literature[5,6] which showed that the effective fugacity is the activity of hydrogen atoms adsorbed on the sample surface. To correlate this value to the hydrogen pressure build-up in the repository, it is necessary to incorporate effects such as adsorption kinetics of hydrogen atoms on the steel surface. Currently, this study is under way.

Figure 9. Fractographs for welded ASTM A216-Grade WCA steel CERT specimen tested at 80°C in concentrated basaltic groundwater at a strain rate of 3.2×10^{-7}/s, (a) fracture surface at low magnification (b) voids/pits on fracture surface (high magnification).

(a)

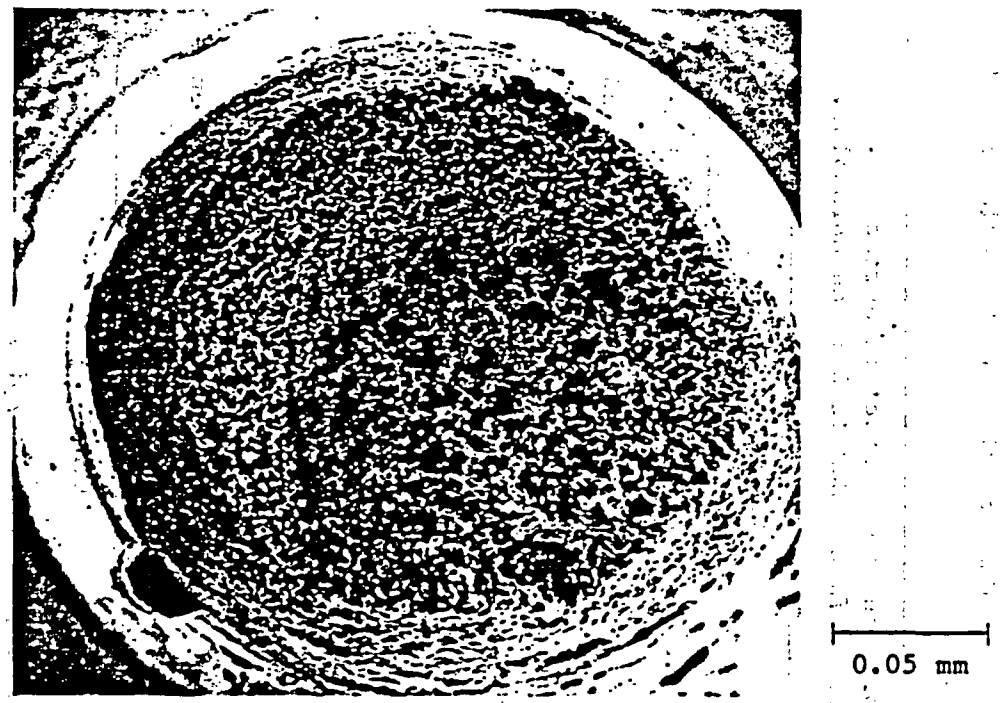

(b)

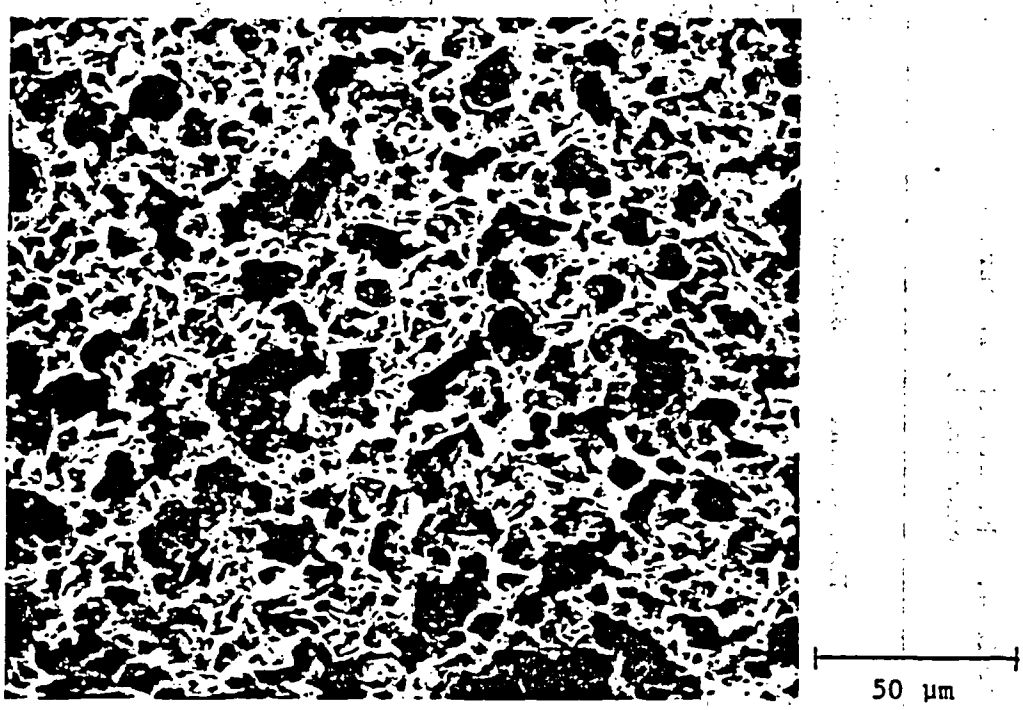

Table 4. Summary of fracture surface morphology after CERT testing of ASTM A216-Grade WCA cast steel.

Environment	Surface Cracking	Voids/pits on the Fracture Surface	Fracture Surface and Sample Surface Morphology
Air.	No	No	Dimpled
Solution	Yes (slight)	Yes (moderate)	Dimpled, some planar regions
Solution[a] (cathodic charging)	Yes (severe)	No	Planar and dimpled regions
Solution[a] (anodic charging)	No	Yes (severe)	Voids/pits cover fracture surface, surface etching seen
Moisture	No	Yes (slight)	Dimpled, some planar regions
Moisture with HCO_3^-	Yes (severe)	Yes (severe)	Voids/pits cover surface, SCC indication on sample surface
Moisture and solution	No	Yes (slight)	Dimpled, SCC indication on sample surface
Air (weld)	No	No	Dimpled
Solution (weld)	No	Yes (severe)	Voids/pits cover surface

[a]Cathodic and anodic potentials are with respect to air saturated solutions at the test temperatures.

4. HYDROGEN UPTAKE IN CAST LOW CARBON STEEL

In order to determine the rate of hydrogen uptake, specimens of the cast steel provided by BCL and Ferrovac-E were immersed in the concentrated basaltic water at 150°C under a gamma dose rate 1.3×10^6 rad/h for two months. The details of the experimental procedures were given in the previous quarterly progress report.[1] The two-month test was repeated and the results are shown in Table 5. In the first run, the specimens were exposed to air for about three hours before hydrogen analysis. Apparently, there was a significant loss of the absorbed hydrogen during this period. Therefore, the results from the second run are more reliable, since the samples were quenched quickly in liquid nitrogen after removal from the gamma pool. The results from run 2 show very high concentrations of hydrogen for as-received cast steel and welded cast steel while those for Ferrovac-E are relatively low. There are two possibilities to explain the observed high hydrogen concentrations. The first is that there is a large hydrogen uptake in salt deposited on the sample surface (mainly a silicon oxide as will be described in the next section). The second is the possible presence of hydrogen blistering[5] formed by the absorbtion of large amounts of hydrogen. Currently, metallographic techniques are being utilized to study these possibilities.

Figure 10 shows the pressure build up during the two-month immersion test under gamma irradiation. These may be compared with data obtained in a prior run, reported previously.[1] Again the pressure change shows an initial fast increase as the temperature of the capsule is raised to 150°C after which it tended to be stabilized. These results are quite consistent with those obtained by Gray[8] who irradiated normal strength Grande Ronde basaltic water at 150°C in the presence of an iron sample. Table 6 shows results of chemical analyses of gas samples collected after radiolysis of the concentrated basaltic water. The reproduciblity of the data is quite satisfactory. Apart from the N_2, originally present in the air cover gas, the main radiolytic product is hydrogen. The oxygen level is slightly less than the anticipated value, possibly indicating that it has reacted with constituents in the groundwater, as will be described in the next section, or with the metal samples. A significant quantity of CO_2 is also present and possibly originates from the decomposition of Na_2CO_3 by radiation effects.

Tests were also conducted to determine hydrogen uptake in the test materials, under non-irradiation conditions (Table 7). There was considerable variation in the data for the two runs made, with relatively low hydrogen levels in the run 2 specimens. This was possibly caused by extended exposure of the samples to room temperature conditions prior to analysis. No systematic variation in hydrogen levels could be found for welded and non-welded materials, nor in deformed and undeformed samples. Since the scatter in the data could be caused by variations in the hydrogen concentrations prior to the corrosion tests, samples of the starting materials were also analyzed for hydrogen using vacuum extraction techniques at 900-950°C. Table 8 shows that as-received steel from BCL contains 22.3 ppm of hydrogen whereas welded BCL steel and Ferrovac-E each contained less than 0.5 ppm. The result for pure iron is expected, and the welded steel most likely suffered hydrogen loss

during the high temperature welding process. A comparison of the data in Tables 7 and 8, therefore, indicates that welded steel and Ferrovac-E do in fact pick up hydrogen, to some extent, during aqueous corrosion. In the case of as-received steel, however, it is difficult to draw such a conclusion since there is a possible problem associated with large variations in the initial hydrogen level. The high hydrogen levels for as-received steel in run 1 (Table 7) may be an indication of a very high initial gas concentration. More data are needed to clarify this point.

Table 5. Hydrogen content of ASTM A216-Grade WCA steel and Ferrovac-E specimens exposed to concentrated basaltic groundwater at 150°C under a gamma dose rate of 1.3×10^6 rad/h for two months.

Material	Concentration (ppm by weight)	
	Run 1[a]	Run 2[b]
Ferrovac-E	c	20
As-received cast steel	19	549
Welded cast steel	10	215

[a]The specimens were exposed to air for about three hours before hydrogen analysis.
[b]The specimens were stored in liquid nitrogen before hydrogen analysis.
[c]Not determined.

Table 6. Chemical analysis of the gas samples collected after gamma radiation of concentrated basaltic water/metal systems at 150°C for two months. The gamma dose rate was 1.3×10^6 rad/h.

Gas	Concentration (mol %)	
	Run 1 (Ref. 1)	Run 2
H_2	44.2	37.3
N_2	43.1	49.6
O_2	3.86	8.2
CO_2	7.5	2.1
H_2O	0.76	0.53
Ar	0.57	0.63
CO	---	1.53
CH_4	---	0.12

Figure 10. Gas pressure changes during gamma irradiation of concentrated basaltic water systems at 150°C for two months. The dose rate was 1.36×10^6 rad/h.

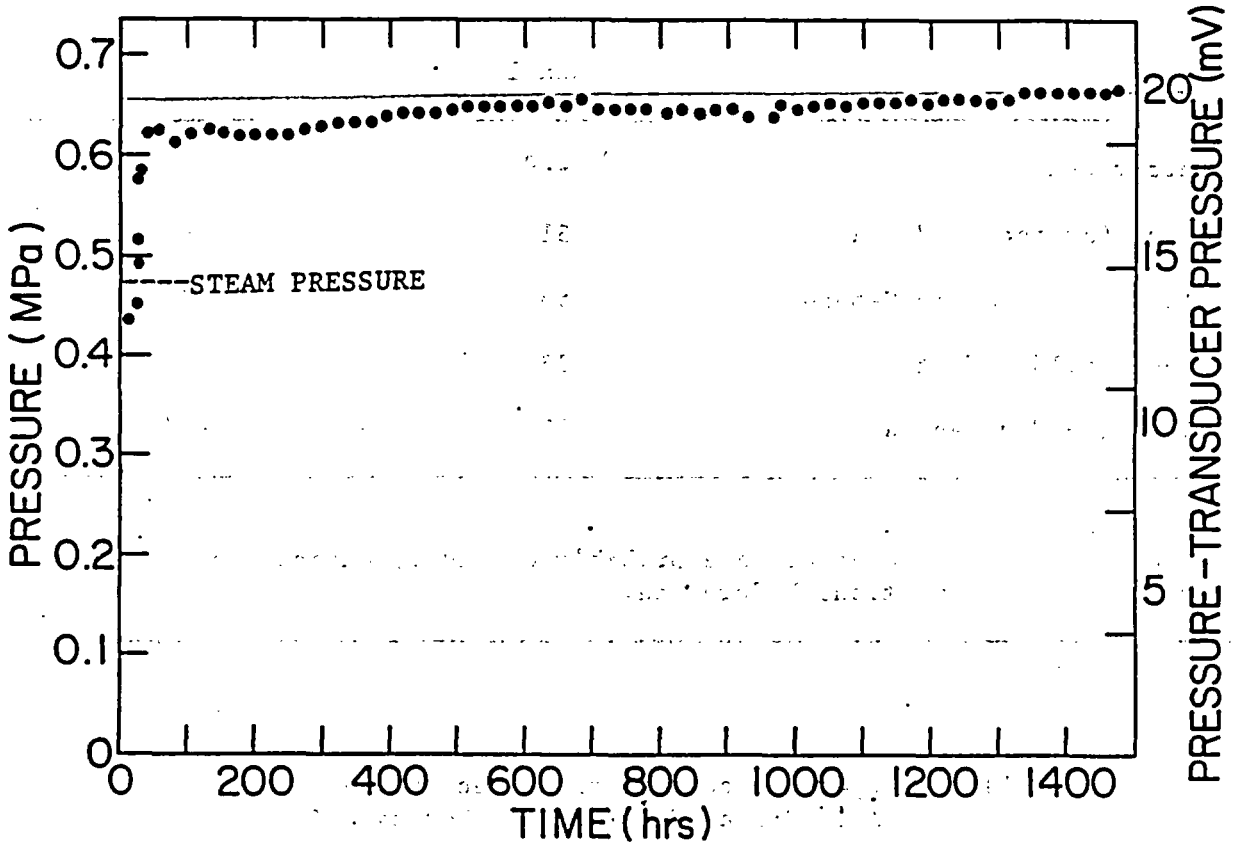

150°C
= 302°F

69 psia
$= 69 \times 10^{-3}$ Ksi $\times$ 6.895

Table 7. Hydrogen concentrations of ASTM A216-Grade WCA steel and Ferrovac-E specimens exposed to concentrated basaltic groundwater at 150°C for two months. The specimens were stored in liquid nitrogen before hydrogen analysis.

Specimen Type	Concentration (ppm by weight)	
	Run 1	Run 2[b]
Ferrovac-E	--[a]	4
Steel (as-received flat)	31	6
Steel (as-received U-bend)	53	5
Steel (welded flat)	23	15
Steel (welded U-bend)	10	--[a]

[a]Not determined.
[b]Low values for hydrogen content were probably caused by extended exposure to room temprature conditions before analysis.

Table 8. Hydrogen content of as-received ASTM A216-Grade WCA steel and Ferrovac-E.

Type	Concentration (ppm by weight)
As-Received Steel	22.3
Welded Steel	<0.5
Ferrovac-E	0.4

5. UNIFORM CORROSION AND RADIATION CORROSION OF CAST LOW CARBON STEEL

Two sets of samples were immersed for two months in concentrated basaltic water at 150°C: one set with and the other set without gamma irradiation as described in the previous quarterly progress report.[1] The samples consisted of flat coupons (welded steel, nonwelded steel and nonwelded Ferrovac-E) and U-bend specimens (non-welded steel and welded steel). These tests are duplicates of prior work to check reproducibility.

Under gamma irradiation, very little uniform corrosion was observed. Most of the surface area on the cast steel was covered with a white layer which had probably precipitated from the solution. The Ferrovac-E sample surface was free of deposits and retained its initial surface polish. The precipitates on the steels were analyzed by x-ray microprobe analysis (EDAX system attached to a scanning electron microscope) and found to be composed mainly of silicon and oxygen. Figure 11 shows an oxygen map and the Si peak obtained in the analysis. There was also an indication of traces of Ca, Na, Cr, Fe, Cl depending on the position of the deposited salt. While the majority of the Ferrovac-E surface was shiny, there was a small area of attack, usually in the area adjacent to the glass spacer. In this area, the corrosion product was a shiny black color and showed surface cracking. Also, deep pits were observed in this area. Figure 12 shows the corrosion product and pits in this area.

Welded and nonwelded steel samples did not show any significant difference in behavior. The majority of the sample surface areas were covered with the precipitate, and only small areas adjacent to the glass spacers, or the inner part of a U-bend specimen showed preferential attack. Typically, such attack was accompanied by pit marks and the shiny black corrosion product, as shown in Figures 13 and 14. When the precipitate was removed by scratching, the underlying metal was usually etched, showing the grain structure, as shown in Figures 13 and 14. In some cases, the etched area is also pitted (Figure 14-a). Apparently, the metal area is attacked by an acid, formed either by solution radiolysis (recombination of gases) or by solution hydrolysis of compounds such as dissolved $MgCl_2$. In U-bend specimens the area beneath the tightening bolt did not show any attack. This result is contrary to the observation of corrosion under the glass spacers.

In contrast to the steel specimens subjected to gamma irradiation, unirradiated specimens showed a thick dark brown layer of rust on the surface. An SEM micrograph of the specimen cross-section shows that the thickness of the oxide layer varies from a few microns to several tens of microns (Figure 15). In the last quarterly progress report[1], some pitting was also reported but the present samples did not show this effect. Apparently, pitting seems to be the initial penetration mode, and subsequent pit coalescence gives a more uniform corrosion. Currently, the corrosion rates are being measured by removing the rust formed.

Figure 11. Irradiation corrosion results for ASTM A216-Grade WCA cast steel exposed for two months to concentrated basaltic groundwater at 150°C and a gamma dose rate of 1.36×10^6 rad/h for two months, (a) SEM micrograph of a flake from a surface precipitate, (b) an oxygen map from EDAX probe, (c) EDAX probe result showing silicon to be a major constituent. Traces of Na, Ca, Cl, Cr and Fe were also detected.

(a)

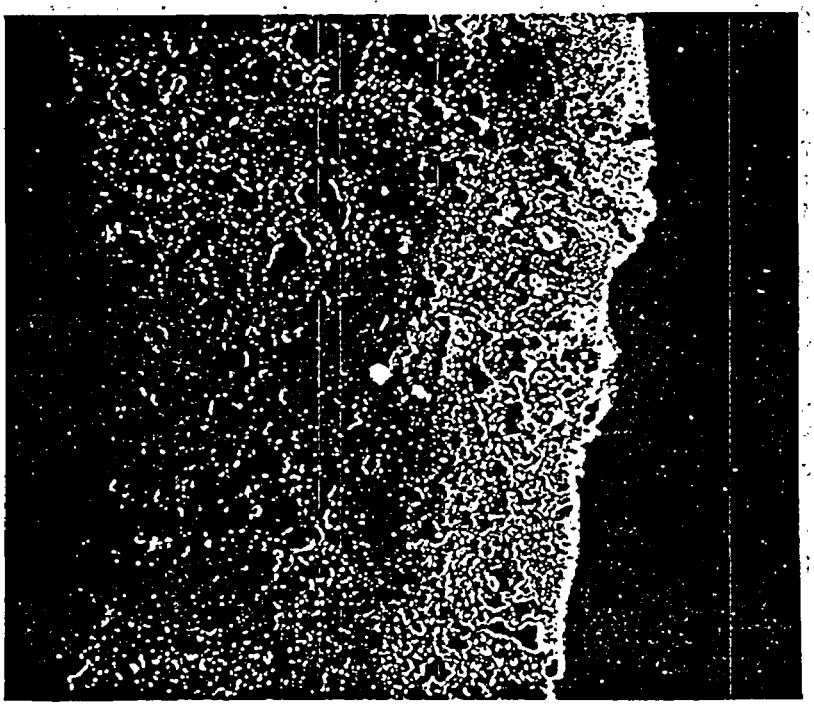

(b)

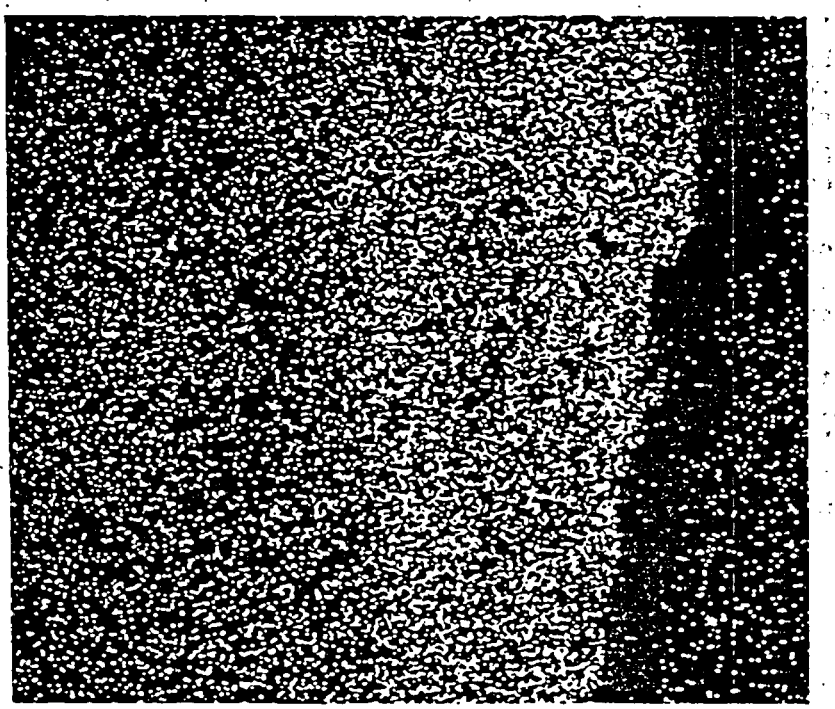

(c)

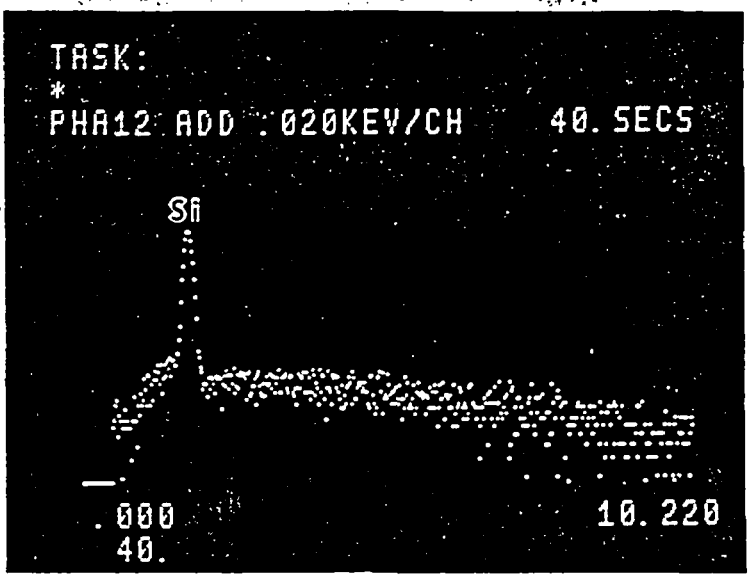

Figure 12. Surface morphology of Ferrovac-E immersed in concentrated basaltic groundwater at 150°C for two months under a gamma dose rate of 1.36×10^6 rad/h. The majority of the exposed surface area was not attacked and there was no salt deposition. Only two or three spots were corroded as shown in (a) and (b), (a) pit mark and (b) shiny black corrosion product.

(a)

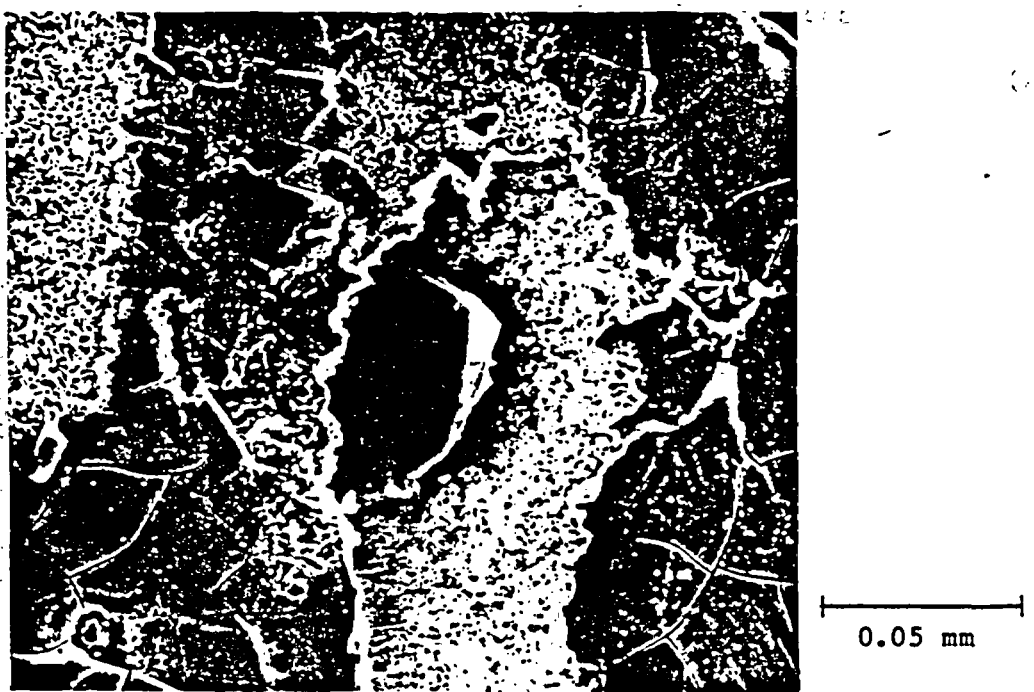

(b)

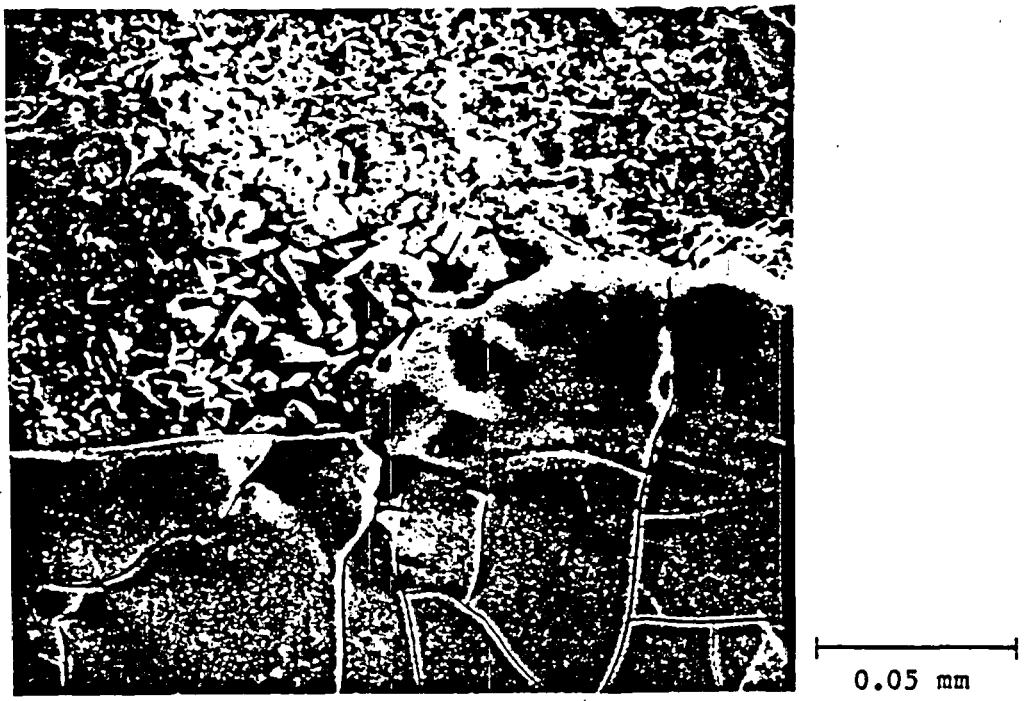

Figure 13. Surface morphology of ASTM A216-Grade WCA cast steel after immersion in concentrated basaltic groundwater at 150°C for two months under a gamma dose rate of 1.36×10^6 rad/h. The majority of the exposed surface area was covered with a salt deposit and there was no significant corrosion except for a few spots adjacent to a glass spacer, (a) pit formation and corrosion product in attacked area, (b) etching of metal substrate beneath the deposited salt layer.

(a)

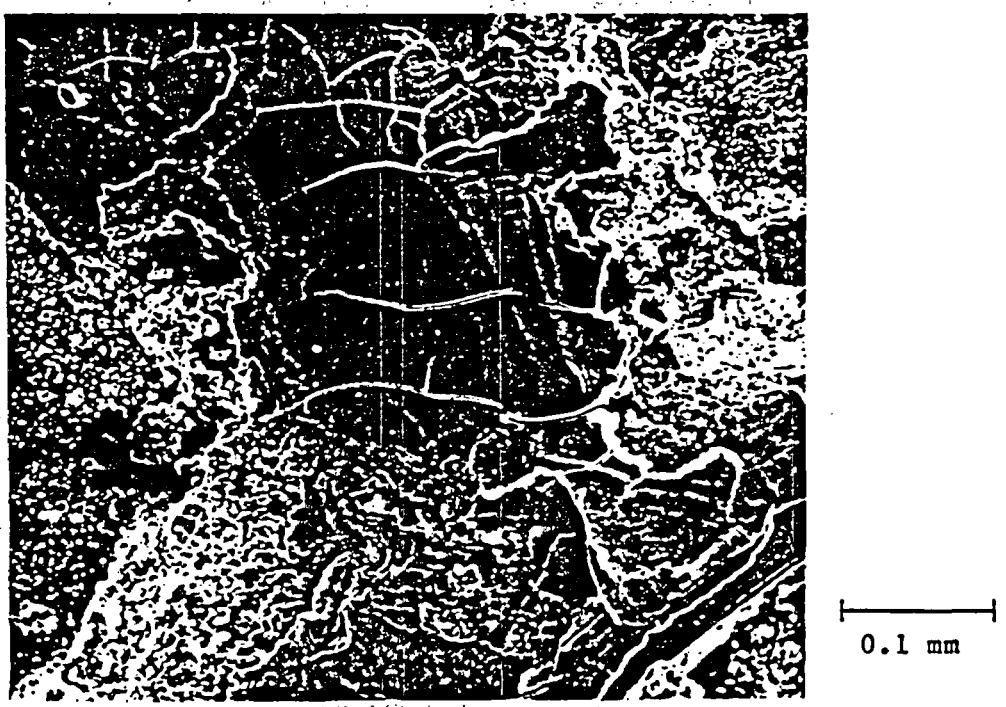

(b)

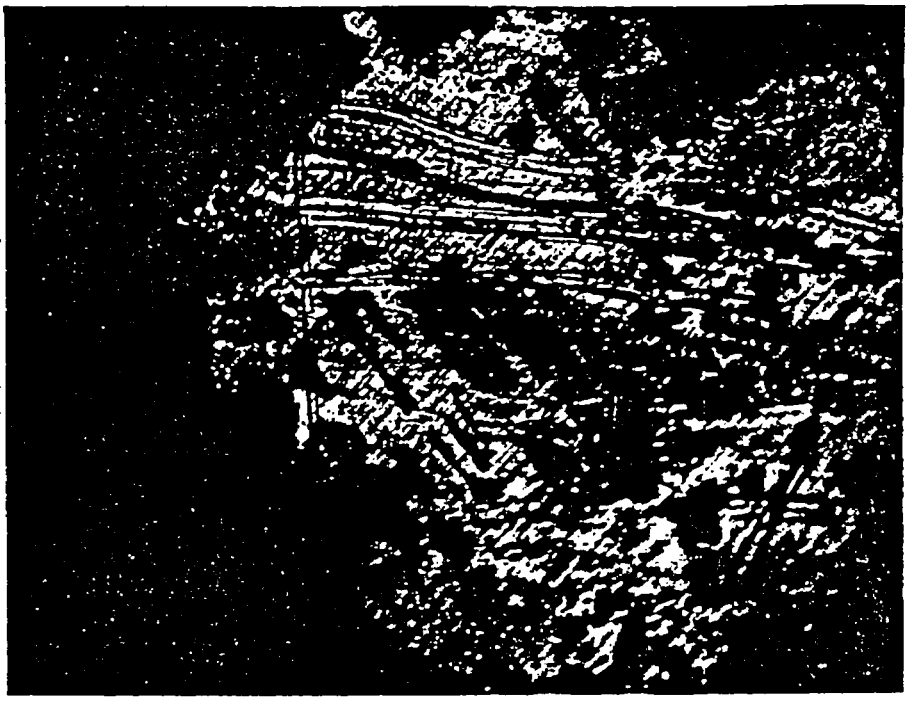

0.1 mm

Figure 14. Surface morphology of welded ASTM A216-Grade WCA cast steel after immersion in concentrated basaltic groundwater at 150°C for two months under a gamma dose rate of 1.36×10^6 rad/h. The majority of the exposed surface area was covered with a salt deposit and there was no significant corrosion. No welding effects on corrosion were observed. When the salt deposit was removed by scratching, pits and an etched metal surface were observed as shown (a) and (b).

(a)

0.1 mm

(b)

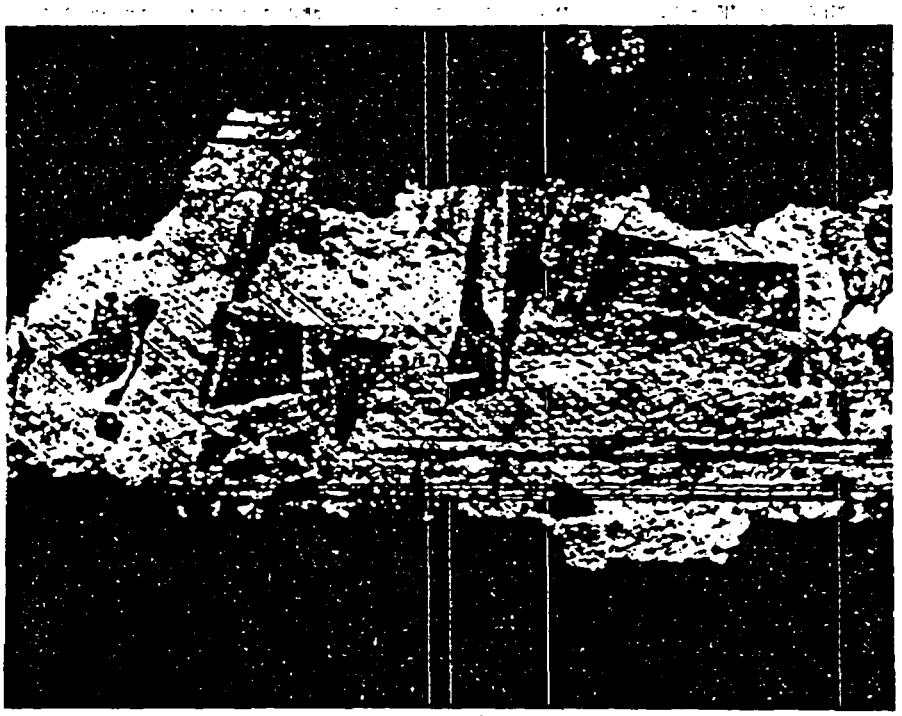

Figure 15. An SEM micrograph for an ASTM A216-Grade WCA steel specimen, exposed to concentrated basaltic groundwater for two months at 150°C, showing a very irregular oxide thickness on the base metal.

The reasons for the inhibition of corrosion under gamma irradiation need to be addressed. There are about five possibilities as described below. (1) Oxygen consumption during salt layer formation: this is unlikely because SiO_2 is usually dissolved in the solution in a hydrated form and it does not need additional oxygen to form a precipitated silicon oxide. Even though different amounts of solution were used in the two tests (25 cc for irradiation corrosion and 200 cc for non-irradiation corrosion), there will be abundant radiolytic oxygen (or oxidizers) to give corrosion in the irradiation environment. Besides the radiolytic oxygen, the majority of the initial oxygen from the air cover gas remained. This can be shown by the ratio of oxygen concentration to nitrogen concentration in Table 6. (2) Passive film formation: under gamma irradiation, oxidizers formed may produce passive surface films. However, the observation of etching beneath the salt film allows this possibility to be discarded. (3) Iron ion saturation: the irradited test solution may be saturated in iron due to its limited volume, leading to decreased dissolution rates. However, the dissolved ions should easily react producing oxides near to the metal surface. Therefore, this possiblity is also unlikely. (4) Hydrogen effects: hydrogen gas produced by radiolysis tends to form a reducing environment. Actually, it will retard the cathodic reaction if hydrogen reduction occurs. In the presence of oxygen, however, oxygen reduction would be the cathodic reaction. (5) Anodic inhibitor effects: Oxidizers formed by radiolysis may affect the anodic reaction. A classical example of such a reaction is:[10]

$$2H_2O_2 \longrightarrow 2H^+ + O_2 + 2e^-$$

When this reaction retards the metal dissolution rate, the corrosion rate is also decreased, and the corrosion potential is increased as depicted in Figure 16. To test this hypothesis, a preliminary DC polarization test was performed in an air-saturated solution, and in an air-saturated solution containing H_2O_2. Reference polarization curves in deoxygenated solutions were reported previously.[11] As shown in Figure 17, the corrosion potential is increased and the corrosion current seems to be decreased by the addition of 36 cc H_2O_2 (120 cc of 30% concentration) in 80°C groundwater. Currently, this test is being repeated for confirmation. Among the five possibilities given above, (1) and (5) are most probable. More work is being carried out to test the two hypotheses.

With respect to the corrosion resistance of Ferrovac-E under gamma irradiation conditions, no detailed explanations can be given at this time. More electrochemical work is necessary to explain this phenomenon.

6. HYDROGEN PERMEATION IN CAST LOW CARBON STEEL

To quantify hydrogen uptake during aqueous corrosion, it is necessary to obtain hydrogen permeation kinetics for iron and steels. In this quarter, we have constructed two types of permeation equipment: (1) a gas phase permeation cell and (2) an electrochemical permeation cell.

Figure 16. A schematic of polarization behavior in the presence of an anodic inhibitor. $V_{e,c}$ and $V_{e,a}$ are the equilibrium potentials for the cathodic and anodic reactions respectively. The corrosion current I_{corr} is decreased (ΔI_{corr}) and the corrosion potential V_{corr} is increased (ΔV_{corr}) by the addition of the inhibitor.(12)

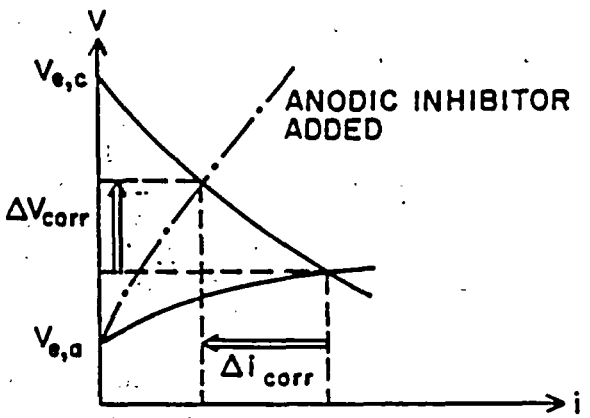

Figure 17. Anodic polarization curve for ASTM A216-Grade WCA cast steel in concentrated basaltic groundwater at 80°C (scan rate 1 mV/sec), (a) air saturated solution and (b) solution contains an addition of 120 mL H_2O_2 of 30% concentration.

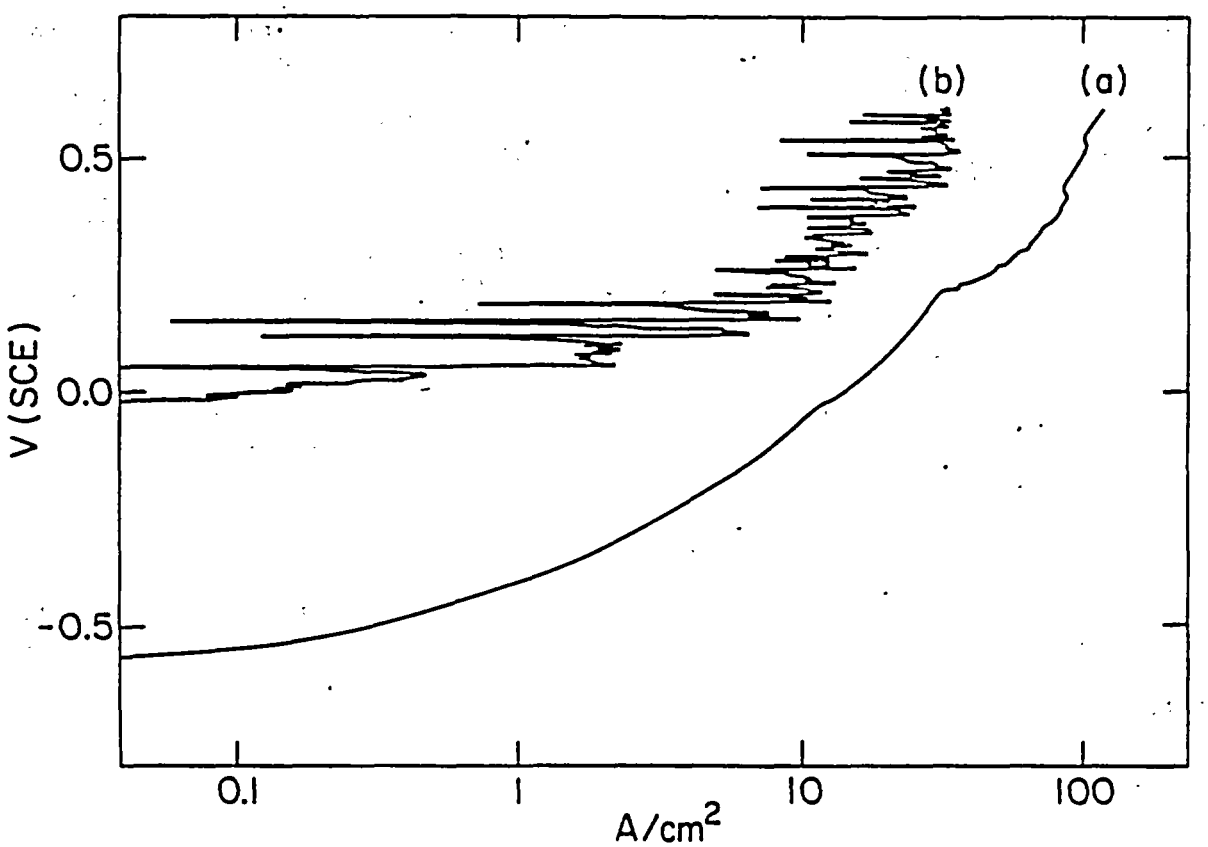

Figure 18 shows a schematic of the hydrogen permeation test cell used in the gamma irradiation work. A 1.27 cm diameter cylinder of the cast steel (wall thickness 1.05 mm) was immersed in the concentrated groundwater which is encapsulated in a stainless steel bomb lined with a silica tube. The upper part of the ast steel cylinder was plated with cadmium to minimize hydrogen entry or loss. The cylinder was connected to a pressure transducer to monitor the pressure change inside the cyliner. The outside of the cylinder was also connected to a pressure transducer to monitor the pressure change. The assembly was heated to 150°C in a gamma flux of 1.3×10^6 rads/h while the pressure changes were contiuously monitored. The first run was not fully successful because of the corrosion of the pressure transducer electrical connections. Neverthelss, Figure 19 shows pressure build-up in the outer container. The build-up is gradual, apparently because of hydrogen absorption in the test cylinder. The data in Figure 20 show that there was some gas permeation through the inner cylinder. The test will be repeated once more using an improved system design.

The electrochemical test cell has been constructed and work in this area will commence in the future.

7. OTHER ACTIVITIES

In this quarter, 15 draft topical reports on titanium corrosion were prepared and are being internally reviewed. A titanium corrosion paper was presented at Corrosion/84 in New Orleans. In January, Dr. K. S. Lee, a visiting scientist, developed a hydrogen permeation test cell. There were two information exchange meetings, one with the Corrosion Research Center of the University of Minnesota and the other with Battelle Columbus Laboratory.

Figure 18. Gas permeation test cell for ASTM A216-Grade WCA steel tube. The shaded component is made of mild steel welded to the tube and coated with Cd. Radiolytic gas (particularly hydrogen) is expected to permeate through the tube.

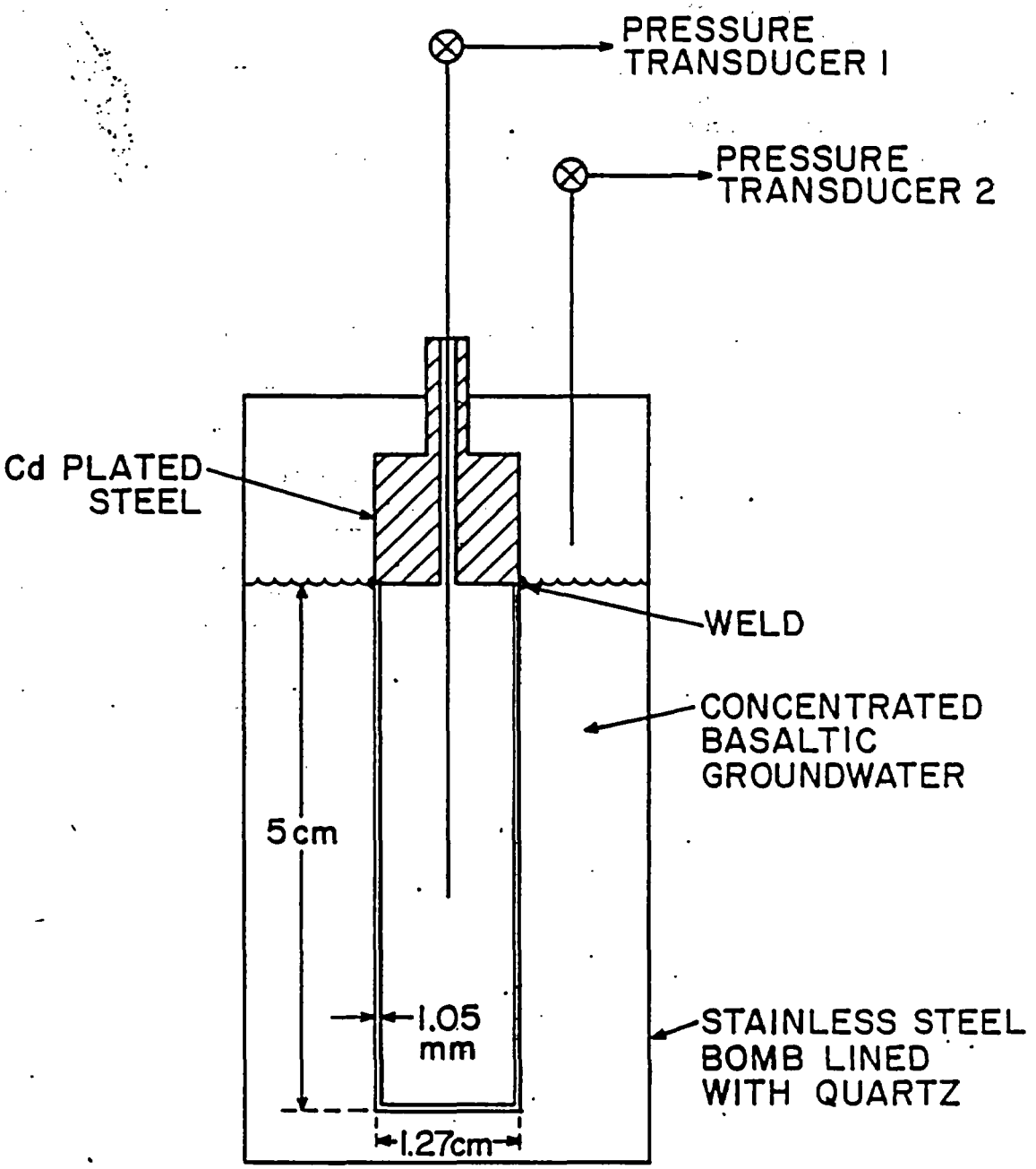

Figure 19. Gas pressure changes outside the cast steel tube during gamma irradiation of concentrated basaltic water at 150°C. The dose rate was 1.36×10^6 rad/h. The open circles are pressures measured after the termination of irradiation.

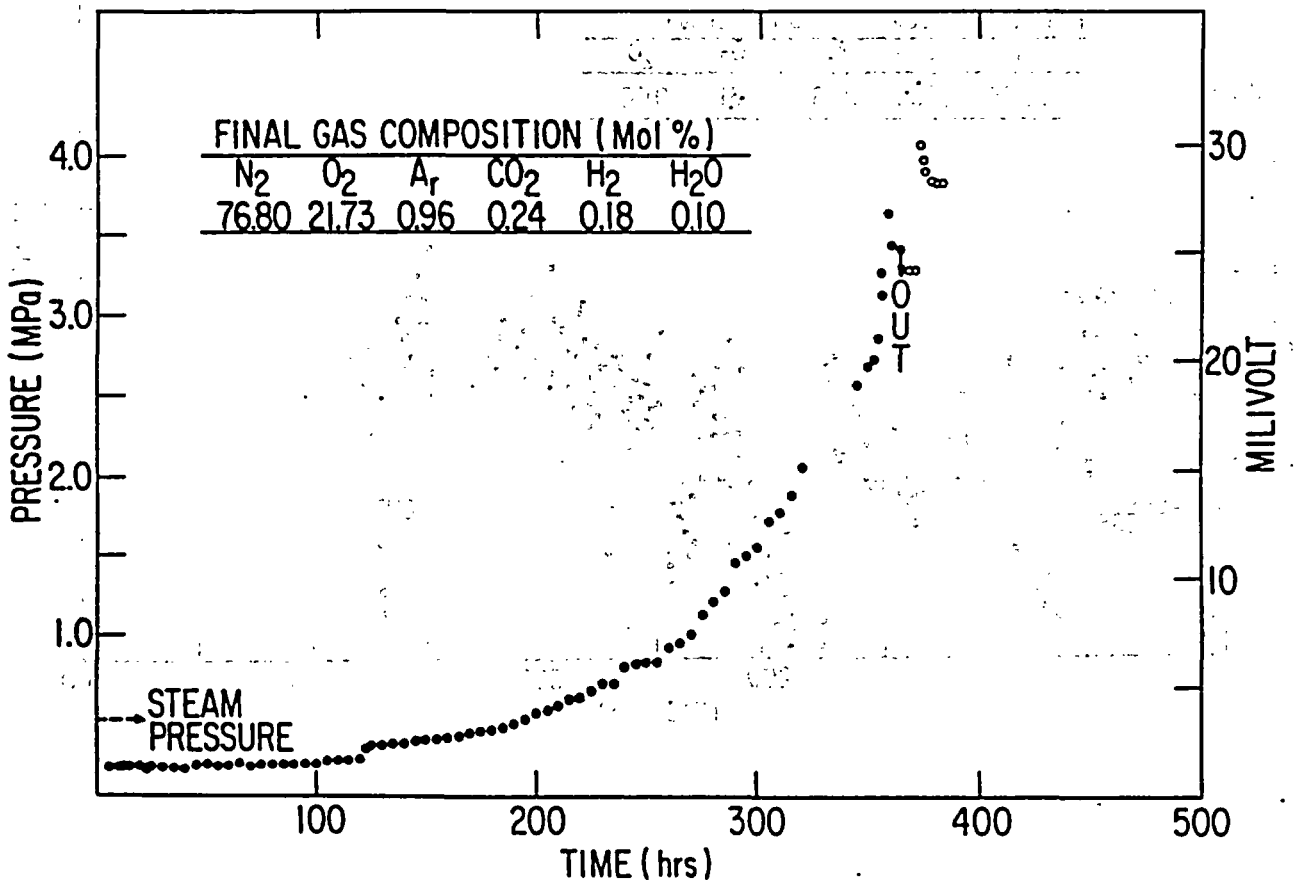

Figure 20. Gas pressure changes inside the cast steel tube of the hydrogen permeation cell. The open circles are pressures measured after the termination of irradiation.

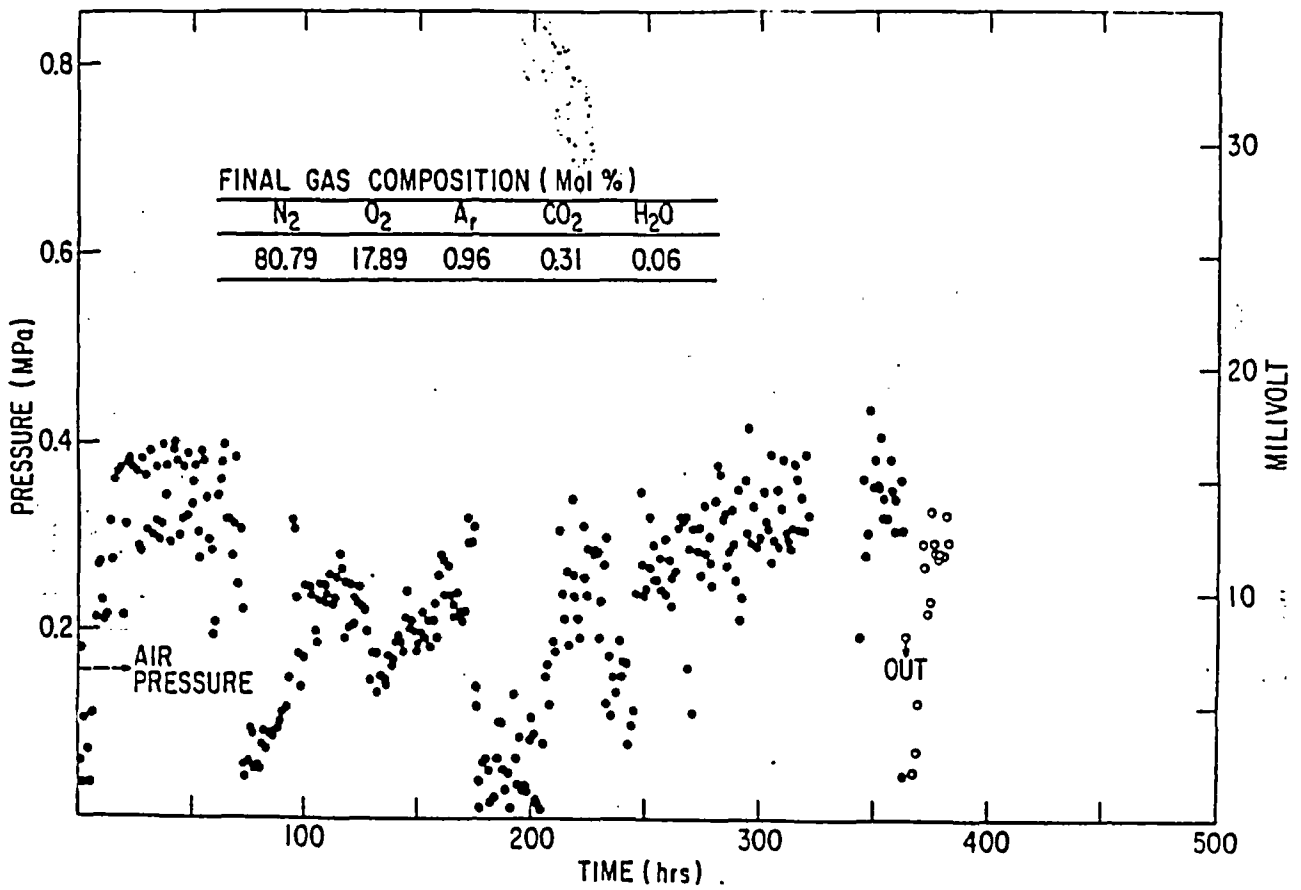

8. REFERENCES

(1) T. M. Ahn and P. Soo, "Container Assessment--Corrosion Study of HLW Container Materials," Brookhaven National Laboratory, Informal Report, BNL-NUREG-34220 (1984).

(2) ASTM Designation A216-83, "Standard Specification for Steel Castings, Carbon, Suitable for Fusion Welding for High Temperature Service," Available from ASTM, Philadelphia, PA.

(3) R. W. Staehle, "Predictions and Experimental Verification of the Slip Dissolution Model for Stress Corrosion Cracking of Low Strength Steel," in Steel Corrosion Cracking and Hydrogen Embrittlement of Iron Base Alloys, edited by R. W. Staehle, J. Hochmann, R. D. McCright and J. E. Slater, NACE (1977).

(4) M. J. Steindler and others, Fuel Cycle Programs Quarterly Progress Report, July--September, 1982, Argonne National Laboratory (1982).

(5) J. O'M. Bockris and P. K. Subramanyan, "The Equivalent Pressure of Molecular Hydrogen in Cavities Within Metals in Terms of the Overpotential Developed During the Evolution of Hydrogen," Electrochemica Acta, 16, 2169 (1971).

(6) J. A. Kargol, N. F. Fiore and R. J. Coyle, Jr., "A Model for H-Absorption by Metals," Met. Trans A, 183 (1981).

(7) M. Smialowski, "Hydrogen Blistering and Surface Microcracks," ibid reference (3), p. 405.

(8) W. J. Gray, "Gamma Radiolysis Effects on Grande Ronde Basaltic Groundwater," Pacific Northwest Laboratory, RHO-BW-SA, p. 315 P (1983).

(9) K. Kikuchi and R. B. McLellan, "The Solubility and Diffusivity of Hydrogen in Well-Annealed and Deformed Iron," Acta Metallurgica, 31, 961 (1983).

(10) A. V. Byalobzheskii, Radiation Corrosion, Translated from Russion, AEC (1967).

(11) D. Stahl and N. E. Miller, "Long Term Performance of Materials Used for High-Level Waste Packaging," NUREG/CR-3427, Vol. 3 (1983).

(12) J. O'M Bockris and D. M. Drazic, Electrochemical Science, p. 251, Barnes and Noble Books, New York (1972).